STUDYING SUBDUCTION ZONE DYNAMICS AND CONTINENTAL EVOLUTION IN SOUTH AMERICA USING DATA-ORIENTED GEODYNAMIC MODELS

BY

JIASHUN HU

DISSERTATION

Submitted in partial fulfillment of the requirements
for the degree of Doctor of Philosophy in Geology
in the Graduate College of the
University of Illinois at Urbana-Champaign, 2018

Urbana, Illinois

Doctoral Committee:

Associate Professor Lijun Liu, Chair and Director of Research
Professor Jay D. Bass
Professor Xiaodong Song
Professor Craig Lundstrom

Abstract

Among all continental plates, South America remains one of the least explored regarding its geological evolution. This continent possesses the longest subduction zone, the second highest continental plateau and tremendous amounts of volcanic eruption on its western coast. On the eastern coast, the Brazilian highlands that reach more than 1 km above the sea level were once submerged by shallow ocean in Mid-Cretaceous. All these magnificent landscapes and the associated dramatic geologic events are potentially linked to the underlying restless mantle convection that has persisted for billions of years.

The purpose of my dissertation is to understand the causes and consequences of the major geological events in South America and evaluate the potential role of mantle convection in driving subduction zone dynamics and continental evolution. Yet, these geological events usually have distinct characteristics. Some of them are extreme events that occur within several minutes to days and have great impact on local societies, such as earthquakes and volcanic eruptions; while others may span a long geological period and exert gradual but significant influence in Earth evolution, such as mountain building and surface uplifts.

Modern observations have contributed a lot to the study of the tectonics in South America, but they usually have limited spatial or temporal coverage. For example, seismic tomography reveals the present mantle structure which is only a snapshot of Earth's history. Thermochronology can tell us the exhumation history of a rock that may span tens to hundreds of millions of years, but the inference is spatially restricted to the sampling area. While numerical modeling can largely overcome these shortcomings, it is affected by uncertain model parameters. As a result, many tectonic questions remain open, with little consensus from decades' of dedicated research.

One promising way to further investigate the tectonics of South America is through the cutting-edge multi-disciplinary research. In this dissertation, we apply numerical modeling with sequential data assimilation that progressively incorporates the paleo-reconstructions of plate kinematics and seafloor ages. The outputs are calibrated by multiple observations, including seismic tomography, earthquake source properties, distribution of volcanisms, seismic anisotropy,

topography and gravity, mineral physics, as well as geological data such as mountain shortening and paleo-altimetry. The synergy among all these disciplines not only increases the spatial and temporal coverage of the research topics, but also narrows down the intrinsic uncertainties in each discipline.

In practice, we tailor our multi-disciplinary models for two research topics, subduction zone dynamics and continental evolution.

For the first topic, we use geodynamic models with plate kinematics and seafloor ages as boundary conditions to reproduce the history of South American subduction since the Late Cretaceous. With this model and the constraints mentioned above, we attempt to investigate the dynamic causes (Chapter 2) and consequences (Chapter 3) of flat subduction, as well as seismic anisotropy caused by subduction-induced mantle flow (Chapter 4). Our model reveals that the flat slabs in South America are caused by the synergy of dynamic suction from the overriding plate and the extra buoyancy provided by subducting oceanic plateau and aseismic ridges. The broken flat slab configuration due to the subduction of aseismic ridges better explains the abnormal distribution of intermediate-depth earthquakes and volcanisms as well as the intra-slab stress patterns than earlier models. This model also suggests that the mantle flow is controlled by the subducting slabs, with Poiseuille flow dominating the sub-continental region and Couette flow dominating the sub-oceanic region. Such a flow pattern best matches the observed patterns of surface wave anisotropy and shear wave splitting.

For the second topic, we further combine this well-established geodynamic model with observations from other disciplines, including residual topography, residual gravity, reconstructed hotspot tracks, and surface geology, to study the temporal evolution of the cratonic lithosphere (Chapter 5). We find that lowermost cratonic lithosphere is compositionally denser than the asthenospheric mantle and can be episodically removed when perturbed by underlying mantle dynamics, while the shallower buoyant lithosphere helps to stabilize cratonic crust over billions of years. We further show that zones where the lithosphere was lost would take tens of millions of years to recover thermally, but the density of the new thermal root would remain less than that of the intact root. This new model challenges the traditional view on the density profile and tectonic stability of cratons, and thus have important implications on continental evolution.

Overall, this dissertation shows that modern multi-disciplinary research that combines data-assimilation numerical modeling with various geological and geophysical observations, could greatly help us understand the tectonic driving forces in continents like South America.

Dedicated to Mom, Dad and Liqun

for their love and support.

Acknowledgements

It has almost been five years since I first step on the land of the United States. Now this place, the college town Urbana-Champaign, has become a place full of good memories and gratitude. I owe many thanks to the people around me. My first thanks, of course, go to my advisor Prof. Lijun Liu. When I first came here as a bewildered foreign student, he was the first person that I could rely on and get help from. Throughout these five years, he's been so supportive and patient on my research. He is always there whenever I need to discuss with him, ask for suggestion from him, get help from him or even just chat with him when I get frustrated. He is so brilliant and knowledgeable, and energetic on research. His insightful ideas have become the paving stone of my academic successes as a PhD student. He is also very considerate and have clear plans that are customized for different personalities and abilities. I have learned a lot from him, including the way to think scientifically, the devotion to scientific research and the spirit of hard-working and never-give-up. These things will influence me for a lifetime. I would like to use this opportunity to express my sincere gratitude to my advisor.

I would also like to acknowledge all the instructors and colleagues in this department. Prof. Xiaodong Song has taught me seismology and has generously offered me a lot of advices on my career development. Every time I talked to him, I would feel encouraged and was more determined to chase my goal. Prof. Craig Lundstrom has broadened my knowledge in petrology and geochemistry. He has been actively participating in my research, with his knowledge being a big complement to my research. Prof. Jay Bass, who introduces me to the realm of mineral physics, has keen insights on everything. As a laboratory scientist, his dedicated work style has stimulated my will to go for science. Prof. Steve Marshak has taught the best geology course I have ever seen. His teaching style has inspired me a lot. Prof. Patricia Gregg and William Guenthner have taught me mid-ocean ridge tectonics and orogenic systems. Their newly joining has made our department stronger in geophysics and tectonics. The department secretaries Marilyn Whalen, Lana Holben and Rachel Davidson have provided a lot of help in routine matters, making sure everything runs well. Many thanks to our Italian friend, Prof. Manuele Faccenda, who has been a key collaborator for years.

I also want to thank all the graduate students in my research group and all my friends at this university: Dr. Jin Zhang, Dr. Jing Jin and Jiangtao Li, for all the helpful discussion in mineral physics and seismology; my fellow graduate student Quan Zhou, for all the collaboration we participate and all the difficulties we have been going through since we came here together, Ching Chang, Yaoyi Wang, Diandian Peng and Zebin Cao for all the time we have spent in the same research group. I am also grateful to Jingtao Lai, Yan Zhan, Yi Yang, Cindy Li, Fangruo Zhao, Xiaobao Lin, Yuchen Liu, Hongyu Xiao, Ran Mei, Shuyang Wang, Qianqi Song and many others, for all your friendship.

Finally, I want to give my sincere gratitude to my parents and my girlfriend Liqun Zeng. My parents have sacrificed the most to raise me and send me to university. I owe them not only my life, but also the good personalities and habits, as well as most of the accomplishments I have made so far. My girlfriend, Liqun, has accompanied me through these years abroad. It is her support and understanding that pull me out from self-suspicion. It is her love to life that lightens my world and makes it colorful. I lack words to express my thanks to Liqun.

Table of Contents

Chapter 1

Introduction

1.1 Motivation

The establishment of *Plate Tectonic* theory in 1960s marked the start of a new era in the study of the Earth's coupled crust-mantle system. It is now widely accepted that the outer rigid layer of the Earth (*lithosphere*) is made of a couple of dozen plates. The motion of the plates can be reconstructed through paleomagnetism (Engebretson et al., 1985). This type of reconstruction has been evolving with increasing amounts of details (Müller et al., 2008; 2016; Torsvik et al., 2008, 2012). Many geologic processes have been attributed to the relative motion between different plates. For example, plate convergence creates mountains such as the Tibet Plateau and the Andes; while plate divergence creates mid-ocean ridges such as those in the Pacific and Atlantic. Inside the Earth's interior, seismic tomographic inversions have, with increasing resolving power, outlined fast anomalies beneath the subduction zones (e.g. Grand, 2002; Ritsema et al., 2011; Obayashi et al., 2013), most of which could represent subducted slabs. These slabs, on the one hand, are thought to drive large-scale mantle convection, and, on the other hand, could pull their surface plates into the mantle, both of which may help to drive the tectonic plates (Conrad and Lithgow-Bertelloni, 2002; Stadler et al., 2010; Becker and Faccenna, 2011). These big concepts outline the most basic dynamic processes of the solid Earth.

On the other hand, numerous studies have been done to refine the Plate Tectonic theory, especially regarding its application to continents. For example, people intensively study the North American plate to understand the structure of the continental lithosphere (e.g. Lin et al., 2008; Yuan and Romanowicz, 2010), the formation of Basin and Range (e.g. Proffett., 1977), the origin of Yellowstone hotspot track (e.g. Carlson and Hart, 1987; Kincaid et al., 2013; Zhou et al., 2018), the topographic evolution of Colorado Plateau (e.g. Roy et al., 2009; Levander et al., 2011), the causes of the Farallon flat slab (Liu et al., 2010; Liu and Currie, 2016) and its impact on the buildup of Rocky Mountains (e.g. Bird, 1988), etc. Compared with North America, South America is much less well explored. Yet, the tectonic features in South America could have important implications on the evolution of the whole Earth. For instance, the formation of the Andes could give insights

on Sevier Orogeny of the North American Cordillera and its impact on global climate change; the deformation of the Sierras Pampeanas is considered a modern analogue to the basement-cored uplifts exemplified by the Laramide orogeny (Jordan & Allmendinger 1986) that bears important implication on lithosphere deformation.

To gain more insights in the evolution of South America, it is important and necessary to study its various tectonic features. The South American plate has the longest continuous subduction zone in the world that stretches 7500 km from ~10°N to ~60°S (Klotz et al., 2001). Subduction along this ocean-continent convergent boundary started no later than the Cretaceous during the final separation of the supercontinent Pangaea (Müller et al., 2016). Along the trench, several segments of flat slab have been identified, including Bucaramanga, Peruvian and central Chile flat slabs (Gutscher et al., 2000), which are intervened by normal to steep subduction. Although a number of possible mechanisms have been proposed to explain the formation of flat slabs (e.g. Gutscher et al., 1999; van Hunen et al., 2000; Jones et al., 2011), a systematic quantitative evaluation of the relative importance of different mechanisms is still missing. As a result, the causes and consequences of flat slabs remain controversial.

The continuous convergence between the South American plate and Nazca plate have also created the second largest plateau in the world, the Altiplano-Puna plateau (Eichelberger et al., 2015), which is part of the Andean orogenic belt. The subduction zone is also characterized by strong shortening in central Andes and weak shortening to no deformation at both ends of the subduction zone since ~45 Ma (Kley and Monaldi, 1998; Schellart, 2008), resulting in the Arica Bend. Accompanying the uplift and shortening is the enigmatic magmatism in central Andes. Extreme broadening of volcanic activities took place in the whole region since 25 Ma, with massive ignimbrite flare-ups taking place at the same time (Trumbull et al., 2006). These first-order events reflect the fundamental mechanism of a convergence boundary, evoking a lot of research interests (e.g. Capitanio et al., 2011; Faccenna et al., 2017). However, not much consensus has been achieved.

Within the continent, the Amazonia craton (AZ), the Sao Francisco craton (SF) and the Rio de la plata craton (RP) have formed the core of the South American continent (Loewy et al., 2004). High topography has been developed within and along the edges of SF, in contrast to the low topography generally observed in most cratons on Earth. This high topography developed during

and since the late Mesozoic, as indicated by the presence of earlier marine-lacustrine depositional environments (Arai and Chapadas, 2000), widespread Cretaceous volcanic eruptions (Harman et al., 1998), and associated surface uplift (Cogné et al., 2011; Read et al., 2004). Understanding the origin of this high topography is important because it may shed light on the density structure and temporal evolution of continental lithosphere, a topic that still lack good understanding.

1.2 Research framework

In this dissertation, we try to combine numerical simulation with multi-disciplinary observational records in South America, aiming to unravel the puzzles of subduction zone dynamics and continental evolution. As this dissertation shows, the models we built successfully explain many major tectonic features of the region. Along the trench, we have investigated the mechanisms of flag slab formation (Hu et al., 2016), the configuration of flat slabs as well as its implication on abnormal seismological and magmatic processes (Hu and Liu, 2016). We find that the modern flat slab segments in South America are caused by a combination of seafloor age variation, hydrodynamic suction from the overriding plate, and subduction of buoyancy features. Slab strength dominates its buoyancy at age > 30 Ma and the opposite for younger ages. While dynamic suction from the overriding plate generates a permanent reduction of the long-wavelength slab dip angle, it is the subducting oceanic plateau and aseismic ridges that shapes the transient and localized flat-slabs as observed. In addition, we find that these slabs are internally torn, as is due to the 3D nature of the subducting buoyancy features. This broken slab configuration, confirmed by regional tomography, naturally explains the abnormal distribution of and stress regimes associated with the intermediate-depth earthquakes as well as the formation of adakitic and ore-forming magmatism.

Within regions below plate interiors, we have discussed the subduction-induced seismic anisotropy (Hu et al., 2017). We find that the dominant control on seismic anisotropy in South America comes from subduction-induced mantle flow, where anisotropy below the subducting Nazca Plate aligns with plate-motion-induced Couette flow and that below the overriding South American Plate follows slab-induced Poiseuille flow. This large-scale mantle flow can be diverted by secondary slabs, such as that below the Antilles subduction zone. In contrast, the contribution to SWS from fossil continental anisotropy and from the effects due to mantle flow modulation by lithosphere thickness variation are minor. The anisotropy study suggests the upper-mantle fast

seismic anomalies beneath the southern Atlantic margin should have close-to-neutral buoyancy, which eventually leads to our investigation on craton-plume interaction (Hu et al., 2018).

We find large portions of the cratonic lithosphere in South America and Africa have experienced significant alteration since the Mesozoic, as evidenced from widespread Cretaceous surface uplift and volcanism, and present-day high topography, thin crust and negative lithospheric gravity anomalies. We show that these observations reflect increased lithospheric buoyancy due to plume-triggered cratonic root loss in the Late Cretaceous. The lithosphere has been thermally reestablished since then, as confirmed by present-day mantle tomography and lithospheric seismic anisotropy. We conclude that lowermost cratonic roots are denser than previously thought and can be episodically removed when perturbed by underlying mantle dynamics, while the shallower buoyant depleted lithosphere helps to stabilize cratonic crust over geological time.

Finally, we discuss the mechanisms that control central Andean shortening, the uplift of Altiplano-Puna Plateau and the broadening of arc magmatism. We show that our data-oriented geodynamic models with a hybrid velocity boundary condition is a very useful tool for the study of such complex systems. We further upgrade our regional model to a global model, to demonstrate the power of such models in evaluating subduction dynamics and mantle flow world-wide.

1.3 Review of sequential data-assimilation techniques

Accompanying the need to address more scientific questions, numerical simulation techniques have become more and more powerful. The overall trend in the development of mantle convection models is that their supporting codes are more and more sophisticated, so that the model can better resolve real Earth scenarios. The first generation of data-oriented convection models using the sequential assimilation technique (Bunge et al., 1998; Gurnis et al., 1998; McNamara and Zhong, 2005) with imposed surface plate motion cannot resolve slabs in the subduction zone, due to their limited numerical resolution and lack of sophisticated subduction zone rheology features. Subsequently, Liu and Stegman (2011) introduced a weak mantle wedge above the slab to facilitate one-side subduction of oceanic plates, and their model could resolve much finer slab structures, such as the segmentation and tearing of the Farallon slab that may be responsible for the Columbia River flood basalt (Liu and Stegman, 2012).

Along this direction, we further improve the subduction model by introducing more mantle compositions to account for chemical buoyancy and composition-dependent viscosity (Hu et al.,

2016; Hu and Liu, 2016). We also include thermal-chemical continents (Hu et al., 2017) in our model, so that the interaction between the subducting plate and overriding plate is more realistic and the coupled crust-mantle system is better represented in subduction zones. Finally, we applied these techniques in and expanded our regional model to a high-resolution global model (Hu et al., in revision). In this model, we incorporate a relatively realistic rheology, including temperature-, composition- and depth-dependent viscosity, composition-based weak oceanic crust and arc-like plate boundary features, all ensuring the generation of realistic subduction. Relative to published works of its kind, our model could better represent the evolution and morphology of slabs, especially at upper mantle depths, the resulting mantle flow that forms seismic anisotropy, as well as the interaction between the slab and overriding plates.

1.4 References

Arai, M., Chapadas: relict of mid-Cretaceous interior seas in Brazil, in Revista Brasileira de Geociencias 30, 436-438 (2000).

Becker, T.W., and C. Faccenna. Mantle conveyor beneath the Tethyan collisional belt, Earth Planet. Sci. Lett. 310, 453-461 (2011).

Bird, P., 1988. Formation of the Rocky Mountains, western United States: A continuum computer model. Science, 239(4847), pp.1501-1507.

Capitanio, F. A., Faccenna, C., Zlotnik, S., & Stegman, D. R. (2011). Subduction dynamics and the origin of Andean orogeny and the Bolivian orocline. Nature, 480(7375), 83-86.

Carlson, R. W. & Hart, W. K. Crustal genesis on the Oregon plateau. J. Geophys. Res. 92, 6191–6206 (1987).

Cogné, N., K. Gallagher, and P.R. Cobbold, Post-rift reactivation of the onshore margin of southeast Brazil: Evidence from apatite (U–Th)/He and fission-track data, Earth Planet. Sci. Lett., 309, 118-130 (2011).

Conrad, C.P., and C. Lithgow-Bertelloni, How mantle slabs drive plate tectonics, Science, 298, 207-209 (2002).

Eichelberger, N., McQuarrie, N., Ryan, J., Karimi, B., Beck, S., & Zandt, G. (2015). Evolution of crustal thickening in the central Andes, Bolivia. Earth and Planetary Science Letters, 426, 191-203.

Engebretson, D.C., A. Cox, Gordon R G. Relative motions between oceanic and continental plates in the Pacific basin, GSA Spec. Pap., 206, 1-60 (1985).

Faccenna, C., Oncken, O., Holt, A.F. and Becker, T.W., 2017. Initiation of the Andean orogeny by lower mantle subduction. Earth and Planetary Science Letters, 463, pp.189-201.

Grand, S.P., Mantle shear–wave tomography and the fate of subducted slabs. Philo. Trans. Roy. Soc. Lond. A, 360(1800), 2475-2491 (2002).

Gurnis, M., Müller, R.D. and Moresi, L., 1998. Cretaceous vertical motion of Australia and the AustralianAntarctic discordance. Science, 279(5356), pp.1499-1504.

Gutscher, M. A., Olivet, J. L., Aslanian, D., Eissen, J. P., & Maury, R.. The “lost Inca Plateau”: cause of flat subduction beneath Peru?. Earth and Planetary Science Letters, 171(3), 335-341 (1999).

Gutscher, M.A., Spakman, W., Bijwaard, H., Engdahl, E. R. (2000). Geodynamics of flat subduction: seismicity and tomographic constraints from the Andean margin. Tectonics, 19(5), 814-833.

Harman, R., K. Gallagher, R. Brown, A. Raza, and L. Bizzi, Accelerated denudation and tectonic/geomorphic reactivation of the cratons of northeastern Brazil during the Late Cretaceous, J. Geophys. Res., 103, 27091-27105 (1998).

Hu, J., Liu, L., Hermosillo, A. and Zhou, Q., 2016. Simulation of late Cenozoic South American flat-slab subduction using geodynamic models with data assimilation. Earth and Planetary Science Letters, 438, pp.1-13.

Hu, J. and Liu, L., 2016. Abnormal seismological and magmatic processes controlled by the tearing South American flat slabs. Earth and Planetary Science Letters, 450, pp.40-51.

Hu, J., Faccenda, M. and Liu, L., 2017. Subduction-controlled mantle flow and seismic anisotropy in South America. Earth and Planetary Science Letters, 470, pp.13-24.

Hu, J., Liu, L., Faccenda, M., Zhou, Q., Fischer, K.M., Marshak, S. and Lundstrom, C., 2018. Modification of the Western Gondwana craton by plume–lithosphere interaction. Nature Geoscience, p.1.

Hu, J., Liu, L. & Zhou, Q. (2018). Reproducing Past Subduction Using High-resolution Global Convection Models. Earth and Planetary Physics, in review.

Jones, C. H., Farmer, G. L., Sageman, B., & Zhong, S. (2011). Hydrodynamic mechanism for the Laramide orogeny. Geosphere, 7(1), 183-201.

Jordan, T.E. and Allmendinger, R.W., 1986. The Sierras Pampeanas of Argentina; a modern analogue of Rocky Mountain foreland deformation. American Journal of Science, 286(10), pp.737-764.

Kincaid, C., Druken, K. A., Grifths, R. W. & Stegman, D. R. Bifurcation of the Yellowstone plume driven by subduction-induced mantle fow. Nat. Geosci. 6, 395–399 (2013).

Kley, J., & Monaldi, C. R. (1998). Tectonic shortening and crustal thickness in the Central Andes: How good is the correlation?. Geology, 26(8), 723-726.

Klotz, J., Khazaradze, G., Angermann, D., Reigber, C., Perdomo, R., & Cifuentes, O. (2001). Earthquake cycle dominates contemporary crustal deformation in Central and Southern Andes. Earth and Planetary Science Letters, 193(3), 437-446.

Levander, A., Schmandt, B., Miller, M.S., Liu, K., Karlstrom, K.E., Crow, R.S., Lee, C.T. and Humphreys, E.D., 2011. Continuing Colorado plateau uplift by delamination-style convective lithospheric downwelling. Nature, 472(7344), p.461.

Lin F.C. Moschetti M.P. Ritzwoller M.H., 2008. Surface wave tomography of the western United States from ambient seismic noise: Rayleigh and Love wave phase velocity maps, Geophys. J. Int. , 173, 281–298.

Liu, L., Gurnis, M., Seton, M., Saleeby, J., Müller, R.D. and Jackson, J.M., 2010. The role of oceanic plateau subduction in the Laramide orogeny. Nature Geoscience, 3(5), p.353.

Liu, L. and Stegman, D.R., 2011. Segmentation of the Farallon slab. Earth and Planetary Science Letters, 311(1-2), pp.1-10.

Liu, L. and Stegman, D.R., 2012. Origin of Columbia River flood basalt controlled by propagating rupture of the Farallon slab. Nature, 482(7385), p.386.

Liu, S. and Currie, C.A., 2016. Farallon plate dynamics prior to the Laramide orogeny: Numerical models of flat subduction. Tectonophysics, 666, pp.33-47.

Loewy, S. L., Connelly, J. N., & Dalziel, I. W. (2004). An orphaned basement block: The Arequipa-Antofalla Basement of the central Andean margin of South America. Geological Society of America Bulletin, 116(1-2), 171-187.

McNamara, A.K. and Zhong, S., 2005. Thermochemical structures beneath Africa and the Pacific Ocean. Nature, 437(7062), p.1136.

Müller, R. D., Sdrolias, M., Gaina, C., & Roest, W. R. (2008). Age, spreading rates, and spreading asymmetry of the world's ocean crust. Geochemistry, Geophysics, Geosystems, 9(4).

Müller, R.D., M. Seton, S. Zahirovic, et al., Ocean basin evolution and global-scale plate reorganization events since Pangea breakup, Ann. Rev. Earth Planet. Sci., 44, 107-138 (2016).

Obayashi, M., J. Yoshimitsu, G. Nolet, et al., Finite frequency whole mantle P wave tomography: Improvement of subducted slab images, Geophys. Res. Lett., 40(21), 5652-5657 (2014).

Proffett Jr, J.M., 1977. Cenozoic geology of the Yerington district, Nevada, and implications for the nature and origin of Basin and Range faulting. Geological Society of America Bulletin, 88(2), pp.247-266.

Read, G., H. Grutter, S. Winter, N. Luckmand, F. Gaunt, F. Thomsen, Stratigraphic relations, kimberlite emplacement and lithospheric thermal evolution, Quiricó Basin, Minas Gerais State, Brazil, Lithos, 77, 803-818 (2004).

Ritsema, J., A. Deuss, H.J. van Heijst, et al., S40RTS: a degree-40 shear-velocity model for the mantle from new Rayleigh wave dispersion, teleseismic traveltime and normal-mode splitting function measurements, Geophys. J. Inter., 184(3), 1223-1236 (2011).

Roy, M., Jordan, T.H. and Pederson, J., 2009. Colorado Plateau magmatism and uplift by warming of heterogeneous lithosphere. Nature, 459(7249), p.978.

Schellart, W. P., Freeman, J., Stegman, D. R., Moresi, L., & May, D. (2007). Evolution and diversity of subduction zones controlled by slab width. Nature, 446(7133), 308-311.

Stadler, S., M. Gurnis, C. Burstedde, L.C. Wilcox, L. Alisic, O. Ghattas, The dynamics of plate tectonics and mantle flow: From local to global scales, Science, 329 (5995), 1033-1038 (2010).

Torsvik, T., R. Dietmar Müller, Rob Van der Voo, Bernhard Steinberger, and Carmen Gaina. Global plate motion frames: toward a unified model. Reviews of geophysics 46, no. 3 (2008).

Torsvik, T., Rob Van der Voo, Ulla Preeden, Conall Mac Niocaill, Bernhard Steinberger, Pavel V. Doubrovine, Douwe JJ van Hinsbergen et al. Phanerozoic polar wander, palaeogeography and dynamics. Earth-Science Reviews 114, no. 3-4, 325-368 (2012).

Trumbull, Robert B., et al. "The time-space distribution of Cenozoic volcanism in the South-Central Andes: a new data compilation and some tectonic implications." The Andes. Springer Berlin Heidelberg, 2006. 29-43.

van Hunen, J., van den Berg, A. P., & Vlaar, N. J. (2000). A thermo-mechanical model of horizontal subduction below an overriding plate. Earth and Planetary Science Letters, 182(2), 157-169.

Yuan, H. and B. Romanowicz. Lithospheric layering in the North American craton. Nature, 466(7310), p.1063 (2010).

Zhou, Q., Liu, L. and Hu, J., 2018. Western US volcanism due to intruding oceanic mantle driven by ancient Farallon slabs. Nature Geoscience, 11(1), p.70.

Chapter 2

Simulation of Late Cenozoic South American Flat-Slab Subduction

2.1 Abstract[1]

The formation mechanisms of flat slabs in South America remain unclear. To quantitatively evaluate the earlier proposed mechanisms, we simulate the post-100 Ma subduction history below South America using 4-D geodynamic models by progressively incorporating plate kinematics, seafloor ages and key tectonic features including the buoyant oceanic crust, continental cratons, oceanic plateaus (i.e. the inferred Inca plateau, subducting Nazca Ridge and Juan Fernandez Ridge), as well as deformable trench profiles according to recent geological reconstructions. We find that, in the absence of an overriding plate and subducting buoyancy features, the seafloor age affects slab dip angle by controlling the slab's mechanical strength (i.e., the resistance to bending) and negative buoyancy (integrated positive density anomaly that enhances bending). Our models show that slab strength dominates its buoyancy at age > 30 Ma and the opposite for younger ages. The existence of a thick overriding plate reduces the slab dip by increasing dynamic suction, and individual cratonic roots further lead to along-trench variations of dip angle reduction. While dynamic suction from the overriding plate generates a permanent reduction of the long-wavelength slab dip angle, it is the final addition of subducting oceanic plateau and aseismic ridges that produces the transient and localized flat-slabs as observed. These results suggest that all mechanisms except the buoyancy features affect the slab dip only at large spatial scales. Our best-fit model with all the above tectonic features included provides a good match to both the upper mantle Benioff zones and the temporal evolution of volcanic arcs since the mid-Miocene. The imperfect match of the Peruvian flat-slab is likely associated with the uncertain 3-D configuration of the Amazonian craton.

---

[1]This chapter has been published as: Hu, J., Liu, L., Hermosillo, A., & Zhou, Q. (2016). *Simulation of late Cenozoic South American flat-slab subduction using geodynamic models with data assimilation.* Earth and Planetary Science Letters, 438, 1-13.

2.2 Introduction

South America has the longest continuous subduction zone in the world that stretches 7500 km from ~10°N to ~60°S (Klotz et al., 2001). Subduction along this ocean-continent convergent boundary started no later than the Cretaceous during the final separation of supercontinent Pangaea (Müller et al., 2008). South America, therefore, provides an ideal test yard for understanding subduction dynamics and the associated mantle processes. The present South American subduction zone is characterized by along-strike variation of slab dipping angles. There are several segments of flat slab including Bucaramanga, Peruvian and central Chile flat slabs (Gutscher et al., 2000), which are intervened by normal to steep subduction (Fig. 2.1).

In theory, the dip angle of a subducting slab is controlled by two competing forces, the negative buoyancy (i.e., integrated density anomaly) of the slab and resistance from the surrounding mantle and the overriding lithosphere (Stevenson & Turner, 1977). Over the past several decades, a number of possible mechanisms have been proposed to explain the formation of flat-slab subduction. These mechanisms include: (a) the subduction of buoyancy anomalies such as oceanic plateaus, aseismic ridges, and seamount chains (Cloos 1993; Gutscher et al., 1999a; van Hunen et al., 2002; Mason et al., 2010); (b) the fast active overriding of a continent over young oceanic lithosphere (van Hunen et al., 2000); (c) the hydrodynamic suction force due to thick continental roots that couples the subducting slab with the overriding plate (Jones et al., 2011; Roda et al., 2011; Rodríguez-González et al., 2012; O'Driscoll et al., 2009; 2012).

According to recent plate reconstructions (Müller et al., 2008; Seton et al., 2012), South America has not experienced exceptionally fast westward motion since the Cretaceous, implying that the fast overriding continent mechanism may not apply to South America, but the young oceanic lithosphere may play a role. Among existing studies, Gutscher et al. (2000) and Anderson et al. (2007) proposed that the central Chile flat slab, one of the most prominent flat slabs in South America, may be flattened by the Juan Fernandez Ridge. However, the same flat slab was also attributed to the suction force of the Rio de la plata craton (Manea at el., 2012). For the Peruvian flat slab, Gutscher et al. (1999a) argued that it was due to subduction of the “lost Inca plateau” and the Nazca Ridge, although in theory it could also be influenced by the thick Amazonian craton (O'Driscoll et al., 2009; 2012).

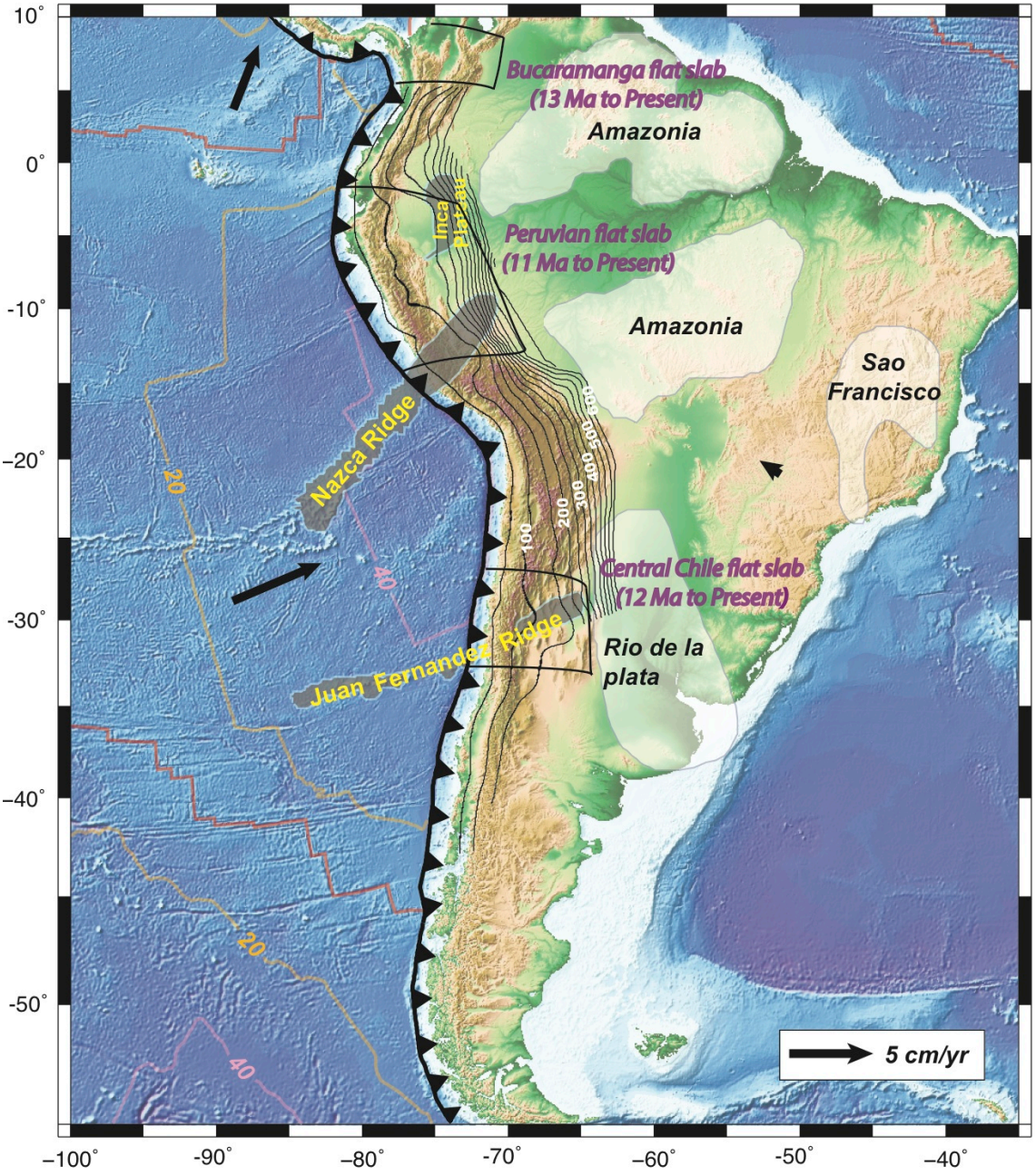

Figure 2.1. Geological setting of South America with depth contours of slab 1.0 (Hayes et al., 2012) indicated by thin black lines, subducting oceanic plateaus translucent gray and continental cratons translucent white. The major flat slabs in South America are outlined with thick black lines. The locations of oceanic plateaus, cratons and flat slabs are modified from Gutscher et al. (2000), Loewy et al. (2004) and Ramos and Folguera (2009), respectively. The present-day plate motion is shown as black arrows. Tooth-shaped line represents the South American trench. Seafloor ages to the west of South America are shown with colorful lines with numbers indicating the age in Ma.

In contrast, some studies proposed that moderate-sized buoyancy features could not result in significant slab flattening (Martinod et al., 2005; Gerya et al., 2009). Furthermore, if the basalt-to-eclogite transformation finishes at shallow depths (<70 km), the subduction of oceanic plateau would prohibit the formation of flat slabs (Arrial and Billen, 2013). It is also suggested that the correlation between South American flat slabs and subducting bathymetric highs is rather poor (Skinner and Clayton, 2013). These existing debates raise the need for a systematic evaluation of the different mechanisms for the formation of flat-slab subduction in South America.

Here we report the first 4D quantitative geodynamic modeling on the subduction history of South America. We test both the respective and accumulative effects of seafloor age variation, hydrodynamic suction, and buoyancy feature subduction on the formation of flat slabs. These mechanisms influence the slab dip angle by controlling the negative buoyancy and mechanical strength (i.e., resistance to bending) of the slab, reducing the dynamic pressure in the mantle wedge, and decreasing slab density locally, respectively. By incorporating all these physical processes in the subduction models, we attempt to predict the present-day slab geometry and the temporal evolution of flat-slab formation, which are evaluated with the distribution of deep seismicity (Hayes et al, 2012) and volcanic arc migration from the online catalog of Peruvian Mining and Metallurgical Geological Institute – INGEMMET (http://www.ingemmet.gob.pe).

Among the three present-day flat-slab segments in South America (Barazangi and Isacks, 1976, 1979; Pennington, 1981; Ramos et al, 2002; Ramos and Folguera, 2009), the central Chile flat-slab (i.e. Pampean flat slab) that has been in existence since ~12 Ma currently extends from 27° to 33°30′S, the Peruvian flat-slab existing since 11 Ma extends from 5° to 14°S, and the Bucaramanga flat-slab since ~13 Ma covers 5° to 9°N. Here, we mainly focus on the present-day Central Chile and Peruvian flat slabs, since the Bucaramanga segment is too close to the edge of our model domain.

2.3 Model setup

We use the 3D spherical finite element code CitcomS (Zhong et al., 2000; Tan et al., 2006) to simulate subduction and mantle convection. Our model domain extends from 10° W to 100° W in longitude, from 70° S to 20° N in latitude, and covers the whole mantle in depth. It is discretized with 257 × 257 × 65 nodes in latitude × longitude × depth using a spatially variable finite-element mesh, with the finest resolution of 27×27×8 (km) occurring in the central 2/3 of the mesh.

2.3.1 Governing equations

We solve the thermal-chemical mantle convection following the conservation of mass, momentum and energy. We assume the mantle flow is incompressible, with a variable viscosity structure, and satisfies the Boussinesq approximation. The governing equations are:

$$\nabla \cdot \vec{u} = 0 \quad (1)$$

$$-\nabla P + \nabla \cdot [\eta(\nabla \vec{u} + \nabla^T \vec{u})] + (\rho_m \alpha \Delta T + \Delta \rho_c)\vec{g} = 0 \quad (2)$$

$$\frac{\partial T}{\partial t} + \vec{u} \cdot \nabla T = \kappa \nabla^2 T \quad (3)$$

$$\frac{\partial C}{\partial t} + \vec{u} \cdot \nabla C = 0 \quad (4)$$

Where $\vec{u}$ is velocity, P is dynamic pressure, T temperature, ρ_m ambient mantle density, $\Delta\rho_c$ compositional density anomaly, ΔT temperature anomaly, η dynamic viscosity, α thermal expansion coefficient, κ thermal diffusivity, $\vec{g}$ gravitational acceleration, and C composition, respectively.

In Equation (2), both thermal and compositional buoyancy are taken into account. Equation (4) describes the advection of chemical particles, and this is solved using a ratio method for Lagrangian particles (Tackley & King, 2003).

2.3.2 Boundary conditions

The model utilizes the plate kinematics and seafloor age evolution from the plate reconstruction of Müller et al (2008) to update the surface velocity boundary condition and the upper thermal boundary layer profile, respectively (Figs. 2.2a-c). All other boundaries are free slip. The core-mantle boundary has a fixed temperature that is set to be the background mantle temperature. The surface velocity and seafloor age are reconstructed over an interval of 1 Ma, using the open source paleo-geographic software GPlates (www.gplates.org/; Gurnis et al., 2012). At any given time within the interval, we linearly interpolate the surface velocity and seafloor age. We also take into account the history of central Andean deformation (Fig. 2.2d) by changing the trench profile through time using the most recent Andean shortening reconstruction (Arriagada et al., 2008).

The model assimilates the seafloor age at each time step to update the top thermal boundary layer within oceanic plates, where we define an error function distribution of thermal profile. In order to overcome the numerical diffusion which exists within the top thermal boundary layer as the finite grid resolution would smear out the sharp thermal gradient in the boundary layer (Davies et al., 2007; Liu and Stegman, 2011), we reduce the thermal gradient across the boundary layer from ~1200 °C to ~700 °C while maintaining the total buoyancy of the boundary layer unchanged by applying an age-dependent correction to the error function (similar to Liu and Stegman, 2011). The continent is assumed at the ambient mantle temperature, in order to maintain its overall neutral buoyancy.

2.3.3 Rheology

Three-dimensional temperature- and composition-dependent viscosity is applied in the model. The background mantle viscosity follows a 4-layer profile (Fig. 2.2e): lithosphere (0-100 km), asthenosphere (100-300 km), transition zone (300-660 km), and lower mantle (660 – 2890 km). Their respective viscosity values are 10^{23}, 3×10^{19}, 10^{21}, and 3×10^{22} Pa s. In the lower mantle, the viscosity increases from 3×10^{22} Pa s right below 660 km depth to 10^{23} Pa s at >1200 km, and then gradually decreases below 2000 km toward the core-mantle boundary to 3×10^{22} Pa s. Such a viscosity profile is obtained by matching the present-day mantle seismic structure with predicted slab geometry. This profile is also consistent with recent petrological experiment by Marquardt and Miyagi (2015), suggesting a significantly increased strength of ferropericlase in the upper part of lower mantle. This is further supported by the observation of global slab stagnancy above 1000 km depth from recent tomography images (Fukao & Obayashi, 2013).

In order to facilitate subduction, the model has also incorporated sharp lateral viscosity variations, including a weak zone (with a viscosity of 10^{19} Pa s) along the subduction zone and a weak mantle wedge above the down-going slab, similar to earlier models by Liu & Stegman (2011). To simulate the dynamic suction force from cratons, we prescribe these continental units as high-viscosity bodies. We first define a 75-100-km thick continental lithosphere, and then prescribe individual cratonic roots, which extends to about 200 km depth. The geometry of cratonic roots at 75 km depth is defined according to Loewy et al. (2004) (Fig. 2.1). The area of the roots shrinks as it goes from the surface to 200 km depth, in order to avoid a step-like craton viscosity profile.

These high-viscosity features regulate the flow pattern in the upper mantle and generate suction force to flatten the slab.

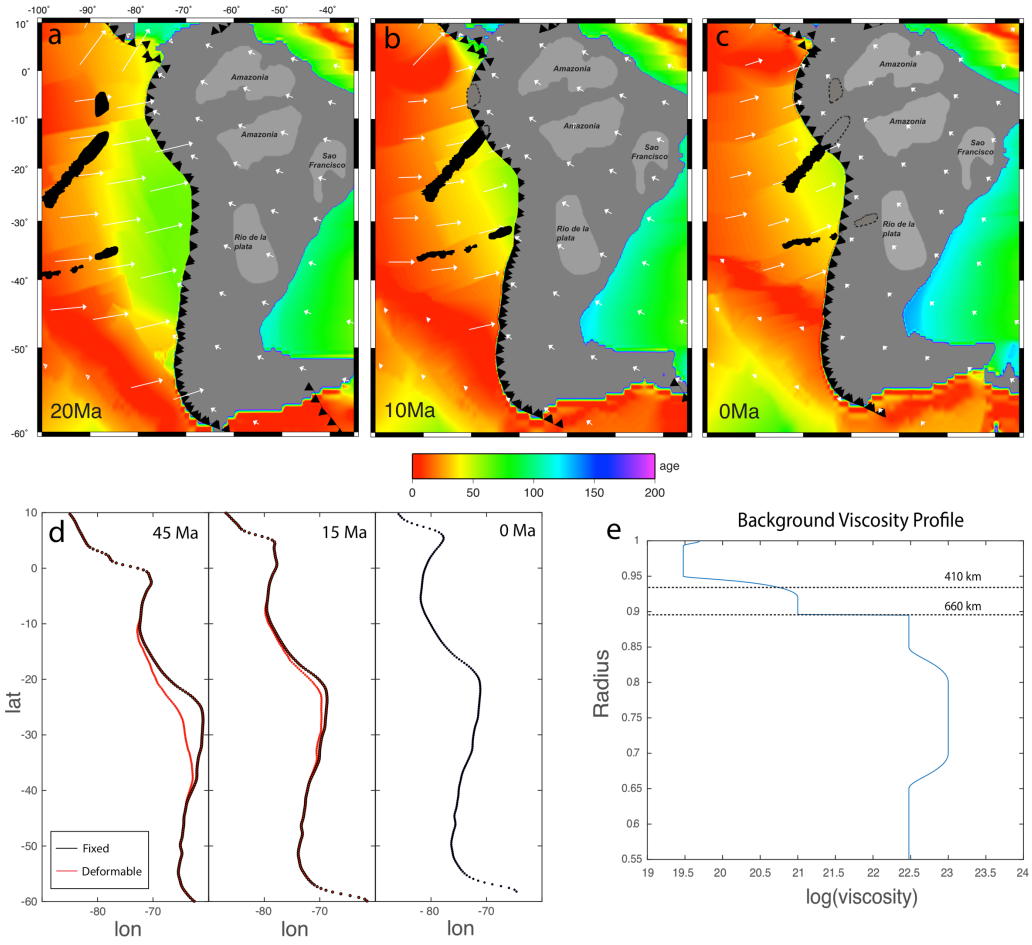

Figure 2.2. Surface velocity boundary conditions and seafloor age distribution at (a) 20 Ma, (b) 10 Ma and (c) present. White arrows show the direction and magnitude of surface velocities. Background color represents the seafloor age. Black regions represent the oceanic plateau and aseismic ridges with dashed contours indicating the already-subducted parts. The South American continent is shown with dark gray with cratons indicated by light gray. (d) Trench profiles at 45 Ma, 15 Ma and present. Red lines indicate the temporally deformable trench profiles (Arriagada et al., 2008), and black lines represent the present-day trench geometry. (e) Background 1D mantle viscosity structure. Key features include a low-viscosity asthenosphere and a viscosity maximum in the upper part of the lower mantle.

2.3.4 Implementation of oceanic crust, plateau and mid-ocean ridges

We use compositional tracers to define the oceanic crust and the oceanic plateaus. The geometry of Inca Plateau, Nazca Ridge and Juan Fernandez Ridge are prescribed according to Gutscher et al. (2000) (Fig. 2.1). These features are embedded in the subducting oceanic plate. We

assume that the oceanic crust is 8 km thick with a density of 2.9 g/cm^3, and that the oceanic plateau and aseismic ridges are 15 km thick with the same density. These features reduce the density of the down-going slab, and thus could potentially flatten the slab. We simulate the density change due to basalt-to-eclogite phase transformation by turning off tracer buoyancy at ~100 km depth for both the crust and oceanic plateaus.

The oceanic crust is implemented into the model since 100 Ma. As seafloor spreads, new oceanic crust forms at the mid-ocean ridge where the seafloor is young. We update the composition of young seafloors (<10 Ma) at each time step, in order to mimic the oceanic crust generation along mid-ocean ridges. We introduce the Inca Plateau, Nazca Ridge and Juan Fernandez Ridge into the model at 15 Ma, with their initial configuration reconstructed starting from their present-day positions (Gutscher et al., 2000) using past plate motions (Müller et al., 2008) with GPlates (Boyden et al., 2011). In our model, the subduction of Inca Plateau and Nazca Ridge began at ~12 Ma and that of Juan Fernandez Ridge began at ~9 Ma. We realize the uncertainty in the earlier subducted length of Juan Fernandez Ridge (Yáñez et al., 2001; Kay and Mpodozis, 2002), but the simulation of a longer ridge subduction history results in a similar present-day slab structure to that of a shorter history. This may be related to the change of the ridge's strike orientation in the past and its southward migration relative to South America (Huene et al., 1997). We conclude that only the recent subduction history (post-10 Ma) of the ridge has contributed to the formation of the Central Chile flat slab.

2.3.5 Assimilation of a deformable South American trench

There are multiple palinspastic reconstructions of the Cenozoic shortening of the central Andes (Isacks, 1998; Kley and Monaldi, 1998; McQuarrie, 2002; Oncken et al., 2006; Arriagada et al., 2008). Among these reconstructions, we choose the one from Arriagada et al. (2008) to represent the trench profile evolution during the geological past. This is because their model incorporates the most extensive tectonic shortening events and paleomagnetically determined tectonic rotations.

In practice, we first collect the trench profiles at 45, 15, and 0 Ma from the reconstruction by Arriagada et al. (2008) (there was no significant shortening before 45 Ma). We then linearly interpolate these trench profiles and calculate the shortening rate at any given time and space, assuming shortening occurs only along the east-west direction. To the first order, this is a valid

approximation, since the convergence rate between the Farallon/Nazca plate and South American plate was mainly along the east-west direction during the past 100 Ma (e.g., Müller et al., 2008). After we obtain these trench profiles, we rotate them back in time, in order to get the absolute locations of the South American trench history (Fig. 2.2d).

Subsequently, we update both the velocity and thermal boundary conditions according to these deformable trench locations. The shortening of the overriding plate was accommodated in a zone of ~700 km width behind the trench, where the shortening rate decreases linearly inland-ward. Effectively, our approach may be similar to the one by Gurnis et al. (2013) and Flament et al. (2014), and their approach also requires substantial work in code-development and data-compilation.

2.4 Results

In this section, we present model results testing various physical mechanisms for flat-slab formation, and the predicted modern slab configuration in South America.

2.4.1 The physical mechanisms for flat-slab formation

As discussed in section 1, among earlier proposed mechanisms for flat-slab formation, those relevant to South American subduction include dynamic suction caused by strong cratonic roots inside the overriding plate (Manea et al., 2012), subduction of intra-slab buoyancy anomalies associated with aseismic ridges and oceanic plateaus (Gutscher et al., 1999a), and subduction of young seafloors (van Hunen et al., 2000). In this paper, we attempt to evaluate the relative contributions of these different mechanisms for the resulting present-day slab geometry.

2.4.1.1 Seafloor age

To explore the seafloor age effect, we first design two different models: one has a uniform seafloor age of 30 Myr during the entire subduction history (model I), and the other has temporal-spatial variations of seafloor age (model II) derived from the plate reconstruction of Müller et al., (2008) (Fig. 2.2). These two models do not include a high-viscosity overriding plate and intra-slab buoyancy features in order to isolate the effect of seafloor age. In model I, the present-day slab subducts steeply along the entire trench (Figs. 2.3a, 2.4). In contrast, the slab in model II is shallower almost everywhere along the trench (Figs. 2.3b, 2.4). The slab dip angle (defined by the

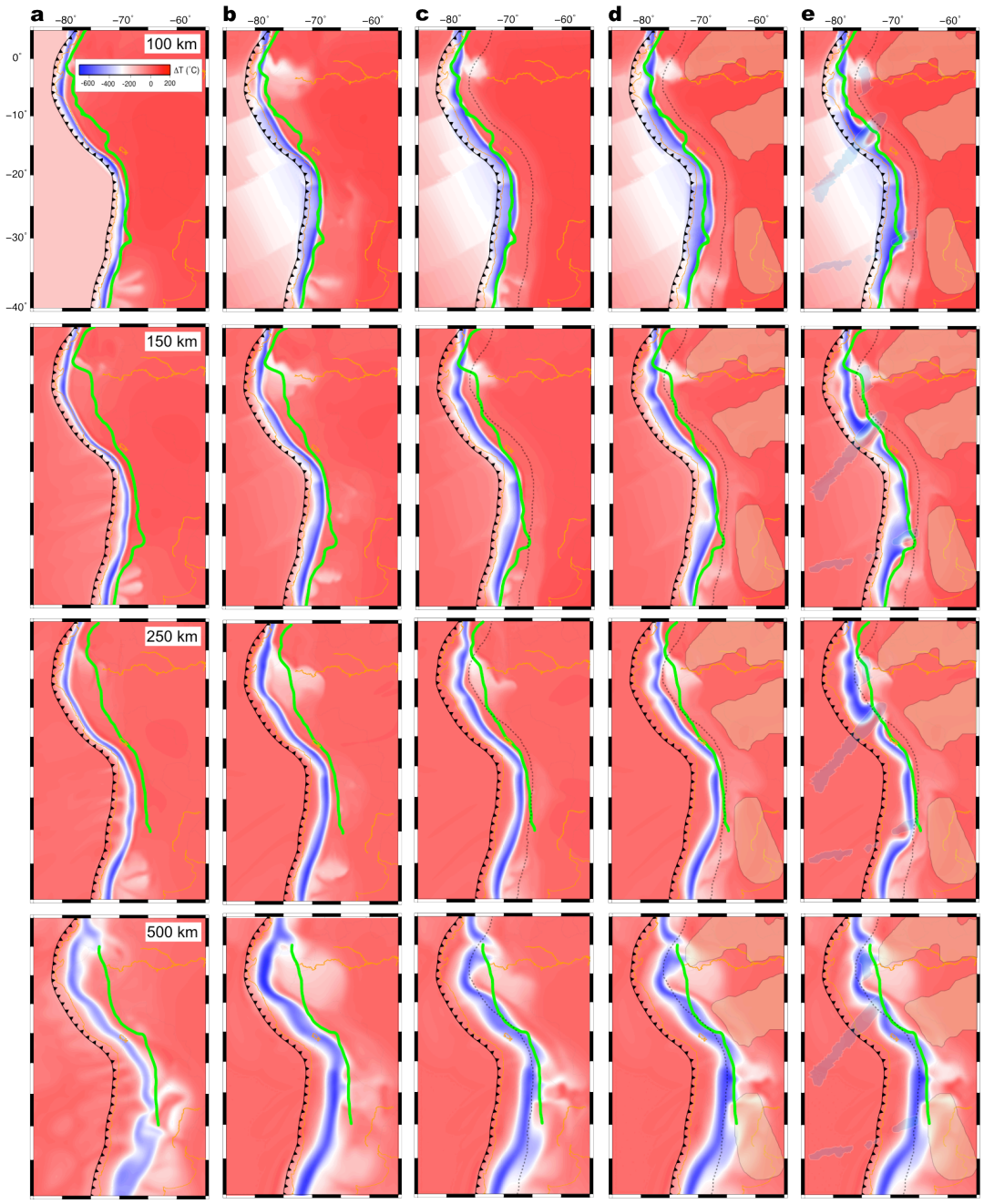

Figure 2.3. Comparison of present-day slab geometry from five different subduction models. (a-e) Predicted slab geometry (blue color) from models I, II, III, IV and V (see main text), respectively. Different rows show different depths with the first row at 100 km, the second at 150 km, the third at 250 km, and the fourth at 500 km depth. Green lines represent the interpolated Benioff zones from *slab 1.0* (Hayes et al., 2012). Present-day configuration of the cratons and buoyancy features are shown with brown and blue, respectively, where we assume no lateral distortion in the geometry of the buoyancy features after subduction. Dotted lines outline the overriding plate. Note the progressive flattening of the slab from model I to model V.

upper surface of the slab between the trench and at 200 km-depth, Fig. 2.5b) varies along the trench, with two shallow-dipping slab segments centered at ~10°S and ~29°S, respectively (Figs. 2.3a, 2.4). Since the only difference between model I and II is the seafloor age distribution (Fig. 2.3a, b), their different dip angles reflect the competition between the slab negative buoyancy and mechanical strength. However, the dependence of this competition, therefore slab dip, on seafloor age is elusive. For example, compared to model I, both younger (<30 Ma, north of 10°S and south of 30°S) and older (>30 Ma, between 10°S and 30°S) seafloors lead to shallower subduction in model II, although we do observe a larger dip angle reduction at the central part of the trench where seafloor is older.

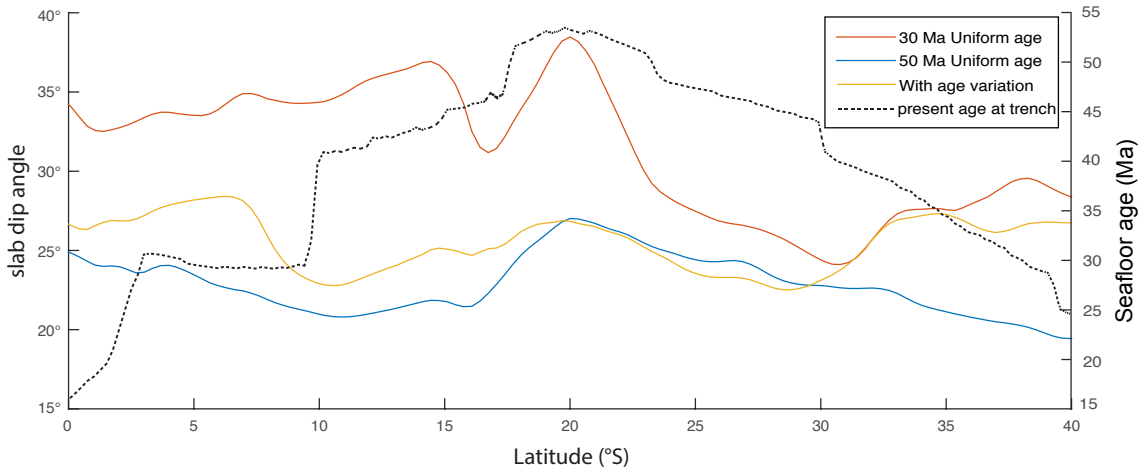

Figure 2.4. Along-trench slab dip angle distribution (solid lines) from models I, II, and S and the present-day seafloor age distribution at trench (dashed line) in model II. Note the similar seafloor age distributions from 10 Ma to the present, the period relevant to the modern flat slab formation. Slab dip angle is measured according to the horizontal distance between the trench and the slab surface at 200 km depth along the east-west direction. Slab surface is defined as the upper interface between the slab and the ambient mantle, where the interface is the isotherm of 300 °C cooler than the ambient mantle.

In order to better discern the effect of seafloor age on slab dip, we run an additional model with a uniform seafloor age of 50 Ma (model S), an age similar to the oldest part (between ~15°S and ~30°S) of that in model II at the present day (Fig. 2.4). The predicted present-day slab in model S is systematically shallower than that in model I. It is also shallower than the slab in model II, except for the central portion (Fig. 2.4), where the two models have similar seafloor ages (Fig. 2.2a-c). Comparing model I (uniform age at 30 Ma) and model S (uniform age at 50 Ma), we can see that older seafloor age tends to induce shallower subduction, which suggests that slab mechanical strength dominates the effect of negative buoyancy on slab bending. This conclusion

can also be drawn from the comparison of model II and model S, where between ~15°S and ~30°S, the slab dip angles in the two models are similar, consistent with their similar seafloor ages in this

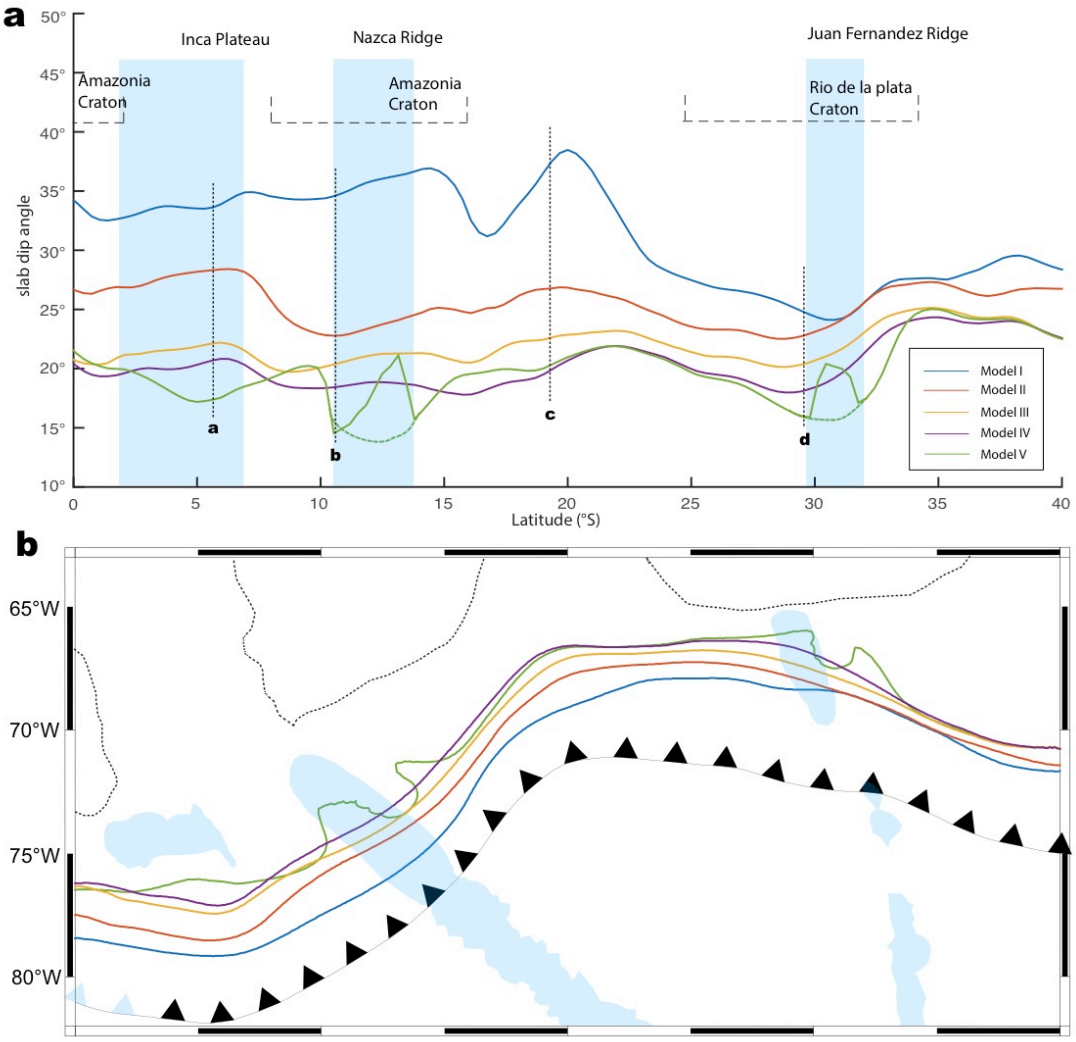

Figure 2.5. (a) Present-day slab dip angle distribution along South American trench in models I, II, III, IV and V. The locations of subducting buoyancy features are marked with light blue, while the location of continental cratons are shown with dashed brackets. The dotted lines mark the location of the cross sections shown in Fig. 2.6. (b) Slab upper surface (300 °C cooler than the ambient mantle) at 200 km depth for the five models. Dashed lines outline the cratons, and light blue represents the buoyancy features.

region; while in the other regions, the slab of model S is clearly shallower, corresponding to its older seafloor ages. Together with the comparison between model I and II, we suggest that for seafloor ages >30 Ma, the slab strength dominates its negative buoyancy in determining the slab dip, and that this relation reverses for ages <30 Ma. It is worth noting that, between ~25°S and

~30°S, all three models have close slab dip angles, which is largely related to the anchoring effect of slabs at greater depth due to early subduction, a topic outside the scope of this paper. Furthermore, in model I, the sharp kinks in slab dip distribution between ~15°S and ~20°S (Fig. 2.4) may be related to the variation of trench curvature (Fig. 2.3b).

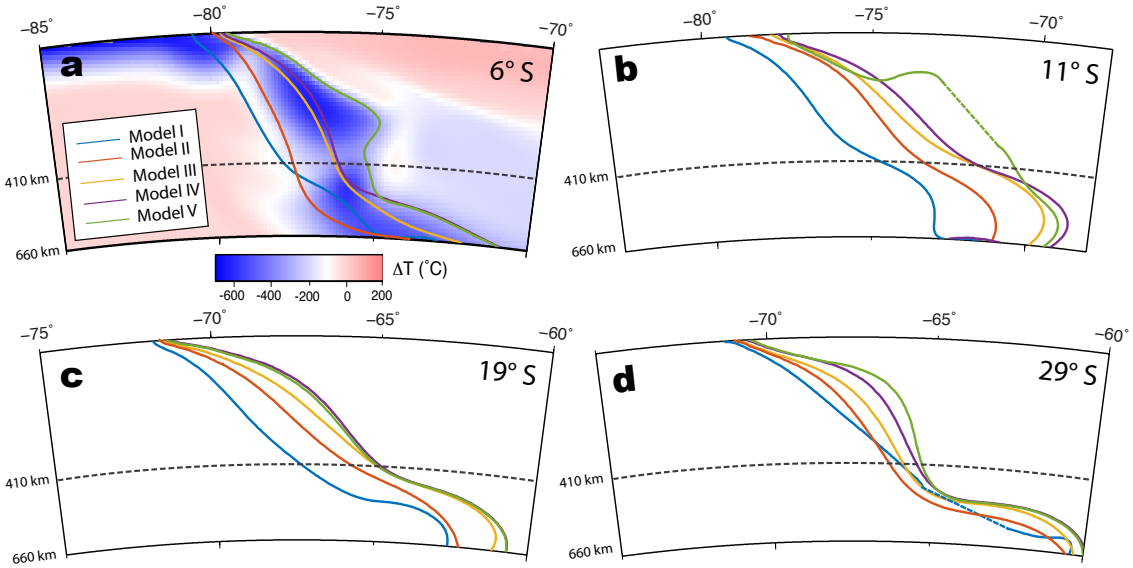

Figure 2.6. Comparison of the slab upper surface of models I, II, III, IV and V at (a) 6°S, (b) 11°S, (c) 19°S and (d) 29°S, respectively, corresponding to the dashed lines in Fig. 2.5a. Notice the progressive flattening of the slabs across different models.

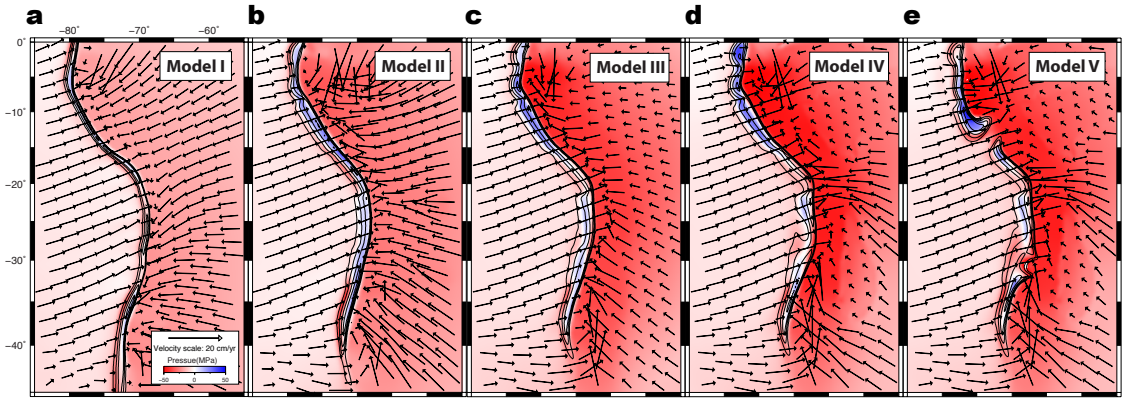

Figure 2.7. Maps showing the dynamic pressure distribution at 140 km depth for models (a) I, (b) II, (c) III, (d) IV and (e) V. The mantle flow field is over-plotted as arrows. Thin black contours indicate slab isotherms with an increment of 100 °C. The dynamic pressure in mantle wedge is progressively lowered from model I to model IV.

Overall, with the tectonically reconstructed seafloor age history (i.e. model II), the predicted present-day slab dip angle distribution along trench is opposite to that outlined with Benioff zones, where shallow-to-flat slabs occur both north and south of central Andes (Figs. 2.1, 2.3b). Furthermore, the predicted subduction dip angle is consistently steeper than that observed (Fig. 2.3b). We note that, although an increase in the background mantle viscosity or slab strength could lead to shallower slabs, it would not explain the N-S variation of slab dip angle. This suggests that additional physical mechanisms are needed in order to explain the observed slab geometry.

2.4.1.2 Hydrodynamic suction

In order to investigate the effect of hydrodynamic suction, we perform two additional models, which have a uniform 100 km-thick overriding plate (model III) and a uniform 75 km-thick overriding plate with three 200 km-thick embedded cratons (model IV), respectively. Compared with model II, inclusion of a mechanically strong overriding plate (model III) leads to a reduction of slab dip along most of the South American trench (Figs. 2.3c, 2.5, 2.6). Addition of thick cratons (Amazonia, Sao Francisco, and Rio de la plata cratons; Fig. 2.1) inside the continent (model IV) reduces the dip angle further and generates long-wavelength (>1000 km) low-amplitude perturbations to the slab dip distribution (Figs. 2.3d, 2.5). This is due to enhanced hydrodynamic suction force from the overriding continent, which is reflected as a reduction of dynamic pressure inside the mantle wedge (Figs. 2.7, 2.8) (Stevenson & Turner, 1977; Manea et al., 2012). Among models II, III and IV, the magnitude of dynamic pressure reduction in the mantle wedge increases progressively (Fig. 2.7b-d), resulting in shallower and shallower slabs (Figs. 2.3b-d, 2.6). Physically, the reduction of dynamic pressure in the mantle wedge, and thus increased suction force, results from the existence of a high-viscosity overriding plate which confines the mantle flow to occur within a narrow region (Fig. 2.7; Stevenson & Turner, 1977). In a vertical profile, when a thick overriding plate exists, the lowered dynamic pressure occurs inside a very broad upper mantle region above the slab (Fig. 2.8), with the lowest pressure present in the asthenosphere whose viscosity is the lowest.

In addition to confirming earlier studies on the origin of hydrodynamic suction force (Manea & Gurnis, 2007; Manea et al., 2012), our results further quantify the magnitude and spatial pattern of this force associated with the 3D geometry of the overriding plate including cratonic roots. The observation that the predicted slab dips at the long-wavelength in models III and IV are

close to that observed suggests that their predicted magnitude of suction force is reasonable, and a further increase of suction force would over-predict the flattening of slabs along most of the trench. Relative to model II, the reduction of slab dip angle in model IV is larger than that in model III, especially along the segments between ~10° and 17°S and between ~25° and 33°S, which correspond to the locations of the Amazonia and Rio de la plata cratons (Fig. 2.5). This is because these cratons further confine the nearby mantle flow, resulting in greater suction (Fig. 2.7d).

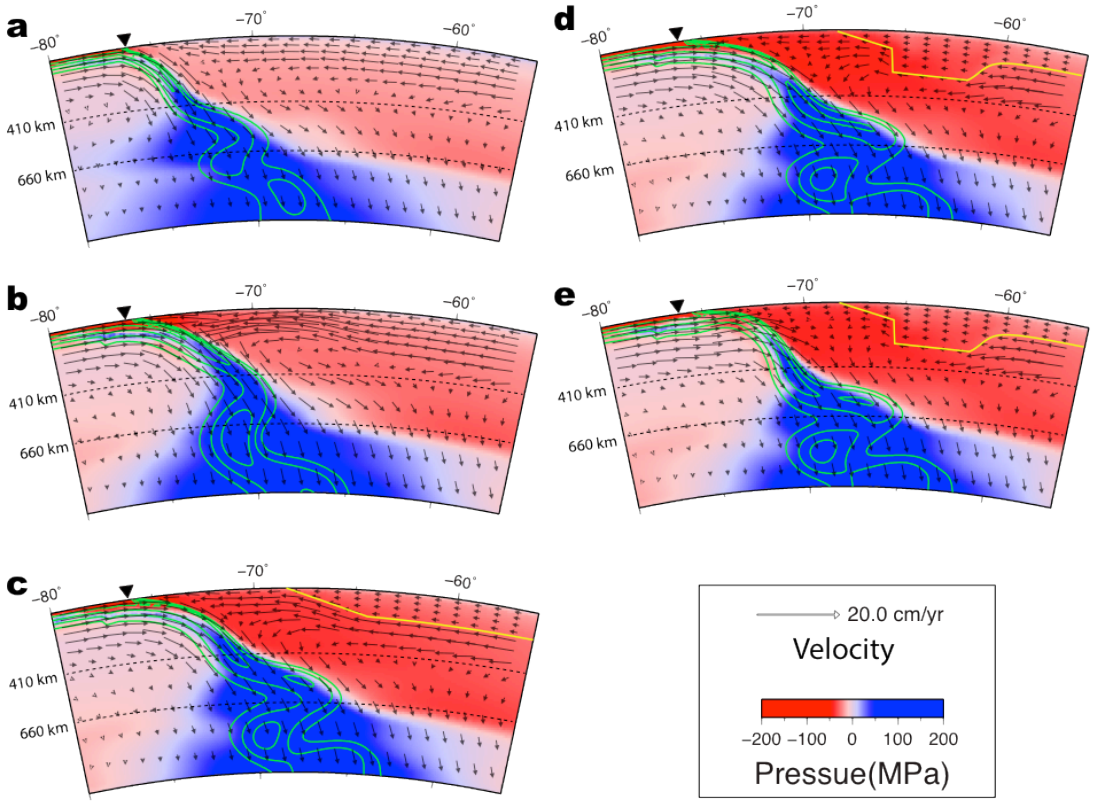

Figure 2.8. Cross sections showing the dynamic pressure distribution at 15°S for model (a) I, (b) II, (c) III, (d) IV and (e) V. Arrows represent mantle velocities. Yellow thick lines outline the overriding plate. Solid green contours indicate slab isotherms with an increment of 100 °C. The dynamic pressure within the mantle wedge is progressively lowered from model I to model IV, indicating an increasing hydrodynamic suction. Notice that the mantle flow above the slab is mainly concentrated in the asthenosphere when a high-viscosity overriding plate is present.

In summary, model IV predicts the observed slab dip angles slightly better than model III, but both models still fail to predict the localized flat slabs in Southern Peru and Central Chile (Fig. 2.3c, d). In fact, the central South American trench flattening is already over predicted at depths above 150 km, but the northern and southern parts, especially the two flat-slab segments, are still under predicted. We do not attempt to improve this fit by tuning the thickness and viscosity profile

of these cratons, because, first, geometry of these craton roots is not well constrained in observation; second, suction-induced flat slabs are likely permanent in time (Manea et al., 2012; Taramón et al., 2015), inconsistent with the recent history of these flat slabs. Finally, the fact that the width of the central Chile flat slab (Fig. 2.1) is much smaller than that of the Rio de la plata craton (thus the dimension of suction-induced permanent flat slab) dismisses a direct causal relationship between the two.

2.4.1.3 Subduction of buoyancy features

We then further incorporate (model V) the three pieces of over-thickened oceanic crusts associated with the Inca Plateau, Nazca Ridge, and Juan Fernandez Ridge (Fig. 2.1) whose subduction started since late Miocene (Gutscher et al., 1999a; Ramos, 2009) (Fig. 2.2a). The extra positive buoyancy from these features relative to the ambient mantle causes additional flattening of the slabs in Peru and Central Chile, greatly improving the fit to the *Slab1.0* contours (Fig. 2.3d, e). The predictions for the Central Chile and Southern Peru flat slabs are almost exact, given the observation that it is the hydrodynamic suction from the continent that slightly over-predicts the slab dip at 100 km depth between 20°S and 30°S (Fig. 2.3c, d). The amount of flattening in Northern Peru at 250 km depth is still slightly under predicted (Fig. 2.3e), and this is likely related to the under-estimation of suction force due to the uncertain geometry of Amazonia Craton. Overall, compared with model IV where only seafloor age variation and dynamic suction are considered (Fig. 2.3d), the buoyancy features contribute to slab flattening at much smaller spatial scales (<500 km), comparable to the widths of these buoyancy features (Fig. 2.5a). We emphasize that the magnitudes of the background mantle viscosity and slab strength affect the overall slab dip along the entire trench but contribute little to the local variations of slab dip angle. So we utilize the same viscosity structure for all five models.

Besides the spatial scales, the temporal effect of subducting buoyancy features also differs from that of continental suction. Since the suction force resulting from the overriding plate exists throughout the subduction history, it exerts a prolonged influence on the subducting slab, which is reflected as a continuous reduction of slab dip angle over depth (thus time) in models III and IV relative to that in model II (Figs. 2.3, 2.8). The addition of aseismic ridges, however, affects the slab dip angle only since their initial subduction during the late Miocene, which corresponds to

~500 km depth at the present. That also explains why there is almost no difference between model IV and model V in slab geometry at greater depths (Figs. 2.3, 2.6, 2.8).

One of the most significant structural differences between our results and earlier studies is the development of a tear inside the flat slab associated with the subduction of buoyancy features (Fig. 2.9). Due to the progressive accumulation of strain at the down-dip side and the two flanks of the aseismic ridge during subduction, the flat slab is highly deformed internally and eventually a slab hole forms. The two pairs of spines in the outline of slab dip angle distribution at ~13°S and ~31°S in Figure 2.5a are caused by these slab holes (Figs. 2.3e, 2.5b and 2.9). In order to be comparable to the Slab 1.0 contours that are spatially interpolated from the seismicity distribution, we also interpolated these parts of the slab dip angle using dashed lines (Fig. 2.5a). This way, we could see more clearly the small spatial scales (< 500 km) of slab flattening due to the extra buoyancy of these over-thickened oceanic crusts (Fig. 2.5a, b).

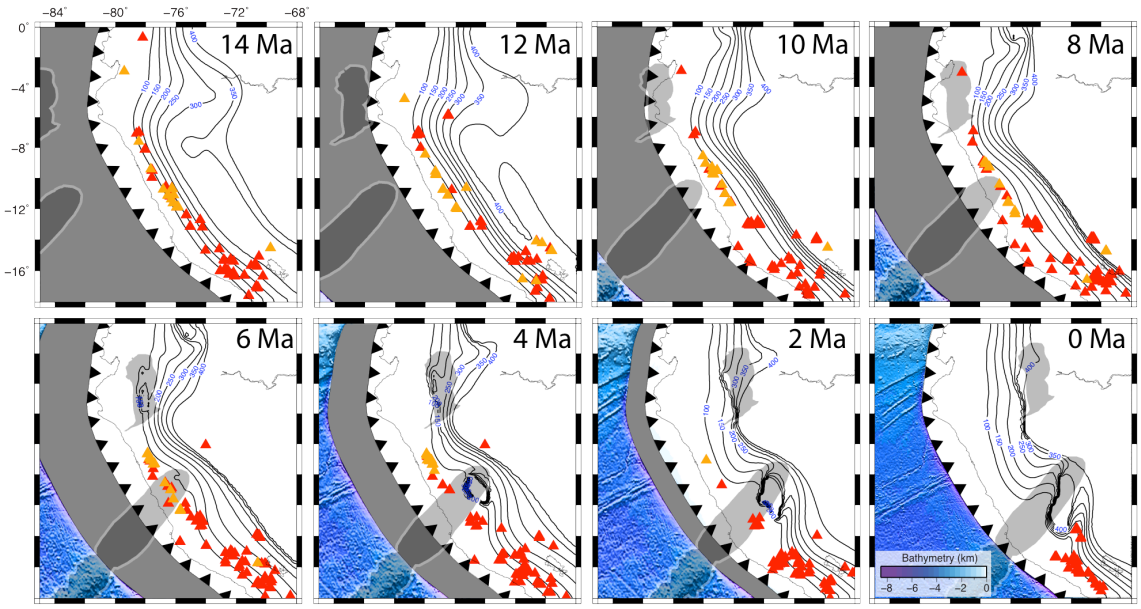

Figure 2.9. The evolution of slab geometry beneath Peru from 14 Ma to present day. Black lines represent the slab upper surface (300 °C cooler than the ambient mantle) at different depths. Dark gray patterns show the reconstructed locations of the Inca Plateau and the Nazca Ridge. Light gray area represents now-subducted seafloors. Red triangles indicate the location of extrusive volcanism, while orange triangles represent that of intrusive volcanism. A slab hole forms since 6 Ma during the Nazca Ridge subduction. Note the delay between initial buoyancy feature subduction and flat slab formation.

Analysis of the temporal evolution of flat slabs in model V suggests that that the formation of flat slabs was usually delayed by several million years relative to the start of buoyancy-feature

subduction. This reflects the 3D structure of a flat slab that consumes the earlier subducted portion of the buoyancy feature to 'raise' the slab relative to its surroundings, consistent with the results of analog models (Espurt et al., 2008). For example, the Nazca Ridge entered the trench at ~12 Ma, but the slab reached its flattest state at ~4 Ma (Fig. 2.9), which is also consistent with the cessation of arc volcanism at this time (Fig. 2.9). A similar situation is seen during the subduction of the Inca Plateau (Fig. 2.9).

2.4.2 The predicted present-day flat slabs

Figure 2.10 shows six different vertical cross sections of our best-fit model (i.e. model V). We compare this model prediction with upper mantle Benioff zone geometry using *slab 1.0* (Hayes et al., 2012) and seismicity catalog from IRIS (http://service.iris.edu/fdsnws/event/docs/1/builder/). Three cross sections through the flat-slab segments (Fig. 2.10a, b, f) and three through the normal subduction parts (Fig. 2.10c-e) are shown. As can be seen, the predicted slab geometry fits the Benioff zone generally well both in the normal and flat slab segments (Fig. 2.3e, 2.10). We do not fine-tune the slab strength and overriding plate thickness, in order to better match these profiles, since we mainly focus on the first order effect of the different physical mechanisms for slab flattening, and these models (I-V) demonstrate a clear improvement toward the final prediction of the observed slab geometry.

In central Chile (Fig. 2.10f), the Juan Fernandez Ridge has effectively flattened the slab locally. This predicted slab geometry fits both the *slab 1.0* contour and the seismicity pattern above 150 km depth very well, but not below this depth (Fig. 2.10f). We suggest that this misfit is due to the interpolated nature of *slab 1.0* below 150 km depth, where there is no seismicity between 250 and 500 km along the entire South American trench (Hayes et al., 2012). The same situation and reasoning apply to the Peruvian flat slab, where the Benioff zone is interpolated with depth (Fig. 2.10a, b). However, a confirmed mismatch in the predicted Peruvian flat slab is that its overall depth is slightly larger compared to the Benioff zone at <200 km depth. This is likely due to two reasons: 1) The buoyancy of Inca Plateau and Nazca Ridge is insufficient to cause a wide flat slab as observed; 2) A larger continental suction is needed in order to generate a shallower slab.

Significantly, our study reveals some important differences from earlier 2-D simulations on flat-slab formation. According to the traditional view, subduction of a buoyancy feature (e.g., van Huneun et al., 2002) or suction from a thick craton (Manea et al., 2012) would result in a local

decrease of dip angle inside a continuous slab. Our results, however, suggest that the down-dip part of the flat-slab steepens abruptly with increasing depth (Fig. 2.10a, b and f). This increase of slab dip below the flat slab is also consistent with analog model for buoyancy feature subduction (Martinod et al., 2005) and confirmed by tomographic images (Gutscher et al., 2000). This geometry variation reflects the reduced sinking speed of the flattening slab segment relative to surrounding slabs, and this different motion ultimately results in the slab holes as discussed earlier (e.g., Fig. 2.9). These apparent 3D effects are missing in earlier 2D models due to the assumption of infinite length in the third dimension.

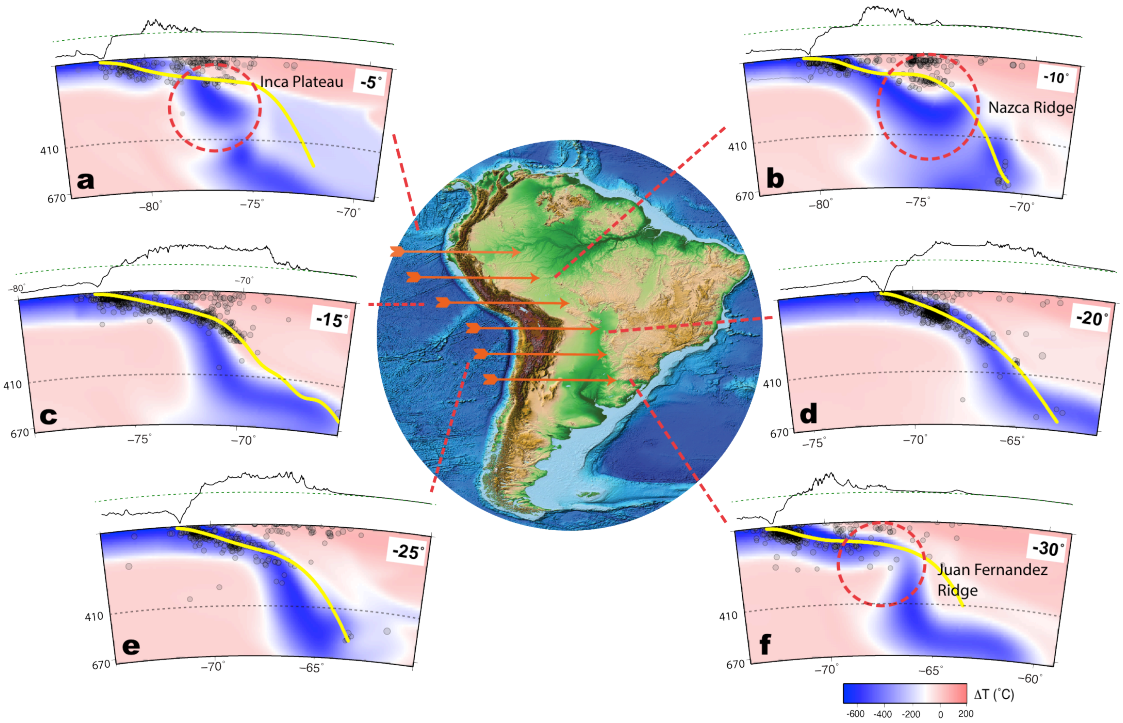

Figure 2.10. Cross sections of the best-fit model from 5° to 30°S at an interval of 5°. Orange arrows mark the location of these cross sections. In each cross section, background color represents the temperature field with the yellow lines indicating the interpolated Benioff zone from *slab 1.0* (Hayes et al., 2012). Gray circles represent the locations of earthquakes with magnitude > 4.0 from IRIS earthquake catalog for years from 1970 to 2015. Black lines above each cross section delineate the topography, with the vertical scale amplified by 20 times. Note the overall match of the slab geometry to both individual seismicity and *slab 1.0 contour*.

2.5 Discussion and conclusion

According to our study, the modern flat slab segments in South America are caused by a combination of seafloor age variation, hydrodynamic suction from the overriding plate, and subduction of buoyancy features. This may explain why there is a lack of clear correlation between

seafloor age and slab dip global-wide (Jarrard 1986; Lallemand et al., 2005; Cruciani et al., 2005). We find that with seafloor age > 30 Ma, older seafloor age (< 60 Ma in South America) tends to cause flatter subduction (model I vs. model S), which is consistent with earlier modeling work (Billen and Hirth, 2007). This suggests that slab strength dominates negative buoyancy in controlling slab dip in this age range. However, with seafloor age < 30 Ma, we find that younger seafloor age leads to shallower slab dip (model I vs. model II), which likely results from the overall small negative buoyancy of the young slabs and the stronger effect of the buoyant oceanic crust, relative to older slabs. This conclusion on how seafloor age influences slab dip, however, should be subject to future verification.

The flexibility of data assimilation models also allows us to quantify the respective roles of the overriding plate and subducting buoyancy features on influencing the slab dip angle. According to our results, hydrodynamic suction only controls the long-wavelength variation of slab dip angle along trench (Figs. 2.3, 2.5). In particular, a uniformly thick overriding plate causes a systematic reduction of the slab dip angel (Fig. 2.5); the incorporation of cratons induces additional perturbations to the slab dip over ~1000 km spatial scale, which is considerably larger than that induced by the subduction of buoyancy features (Fig. 2.5). As a result, the sharp kinks of the slab contour at 100 km depth in Chile and Peru (Fig. 2.1) are most likely caused by the subduction of two narrow aseismic ridges, since the suction from nearby cratons would have elevated a much wider segment of the slab.

It is worth noting that, in our model, flattening of the Peruvian slab is slightly under-predicted (Fig. 2.3e). This requires either further reduced slab density or a stronger interpolate coupling across this region. The latter case could result from either a thicker overriding plate or a higher mantle-wedge viscosity (Manea and Gurnis, 2007; Rodríguez-González et al., 2012; 2014) than those assumed in our models. In reality, the subduction of buoyancy features could have flattened the slab to a critical angle, which then initiated a positive feedback between slab flattening and increased suction (Stevenson & Turner, 1977; Taramón et al., 2015), further reducing the slab dip angle (Fig. 2.1). As shown in a recent modeling study with non-linear rheology (Taramón et al., 2015), this positive feedback could have formed a permanent flat slab in Peru where the seafloor is relatively young (Fig. 2.2).

There is still an ongoing debate on whether subducting buoyancy features can cause flat slabs. While earlier 2D numerical models (e.g., van Hunen et al., 2000) support this hypothesis, a recent study (Gerya et al., 2009) suggests that aseismic ridges with moderate sizes could not generate flat slabs. Our 3D models with data assimilation demonstrate that the subduction of buoyancy features clearly contributes to the formation of the localized flat slabs in Peru and Chile (Fig. 2.5a). By simultaneously considering other physical mechanisms, we show that although down-going buoyancy features can effectively reduce the slab dip angle, the presence of other mechanisms such as dynamic suction is also necessary in order to predict the exact amount of flattening. The inadequate flattening of the Peruvian slab in our model represents a potential example for the need of additional lifting forces besides slab buoyancy.

The same reasoning may help to explain the poor spatial and temporal correlation between subducting buoyancy features and observed flat slabs (Skinner and Clayton, 2013), since buoyancy perturbation within the down-going slab is not the only driving force for flat slabs to form. Another possible reason is related to the temporal delay between flab slab formation and the initiation of buoyancy feature subduction. For example, the Juan Fernandez Ridge started to subduct at ~12 Ma (Yáñez et al., 2001), but the cessation of volcanism began at ~5 Ma (Espurt et al., 2008). A similar delay is also observed in Peru as discussed earlier (Fig. 2.9). This may further explain why the subduction of Carnegie Ridge and Iquique Ridge do not correlate with on-going flat slabs, given the short history of the Iquique Ridge subduction (<2 Ma, Rosenbaum et al., 2005) and the nascent slab flattening process associated with the Carnegie Ridge (Gutscher et al. 1999b). In addition, the poor correlation between flat slabs and buoyancy feature subduction can also be due to the tendency of the slab to stay flat long after the subduction of the buoyancy feature, as observed in both analog (Martinod et al., 2005) and numerical (Taramón et al., 2015) models. In this case, an extant flat slab could be due to an ancient buoyancy feature subduction.

The volcanic history in Peru provides useful constraints on the development of flat slabs during the subduction of buoyancy features. Prior to 4 Ma, the arc volcanism is largely continuous in Southern Peru. After this time, a clearly defined volcanic gap emerged (Fig. 2.9), which coincides with the slab flattening due to the Nazca Ridge subduction. While this confirms the general belief on the relation between volcanic gap and flat slab (Nur and Ben-Avraham, 1981; McGeary et al., 1985; Ramos and Folguera, 2009), our model further shows a significant delay of slab flattening and the cessation of volcanism, relative to the initial subduction of the buoyancy

feature. Furthermore, a possible delay by ~2-4 Myr of the volcanic gap formation from initial slab flattening is also observed (Fig. 2.9). If correct, this may reflect the secular cooling of the mantle wedge above a flat slab (van Hunen et al., 2002).

On the other hand, there seems to be long-lived magmatic quiescence between the equator and 6°S (Fig. 2.9). Subduction of the Inca Plateau further cleared out some sporadic volcanisms along these latitudes that were erupted prior to 8 Ma (Fig. 2.9). Temporally and spatially, this lack of volcanism correlates with an overall shallow to flat slab segment that has been in existence for more than 14 Myr (Fig. 2.9). This abnormal slab segment is not due to the subduction of buoyancy features. Possible reasons for its formation may include the small trench curvature, past plate motions, and the earlier subduction history, given the presence of this slab feature in most models presented (Fig. 2.3). Since all our models use the same plate kinematics, we could not separately evaluate the dependence of slab dip on the overriding plate motion (Jarrard, 1986; van Hunen et al., 2000; Lallemand et al., 2005), or trench curvature (Tovish and Gerald, 1978; Schellart et al., 2007). A better understanding on this phenomenon will require future modeling efforts.

Finally, we emphasize that future research is necessary to further verify the dynamics of flat slab subduction. An important aspect is mantle rheology. In our models, we search for an effective viscosity structure that best matches the present-day mantle seismic image. A more physically self-consistent mantle rheology is non-linear viscosity including pseudo-plasticity (Bello et al., 2015) and strain rate-weakening (Taramón et al., 2015). However, to what extent the nonlinear rheology can approximate subduction dynamics is still debated (Stegman et al., 2006; Stadler et al., 2010; Liu and Stegman, 2011; Arrial and Billen, 2013), which is likely due to the incapability of any single rheology to capture the natural complexity of the Earth. Since we are modeling the long-term subduction history of South America by assimilating many different data types, it is impractical to include such a complex rheology into our model. Future research, therefore, should focus on improved data assimilation techniques and more efficient computation methods.

2.6 References

Anderson, M., Alvarado, P., Zandt, G., & Beck, S. (2007). Geometry and brittle deformation of the subducting Nazca Plate, Central Chile and Argentina. Geophysical Journal International, 171(1), 419-434.

Antonijevic, S. K., Wagner, L. S., Kumar, A., Beck, S. L., Long, M. D., Zandt, G., ... & Condori, C. (2015). The role of ridges in the formation and longevity of flat slabs. Nature, 524(7564), 212-215.

Arriagada, C., Roperch, P., Mpodozis, C., & Cobbold, P. R. (2008). Paleogene building of the Bolivian Orocline: Tectonic restoration of the central Andes in 2-D map view. Tectonics, 27(6).

Arrial, P. A., & Billen, M. I. (2013). Influence of geometry and eclogitization on oceanic plateau subduction. Earth and Planetary Science Letters, 363, 34-43.

Barazangi, M., & Isacks, B. L. (1976). Spatial distribution of earthquakes and subduction of the Nazca plate beneath South America. Geology, 4(11), 686-692.

Barazangi, M., & Isacks, B. L. (1979). Subduction of the Nazca plate beneath Peru: evidence from spatial distribution of earthquakes. Geophysical Journal International, 57(3), 537-555.

Bello, L., Coltice, N., Tackley, P. J., Müller, R. D., & Cannon, J. (2015). Assessing the role of slab rheology in coupled plate-mantle convection models. Earth and Planetary Science Letters, 430, 191-201.

Billen, M. I., & Hirth, G. (2007). Rheologic controls on slab dynamics. Geochemistry, Geophysics, Geosystems, 8(8).

Boyden, J. A., Müller, R. D., Gurnis, M., Torsvik, T. H., Clark, J. A., Turner, M., ... & Cannon, J. S. (2011). Next-generation plate-tectonic reconstructions using GPlates. Geoinformatics: cyberinfrastructure for the solid earth sciences, 95-114.

Cloos, M. (1993). Lithospheric buoyancy and collisional orogenesis: Subduction of oceanic plateaus, continental margins, island arcs, spreading ridges, and seamounts. Geological Society of America Bulletin, 105(6), 715-737.

Cruciani, C., Carminati, E., & Doglioni, C. (2005). Slab dip vs. lithosphere age: no direct function. Earth and Planetary Science Letters, 238(3), 298-310.

Davies, D. R., Davies, J. H., Hassan, O., Morgan, K., & Nithiarasu, P. (2007). Investigations into the applicability of adaptive finite element methods to two-dimensional infinite Prandtl number thermal and thermochemical convection. Geochemistry, Geophysics, Geosystems, 8(5).

Espurt, N., Funiciello, F., Martinod, J., Guillaume, B., Regard, V., Faccenna, C., & Brusset, S. (2008). Flat subduction dynamics and deformation of the South American plate: Insights from analog modeling. Tectonics, 27(3).

Flament, N., Gurnis, M., Williams, S., Seton, M., Skogseid, J., Heine, C., & Müller, R. D. (2014). Topographic asymmetry of the South Atlantic from global models of mantle flow and lithospheric stretching. Earth and Planetary Science Letters, 387, 107-119.

Fukao, Y., & Obayashi, M. (2013). Subducted slabs stagnant above, penetrating through, and trapped below the 660 km discontinuity. Journal of Geophysical Research: Solid Earth, 118(11), 5920-5938.

Gerya, T. V., Fossati, D., Cantieni, C., & Seward, D. (2009). Dynamic effects of aseismic ridge subduction: numerical modelling. European Journal of Mineralogy, 21(3), 649-661.

Gurnis, M., Turner, M., Zahirovic, S., DiCaprio, L., Spasojevic, S., Müller, R. D., ... & Bower, D. J. (2012). Plate tectonic reconstructions with continuously closing plates. Computers & Geosciences, 38(1), 35-42.

Gurnis, M., TURNER, M., BOWER, D., FLAMENT, N. E., & MÜLLER, R. D. (2013, October). Advancing cyberinfrastructure for plate reconstructions: Present day mantle structure and the stratigraphic architecture of continents as signals of a dynamic Earth. In Geol. Soc. Am. Abstr. Programs (Vol. 45, No. 7).

Gutscher, M. A., Olivet, J. L., Aslanian, D., Eissen, J. P., & Maury, R. (1999a). The “lost Inca Plateau”: cause of flat subduction beneath Peru?. Earth and Planetary Science Letters, 171(3), 335-341.

Gutscher, M. A., Malavieille, J., Lallemand, S., & Collot, J. Y. (1999b). Tectonic segmentation of the North Andean margin: impact of the Carnegie Ridge collision. Earth and Planetary Science Letters, 168(3), 255-270.

Gutscher, M.A., Spakman, W., Bijwaard, H., Engdahl, E. R. (2000). Geodynamics of flat subduction: seismicity and tomographic constraints from the Andean margin. Tectonics, 19(5), 814-833.

Hayes, G. P., Wald, D. J., & Johnson, R. L. (2012). Slab1. 0: A three-dimensional model of global subduction zone geometries. Journal of Geophysical Research: Solid Earth (1978–2012), 117(B1).

Huene, R. V., Corvalán, J., Flueh, E. R., Hinz, K., Korstgard, J., Ranero, C. R., & Weinrebe, W. (1997). Tectonic control of the subducting Juan Fernández Ridge on the Andean margin near Valparaiso, Chile. Tectonics,16(3), 474-488.

Isacks, B. L. (1988). Uplift of the central Andean plateau and bending of the Bolivian orocline. Journal of Geophysical Research: Solid Earth (1978–2012), 93(B4), 3211-3231.

Jarrard, R. D. (1986). Relations among subduction parameters. Rev. Geophys, 24(2), 217-284.

Jones, C. H., Farmer, G. L., Sageman, B., & Zhong, S. (2011). Hydrodynamic mechanism for the Laramide orogeny. Geosphere, 7(1), 183-201.

Kay, S. M., & Mpodozis, C. (2002). Magmatism as a probe to the Neogene shallowing of the Nazca plate beneath the modern Chilean flat-slab. Journal of South American Earth Sciences, 15(1), 39-57.

Kley, J., & Monaldi, C. R. (1998). Tectonic shortening and crustal thickness in the Central Andes: How good is the correlation?. Geology, 26(8), 723-726.

Klotz, J., Khazaradze, G., Angermann, D., Reigber, C., Perdomo, R., & Cifuentes, O. (2001). Earthquake cycle dominates contemporary crustal deformation in Central and Southern Andes. Earth and Planetary Science Letters, 193(3), 437-446.

Lallemand, S., Heuret, A., & Boutelier, D. (2005). On the relationships between slab dip, back-arc stress, upper plate absolute motion, and crustal nature in subduction zones. Geochemistry, Geophysics, Geosystems, 6(9).

Liu, L., & Stegman, D. R. (2011). Segmentation of the Farallon slab. Earth and Planetary Science Letters, 311(1), 1-10.

Loewy, S. L., Connelly, J. N., & Dalziel, I. W. (2004). An orphaned basement block: The Arequipa-Antofalla Basement of the central Andean margin of South America. Geological Society of America Bulletin, 116(1-2), 171-187.

Marquardt, H., & Miyagi, L. (2015). Slab stagnation in the shallow lower mantle linked to an increase in mantle viscosity. Nature Geoscience.

Mason, W. G., Moresi, L., Betts, P. G., & Miller, M. S. (2010). Three-dimensional numerical models of the influence of a buoyant oceanic plateau on subduction zones. Tectonophysics, 483(1), 71-79.

Manea, V., & Gurnis, M. (2007). Subduction zone evolution and low viscosity wedges and channels. Earth and Planetary Science Letters, 264(1), 22-45.

Manea, V. C., Pérez-Gussinyé, M., & Manea, M. (2012). Chilean flat slab subduction controlled by overriding plate thickness and trench rollback.Geology, 40(1), 35-38.

Martinod, J., Funiciello, F., Faccenna, C., Labanieh, S., & Regard, V. (2005). Dynamical effects of subducting ridges: insights from 3-D laboratory models. Geophysical Journal International, 163(3), 1137-1150.

McGeary, S., Nur, A., & Ben-Avraham, Z. (1985). Spatial gaps in arc volcanism: the effect of collision or subduction of oceanic plateaus. Tectonophysics, 119(1), 195-221.

McQuarrie, N. (2002). Initial plate geometry, shortening variations, and evolution of the Bolivian orocline. Geology, 30(10), 867-870.

Müller, R. D., Sdrolias, M., Gaina, C., & Roest, W. R. (2008). Age, spreading rates, and spreading asymmetry of the world's ocean crust. Geochemistry, Geophysics, Geosystems, 9(4).

Nur, A., & Ben-Avraham, Z. (1981). Volcanic gaps and the consumption of aseismic ridges in South America. Geological Society of America Memoirs, 154, 729-740.

Oncken, O., Hindle, D., Kley, J., Elger, K., Victor, P., & Schemmann, K. (2006). Deformation of the central Andean upper plate system—Facts, fiction, and constraints for plateau models. In The Andes (pp. 3-27). Springer Berlin Heidelberg.

O'Driscoll, L. J., Humphreys, E. D., & Saucier, F. (2009). Subduction adjacent to deep continental roots: Enhanced negative pressure in the mantle wedge, mountain building and continental motion. Earth and Planetary Science Letters, 280(1), 61-70.

O'Driscoll, L. J., Richards, M. A., & Humphreys, E. D. (2012). Nazca–South America interactions and the late Eocene–late Oligocene flat-slab episode in the central Andes. Tectonics, 31(2).

Pennington, W. D. (1981). Subduction of the eastern Panama Basin and seismotectonics of northwestern South America. Journal of Geophysical Research: Solid Earth (1978–2012), 86(B11), 10753-10770.

Ramos, V. A., Cristallini, E. O., & Pérez, D. J. (2002). The Pampean flat-slab of the Central Andes. Journal of South American Earth Sciences, 15(1), 59-78.

Ramos, V. A., & Folguera, A. (2009). Andean flat-slab subduction through time. Geological Society, London, Special Publications, 327(1), 31-54.

Roda, M., Marotta, A. M., & Spalla, M. I. (2011). The effects of the overriding plate thermal state on the slab dip in an ocean-continent subduction system. Comptes Rendus Geoscience, 343(5), 323-330.

Rodríguez-González, J., Negredo, A. M., & Billen, M. I. (2012). The role of the overriding plate thermal state on slab dip variability and on the occurrence of flat subduction. Geochemistry, Geophysics, Geosystems,13(1).

Rodríguez-González, J., Billen, M. I., & Negredo, A. M. (2014). Non-steady-state subduction and trench-parallel flow induced by overriding plate structure. Earth and Planetary Science Letters, 401, 227-235.

Rosenbaum, G., Giles, D., Saxon, M., Betts, P. G., Weinberg, R. F., & Duboz, C. (2005). Subduction of the Nazca Ridge and the Inca Plateau: Insights into the formation of ore deposits in Peru. Earth and Planetary Science Letters, 239(1), 18-32.

Schellart, W. P. (2008). Overriding plate shortening and extension above subduction zones: A parametric study to explain formation of the Andes Mountains. Geological Society of America Bulletin, 120(11-12), 1441-1454.

Seton, M., Müller, R. D., Zahirovic, S., Gaina, C., Torsvik, T., Shephard, G., ... & Chandler, M. (2012). Global continental and ocean basin reconstructions since 200Ma. Earth-Science Reviews, 113(3), 212-270.

Skinner, S. M., & Clayton, R. W. (2013). The lack of correlation between flat slabs and bathymetric impactors in South America. Earth and Planetary Science Letters, 371, 1-5.

Stadler, G., Gurnis, M., Burstedde, C., Wilcox, L. C., Alisic, L., & Ghattas, O. (2010). The dynamics of plate tectonics and mantle flow: From local to global scales. science, 329(5995), 1033-1038.

Stegman, D. R., Freeman, J., Schellart, W. P., Moresi, L., & May, D. (2006). Influence of trench width on subduction hinge retreat rates in 3-D models of slab rollback. Geochemistry, Geophysics, Geosystems, 7(3).

Stevenson, D. J., & Turner, J. S. (1977). Angle of subduction. Nature, 270, 334–336

Tackley, P. J., & King, S. D. (2003). Testing the tracer ratio method for modeling active compositional fields in mantle convection simulations.Geochemistry, Geophysics,

Geosystems, 4(4).

Tan, E., Choi, E., Thoutireddy, P., Gurnis, M., & Aivazis, M. (2006). GeoFramework: Coupling multiple models of mantle convection within a computational framework. Geochemistry, Geophysics, Geosystems, 7(6).

Taramón, J. M., Rodríguez-González, J., Negredo, A. M., & Billen, M. I. (2015). Influence of cratonic lithosphere on the formation and evolution of flat slabs: Insights from 3-D time-dependent modeling. Geochemistry, Geophysics, Geosystems, in press.

Tovish, A., & Gerald, S. (1978). Island arc curvature, velocity of convergence and angle of subduction. Geophysical Research Letters, 5(5), 329-332.

van Hunen, J., van den Berg, A. P., & Vlaar, N. J. (2000). A thermo-mechanical model of horizontal subduction below an overriding plate. Earth and Planetary Science Letters, 182(2), 157-169.

van Hunen, J., Van Den BERG, A. P., & Vlaar, N. J. (2002). On the role of subducting oceanic plateaus in the development of shallow flat subduction.Tectonophysics, 352(3), 317-333.

Yáñez, G., Cembrano, J., Pardo, M., Ranero, C., & Selles, D. (2002). The Challenger–Juan Fernández–Maipo major tectonic transition of the Nazca–Andean subduction system at 33–34 S: geodynamic evidence and implications. Journal of South American Earth Sciences, 15(1), 23-38.

Zhong, S., Zuber, M. T., Moresi, L., & Gurnis, M. (2000). Role of temperature-dependent viscosity and surface plates in spherical shell models of mantle convection. Journal of Geophysical Research: Solid Earth (1978–2012), 105(B5), 11063-11082.

Chapter 3

Abnormal Seismological and Magmatic Processes Controlled by Tearing Flat Slabs

3.1 Abstract[2]

The influence of flat slab subduction on the formation of intra-slab earthquakes, volcanic activities and mantle seismic velocity anomalies remains unclear. We attempt to better understand these processes by simulating the two flat slabs in Peru and Chile using data-orientated geodynamic models. Our results successfully reproduce the observed flat slabs as mainly due to two subducting aseismic ridges. In contrast to the traditional view of flat-slab subduction, we find that these slabs are internally torn, as is due to the 3D nature of the subducting buoyancy features. This broken slab configuration, confirmed by regional tomography, naturally explains the abnormal distribution of and stress regimes associated with the intermediate-depth earthquakes. We further show that the slab tearing process could also better explain the formation of adakitic and ore-forming magmatism, the evolution of the magmatic arc, and the enigmatic mantle seismic structures beneath these regions. We propose that slab tearing may represent a common result of buoyancy feature subduction and that the resulting mantle processes could affect the long-term geodynamic evolution of continents.

---

[2]This chapter has been published as: Hu, J., & Liu, L. (2016). *Abnormal seismological and magmatic processes controlled by the tearing South American flat slabs.* Earth and Planetary Science Letters, 450, 40-51.

3.2 Introduction

The formation of flat slabs strongly affects the volcanic history, earthquake generation, and ore deposits along convergent plate boundaries. In South America, the two most prominent flat slabs, located in Peruvian and Central Chilean (Fig. 3.1), display several unique characteristics, which apparently deviate from the traditional understanding of flat-slab subduction. First, the distribution of intra-slab seismicity and volcanic activities (Fig. 3.1a) along the South American subduction zone, especially at these two flat-slab segments, show irregular spatial patterns (Brudzinski and Chen, 2005; Gutscher et al., 1999). Although the location of earthquakes and the position of volcanic arcs are routinely used to define the geometry of subducting slabs (Coney et al., 1977; Cahill and Isacks, 1992; Hayes et al., 2012), the distribution of intermediate-depth earthquakes in South America is spatially heterogeneous with apparent gaps along the trench (Fig. 3.1a, 3.1b), and the principal stress directions also deviate significantly from a simple configuration of flat slab (Anderson et al., 2007; Fig. 3.2). Consequently, the exact geometry of these flat slabs remains debated (Hayes et al., 2012; Anderson et al., 2007; Antonijevic et al., 2015) (Fig. 3.2). Furthermore, the two flat slabs in Peru and Central Chile do not show clear inland migration of arc volcanism (Antonijevic et al., 2015; Rosenbaum et al., 2005; Supplementary Figs. A.1 and A.2), suggesting that the flattening process of the slabs may be more complex than a mere reduction of local slab dip angle as traditionally assumed (e.g., Coney et al., 1977).

Second, recent seismic tomography has imaged fast shear-wave velocity (Vs) anomalies at ~70-100 km depth underlain by slow Vs anomalies in both the Peruvian (Antonijevic et al., 2015; Scire et al., 2016; Fig. 3.3) and Central Chilean flat-slab regions (Wagner et al., 2005; Young, 2008; Porter et al., 2012; Pesicek et al., 2012; Marot et al., 2014). Apparently, the nature of these seismic anomalies has important implications on the property of the overriding plate, the subducting slab, as well as the ambient mantle. Various explanations were proposed to interpret these seismic structures, including petrological anomalies due to dehydration reactions (Wagner et al., 2005), dry versus wet continental lithosphere (Marot et al., 2014), hydrated flat slab overlain by depleted mantle lithosphere (Porter et al., 2012; Wagner et al., 2006), or the flat slab sitting on a warm asthenosphere (Antonijevic et al., 2015; Pesicek et al., 2012; Calkins et al., 2008). As a result, the origin of these seismic anomalies remains uncertain.

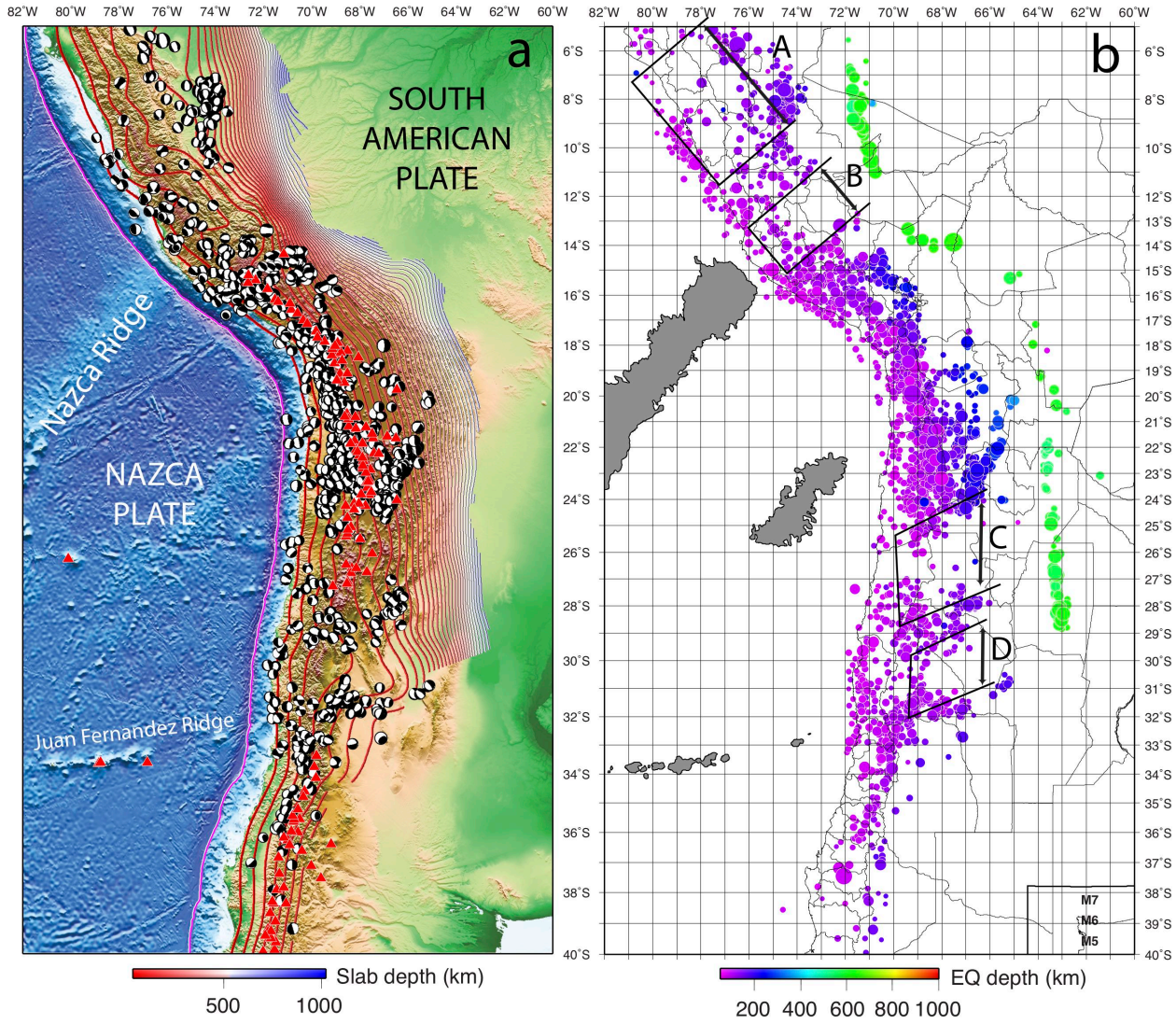

Figure 3.1. Geological and geophysical settings of South American subduction zone. **a**) Topography of the western South America overlain by depth contours of the interpolated Benioff zones (Hayes et al., 2012), modern volcano locations based on www.ngdc.noaa.gov/hazard as well as CMT solutions from the IRIS database (ds.iris.edu/spud/momenttensor). **b**) Seismicity distribution with depth (>70 km) from the IRIS seismic catalog. Seismically quite regions are highlighted with brackets labeled with A, B, C, and D. We propose A, B and D may be caused by the subduction of Inca Plateau, Nazca Ridge and Juan Fernandez Ridge, respectively, while C is likely due to lithospheric delamination (Mulcahy et al., 2014). We used IRIS EMC (Trabant et al., 2012) to prepare the data in this figure.

Third, both the Peruvian and Central Chilean flat slabs are associated with magmatic formation of adakites (Gutscher et al., 2000; Fig. A.1 and A.2 in APPENDIX A). On the one hand, since the chemical composition of adakite is similar to that of Archaean tonalite–trondhjemite–granodiorite (TTG), it has been proposed as a potential analogue for ancient continental growth (Drummond et al., 1996; Martin et al., 2005). On the other hand, the existence of adakites represents unusual (i.e., hot) thermal states of subduction zones, and thus may have important implications on subduction dynamics. Initially, the formation of adakites was attributed to the melting of young slabs (Drummond and Defant, 1990). However, this hypothesis was challenged with the discovery of adakitic suites over old subducting slabs (>25 Ma) (Macpherson et al., 2006). Consequently, many other models were proposed, for instance, melting of the subduction-eroded fore-arc crust (Kay and Mpodozis 2002; Goss et al. 2013), flux-induced mantle melting that fractionates in the garnet-stable lower continental crust (Macpherson et al. 2006; Hidalgo and Rooney 2014), melting of the

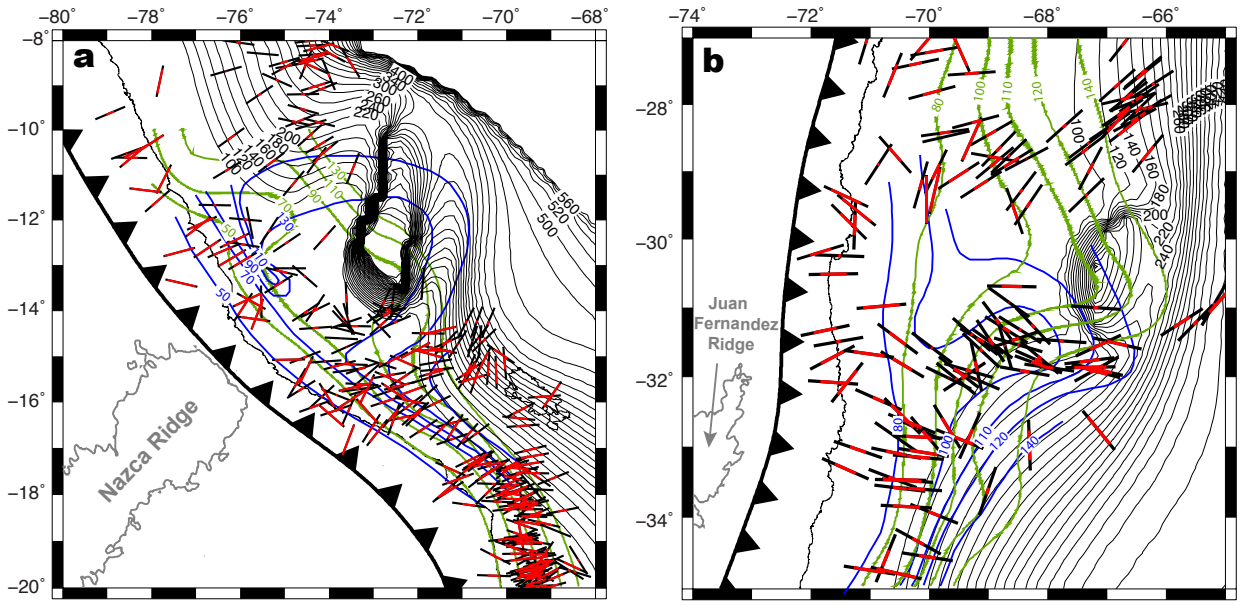

Figure 3.2. Different proposed flat-slab geometries in Peru (**a**) and Central Chile (**b**) overlain by the earthquake T-axes of CMT solutions from the IRIS database (ds.iris.edu/spud/momenttensor). Green lines represent Benioff zone contours of slab 1.0. Blue lines are contours of two alternative models (Antonijevic et al., 2015 in **a**; Anderson et al., 2007 in **b**). Thin black lines are slab contours predicted from this study. Thick black bars with identical length indicate the azimuths of the T-axes, and the overlying red bars with variable lengths represent the horizontal components of the T-axes normalized by the total length of the vector. Therefore, a shorter red bar represents a stronger vertical component of T-axis, compared to a longer one. The observation that vertical component-dominated T-axes are mostly surrounding the slab tears outlines a chimney-configuration of the tearing slab, consistent with our model prediction.

thick arc crust (Petford and Atherton 1996; Wang et al. 2005), as well as slab melting under various conditions (Sajona et al., 1993; Gutscher et al., 2000). Overall, the origin of adakites also remains controversial.

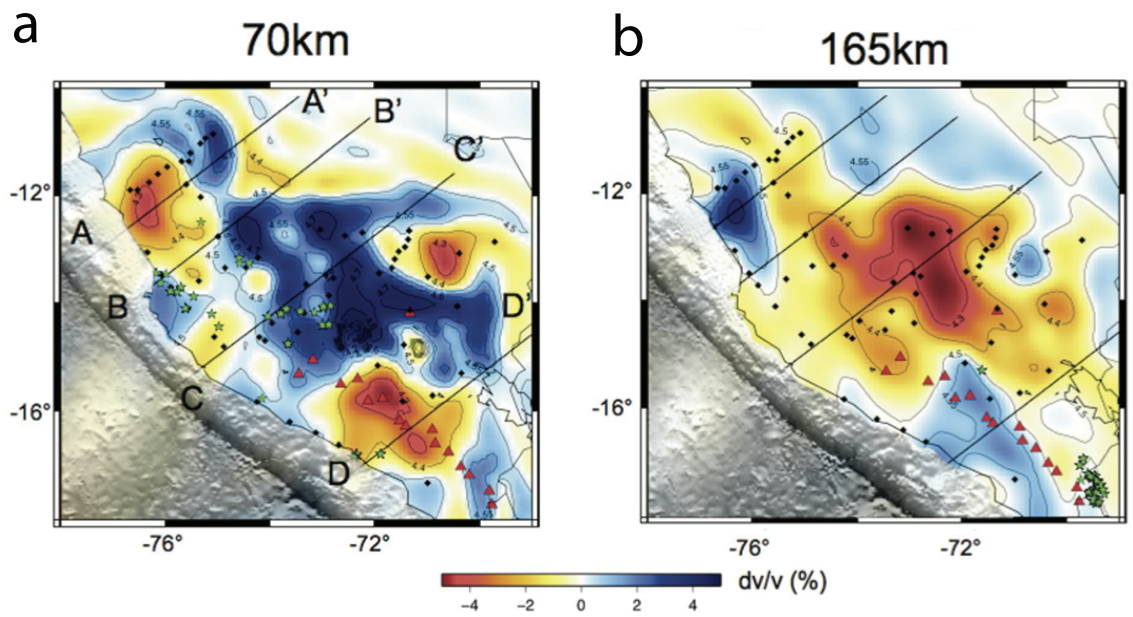

Figure 3.3. Surface-wave tomography models at depth 70 km (a) and 165 km (b) showing the slow and fast Vs anomalies beneath the Peruvian flat slabs (from Antonijevic et al., 2015).

Here, we try to address these questions related to the Peruvian and Central Chilean subduction by investigating the temporal and spatial evolution of the South American flat-slabs. We performed a numerical simulation of the South American subduction history since 100 Ma, using geodynamic models with data assimilation (Hu et al., 2016). On the one hand, our model incorporates all major tectonic elements of past subduction including the plate motion history, seafloor ages, and a deformable Andean trench. On the other hand, we further consider the effects of tectonic features that are potentially related to flat-slab subduction, such as buoyant oceanic crusts, an over-thickened oceanic plateau (Inca Plateau) and two aseismic ridges (Nazca Ridge and Juan Fernandez Ridge) (Gutscher et al., 1999), and thick continental cratons (Fig. A.3). Other model parameters that are more uncertain such as the viscosity structure of the background mantle and the down-going slab are constrained by predicting the present-day slab geometry (Hu et al., 2016) outlined with intra-slab seismicity distribution (Hayes et al., 2012) and seismic tomography

images (Scire et al., 2015). Finally, we evaluate the abnormal seismological and magmatic observations using this constrained model of flat-slab subduction.

3.3 Methods

Following the numerical simulation in Hu et al. (2016), we use the finite element code CitcomS (Tan et al., 2006; Zhong et al., 2008) to solve thermal-chemical convection governed by the conservation of mass, momentum and energy. We assume that an incompressible mantle that has a variable viscosity and satisfies the Boussinesq approximation.

The model domain covers the region from 10° W to 100° W in longitude, 70° S to 20° N in latitude, and from the surface to 2890 km depth in radius, which is unevenly discretized by 257×257×65 grids with the finest resolution of 27×27×8 (km) in the upper central domain. Viscosity is both temperature- and composition-dependent, superimposed on a 4-layer background viscosity profile (Fig. 3.4): lithosphere (0-100 km), asthenosphere (100-300 km), transition zone (300-660 km), and lower mantle (660 – 2890 km). The background viscosity ranges from 5×10^{19} Pa s within the asthenosphere to 10^{23} Pa s within the lithosphere and at around 1500 km depth, while the transition zone viscosity is 10^{21} Pa s. The lower mantle viscosity increases from 660 km to about 1500 km depth, and then gradually decreases toward the core-mantle boundary. We also include a uniformly shallow-dipping weak plate interface (decoupling weak zone) along the subduction zone, a maximum viscosity cutoff within the slab hinge and a weak mantle wedge above the slab in our models to facilitate asymmetric subduction, similar to our earlier models (Liu and Stegman, 2011). This 3-D mantle viscosity structure is required to best match the present-day slab geometry as geophysical data reveal (Hu et al., 2016).

All models use free-slip sidewalls and core-mantle boundary, and imposed tangential velocities at the surface. The imposed surface plate motion is from a recent plate reconstruction by Müller et al. (2008). We use the seafloor age taken from the same plate reconstruction to define and update the thermal profile of oceanic lithosphere by assuming a modified error function based on the half-space cooling model (Hu et al., 2016). The continent is defined as a high viscosity sheet that has a thickness of 75 km. To simulate the dynamic suction force from cratons, we also parameterize thicker cratonic roots that extend to about 200 km depth. The geometry of the cratonic roots at 75 km depth follows that of Loewy et al. (2004), and their horizontal area shrinks as it goes from 75 km to 200 km depth. The temporally variable geometry of paleo-trenches is

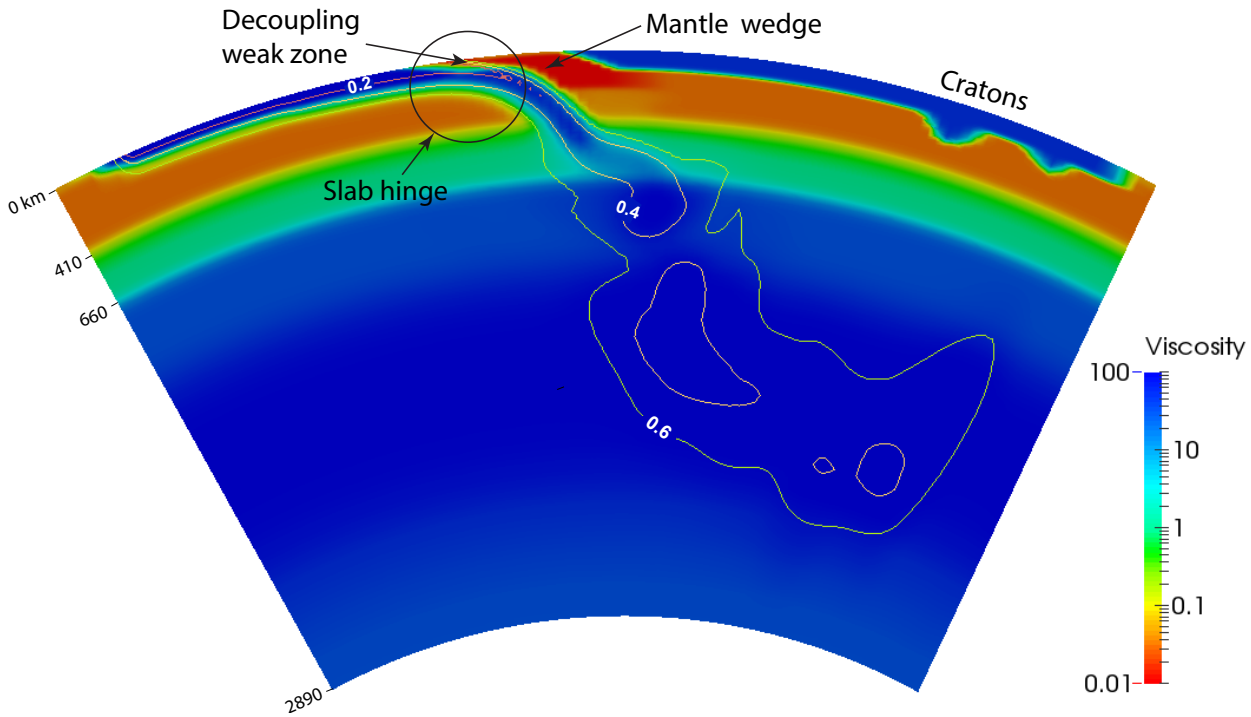

Figure 3.4. Viscosity structure of an east-west cross-section at 20°S. Normalized viscosity is shown, with the reference viscosity being 10^{21} Pa s. The background viscosity follows a 4-layer profile from the lithosphere to the lower mantle. A uniform east-dipping narrow weak zone and a weak mantle wedge are on top of the slab in order to decouple the slab from the surface and to allow for asymmetric subduction. Because the maximum depth of the weak zone and the maximum viscosity cutoff within the slab hinge determine the slab strength, they are varied in Figure 3.6 to test the robustness of the predicted slab tears. Over-plotted contours are isotherms with different values of the non-dimensional temperature.

reconstructed by taking into account the shortening history of the central Andes (Arriagada et al., 2008). We use compositional tracers to represent the geometry and volume of oceanic crust, oceanic plateau and aseismic ridges. The buoyancy of these features is equivalent to an 8-km thick crust with a density of 2.9 g/cm^3, and 15-km thick oceanic plateau/aseismic ridges with the same density, respectively. More details about the geodynamic models could be found in Hu et al. (2016).

3.4 Results

3.4.1 Present-day slab geometry

Figure 3.5 illustrates the predicted 3-D present-day slab geometry that best-fits the available observational constraints (Hu et al., 2016). In particular, this model successfully satisfies the overall shape of the Benioff zones along South America (Fig. 3.5a). Minor mismatches include a slightly shallower (steeper) predicted slab dip along the central Andes (northern Peru), compared

to that outlined by seismicity (Hayes et al., 2012). The predicted slab geometry is also consistent with recent high-resolution tomography images (Scire et al., 2015). More importantly, the predicted along-trench variation of slab geometry closely matches the sharp slab curvature changes across the flat slab segments (Figs. 3.5a, A.4 and A.5).

Among the various proposed physical mechanisms for flat-slab formation including subduction of buoyancy features (Gutscher et al., 1999), hydrodynamic suction from a thick overriding plate (Manea et al., 2012), and fast overriding motion of continents (van Hunen et al., 2000), we find that the long-wavelength slab curvatures result from the viscous suction force from the overriding plate, and that the local flat slab geometry is mainly controlled by the subducting oceanic plateau and aseismic ridges (Hu et al., 2016). Therefore, it is the combined effects of these different mechanisms that lead to the observed present-day slab geometry along the entire South American trench.

An important result from these models is a major difference in the geometry of flat slabs from the traditional view: the central part of the flat slab tears apart with the two open limbs spanning a seemingly flat configuration (Figs. 3.5a, A.4). In order to test the robustness of this model prediction, we perform three additional models by varying the viscosity structure of the slab hinge (Fig. 3.4), a key parameter controlling slab deformation (Fig. 3.6). These tests show that the slab tearing process does depend on slab-hinge viscosity and the degree of inter-plate decoupling. For example, the extent of slab tearing in Central Chile decreases (Fig. 3.6b-d) when the slab hinge becomes progressively stronger and the decoupling weak zone gets shallower, relative to those in the best-fit model (Fig. 3.6a). However, even in the case where the slab is the strongest (Fig. 3.6d), the Chilean flat slab still severely stretches and thins due to internal deformation caused by local buoyancy of the aseismic ridge. The fact that this model predicts a steeper Central Chilean slab but shallower slabs at greater depths than implied by the Benioff zones (Fig. 3.6d) suggests that this viscosity structure is inappropriate.

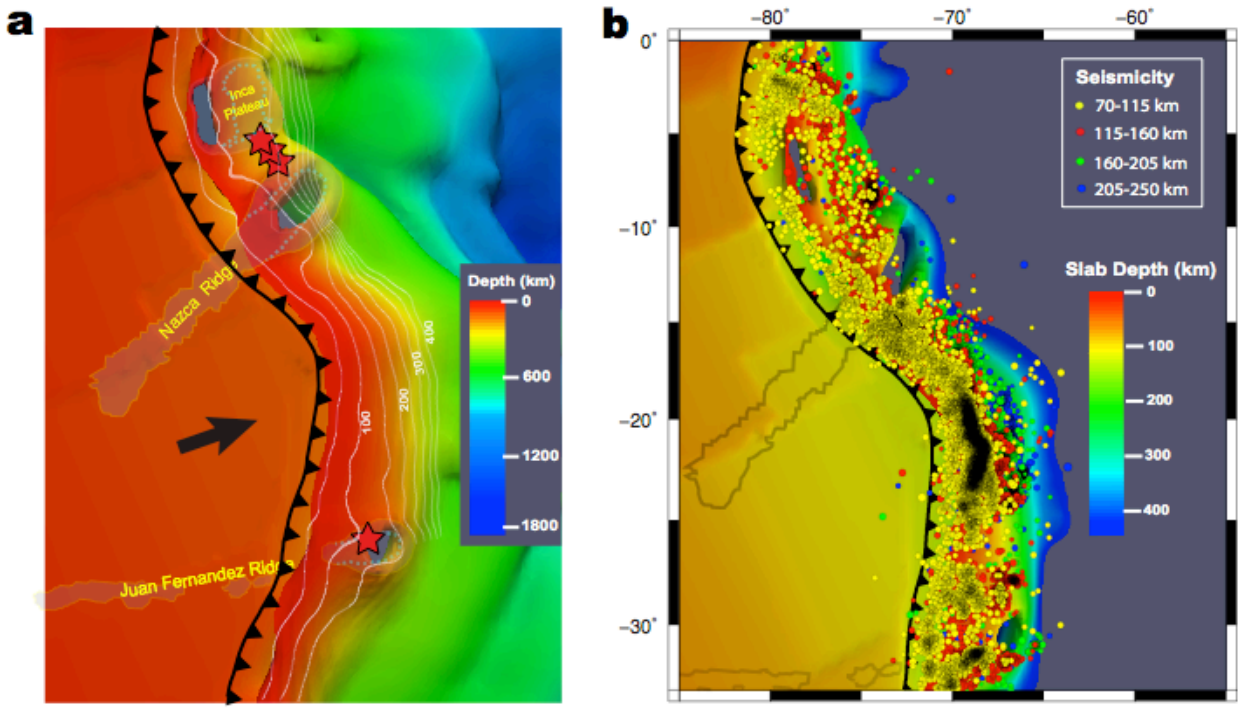

Figure 3.5. 3-D geometry of the predicted present-day slab beneath South America and that of the Nazca Plate west of the trench (outlined using an isotherm of 300 °C cooler than the ambient mantle). **a**) 3D aerial view of the subducting Nazca Plate (temperature isosurface), with colors representing the depth of the slab's upper surface on the right side of the trench and depth of the plate's lower surface on the left side. The slab tears are illustrated with both the isosurface of temperature and the evolution of buoyancy features (translucent gray areas). Thin white lines are the interpolated Benioff zones from Hayes et al. (2012). Dashed lines within the subducting buoyancy features outline their original intact geometry. Red stars indicate the locations of adakitic eruptions. **b**) Map-view comparison of the slab geometry with the distribution of intermediate-depth seismicity (M_b>3.0 from ISC seismic catalog).

For the Peruvian flat slab, the tearing event is a robust model prediction as long as the subducting buoyancy feature is included in the simulation (Fig. 3.6a-d). We emphasize that the slab tear in visualization is defined for a given isotherm. This means a seemingly continuous slab outlined with a hotter isotherm (e.g., Fig. 3.6d) may appear torn when using a cooler isotherm. In general, these models suggest that a broken or severely stretched flat slab is required in order to best match the sharp slab dip variations associated with both the Peruvian and Central Chilean flat slabs (Fig. 3.5, 3.6). This internal slab deformation is confirmed by recent seismic anisotropy measurements within the subducting Peruvian slab (Eakin et al., 2015). As we subsequently further demonstrate with more observational constraints, both these two flat slabs are very likely to be torn.

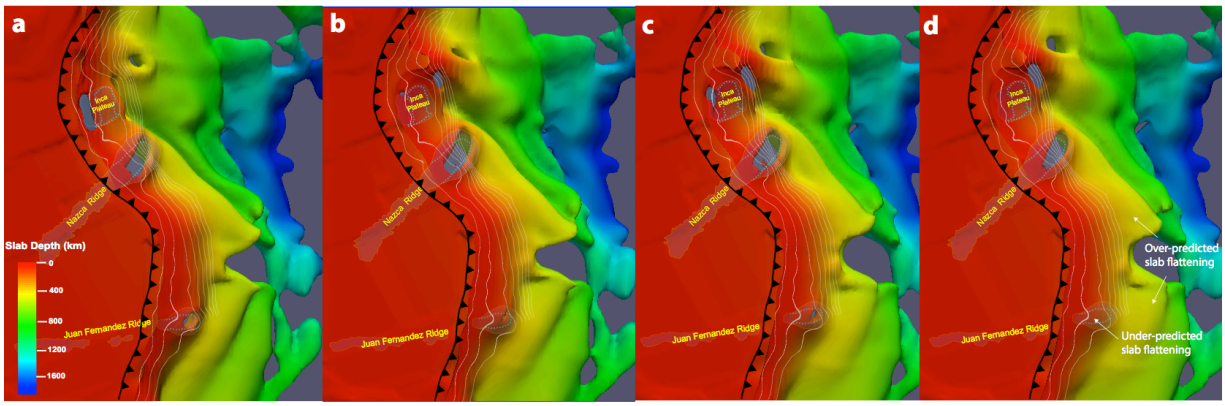

Figure 3.6. The predicted present-day geometry of the subducting Nazca Plate (see Fig. 3.5 for a more detailed description) with different viscosity structures. **a**) The model with a decoupling weak zone extending from 0 to 120 km depth. The maximum viscosity at the slab hinge is 5×10^{22} Pa s. **b**) Same as **a**, except that the decoupling weak zone terminates at 60 km depth. **c**) Same as **b**, except that the maximum viscosity at the slab hinge is 7.5×10^{22} Pa s. **d**) Same as **b**, except that the maximum slab hinge viscosity is 10^{23} Pa s.

3.4.2 Formation of internal slab tears

In order to better understand the formation of these slab tears, we examine the temporal evolution of the flat-slab geometry during subduction of the buoyancy features (Figs. 3.7 and 3.8). We find that the initiation of the slab tear could be intuitively explained by the differential sinking rates between the subducting aseismic ridges and the surrounding slab portions: since the aseismic ridges are less dense than the surrounding slab (Gutscher et al., 1999), they tend to sink more slowly, which causes extensional strain to accumulate at the down-dip tips of these subducting ridges. Another way to think of this process is to consider the conservation of mass: since formation of the two prominent flat slabs requires an increase of local slab surface area relative to the steeply subducting parts (Fig. 3.6), the slab has to stretch internally. This can be seen from the subtle divergence of the horizontal velocity field across these growing slab tears and associated toroidal mantle flow around the open limbs of these slab tears (Fig. 3.8). Due to the localized distribution of buoyancy force within the aseismic ridges, this internal strain effectively stretches and thins the slab, eventually forming a gap. In contrast, the stress originated from hydrodynamic suction due to a thick overriding plate (Hu et al., 2016) is more distributed and temporally varying, and thus is less likely to cause the slab to tear (Taramón et al., 2015).

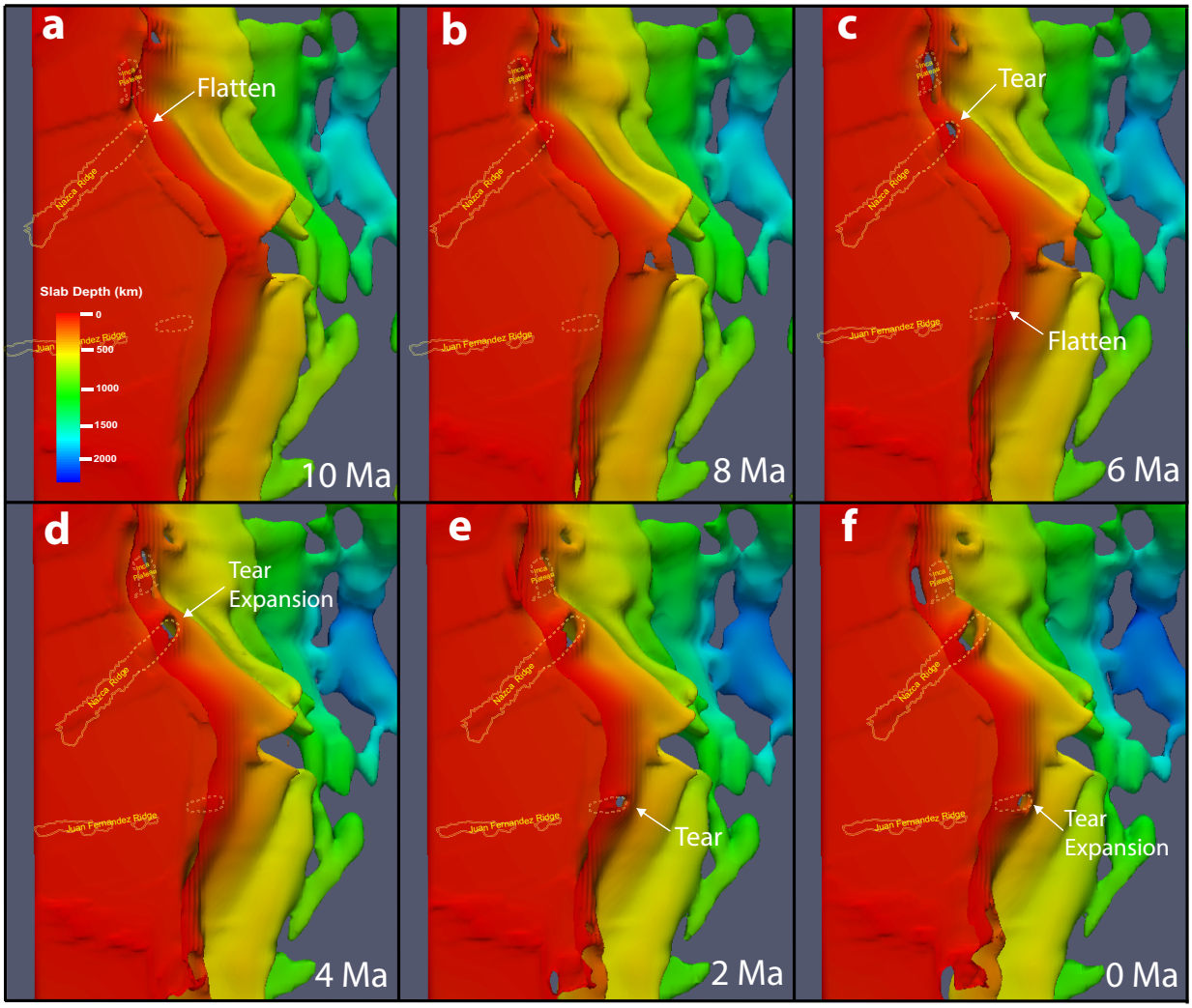

Figure 3.7. 3-D view on the temporal evolution of the subducting Nazca Plate (outlined using an isotherm of 300 °C cooler than the ambient mantle) from 10 Ma to present day. The figure shows the evolution of initial slab flattening and deformation (**a, b, d**), and subsequent slab tearing and tear expansion (**c-f**) with time, for both the Peruvian and Central Chilean flat slabs.

When subduction continues, the area of slab tear expands and the upper edge of the tear propagates toward the trench as the aseismic ridges subduct deeper (Fig. 3.7). The expansion of these slab tears is likely further related to the over-pressure of the sub-slab mantle (Liu and Stegman, 2011). The pressure beneath the slab is overall higher than that above because the slab's weight presses the mantle below but reduces the pressure above (Tovish et al., 1978). As a hole forms within the slab hinge, the high-pressure mantle beneath it pushes though the hole and moves upward; this local mantle upwelling warms up the surrounding slab and causes the slab to weaken further and the area of the slab tear to expand (vertical cross-sections in Fig. 3.8).

Furthermore, the temperature-dependence of slab strength suggests that a small extensional strain within the slab would quickly accumulate, because the positive feedback between temperature and viscosity facilitates strain localization. In addition, the strain-rate dependence of rheology, which is not included in our model, may further enhance this process (Arrial and Billen, 2013). In reality, possible existence of faults within the aseismic ridges during their emplacement into the subduction zone (Kopp et al., 2004) and a perturbed thermal structure due to the initial hot spot associated with the aseismic ridge (Yáñez et al., 2001) may also weaken the slab. Collectively, these factors should lead to stronger and faster local slab deformation compared to without. In our model, since the buoyancy features are the original source of stress for deformation to occur, the narrow aseismic ridges and oceanic plateaus ultimately become the location of slab detachment, which initiates at the down-dip end of these buoyancy features and propagates upwards as subduction continues (Figs. 3.7, 3.8).

According to our results, the formation of slab tears is associated with localized asthenosphere upwelling below these regions (Fig. 3.8). Dynamically, this upwelling is both passively driven by the outward extension of the flat slab (Figs. 3.6, 3.7) and actively driven by the excess sub-slab dynamic pressure as mentioned above (Liu and Stegman, 2011; Hu et al., 2016), which in the extreme case may form a large igneous province (Liu and Stegman, 2012). In Peru, strong localized upwelling occurred at 9 Ma along the eastern edge of the subducting Inca Plateau and at 4 Ma along the western edge of this Plateau as it further subducts (Fig. A.6). Another phase of prominent upwelling started at 7 Ma along the down-going Nazca Ridge and sustained to the present (Fig. 3.8a). As subduction continues, these slab gaps and associated asthenosphere upwelling in Peru migrated southeastward (Fig. 3.8a). In Central Chile, a similar yet weaker upwelling started around 5 Ma when the slab tear initiated, and subsequently waned toward the present-day (Fig. 3.8b).

Formation of these slab tears explains several otherwise counter-intuitive observations. Since a slab tear releases sub-slab dynamic pressure (Stegman et al., 2006; Liu and Stegman, 2011) that initially facilitates slab flattening (Fig. 3.8), the mechanically detached frontal part of the slab would sink more easily than the intact rear part. Therefore, the larger slab gap inside the down-going Nazca Ridge than that in the Juan Fernandez Ridge explains why the former that has a greater buoyancy generates a shorter (~400 km) flat slab than that due to a less buoyant ridge in central Chile where the flat slab is ~700 km long (Figs. 3.5, A.4; Hayes et al., 2012). Furthermore,

the observation that the Inca Plateau that is shorter in the trench-normal direction than the aseismic ridges only partially tears along its edges (Fig. 3.5a,) suggests that an oceanic plateau could likely translate a more intact flat slab far inland. This is consistent with the observation that a landward migration of volcanic arcs occurred over a large subducting oceanic plateau, best illustrated as the Late Cretaceous subduction of the Shatsky conjugate beneath western United States (Henderson et al., 1984; Liu et al., 2010). In contrast, a landward arc migration is largely absent during the Peruvian and Chilean slab flattening where aseismic ridges subduct (Rosenbaum et al., 2005) (Figs. A.1 and A.2). More implications of the slab tearing process are discussed in the next section.

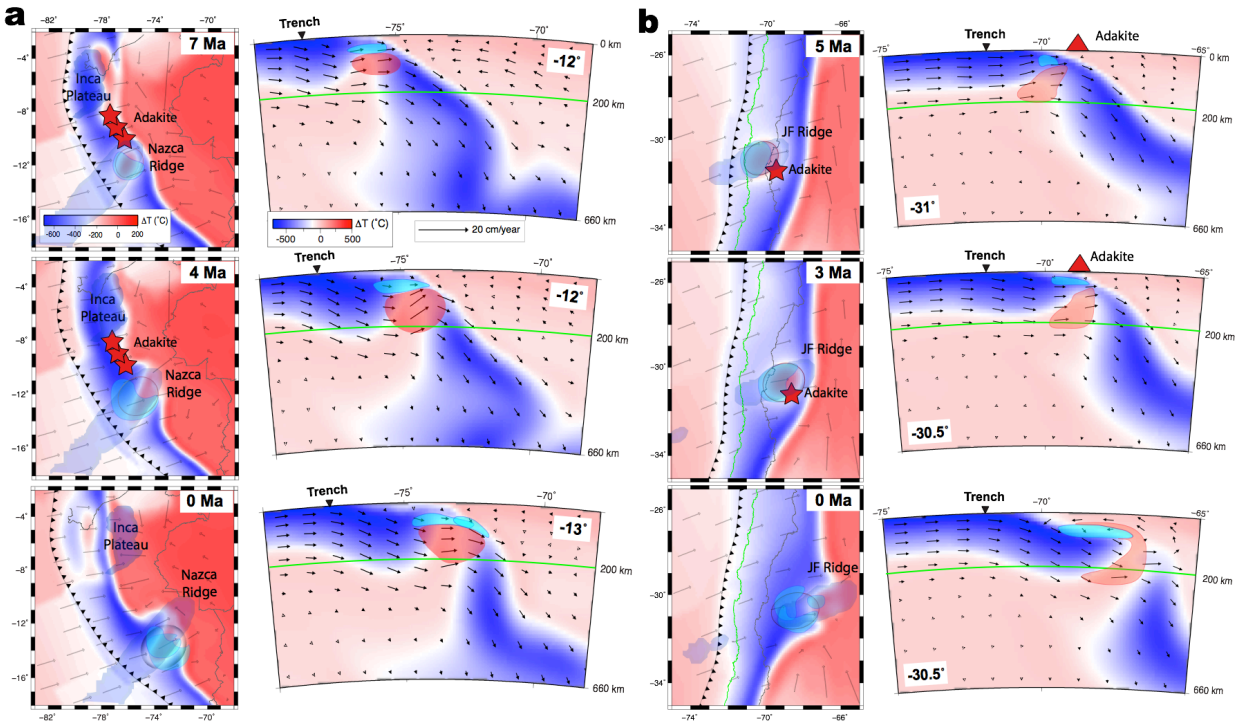

Figure 3.8. 2-D view on the temporal evolution of the Peruvian (**a**) and central Chilean (**b**) slab tears. In each panel, both the map (left) and cross sectional (right) views are shown, corresponding to different times. All maps are at 100 km depth, and cross sections are E-W at the given latitude. The background color is for temperature (note the different color scales for the maps and cross sections) and arrows for velocity fields. The slab-tear induced upwelling likely generates partial melting (red transparent pattern), eclogitized crustal fragments at shallower depths (cyan transparent patterns) and adakitic eruptions (red stars in map views and triangles in cross sectional views).

3.4.3 Abnormal seismological and volcanic observations controlled by tearing flat slabs

Both the tearing flat-slab geometry and the associated asthenosphere upwelling provide new perspectives to better understand the abnormal seismological and volcanic observations along the South American subduction zone.

3.4.3.1 The distribution of intermediate-depth earthquakes

Our new flat-slab configuration naturally explains the enigmatic spatial variation of intermediate-depth (>70 km) seismicity along the South American trench (Brudzinski and Chen, 2005). At a glance, the map view (Fig. 3.5b) reveals a strong correlation between the three slab holes and a scarcity or lack of seismicity over these regions. All proposed models for the generation of intermediate-depth earthquakes require the presence of an oceanic lithosphere (Houston, 2007). Therefore, the predicted slab gaps explain the lack of seismicity in these regions, which are otherwise counter-intuitive since flat slabs likely concentrate large stresses and should, therefore, produce more earthquakes than the surrounding regions (Anderson et al., 2007). The other two regions in South America where reduced seismicity is observed are the equator and ~27 °S (Fig. 3.5b), with the former corresponding to the subducting Carnegie Ridge (Fig. A.7) that is not simulated in our model and the latter attributed to possible lithospheric delamination (Mulcahy et al., 2014).

To better understand the spatial correlation between earthquakes and slab configuration, we compare the detailed 3-D distribution of seismicity with the predicted slab geometry at four different depth ranges (Fig. 3.9). For each range, we plot earthquake epicenters with M_b magnitude > 4.0, and compare their locations with the geometry of the slab at a similar depth. We note that earthquake location errors for these regions are about 10-30 km (Anderson et al., 2007; Dougherty and Clayton, 2015), which is minor compared to the overall slab dimension considered here. Figure 3.9 reveals that almost all earthquakes fall into the slab interior at all depth ranges for both the Peruvian (Fig. 3.9b) and Chilean (Fig. 3.9a) slab segments. This provides another strong support to our model prediction, especially in Chile where high-resolution tomography is still lacking and the slab tear is more localized.

A closer examination of the modeled slab configuration suggests that the central Chilean slab gap with a west-downward tilting geometry between 30 °S and 32 °S is clearly delineated by the westward retreating seismicity distribution from 70 km to 200 km depths. The predicted reconnection of the slab below ~150 km depth on the eastern side also coincides with a chain of deep seismicity at a similar location (Fig. 3.9a). The predicted Peruvian slab gap (between 10 °S and 14 °S) goes largely vertically except near the trench where the slab reconnects at shallow depth (Fig. 3.9b). And this geometry is also delineated by the associated seismicity distribution, with the

deeper side of the Peruvian slab gap aligned with some small-magnitude earthquakes (Figs. 3.1b, 3.5b).

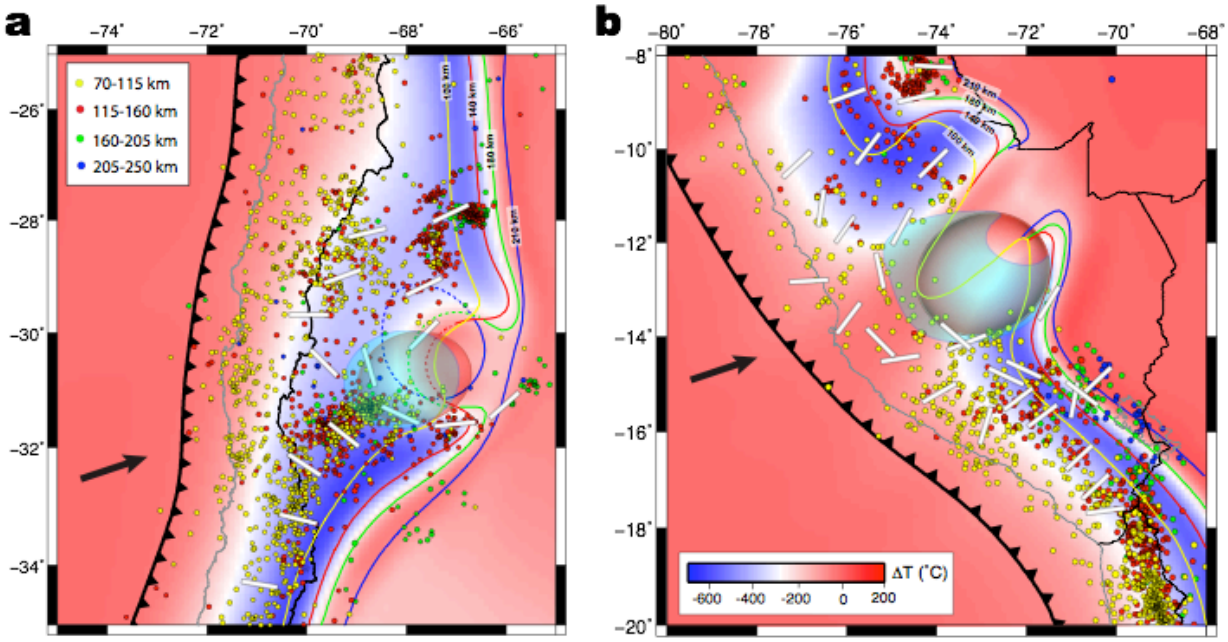

Figure 3.9. Model comparison with seismic properties. **a**) Comparison of slab geometry (outlined using an isotherm of 200 °C cooler than the ambient mantle) at different depths (using different color lines) with seismicity (M_b>4.0 from ISC seismic catalog, larger than the M_b threshold of 3.0 in Fig. 3.1b in order to show the background slab geometry). Overplotted are earthquake T-axis orientation (horizontal component; white bars) and the position of a vertical pair of slow (red sphere) and fast (cyan disk) Vs anomalies. **b**) Same as **a**, but for the tearing Peruvian flat slab region.

3.4.3.2 The stress state of flat slabs

Our model results also better explain the unusual stress pattern of flat slabs in South America and, therefore, help to reconcile the existing debates on their geometry (Cahill and Isacks, 1992; Hayes et al., 2012; Anderson et al., 2007; Antonijevic et al., 2015). The analysis of earthquake focal mechanisms in Central Chile suggests a spatial pattern of slab stress (Anderson et al., 2007) (Fig. 3.9a) that is inconsistent with a wide flat slab traditionally defined by interpolating earthquake locations (Cahill and Isacks, 1992), and this stress pattern has been argued to imply a much narrower flat slab (Anderson et al., 2007) (Fig. 3.2b). Similarly in Peru, a recent tomography and focal mechanism analysis suggest a more localized flat slab (Antonijevic et al., 2015; Kumar et al., 2016), compared to that based on interpolated Benioff zones (Hayes et al., 2012) (Fig. 3.2a). From our model, the remarkable matches between the predicted tearing flat slabs

and earthquake locations suggest that the debated flat slab geometry may be reconciled by realizing the existence of these internal slab tears.

More specifically, we examine the pattern of earthquake focal mechanisms by first plotting the representative horizontal component of T-axis (i.e., extensional stress direction, white bars in Fig. 3.9) inferred from relocated earthquakes in Central Chile (Anderson et al., 2007) and Southern Peru (Kumar et al., 2016). We can see that while the stress field to the north and south of these flat slabs is generally consistent with down-dip extension that is generally perpendicular to the trench, an obvious change in the T-axis orientation occurs both at 29°S-32°S (Fig. 3.9a) and at 10°S-15°S (Fig. 3.9b); they both form a quasi-circular pattern that strongly resembles the outline of the two slab tears. This intuitively suggests that the abnormal stress pattern reflects the spatial distribution of slab deformation during the formation of these tears (Figs. 3.7, 3.8).

By further analyzing the 3-D orientation of the dilatational focal mechanisms around the two flat slabs using data from IRIS (ds.iris.edu/spud/momenttensor), we find that most of the T-axes close to the edges of our predicted slab tears have a dominant vertical component over the horizontal one (Figs. 3.2a, 3.2b), and that those farther away from the two slab tears demonstrate a stronger horizontal component. This observation strongly reinforces our proposition that these T-axes outline the chimney-shaped slab edge geometry around the tearing flat slabs in both Peru and Chile (Figs. 3.2, 3.5, 3.9). Indeed, these T-axis orientations could be best interpreted as a superposition of the local down-dip direction following the highly distorted slab geometry and slab-edge parallel extension due to the expanding tears, with the former representing the major component of slab stress. Therefore, we conclude that our predicted broken slab geometry reconciles contrasting earlier hypotheses on the slab geometry using different observational proxies (Fig. 3.2), and that new insights on intra-slab earthquake formation emerge from these geodynamic simulations.

3.4.3.3 Seismic velocity structures

The asthenosphere upwelling associated with the breaking flat slabs helps to explain unusual seismic velocity structures below these regions. Recent shear-wave tomography imaged a fast Vs anomaly at depth between ~70 km and ~100 km in Central Chile, underlain by a slow Vs anomaly with a similar size (Wagner et al., 2005; Porter et al., 2012; Marot et al., 2014; Calkins et al., 2008). Interestingly, a recent ambient noise tomography investigating the Peruvian flat slab (Antonijevic

et al., 2015) discovered similar seismic structures and with an even larger size (Fig. 3.3). Although the p-wave property of these fast Vs anomalies are uncertain or somewhat inconsistent among different studies (Wagner et al., 2005; Marot et al., 2014; Pesicek et al., 2012), reduced p-wave velocities associated with the slow Vs anomalies seem to be confirmed, especially in Peru (Scire et al., 2016; Marot et al., 2014; Pesicek et al., 2012). According to our models, both the present-day geometry and position of asthenosphere upwelling are consistent with those of the observed slow seismic anomalies (Figs. 3.3, 3.8, 3.9). This strong correlation suggests that the slow seismic anomalies very likely represent the hot asthenospheric mantle with possible partial melts due to decompression melting.

In contrast, the nature of the fast Vs anomalies is more elusive. If these structures have low p-wave velocities as proposed by Wagner et al. (2005), the resultant low Vp/Vs ratio of ~1.70 may indicate a highly depleted, pyroxene and Mg rich continental lithosphere (Wagner et al., 2006; Porter et al., 2012). A remaining question for this interpretation is why these lithosphere segments that are clearly outside of the tectonic cratons strongly correlate with the underlying slow seismic anomalies and the slab tears. If the fast Vs anomalies have fast p-wave velocities, they may instead represent the fragmented oceanic crusts. Since the flat slab has been thinned and stretched significantly, some oceanic crust could be easily stripped off and entrained by the asthenosphere upwelling. Due to the appropriate temperature and pressure conditions, these crustal fragments would easily convert to eclogite (Aoki et al., 2004), which at this depth range is seismically faster than both the continental crust (Anderson and Bass, 1984) and ambient mantle lithosphere (Worthington et al., 2013). Although future work is needed to further distinguish the above two scenarios, they both suggest that these fast Vs anomalies are not part of the flat slabs. Consequently, both these interpretations explain the apparent lack of seismicity in these regions, since these fast anomalies are mechanically decoupled from the subducting oceanic slabs (Fig. 3.8).

3.4.3.4 The formation of adakites

The upwelling asthenosphere beneath the tearing flat slabs also provides an ideal condition for the slab, especially its crust, to melt, which could be responsible for the formation of adakitic magmatism. In Central and South America, adakites formed above the subducting Chile Rise, Cocos Ridge, Carnegie Ridge, Nazca Ridge and Juan Fernendez Ridge (Gutscher et al., 2000). Among these, subduction of active mid-ocean ridges, such as Chile Rise and Cocos Ridge, can

naturally result in slab melting (Drummond and Defant, 1990). But this is unclear for the latter three Ridges that are far away from spreading centers. Our model, with the asthenosphere upwelling beneath a tearing slab, provides a natural explanation for the observed adakites at these sites where the internal extension of the flat slab causes local temperature increase, which, together with the upwelling asthenosphere, could easily melt the much-thinned slab and its basaltic crust (Fig. 3.8).

In observation, adakitic eruptions in central Chile took place around 6-3 Ma, along ~31°S (Gutscher et al., 2000), which correlates remarkably with the initial formation of the slab gap (Fig. 3.8b). In Peru, the adakitic eruptions occurred along a ~300 km N-S distance range during 10-4 Ma (Gutscher et al., 2000). This process could have resulted from the joint contribution of slab tearing due to subduction of the Inca Plateau and the Nazca Ridge, during which toroidal flows advecting the hot mantle around local slab edges converge at the location of the adakite formation (Fig. 3.8a). Toward the present day, the cessation of adakitic eruption is largely correlated with the waning asthenosphere upwelling after the initially accumulated sub-slab dynamic pressure was released and with the gradual cooling of the mantle wedge as the slab further flattens (Fig. 3.8). These dynamic processes seem also consistent with the ore deposition history over these flat-slab segments (Rosenbaum et al., 2005).

3.5 Discussion

Our subduction model provides new perspectives for multiple enigmatic observations associated with the South American flat slabs. Consequently, this requires us to reconsider several consequences of flat slab subduction.

First, the mechanism for intermediate-depth earthquakes in Peru and Central Chile is uncertain. Currently, dehydration embrittlement (Raleigh and Paterson, 1965; Kirby et al., 1996; Peacock and Wang, 1999; Houston, 2007) represents a popular hypothesis for the cause of these earthquakes. Accordingly, Porter et al. (2012) suggest that the intermediate-depth seismicity in Central Chile occurs in the subducting oceanic mantle (Gans et al., 2011), where dehydration reaction of antigorite takes place (Kirby et al., 1996). They further suggest that the reduced seismicity below the front of the flat slab where steep subduction resumes, results from the cessation of dehydration, as the increased bending and extension within the upper half of the slab thickness release all the water (Porter et al., 2012). However, this hypothesis is not entirely

consistent with the facts that the seismicity is already significantly diminished or absent along the flat part before the slab resumes steep subduction, especially in Peru (Figs. 3.1b and 3.9b) and that a small number of earthquakes reappear at greater depth below the inland portions of the flat slabs that are seismically quite (Figs. 3.5b and 3.9).

In order to reconcile this paradox, Kumar et al. (2016) propose that the thick crust due to the emplacement of the Nazca Ridge diminishes the initial hydration of oceanic mantle lithosphere, which limits the amount of subsequent mantle dehydration as the ridge subducts, resulting in the reduced seismicity within the inboard projection of the Ridge. However, this explanation needs to be further verified, since dehydration embrittlement is not a fully confirmed hypothesis for intermediate-depth earthquake formation (Houston, 2007), and it is also unclear how the aseismic ridge could reduce the amount of hydration within the oceanic plate. In comparison, the slab gaps revealed by our model could explain both the reduced seismicity (Figs. 3.5, 3.9) and the slab stress state (Figs. 3.2, 3.9) more naturally, without the need to further modify the dehydration hypothesis. In addition, the locally elevated temperature of the torn or severely stretched flat slabs, below which hot mantle upwelling occurs, may be also responsible for the reduced seismicity.

Second, the exact geometry of flat slabs, especially that in Central Chilean, has been debated. Early receiver functions (Gilbert et al., 2006; Heit et al., 2008) could not resolve the flat slab due to the limited data coverage. As more regional seismic arrays are deployed, tomography models with relatively high resolution emerged. However, the presence of strong fast Vs anomalies at shallow depth (Wagner et al., 2005; Porter et al., 2012; Antonijevic et al., 2015), which were interpreted as depleted mantle lithosphere (Wagner et al., 2005) and/or eclogite converted from fragmented oceanic crust (this study), has severely obscured the detection of the down-going slab. Our best-fit model shows that in Central Chile much of the flat slab remains intact and the slab tear mainly occurs where the slab resumes steep subduction at the tip of the Juan Fernandez ridge. A more recent receiver function analysis by Gans et al. (2011) confirmed the existence of this flat slab on the west, but they could not resolve the slab geometry further east. In fact, Gans et al. (2011) observed multiple offsets of oceanic Moho depth trenchward of our predicted slab gap along the Juan Fernandez ridge and implies severe deformation within the flat slab, consistent with our model (Fig. 3.8). Alternatively, the flat slab in Central Chile may be severely deformed and thinned, but has not been fully torn apart yet (Fig. 3.6d). This slab configuration, alternative to our best-fit model, is still potentially consistent with the stress pattern and the adakitic magmatism

above a localized mantle upwelling. However, this model is likely inconsistent with the distribution of intermediate-depth earthquakes. Nevertheless, the existing uncertainty in the mechanisms of intermediate-depth earthquakes requires more observational work to verify the existence of the Central Chilean slab gap.

Future research also needs to address several new questions raised from this study. In Peru, our modeling results show that the slab tear is a robust feature and has a lager slab gap compared with the one in Central Chile (Figs. 3.5 and 3.6), but its southern and northern edges are still continuous. This is consistent with the receiver function analysis by Phillips and Clayton (2014) that reveals a continuous southern side of the flat slab. However, along the northern side, Scire et al. (2016) imaged a ridge-parallel slab tear through body wave tomography, although the seismic resolution of this feature is limited. Antonijevic et al. (2015), based on ambient noise tomography, imaged a ridge-normal slab tear (Fig. 3.3) much closer to the trench and further north than that implied by both Scire et al. (2016) and this study. We suggest that the slab tear imaged by Antonijevic et al. (2015) could be related to the subduction of the Inca Plateau, although the latter is slightly more to the north (Figs. 3.5 and 3.8).

These inconsistencies between the two tomography models (Antonijevic et al., 2015; Scire et al., 2016) and with our geodynamical predictions also propagate into different interpretations of the observed fast Vs anomaly: the tomography model in Peru (Antonijevic et al., 2015) interprets the associated fast anomaly as part of the flat slab, but a similar fast anomaly in Central Chile is interpreted as depleted mantle lithosphere (Wagner et al., 2006; Porter et al., 2012; Marot et al., 2014). However, the fact that the fast Vs anomaly in Peru does seem to have a low Vp velocity as revealed by a recent body-wave tomography (Young, 2014) questions the slab interpretation. In addition, a new slab gap is tomographically detected at 33°S to the southeast of the Central Chilean flat slab (Anderson et al., 2007; Burd et al., 2013; Pesicek et al., 2012). This slab gap might be due to other dynamic processes, such as a locally hot mantle eroding the slab, which are not simulated in our model. Overall, the existing discrepancies in both seismic imaging and geodynamic interpretation suggest additional work is needed to better constrain the nature of these abnormal mantle structures.

Another outstanding question is the formation mechanism of adakites in South America. Petford and Atherton (1996) attributed adakites in Peru to be derived from the newly underplated

basaltic sources. Kay et al. (1994) and Kay and Abbruzzi (1996) argued for melting of the over-thickened continental crust followed by delamination as the source of adakites in the Argentine-Puna Plateau. Kay and Mpozodis (2002) and Goss et al. (2013) proposed that the chemical signature of adakite in Central Chile was generated through the melting of the fore-arc crust that was eroded and transported by the slab into the mantle wedge. On the contrary, Gutscher et al. (2000) proposed that warming up of the leading edge of the flat slab as it propagates into the hotter asthenosphere accounts for the formation of adakite both in Peru and Central Chile.

While these hypotheses are probably petrologically feasible, they all seem to have limitations. For example, Kay and Kay (2002) pointed out that the underplating rate of basaltic magma proposed by Petford and Atherton (1996) is too slow to account for crustal thickening that is required for adakitic magmatism. They also questioned the slab melting model of Gutscher et al. (2000) by querying the existence of the 1200°C isotherm at 60 km depth much east of the trench that is required by their model. On the contrary, Gutscher et al. (2000) argued that the crustal melting model of Kay et al. (1994) could not explain the paradox that adakitic eruption in Peru and Central Chile ceased in Pliocene but the thick crust preserves to the present. These arguments may not necessarily rule out the questioned hypotheses, due to the apparent complexity of geological processes. In stead, different hypotheses may account for different adakitic suites (Kay and Kay, 2002).

By reproducing the 4-D evolution of subduction, our model shows that the intense adakite production correlates well with the pulses of asthenosphere upwelling accompanying the slab tearing process. We propose that the asthenosphere upwelling may have significantly heated and partially melted the fragmented oceanic crust, which eventually leads to the formation of adakites. Therefore, our model is similar to Gutscher et al. (2000), but with a different geodynamic process to form slab melting. On the other hand, our model is not inconsistent with the "crustal melting" hypotheses. In these earlier models, a locally enhanced temperature is required in order to melt the crust to form adakites. Our model, by showing localized upwelling beneath a thinned or torn slab, provides the heat source for these models. In addition, the transient upwelling also gives a natural explanation for the short duration of adakitic magmatism which is not fully explained by the two "crustal melting" hypotheses (Kay et al., 1994; Kay and Abbruzzi, 1996; Kay and Mpozodis, 2002; Goss et al., 2013). To further narrow down on the exact mechanism, more research should focus on the detection of melt sources of these adakites.

3.6 Conclusion

In this paper, we present a new flat-slab configuration that reconciles multiple observations, including spatial discontinuities in intermediate-depth earthquake distribution, unusual slab stress patterns revealed by earthquake focal mechanisms, the elusive seismic anomalies around the flat slab regions, as well as the formation of adakites above the subducting aseismic ridges.

This new configuration of flat-slab subduction is illustrated in Figure 3.10. The key feature is a down-dip oriented slab tear within the subducting aseismic ridge, where the two limbs of the broken slab span a geometry that is consistent with the traditional flat-slab geometry based on interpolated Benioff zones. Formation of the slab tear induces asthenosphere upwelling from beneath the slab, similar to processes occurring at a mid-ocean ridge (Key et al., 2013). The upwelling asthenosphere warms up and melts the severely stretched oceanic crust, leading to adakitic eruption and mineral enrichment at the surface during the initial stage of slab tearing. We propose that our discovered slab tearing events should represent a common consequence of flat-slab formation due to subduction of small to medium sized buoyancy features. The implied lithosphere buoyancy change and rheological variations due to the slab breaking process would likely affect the long-term dynamic evolution of the overriding continent.

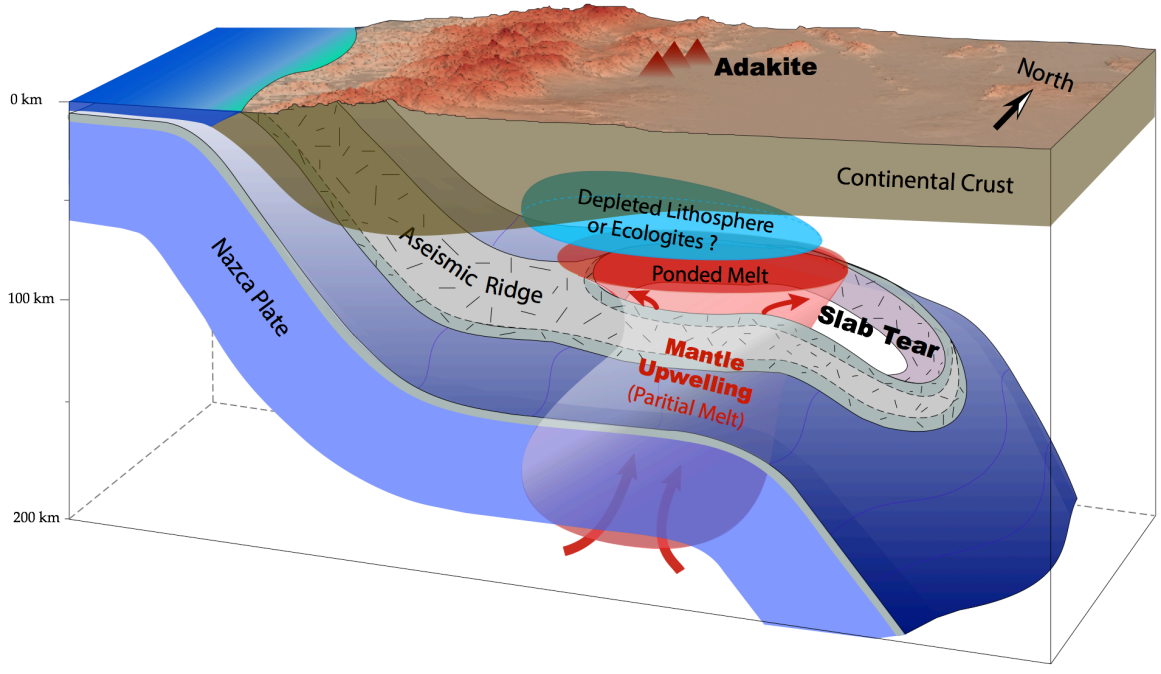

Figure 3.10. Schematic representation of the broken flat slab during aseismic ridge subduction. In the overriding plate, only the crustal layer is shown. The vertical axis is exaggerated in scale.

3.7 References

Anderson, D.L. & J. D. Bass, Mineralogy and composition of the upper mantle, Geophys. Res. Lett., 11, 637-640 (1984).

Anderson, M., P. Alvarado, G. Zandt & S. Beck, Geometry and brittle deformation of the subducting Nazca Plate, Central Chile and Argentina, Geophys. J. Int., 171, 419-434 (2007).

Antonijevic, S.K., L.S. Wagner, A. Kumar, S.L. Beck, M.D. Long, G. Zandt, H. Tavera, C. Condori, The Role of Ridges in the Formation and Longevity of Flat Slabs, Nature, 524, 212-215 (2015).

Aoki, I., Takahashi, E., Density of MORB eclogite in the upper mantle. Phys. Earth Planet. Inter.143–144, 129–143 (2004).

Arriagada, C., P. Roperch, C. Mpodozis, & P. R. Cobbold, Paleogene building of the Bolivian Orocline: Tectonic restoration of the central Andes in 2-D map view, Tectonics 27.6 (2008).

Arrial, P-A, M.I. Billen, Influence of geometry and eclogitization on oceanic plateau subduction, Earth Planet. Sci. Lett., 363, 34-43 (2013).

Brudzinski, M.R., Chen, W.-P., Earthquakes and strain in subhorizontal slabs. J. Geophys. Res.110, B08303 (2005).

Burd, A. I., Booker, J. R., Mackie, R., Pomposiello, C., & Favetto, A. (2013). Electrical conductivity of the Pampean shallow subduction region of Argentina near 33 S: evidence for a slab window. Geochemistry, Geophysics, Geosystems, 14(8), 3192-3209.

Cahill, T., and B. L. Isacks, Seismicity and shape of the subducted Nazca Plate, J. Geophys. Res., 97, 17,503–17,529 (1992).

Calkins, J., S. Beck & A. Li, Lithospheric structure of the Pampean flat slab region of Chile and Argentina from analysis of Rayleigh wave propagation, PhD thesis, Univ. Arizona (2008).

Coney, P. J., S. J. Reynolds, Cordilleran benioff zones. Nature, 270, 403-406 (1977).

Dougherty S L, Clayton R W. Seismic structure in southern Peru: evidence for a smooth contortion between flat and normal subduction of the Nazca Plate[J]. Geophysical Journal International, 2015, 200(1): 534-555.

Drummond, M.S., M.J., Defant, A model from trondhjemite–tonalite–dacite genesis and crustal growth via slab melting: Archaean to modern comparisons, Journal of Geophysical Research 95, 21503–21521 (1990).

Drummond, M. S., Defant, M. J., & Kepezhinskas, P. K. (1996). Petrogenesis of slab-derived trondhjemite–tonalite-dacite/adakite magmas. Geological Society of America Special Papers, 315, 205-215.

Eakin, C. M., M. D. Long, A. Scire, S. L. Beck, L. S. Wagner, G. Zandt, & H. Tavera, Internal deformation of the subducted Nazca slab inferred from seismic anisotropy. Nature Geoscience (2015).

Gans C R, Beck S L, Zandt G, et al. Continental and oceanic crustal structure of the Pampean flat slab region, western Argentina, using receiver function analysis: new high-resolution results[J]. Geophysical Journal International, 2011, 186(1): 45-58.

Gilbert, H., Beck, S., & Zandt, G. (2006). Lithospheric and upper mantle structure of central Chile and Argentina. Geophysical Journal International, 165(1), 383-398.

Goss, A. R., Kay, S. M., & Mpodozis, C. (2013). Andean adakite-like high-Mg andesites on the northern margin of the Chilean–Pampean flat-slab (27–28· 5 S) associated with frontal arc migration and fore-arc subduction erosion. Journal of Petrology, 54(11), 2193-2234.

Gutscher, M.-A., J.-L. Olivet, D. Aslanian, J.-P. Eissen and R. Maury, The “lost Inca Plateau”: cause of flat subduction beneath Peru? Earth Planet. Sci. Lett. 171, 335-341 (1999).

Gutscher M-A., R. Maury, J. P. Eissen, et al, Can slab melting be caused by flat subduction?, Geology, 28(6): 535-538 (2000).

Hayes, G.P., D.J. Wald & R.L. Johnson, Slab1.0: A three-dimensional model of global subduction zone geometries, J. Geophys. Res., 117, B01302 (2012).

Heit, B., Yuan, X., Bianchi, M., Sodoudi, F., & Kind, R. (2008). Crustal thickness estimation beneath the southern central Andes at 30 S and 36 S from S wave receiver function analysis. Geophysical Journal International, 174(1), 249-254.

Henderson, L. J., R. G. Gordon, and D. C. Engebretson (1984), Mesozoic aseismic ridges on the Farallon plate and southward migration of shallow subduction during the Laramide orogeny, Tectonics, 3, 121–132.

Hidalgo, P. J., & Rooney, T. O. (2014). Petrogenesis of a voluminous Quaternary adakitic volcano: the case of Baru volcano. Contributions to Mineralogy and Petrology, 168(3), 1-19.

Houston, H., Deep earthquakes. In: Schubert, G. (Ed.), Treatise on Geophysics, vol.4. Elsevier, pp.321–350 (2007).

Hu, J., L. Liu, A. Hermosillo, Q. Zhou, Simulation of Late Cenozoic South American Flat-Slab Subduction Using Geodynamic Models with Data Assimilation, Earth Planet. Sci. Lett., 2016, 438: 1-13.

Kay S M, Coira B, Viramonte J. Young mafic back arc volcanic rocks as indicators of continental lithospheric delamination beneath the Argentine Puna plateau, central Andes[J]. Journal of Geophysical Research: Solid Earth, 1994, 99(B12): 24323-24339.

Kay S M, Abbruzzi J M. Magmatic evidence for Neogene lithospheric evolution of the central Andean “flat-slab” between 30 S and 32 S[J]. Tectonophysics, 1996, 259(1): 15-28.

Kay R. W., S. M. Kay, Andean adakites: three ways to make them[J]. Acta Petrologica Sinica, 18(3): 303-311 (2002).

Kay S M, Mpodozis C. Magmatism as a probe to the Neogene shallowing of the Nazca plate beneath the modern Chilean flat-slab[J]. Journal of South American Earth Sciences, 2002, 15(1): 39-57.

Key, K., S. Constable, L. Liu & A. Pommier, Electrical image of passive mantle upwelling beneath the northern East Pacific Rise, Nature, 495, 499-502 (2013).

Kirby S, Engdahl R E, Denlinger R. Intermediate-depth intraslab earthquakes and arc volcanism as physical expressions of crustal and uppermost mantle metamorphism in subducting slabs[J]. Subduction top to bottom, 1996: 195-214.

Kopp H, Flueh E R, Papenberg C, et al. Seismic investigations of the O'Higgins Seamount Group and Juan Fernández Ridge: Aseismic ridge emplacement and lithosphere hydration[J]. Tectonics, 2004, 23(2).

Kumar A, Wagner L S, Beck S L, et al. Seismicity and state of stress in the central and southern Peruvian flat slab[J]. Earth and Planetary Science Letters, 2016, 441: 71-80.

Liu, L., M. Gurnis, M. Seton, J. Saleeby, R.D. Muller and J. Jackson, The role of oceanic plateau subduction in the Laramide Orogeny, Nature Geosci., 3, 353-357 (2010).

Liu, L., Dave R. Stegman, "Segmentation of the Farallon slab", Earth and Planetary Science Letters, 311, 1-10 (2011).

Liu, L. & D.R. Stegman, Origin of Columbia River flood basalt controlled by propagating rupture of the Farallon slab, Nature, 482, 386-389 (2012).

Loewy, S. L., Connelly, J. N., & Dalziel, I. W. (2004). An orphaned basement block: The Arequipa-Antofalla Basement of the central Andean margin of South America. Geological Society of America Bulletin, 116(1-2), 171-187.

Manea, V. C., M. Pérez-Gussinyé, & M. Manea, Chilean flat slab subduction controlled by overriding plate thickness and trench rollback.Geology, 40(1), 35-38 (2012).

Marot, M., T. Monfret, M. Gerbault, G. Nolet, G. Ranalli & M. Pardo, Flat versus normal subduction zones: a comparison based on 3-D regional traveltime tomography and petrological modeling of central Chile and western Argentina (29°–35°S), Geophys. J. Int., 199, 1633-1654 (2014).

Macpherson C G, Dreher S T, Thirlwall M F. Adakites without slab melting: high pressure differentiation of island arc magma, Mindanao, the Philippines[J]. Earth and Planetary Science Letters, 2006, 243(3): 581-593.

Martin, H., Smithies, R. H., Rapp, R., Moyen, J. F., & Champion, D. (2005). An overview of adakite, tonalite–trondhjemite–granodiorite (TTG), and sanukitoid: relationships and some implications for crustal evolution. Lithos, 79(1), 1-24.

Mulcahy, P., C. Chen, S.M. Kay, L.D. Brown, B.L. Isacks, E. Sandvol, B. Heit, X. Yuan & B.L. Coira, Central Andean mantle and crustal seismicity beneath the Southern Puna plateau and the northern margin of the Chilean-Pampean flat slab, Tectonics, 33, doi:10.1002/2013TC003393 (2014).

Müller, R. D., M. Sdrolias, C. Gaina, & W. R. Roest, Age, spreading rates, and spreading asymmetry of the world's ocean crust, Geochemistry, Geophysics, Geosystems, 9(4) (2008).

Peacock S M, Wang K. Seismic consequences of warm versus cool subduction metamorphism: Examples from southwest and northeast Japan[J]. Science, 1999, 286(5441): 937-939.

Pesicek, J.D., E.R. Engdah, C.H. Thurber, H.R. DeShon & D. Lange, Mantle subducting slab structure in the region of the 2010M8.8 Maule earthquake (30–40°S), Chile, Geophys. J. Int., doi: 10.1111/j.1365-246X.2012.05624.x (2012).

Petford, N., & M. Atherton, Na-rich partial melts from newly underplated basaltic crust: the Cordillera Blanca Batholith, Peru, Journal of Petrology, 37(6), 1491-1521 (1996).

Phillips K, Clayton R W. Structure of the subduction transition region from seismic array data in southern Peru[J]. Geophysical Journal International, 2014, 196(3): 1889-1905.

Porter R, Gilbert H, Zandt G, et al. Shear wave velocities in the Pampean flat-slab region from Rayleigh wave tomography: Implications for slab and upper mantle hydration[J]. Journal of Geophysical Research: Solid Earth, 2012, 117(B11).

Raleigh, C. B. & Paterson, M. S. Experimental deformation of serpentinite and its tectonic implications. J. Geophys. Res. 70, 3965–3985 (1965).

Rosenbaum, G., D. Giles, M. Saxon, P. G. Betts, R. F. Weinberg, & C. Duboz, Subduction of the Nazca Ridge and the Inca Plateau: Insights into the formation of ore deposits in Peru. Earth and Planetary Science Letters, 239(1), 18-32 (2005).

Sajona, F. G., Maury, R. C., Bellon, H., Cotten, J., Defant, M. J., & Pubellier, M. (1993). Initiation of subduction and the generation of slab melts in western and eastern Mindanao, Philippines. Geology, 21(11), 1007-1010.

Scire, A., C.B. Biryol, G. Zandt, S. Beck, Imaging the Nazca slab and surrounding mantle to 700 km depth beneath the central Andes (18°S to 28°S), GSA Mem., 212 (2015).

Scire, Alissa, George Zandt, Susan Beck, Maureen Long, Lara Wagner, Estela Minaya, Hernando Tavera, Imaging the transition from flat to normal subduction: variations in the structure of the Nazca slab and upper mantle under southern Peru and northwestern Bolivia. Geophysical Journal International, 204(1), 457-479 (2016).

Stegman, D.R., R. Farrington, F.A. Capitanio, and W.P. Schellart, A regime diagram for subduction styles from 3-D numerical models of free subduction, Tectonophysics, 483, 29-45 (2010).

Tan E, E Choi, P Thoutireddy, [SPELL OUT ALL AUTHORS] GeoFramework: Coupling multiple models of mantle convection within a computational framework[J], Geochemistry, Geophysics, Geosystems, 7(6) (2006).

Taramón, J.M., Rodríguez-González, J., Negredo, A.M., Billen, M.I., Influence of cratonic lithosphere on the formation and evolution of flat slabs: insights from 3-D time-dependent modeling. Geochem. Geophys. Geosyst.16 (9), 2933–2948 (2015).

Tovish, A., G. Schubert, and B. P. Luyendyk (1978), Mantle flow pressure and the angle of subduction: Non-newtonian corner flows, J. Geophys. Res.: Solid Earth, 83 (B12), 5892–5898, doi:10.1029/JB083iB12p05892.

Trabant, C., A. R. Hutko, M. Bahavar, R. Karstens, T. Ahern, and R. Aster (2012), Data Products at the IRIS DMC: Stepping Stones for Research and Other Applications, Seismological Research Letters, 83(5), 846–854, doi:10.1785/0220120032.

van Hunen, J., A. P. van den Berg, & N. J. Vlaar, A thermo-mechanical model of horizontal subduction below an overriding plate. Earth and Planetary Science Letters, 182(2), 157-169 (2000).

Wagner, L.S., S. Beck & G. Zandt, Upper mantle structure in the south central Chilean subduction zone (30° to 36°S), J. Geophys. Res., 110, B01308 (2005).

Wagner L S, Beck S, Zandt G, et al. Depleted lithosphere, cold, trapped asthenosphere, and frozen melt puddles above the flat slab in central Chile and Argentina[J]. Earth and Planetary Science Letters, 2006, 245(1): 289-301.

Wang, Q., McDermott, F., Xu, J. F., Bellon, H., & Zhu, Y. T. (2005). Cenozoic K-rich adakitic volcanic rocks in the Hohxil area, northern Tibet: lower-crustal melting in an intracontinental setting. Geology, 33(6), 465-468.

Worthington, J.R., B.R. Hacker & G. Zandt, Distinguishing eclogite from peridotite: EBSD-based calculations of seismic velocities, Geophys. J. Int., doi: 10.1093/gji/ggt004 (2013).

Yáñez G A, Ranero C R, Huene R, et al. Magnetic anomaly interpretation across the southern central Andes (32–34 S): The role of the Juan Fernández Ridge in the late Tertiary evolution of the margin[J]. Journal of Geophysical Research: Solid Earth, 2001, 106(B4): 6325-6345.

Young B E. Regional body-wave tomography of the Peruvian flat slab[M]. 2014.

Zhong S, McNamara A, Tan E, et al. A benchmark study on mantle convection in a 3-D spherical shell using CitcomS[J]. Geochemistry, Geophysics, Geosystems, 2008, 9(10).

Chapter 4

Subduction-controlled Mantle Flow and Seismic Anisotropy in South America

4.1 Abstract[3]

Seismic anisotropy records both the past and present deformation inside the solid Earth. In the mantle, seismic anisotropy is mainly attributed to the lattice preferred orientation (LPO) of mineral fabrics, caused by the shear deformation due to mantle flow. However, contributions from different tectonic processes remain debated, and a single geodynamic model that simultaneously explains the observed mantle structures and various seismic anisotropy measurements is still lacking. Here, we present a model for the Cenozoic subduction history in South America using a geodynamic simulation constrained by both past plate reconstructions and present mantle seismic structures. With a recently developed software package DRexS, we further predict azimuthal seismic anisotropy at different depths and generate synthetic shear wave splitting (SWS) measurements using the resulting mantle flow. Our results provide a good match to both depth-dependent surface wave anisotropy and various land-based SWS records. We find that the dominant control on seismic anisotropy in South America comes from subduction-induced mantle flow, where anisotropy below the subducting Nazca Plate aligns with plate-motion-induced Couette flow and that below the overriding South American Plate follows slab-induced Poiseuille flow. This large-scale mantle flow can be diverted by secondary slabs, such as that below the Antilles subduction zone. In contrast, the contribution to SWS from fossil continental anisotropy and from the effects due to mantle flow modulation by lithosphere thickness variation are minor. Upper-mantle fast seismic anomalies beneath the southern Atlantic margin should have close-to-neutral buoyancy in order to satisfy the observed seismic anisotropy.

---

[3]This chapter has been published as: Hu, J., Faccenda, M., & Liu, L. (2017). *Subduction-controlled mantle flow and seismic anisotropy in South America.* Earth and Planetary Science Letters, 470, 13-24.

4.2 Introduction

Seismic anisotropy is defined as the dependence of wave speed on the direction of seismic polarization and wave propagation. It has been generally attributed to lattice preferred orientation (LPO) of anisotropic minerals (Nicolas and Christensen, 1987; Zhang and Karato, 1995; Kaminski and Ribe, 2001) or shape preferred orientation (SPO) of locally concentrated isotropic materials with distinct elastic properties (Mainprice and Nicolas, 1989; Kendall and Silver, 1996). Since the first observation of seismic anisotropy made by Hess (1964), an enormous amount of research has been done both globally and regionally. However, the origin of seismic anisotropy remains debated and the proposed causes of anisotropy vary from place to place (Long and Silver, 2009; Long and Becker, 2010).

By analyzing shear wave splitting (SWS), Silver and Chan (1991) and Silver (1996) argued that the fast-polarization direction in stable continents correlated well with tectonic structures in the crust, implying that "frozen anisotropy" (e.g. Ismaïl and Mainprice, 1998) imprinted by past crustal deformation was the dominant source. This idea was adopted in some regional studies, such as in SE Brazil (James and Assumpção, 1996) and Fennoscandia (Vecsey et al. 2007; Eken et al., 2010). In contrast, Vinnik et al. (1992) and Fouch et al. (2000) analyzed SKS splitting in North America and argued that most of the anisotropy is parallel to the plate motion. Recent studies further invoked the role of lithosphere thickness variation in the formation of SWS (Fouch et al., 2000; Assumpção et al., 2006; Wang et al., 2008; Assumpção et al., 2011; Miller and Becker, 2012; Foster et al., 2014). For example, Forch et al. (2000) and Wang et al. (2008) related the SWS to mantle flow perturbed by the North American Craton and Colorado Plateau. Similarly, Assumpção et al. (2006; 2011) and Miller and Becker (2012) proposed the thick continental roots in South America modulate the anisotropy pattern by diverting mantle flow below southeastern Brazil and northern South America, respectively. However, SWS measurements have little depth resolution (Favier & Chevrot 2003), which renders the associated tectonic interpretation non-unique.

Relative to SWS, surface wave and normal mode studies could better resolve the depth distribution of seismic anisotropy (Gung et al., 2003; Debayle et al., 2005; Marone and Romanowicz, 2007; Yuan and Beghein, 2013). For example, Gung et al. (2003) measured radial anisotropy at depths from 250-400 km that reconciles the discrepancy of different isotropic tomography models. Debayle et al. (2005) observed significant azimuthal anisotropy beneath

Australia at 175–300 km depths that correlates well with the present plate motion. By simultaneously matching waveforms and shear wave splitting data, Marone and Romanowicz (2007) proposed a layered anisotropy structure in the cratonic part of North America, implying contributions from both the lithosphere and the underlying asthenosphere. Although with a likely different origin, a layered anisotropy structure was also observed in the Pacific (Smith et al., 2004; Beghein et al., 2014), where the Pacific upper lithosphere records the paleospreading direction, while anisotropy at greater depth reflects present-day plate motion. However, this interpretation was challenged by a more recent study by Lin et al. (2016), who showed that the anisotropy at asthenosphere depth has a different fast direction from that due to present plate motion, and they attributed this to pressure-driven channel flow beneath the ocean basin (e.g., Höink et al., 2004).

The diverse observations of seismic anisotropy have propelled many geodynamic modeling efforts (Conrad et al., 2007, 2010; Faccenda et al., 2008; Faccenda and Capitanio, 2013; Becker et al., 2003, 2006, 2014). Conrad et al. (2007; 2010) and Becker et al. (2003; 2014) built global mantle convection models based on seismic tomography. They demonstrated that LPO due to density-driven mantle flow matches the observation of asthenospheric anisotropy beneath ocean basins, a better prediction than that only due to plate motions. By matching the SWS data at the South American-Caribbean plate margin, Miller and Becker (2012) showed that mantle flow in the region can be deflected by cratonic keels and nearby subduction zones, suggesting a significant effect of cratons on SWS. However, these studies only utilized instantaneous mantle flow models when calculating LPO. In theory, a time-dependent flow is needed to accurately predict seismic anisotropy, due to the response of anisotropic minerals to the cumulative strain (Ribe, 1992). Recently, such efforts have been made to account for both the deformation history and the full 3D strain field (Faccenda & Capitanio, 2012; 2013).

In this paper, we simultaneously investigate the origin of surface wave anisotropy and SWS data in South America (Fig. 4.1). We present a data-oriented convection model that simulates South American subduction since the Mid-Cretaceous. Then we use the resulting Cenozoic mantle flow to generate synthetic seismic anisotropy that is subsequently compared with SWS measurements and surface wave anisotropy (Fig. 4.1). This new approach represents several potential advances from earlier modeling efforts. First, our model utilizes time-dependent rather

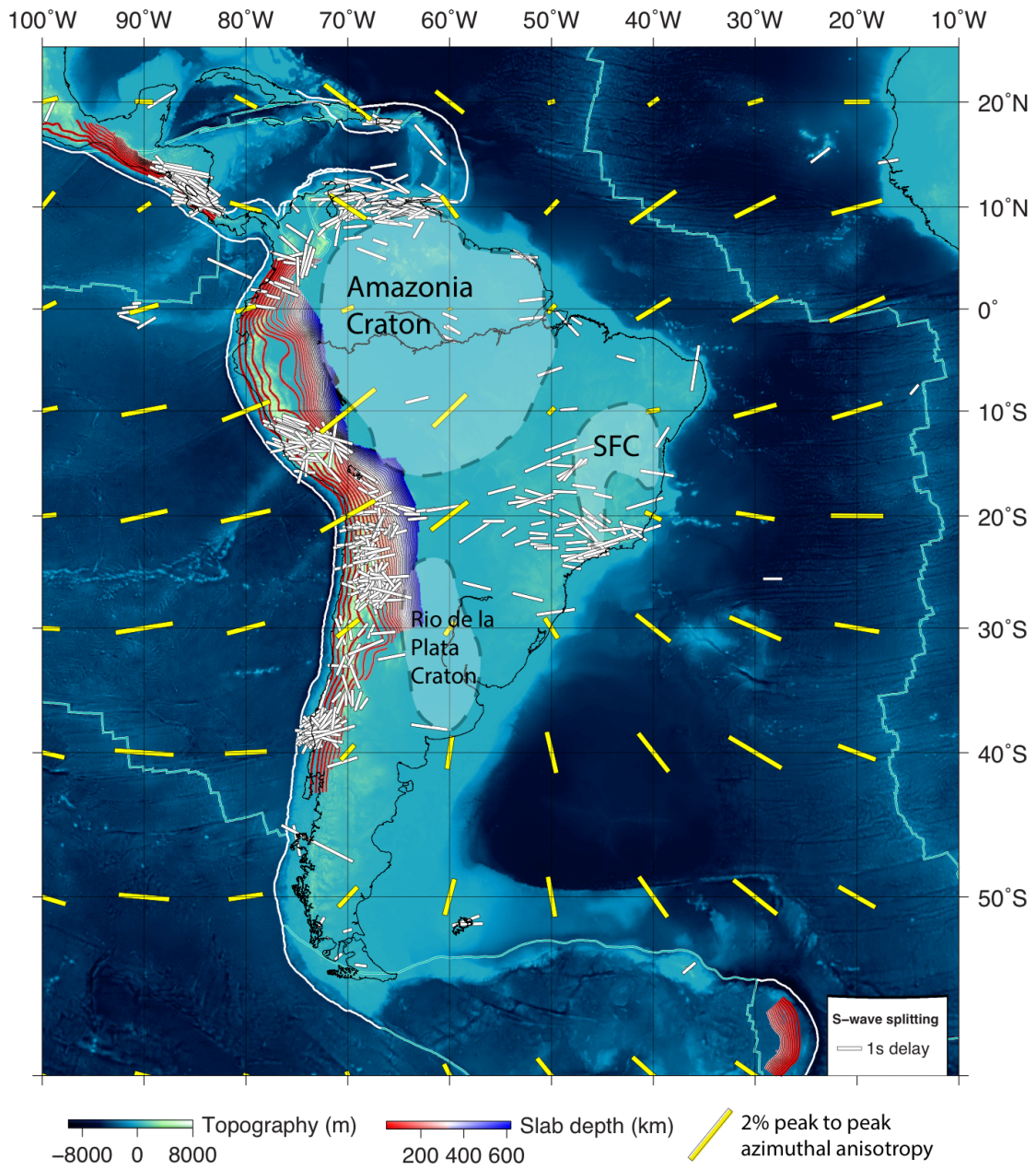

Figure 4.1. Geological settings of South America. The topography and bathymetry are shown with background colors. The yellow bars represent the azimuthal anisotropy of Rayleigh waves at 200 km depth from Yuan and Beghein (2013), while the white bars are station-averaged shear wave splitting from Becker et al. (2012). Purple lines show slab depth contours represented by Benioff zones (Hayes et al., 2012). Dashed lines outline the shape of major cratons (modified from Loewy et al., 2004) in South America. SFC: Sao Francisco Craton.

than instantaneous mantle flow, and therefore is more appropriate for the prediction of LPO, which is intrinsically evolving with time. Second, we employ a more accurate anisotropy generator by upgrading the 3-D DRex code implemented by Faccenda & Capitanio (2013) to further consider the 4-D deformation history within a spherical Earth; this is more accurate than earlier anisotropy approximations using infinite strain axes (ISA) or finite strain ellipsoid (FSE). Third, the subduction history and resulting slab geometry in our model are tightly constrained by past plate reconstructions and present mantle structures (Hu et al., 2016; Hu & Liu, 2016); the resulting mantle flow should better represent the real Earth, compared to that estimated based on tomography images or parameterized slab geometry.

Consequently, our new approach has the potential to reconcile existing uncertainties and to discover new insights on the origin of seismic anisotropy. Our results reveal a multi-scale mantle flow pattern that is confirmed by the seismic anisotropy data. At the plate-scale, a broad upper mantle poloidal flow originated from both sides of the subducting Nazca slab dominates the entire region, as is opposed to the previously suggested plate-motion-dominant origin. At local scales, this flow is modulated by the secondary slab below the Antilles trench and by large-sized cratonic keels within the continent, although the effect of the latter is relatively minor to fit SWS. Both the predicted depth-dependent anisotropy within the region and the predicted SWS on land match observation very well, with the exception being SWS along the Nazca trench where the fit is marginal. Therefore, our study suggests a subduction-dominant mechanism for mantle deformation in South America.

4.3 Methods

In this section, we describe the methods used to generate mantle flow and to calculate seismic anisotropy. These involve three open-source software packages, including 1) CitcomS (Tan el al., 2006; Zhong et al., 2008) that simulates mantle convection using data assimilation algorithms (Liu and Stegman, 2011; Hu et al., 2016), 2) DRexS, an upgraded version of the original 2-D DRex (Kaminski et al., 2004) and the recent version 3-D Rex (Faccenda and Capitanio, 2013), that now also calculates LPO based on time-dependent mantle flow in spherical geometry, as well as 3) FSTRACK (Becker et al., 2006), which is used to predict SKS with the elastic tensors produced by DRexS.

4.3.1 Calculating time-dependent mantle flow

Following the modeling approach used in Hu et al. (2016), we simulate the South American subduction history since 100 Ma with data assimilation techniques. Both boundary conditions and main tectonic features assimilated in the subduction model were discussed in Hu et al. (2016) (Fig. 4.2). To reiterate, we take the plate motion history from a recent plate reconstruction (either Müller et al., 2008 or Müller et al., 2016; Fig. B.2 in APPENDIX B) as the surface velocity boundary condition, and use the seafloor age from the same reconstruction to update the thermal structure of the oceanic lithosphere assuming a plate model (Hasterok, 2013). The initial condition is a mantle with a uniform temperature, with a prescribed plate thermal structure on top. Over time, oceanic plates subduct following the observed plate motion, and eventually lead to a complex mantle structure as observed today (Hu et al., 2016).

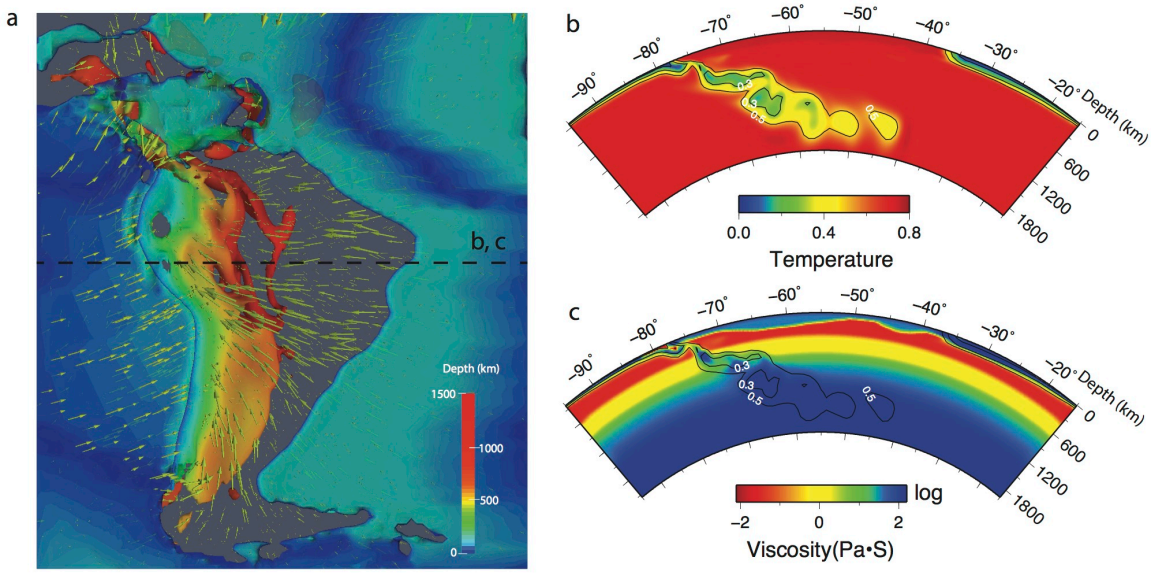

Figure 4.2. Predicted slab geometry and mantle flow from the time-dependent model with the plate reconstruction of Mülle et al. (2008). (**a**) 3D representation of the geodynamic model at present day. The 3D isosurface with a non-dimensional temperature of 0.4 is shown with color representing depth. Oceanic plates and slabs are semi-transparent, while continents are entirely transparent. Green arrows represent velocity vectors in the mantle. The dashed line marks the location of the cross-section showing temperature (**b**) and viscosity (**c**). In **b**, temperature is shown as the background color. Temperature contours are annotated with non-dimensional values. Continents have a similar temperature as the ambient mantle. In **c**, both the depth-dependence and lateral variation of viscosity are shown. Continents are assumed to be compositionally strong.

The viscosity in the model is temperature, pressure and composition – dependent, with a pre-factor following a radial viscosity profile shown in Fig. B.3b. This profile includes a weak asthenosphere and a strong middle lower mantle as suggested by recent petrological experiment (Marquardt and Miyagi, 2015) and geophysical inversions (Rudolph et al., 2015). We use compositional tracers to define high-viscosity continent and cratons (Fig. 4.2c; Fig. B.3a). Geometry of the cratons is based on Loewy et al. (2004). The maximum thickness of cratons is assumed to be 250 km, while the rest of the continent is 100 km thick (Fig. B.3a). Both the continent and the cratons are 1000 times stronger than the asthenosphere, which allows them to persist over the subduction history. To test the effect of cratons on SWS, we also run models without cratons for comparison. In these models, a uniform 100 km-thick continent is assumed.

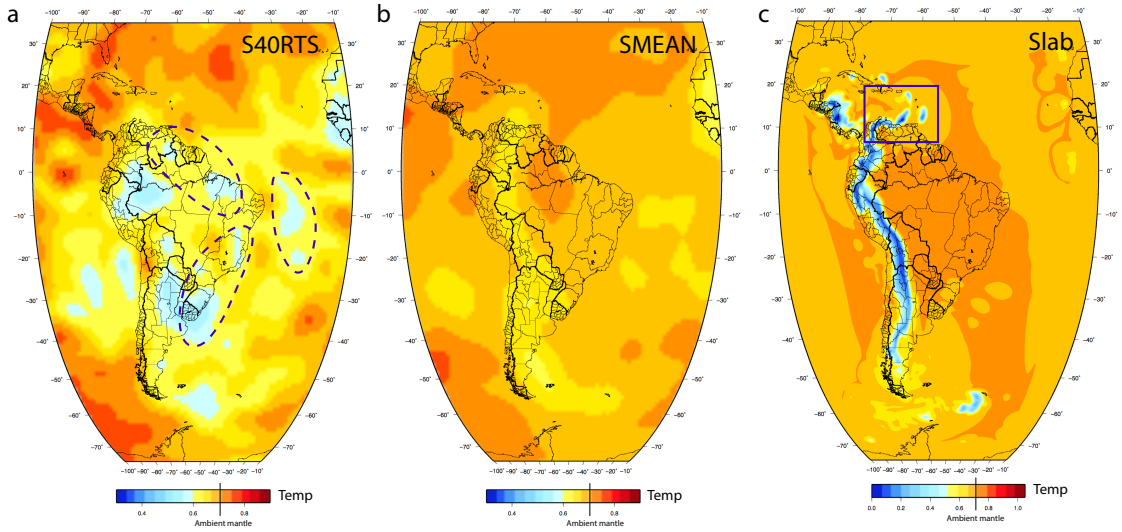

Figure 4.3. The non-dimensional temperature fields at 450 km depth of the instantaneous models based on S40RTS (a) and SMEAN (b), and that of the time-dependent slab model (c). The temperature fields in (a) and (b) are directly scaled from tomography models S40RTS and SMEAN, respectively, while that in (c) is the model output. The ambient mantle temperature is 0.7. The anomalies with a higher temperature have positive buoyancy, while those with a lower temperature have negative buoyancy. In (a), the dashed circles highlight the anomalies that are likely delaminated lithosphere. In (c), solid rectangle highlights the slabs that are crucial for the fit of SWS surrounding the Caribbean Plate.

Compared to Hu et al. (2016), this study covers a larger geographic region along the north-south direction, which now extends from 75° S to 35° N, while keeping the same east-west (260° W to 350° W) and vertical (down to 2900 km depth) dimensions. This allows us to further consider the anisotropy within the Caribbean Sea that was close to the edge of the previous model. We also

increased the number of grids from 257 to 513 in the north-south dimension, where the increased resolution (~23×27×8 km3) allows us to better resolve the variation of mantle flow along the Nazca trench and the east Caribbean trench.

In order to place this work in the context of previous studies (Conrad et al., 2007, 2010; Becker et al., 2006; 2014), we further construct tomography-based instantaneous models, with imposed plate motions. In these models, we only consider density anomalies below 300 km, which are scaled from the tomography model S40RTS (Ritsema et al., 2011) (Fig. 4.3a) or SMEAN (Becker and Boschi, 2002) (Fig. 4.3b), similar to previous studies. In these models, the same geometry of continent and cratons (Fig. B.3a) as that in the slab models is used.

4.3.2 Computing strain-induced LPO

The development of LPO in the upper mantle depends on several deformation mechanisms, including plastic deformation, dynamic recrystallization, and grain-boundary sliding (Kaminski et al., 2004). Here, we use the kinematic model of Kaminski et al. (2004) that incorporates these deformation mechanisms to compute the LPO using the constrained mantle flow histories.

The computation of LPO (e.g. in Fig. B.1a) is carried out by a FORTRAN code DRexS which is modified from 3-D DRex (Faccenda and Capitanio, 2013). DRexS is able to calculate LPO in spherical coordinates, allowing a seamless communication with mantle convection models using CitcomS. In addition, it supports both hybrid MPI and OpenMP. This significantly speeds up the computation and enables the usage of the full memory across many computation nodes, which allow tracking elastic properties of the mantle with a relatively high resolution as presented here.

To calculate LPO, the code first initializes a large number of Lagrangian particles representing mineral aggregates. The horizontal distance between these particles is 50 km and the vertical distance is 30 km. Each particle consists of 1000 crystals with 70% A-type olivine and 30% enstatite that are representative of a harzburgitic upper mantle (0-410 km) composition. Initially, these crystals are randomly oriented, forming an isotropic mantle. These particles are then advected in the evolving mantle flow field. The code solves the advection equation with a fourth-order Runge-Kutta scheme. As the mineral aggregates advect in the mantle, the orientations of these crystals change in response to shear deformation, generating LPO. When reaching the present day, the elastic tensor of each mineral aggregate is computed using a Voigt average of all crystal

elastic tensors in the aggregate scaled by their volume fractions. With the projection method of Browaeys and Chevrot (2004), the optimized transverse isotropy is extracted from the full elastic tensor. As transverse isotropy dominates the anisotropic part of the full elastic tensor in upper mantle crystal aggregates, the magnitude and orientation of the symmetry axis of the transverse isotropy, i.e. TI axis, outline the configuration of the elastic anisotropy. Once the mineral aggregates advect below the depths of the 410-km phase transformation, the LPO of these aggregates will be reset to random orientations.

The TI axis of upper mantle aggregates approximately coincides with the direction of maximum stretching, fastest seismic velocity and little SWS (Faccenda and Capitanio, 2013). When sub-horizontal, such TI axes define the orientation of the SKS fast component and maximum SWS is expected. Conversely, sub-vertical TI axes yield little or no SWS for SKS waves. For all the time-dependent models, we take the evolving mantle flow fields from 40 Ma to the present day to compute LPO. For the instantaneous models, we use the present-day mantle flow to represent the flow fields in the past 40 Myr, i.e. assuming the mantle flow field does not change since 40 Ma, and then take them as input to compute LPO.

4.3.3 Predicting SKS splitting

Using the software package FSTRACK (Becker et al., 2006b), we further compute synthetic SKS splitting at the same sites where SKS measurements are made. The code first computes a synthetic seismogram and then uses the cross-correlation method (Menke and Levin, 2003) to determine SKS splitting. The cross-correlation method is similar to the transverse-component-minimization method (Silver and Chan, 1991). It utilizes a grid-search approach to determine the splitting parameters (Φ, δt), where Φ represents fast direction and δt splitting time. However, it is worth noting that in the presence of complex anisotropy, the two methods may disagree (Long and van der Hilst, 2005), and both of them may be inaccurate in certain situations (Long and Silver, 2009). In principle, the code should employ the same method to compute SKS as that used in observation. However, due to difficulties in classifying the SKS measurements calculated with different methods and in implementing all these methods including Multichannel (Chevrot, 2000) and Cross-convolution (Menke and Levin, 2003), the code FSTRACK simply uses the cross-correlation method for all the calculations. This approach is proved to be more robust compared with the transverse-component-minimization method (Vecsey et al., 2008).

To predict SKS splitting (Fig. B.1b), the code first gathers the elastic tensors of all upper mantle mineral aggregates from the output of DRexS that are located within a horizontal distance of 50 km from each virtual seismic station and stack them into distinct layers below the station. Then it computes the harmonic response of an incident plane wave to the horizontal layers, assuming an incident angle of 5° that is typical for SKS waves. These harmonic responses are computed over a range of frequencies from 0 to 25 Hz and are summed up to obtain a pulse of seismogram via inverse Fourier transformation. The synthetic seismogram is further filtered to construct SKS waves that have a frequency band of 0.1 to 0.3 Hz. Finally, the SKS splitting parameters are determined by the cross-correlation method (Menke and Levin, 2003). Since the SKS splitting parameters depend on back-azimuth given the presence of low-symmetry component of the elastic tensor or tilted hexagonal symmetry axis (Becker et al., 2006b), the code averages all the fast azimuths and delay times at each station measured by rotating the elastic tensors around the vertical axis for 360° with an interval of 2°, which is equivalent to rotating the back-azimuth. The resultant mean fast azimuth and delay time represent the geometry of SKS splitting at that station.

4.4 Results

In this section, we present the geodynamic model with mantle flow, the predicted seismic anisotropy at depths, and synthetic SWS measurements at stations where observations are available. By comparing the prediction with the observed anisotropy, we provide an explanation for the origin of the seismic anisotropy at various places across the study region.

4.4.1 Different proxies for seismic anisotropy

Various proxies have been used to represent the orientation of seismic anisotropy, including mantle velocity (e.g. Zandt and Humphreys, 2008; Assumpcao et al, 2011), infinite strain axis (ISA) (e.g. Conrad et al., 2007; Conrad and Behn, 2010), the longest axis of finite strain ellipsoid (FSE) (e.g. Becker et al., 2003), and LPO predicted by fabric development models (Becker et al., 2006; Faccenda et al., 2008; Faccenda and Capitanio, 2013; Becker et al., 2014).

However, these proxies use different assumptions and may be inconsistent with each other. To show the differences, we compare the four different proxies at 200 km depth (Fig. 4.4) computed from the same geodynamic model with a plate reconstruction of Müller et al. (2008). Although all four proxies show some consistencies in their overall patterns, they also show

important differences (Fig. 4.4). For example, below the Nazca Plate and west of central Andes, the orientations of the proxies are noticeably different, where LPO orientates along the east-west direction (Fig. 4.4d), velocity and FSE have a clear north-south component (Fig. 4.4a, c), and ISA shows somewhat random orientations (Fig. 4.4b). A similar conclusion can be drawn for the Amazonian craton: while both velocity and ISA have large values, FSE and LPO show little anisotropy, consistent with the lack of internal deformation within strong cratonic roots. It is understandable that the velocity proxy is oversimplified, since formation of LPO depends on velocity gradient rather than velocity (Ribe, 1992; Kaminiski et al., 2004). ISA cannot represent LPO in the regime of complex and rapidly varying mantle flow, because it does not consider the flow history (Kaminski and Ribe, 2002; Conrad et al., 2007). Furthermore, dynamic recrystallization accelerates the alignment of olivine A axis with the maximum stretch direction (Faccenda and Capitanio, 2013); enstatite decreases the strength of anisotropy as its slow axis aligns with the fast axis of olivine (Ribe, 1992; Kaminski et al., 2004). The fact that DRexS incorporates these processes should yield more accurate LPO than that approximated by FSE. Therefore, we use LPO (represented by TI axes) for further analysis.

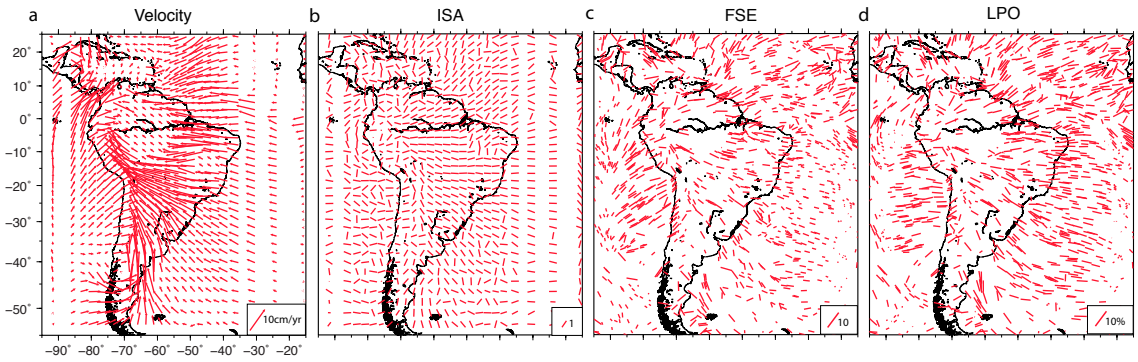

Figure 4.4. Different proxies of seismic anisotropy. Red arrows in (**a**) show velocity vectors, red bars in (**b**), (**c**) and (**d**) represent infinite strain axes (ISA) of the velocity field, the longest axes of finite strain ellipsoid (FSE) and TI axes of LPO, respectively. Results in (**c**) and (**d**) are based on temporally evolving mantle flow during the past 40 Ma. The mantle fabrics are estimated using the same values of key model parameters as those in Faccenda and Capitanio (2013), including the dimensionless nucleation rate $\lambda^* = 5$, the dimensionless "intrinsic" grain-boundary mobility $M^* = 10$, the threshold volume fraction that triggers grain-boundary sliding $\chi = 0.3$, and the relative strength of olivine slip systems yielding upper mantle A-type fabrics.

4.4.2 Surface-wave anisotropy

Surface wave studies have revealed significant azimuthal anisotropy in the upper mantle above the transition zone (Debayle et al., 2005; Debayle & Richard, 2013; Yuan and Beghein, 2013; Schaeffer et al., 2016). Here, we investigate the origin of the upper mantle anisotropy using an observationally constrained mantle flow model with the plate reconstruction of Müller et al. (2008) (Hu et al., 2016). Using the TI axes as the proxy, we derive the flow-induced LPO at different depths (Fig. 4.5). Overall, the predicted LPO matches the surface wave anisotropy (Yuan and Beghein, 2013) quite well at all depths. Degraded fits occur near the model boundaries due to artificial return flow and within western South America where orogeny- and subduction-related deformation and metasomatism may be important. This validates our attempt to understand seismic anisotropy using realistic geodynamic models.

Several interesting observations emerge from comparison of the azimuthal anisotropy with the predicted LPO (Fig. 4.5). First, at 150 and 200 km depths, the orientation of azimuthal anisotropy from Nazca converges with that from Atlantic, forming a large radiating pattern emanating from the South American continent (bold arrows in Fig. 4.5a, b). This anisotropy geometry is also observed in other surface wave anisotropy studies (Debayle et al., 2005; Schaeffer et al., 2016). This radiation pattern over the South America Plate is inconsistent with mantle flow dominated by the absolute plate motion that moves largely in one direction (e.g., Assumpção et al., 2011). Second, a continuous counter-clockwise rotation of anisotropy orientation occurs from 150 to 350 km depths beneath the Nazca Plate, where the shallower east-west direction rotates to a deeper north-south direction (Fig. 4.5b, c, d). The shallower azimuthal anisotropy largely follows the absolute motion of the Nazca Plate, while the deeper anisotropy becomes orthogonal to plate motion (Fig. 4.1).

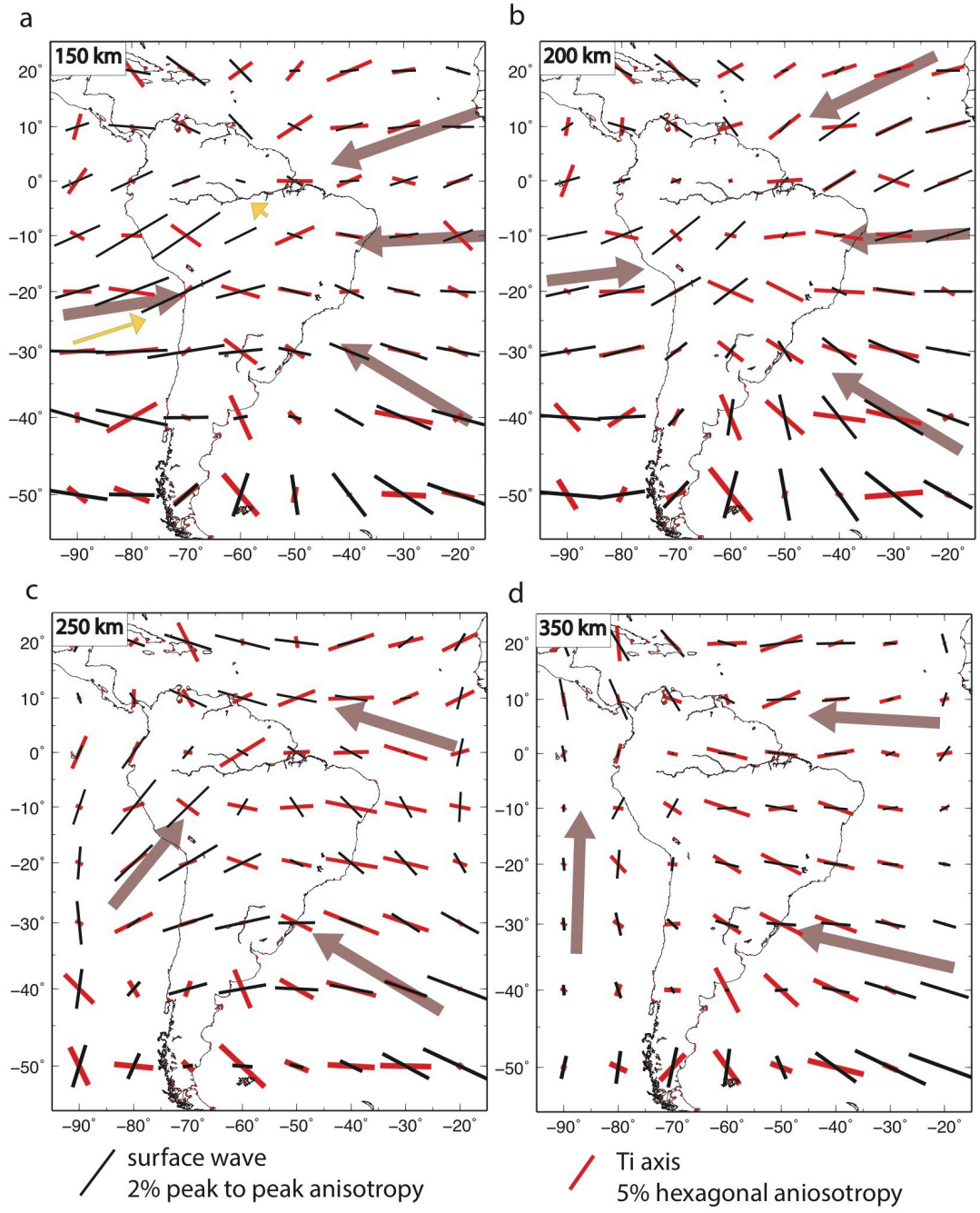

Figure 4.5. Comparison of azimuthal anisotropy with the prediction from the time-dependent model using Müller et al. (2008). Observed azimuthal anisotropy (Yuan and Beghein, 2013) at depths of (**a**) 150 km, (**b**) 200 km, (**c**) 250 km and (**d**) 350 km are shown as thin black bars, and the TI axes of predicted LPO are represented as thick red bars. The bold gray arrows indicate the dominant fast directions of azimuthal anisotropy for the adjacent regions. Yellow arrows in (a) indicate the present absolute plate motion.

The prominent radiating anisotropy pattern could be naturally explained using the subduction-induced poloidal mantle flow (Fig. B.4). Beneath the study region, we find a prominent westward converging asthenospheric channel flow originated from the Atlantic Ridge to the South American subduction zone, and an eastward plate-driven flow beneath the down-going Nazca plate. The former represents a typical Poiseuille flow converging towards the Andes (Fig. 4.6a, c), driven by the lateral pressure gradient above the concaved Nazca slab (Hu et al., 2016). The latter is a Couette flow due to the viscous entrainment from the subducting oceanic plate (Fig. 4.6b). These plate-scale poloidal flow fields form the radiating pattern of azimuthal anisotropy (Fig. 4.5). The fact that this pattern only extends to ~250 km depth (Fig. 4.5) may reflect the change of poloidal velocity direction due to the increasing viscosity and different mantle buoyancy at greater depth (Fig. 4.2c). It is worth noting that the continental-scale asthenosphere flow is perturbed by the strong cratonic roots within the continent and the secondary slab at the Antilles subduction zone, whose effects on seismic anisotropy is discussed later.

The depth-varying mantle flow field also explains the observed transition of azimuthal anisotropy beneath the Nazca Plate. At shallow depth (<200 km), mantle deformation is dominated by the eastward Couette flow due to Nazca subduction (Fig. B.4a, b), which leads to the east-west oriented fast direction (Fig. 4.5a, b). At greater depth (>200 km), the trench-parallel toroidal flow and extension (Long and Silver, 2008; Faccenda and Capitanio, 2012) beneath the retreating Nazca slab becomes dominant (Fig. B.4c, d), resulting in the north-south oriented anisotropy (Fig. 4.5c, d). However, this trench-parallel flow is of broad scale and asymmetric below the northern and southern half of the South American trench (Fig. B.4). This is because, first, the slab (and the associated trench) geometry is asymmetric with a more curved shape in the northern side (Figs. 4.1, 4.2); second, the northern half of the subduction zone has accumulated more slab material (Fig. 4.2a) at depths, which generates a stronger downward pull, drawing the mantle toward the north (Figs. 4.5, B.4).

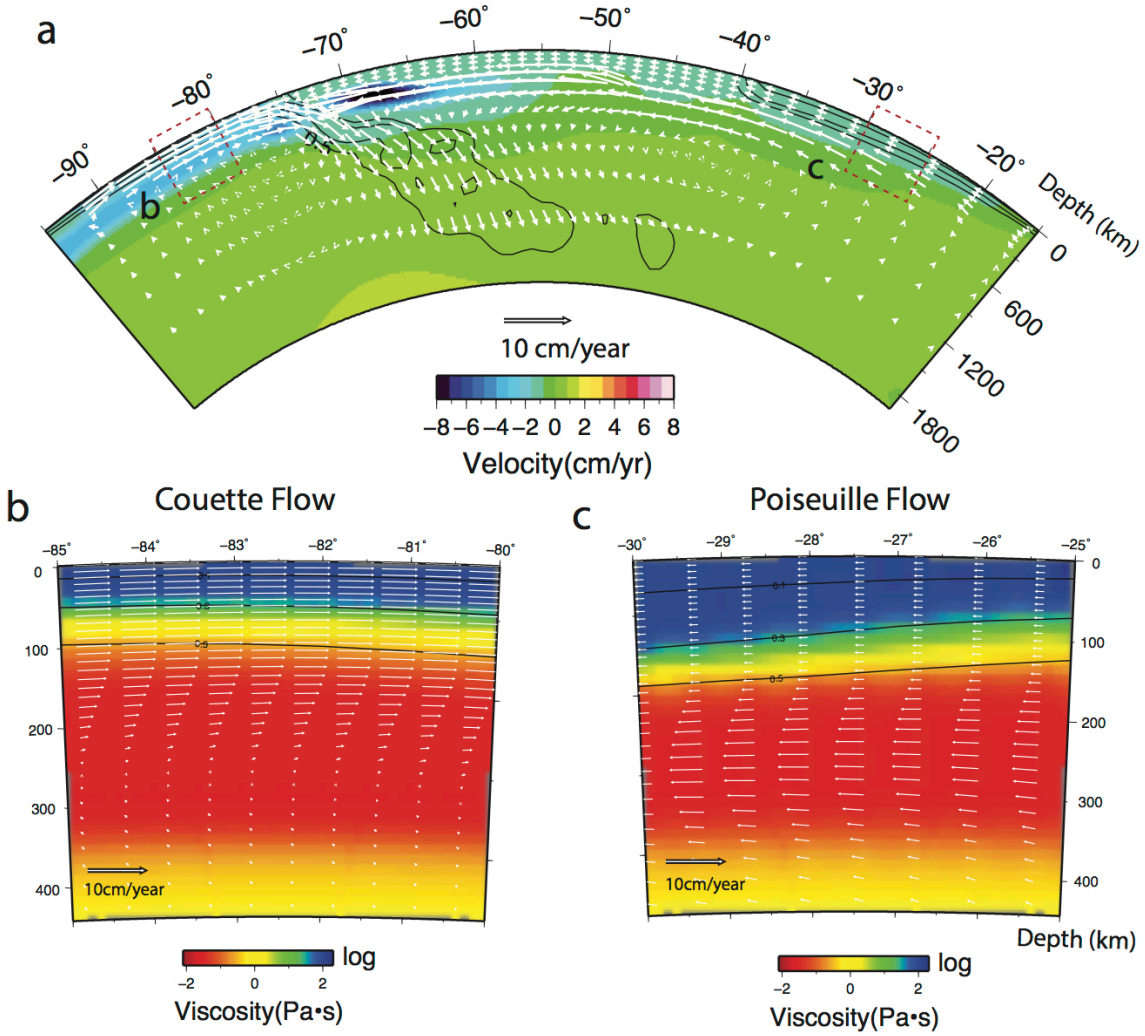

Figure 4.6. A cross section at 15°S of the flow model in Figure 4.5. (**a**) Cross-section of mantle velocity, with the background color representing the longitudinal (N-S) component of the velocity where the positive values represent southward. (**b**) and (**c**) are the zoomed-in cross sections beneath the Nazca Plate and the Atlantic Ocean, respectively, with the background color showing viscosity. For all the panels, white arrows represent the velocity components within the vertical plan.

These observations confirm the dominant role of the down-going slab in generating the observed seismic anisotropy. As discussed above, the overall pattern of seismic anisotropy is controlled by the geometry of the slab instead of the absolute plate motion. To further validate this conclusion, we performed another geodynamic model that incorporates a different plate reconstruction (Müller et al., 2016). In this model, the South American Plate moves toward west-southwest at present (Fig. B.5g-i), as is opposed to the northwest motion in Müller et al. (2008)

(Fig. 4.5). And the velocity of Nazca Plate rotates clockwise from east-northeast in Müller et al. (2008) to east direction in Müller et al., (2016). In the new model, the depth-dependent flow and anisotropy below South America remains largely invariant (Figs. B.5g-i & B.6g-i vs. Figs. 4.5 & B.4). The passive asthenosphere flow at 150 km depth below Nazca is slightly influenced by the plate motion (Fig. B.4 vs. Fig. B.6g-i), but it is not distinguishable from the predicted azimuthal anisotropy (Fig. 4.5 vs. Fig. B.5g-i). This suggests that the present-day plate motion plays a minor role in defining the azimuthal anisotropy in the mantle. For the rest of the paper, we will focus on one of these models, given their overall similarity.

Another way to demonstrate the dominant role of the slab in generating mantle flow is to compare the time-dependent slab model (Figs. 4.5 and B.4) with an instantaneous model that is based on a buoyancy structure converted from seismic tomography such as S40RTS (Ritsema et al., 2011) (Figs. B.5a-c and B.6a-c) or SMEAN (Becker and Boschi, 2002) (Figs. B.5d-f and B.6d-f). Since predictions from the two tomography-based models are similar, we only compare the S40RTS model with the slab model for the variation of misfit with depth (Fig. 4.7). The fit to azimuthal anisotropy from the S40RTS model show a noticeable degradation at all depths (Fig. 4.7). The average misfit within the upper mantle beneath the entire region increases from 32.5° for the slab model to 41° for the S40RTS model; the misfit for oceanic regions degrades from 30.5° to 42°. Here, we emphasize that the slab model has done a good job fitting the observation, given the low lateral resolution of surface-wave anisotropy. In fact, most poor fits occur near the boundaries of the model, due to edge effects of the regional model used here (Fig. 4.5).

In contrast, the tomography-based models have a relatively poor fit even far away from the boundaries (Fig. B.5). This is likely due to the fact that these global tomography models do not accurately capture the slab structure (Fig. 4.3a,b) as that in the slab model (Fig. 4.3c). More importantly, the fast anomalies beneath the eastern South American Plate (outlined in Fig. 4.3a) are converted to high density structures in this calculation, similar to previous assumption of convective downwelling (King and Ritsema, 2000); these local convection patterns destroy the large-scale Poiseuille channel flow excited by the Nazca slab, and thus degrade the fit to seismic anisotropy. Therefore, an important conclusion is that these south Atlantic fast anomalies should have close-to-neutral buoyancy, implying a compositional instead of thermal origin. We suggest that future studies are needed to better evaluate their dynamic properties and tectonic implication.

By comparing these models, we suggest that the slab plays a predominant role in shaping the pattern of azimuthal anisotropy.

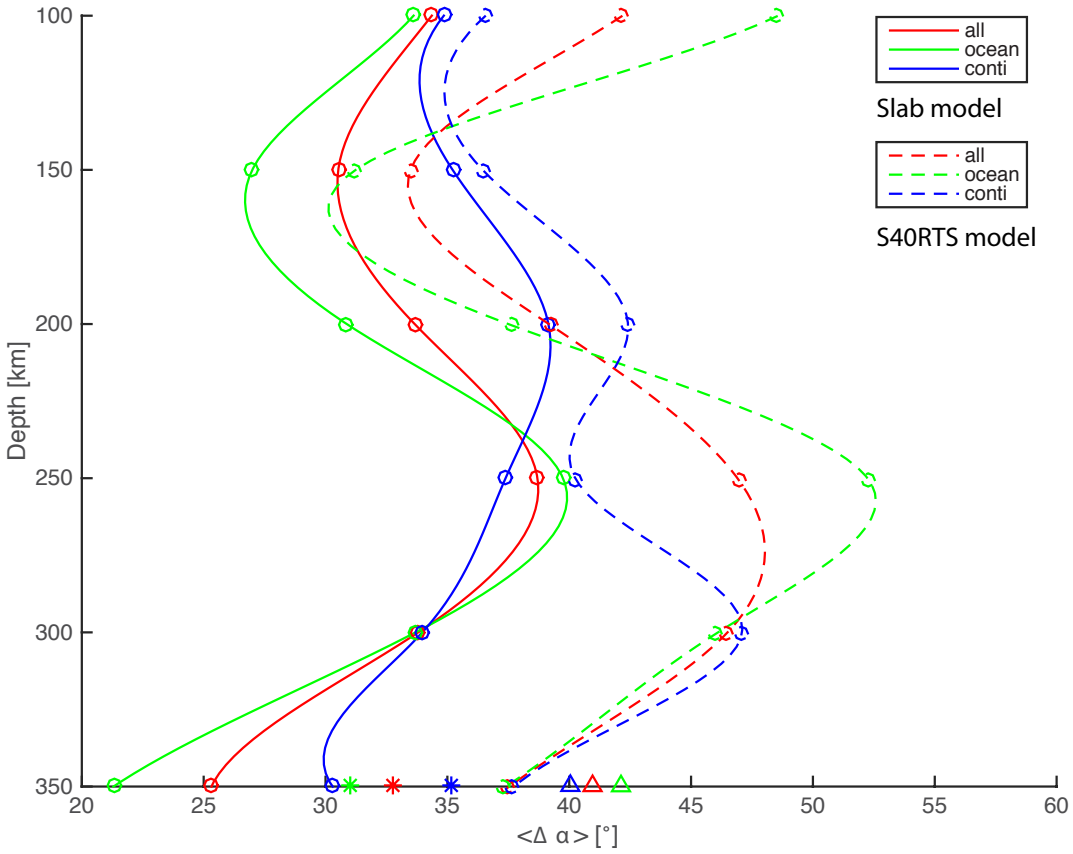

Figure 4.7. Misfit between the observed and predicted azimuthal anisotropy for two different geodynamic models. Solid lines show the misfit for the time-dependent slab model with Müller et al. (2008), while dashed lines show the misfit for the instantaneous tomography (S40RTS) -based model. Green, blue and red lines represent the horizontal average for oceanic regions, continental regions and the entire model region, respectively. Stars and triangles with different colors show the volumetric average of misfit for different regions of the slab and tomography-based models, respectively.

4.4.3 Shear wave splitting (SWS)

Relative to the azimuthal anisotropy, shear wave splitting data provide a higher lateral resolution. The calculated synthetic SWS remarkably matches the observed data compiled by Becker et al. (2012) (Fig. 4.8), except for some regions along the subduction zone where the fit is marginally good. This is likely due to the presence of other anisotropy sources not considered in this study, such as B-type Olivine fabric or LPO of strongly anisotropic hydrous phases in the wet

cold nose of the mantle wedge (Jung and Karato, 2001; Karato, 2008), as well as fossil fabrics, hydrated normal faults and laminated structures within the subducting slab (Faccenda et al, 2008; Sun et al., 2014). Here, we will focus on regions to the east of the Nazca-South America trench (Figs. 4.8 and 4.9).

4.4.3.1 SWS at the Caribbean–South American Plate margin

The tectonic setting of Caribbean-South American Plate margin is quite complex. To the east, the oceanic part of South American Plate is subducting beneath the Caribbean Plate at the Antilles subduction zone (Fig. 4.8). To the west, the Nazca Plate and Cocos Plate are subducting beneath South America and Caribbean Plates (Müller et al., 2008; 2016). The relative motion of Caribbean and South America created the San Sebastian-El Pilar right lateral strike-slip system (Fig. 4.8) along the plate margin (Pérez et al., 2001). Slightly to the south of this margin, the root of the Amazonian Craton extends to at least 200 km depth (Ritsema et al., 2011). The observed SWS demonstrates an overall east-west orientation along this margin, while trench-parallel SWS dominates the Antilles subduction zone on the eastern side of the Caribbean Plate (Figs. 4.1, 4.8 and 4.9).

These observed SWS patterns are well reproduced in the slab models (Fig. 4.9b,c), with the best-fit one being the time-dependent model based on Müller et al. (2016). By examining the mantle flow in the upper mantle (Figs. B.6g-i), we find that the large-scale asthenospheric flow converging toward the subducting Nazca slab is locally diverted by the slab below the Antilles trench, resulting in a strong focused east-west asthenosphere flow with large velocity gradient below this region (Figs. B.6g-i; black arrows in Fig. 4.9c). The predicted east-west SWS orientation in this region strongly resembles observation (Fig. 4.9). This suggests the Antilles slab plays a key role in generating the observed SWS pattern in the region.

This conclusion can be further verified by comparing the instantaneous models that are based on either the predicted present slab structure (Fig. 4.9b) or derived from seismic tomography (Fig. 4.9a and Fig. B.7b). The prediction for SWS from the tomography-based models is significantly worse than that from the slab model. This is mainly due to the fact that these global tomography models do not capture the slab structure surrounding the Caribbean Plate (Fig. 4.3), while the slab model closely resemble the slab structure revealed by regional tomography models (e.g. Benthem et al., 2013). However, compared with the time-dependent slab model (Fig. 4.9c), the

instantaneous slab model has a notably worse fit (Fig. 4.9b), which suggests that the past mantle flow should be taken into account in complex tectonic settings.

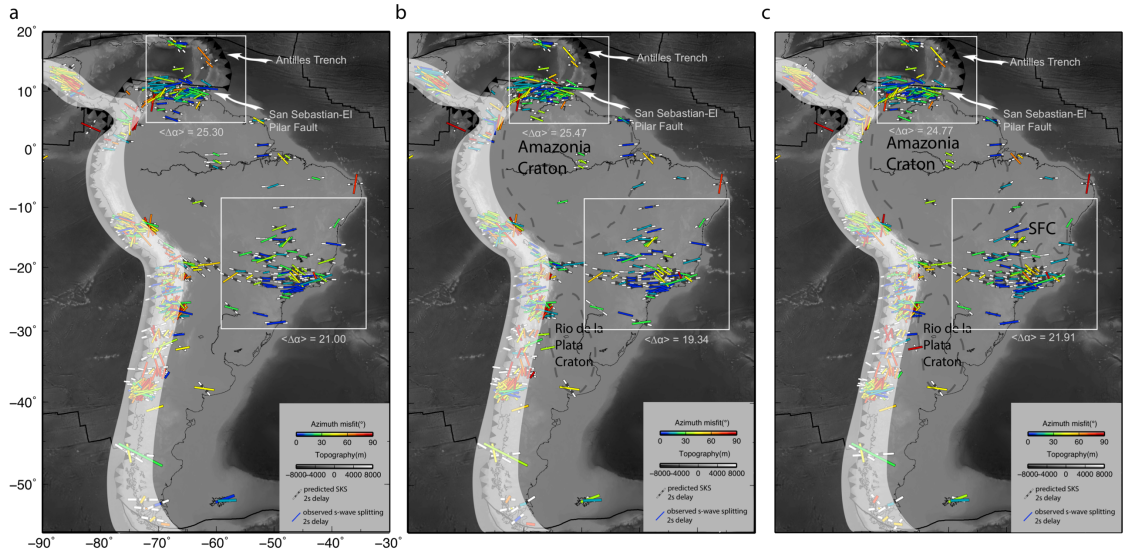

Figure 4.8. Comparison of the observed and predicted shear wave splitting for the slab model with the plate reconstruction of Müller et al. (2016). (**a**) shows the model that has a uniform 100 km-thick continent and does not include any cratons. (**b**) shows the model that includes the 250-km-thick Amazonia Craton and the Rio de la Plata Craton but not the Sao Francisco Craton. (**c**) shows the model that includes all three cratons. The dashed contours represent thick cratonic lithospheres included in this model. The angular misfit between observed (white bars) and predicted (color bars) station-averaged splitting is shown with different colors. Since the fast direction of SWS depends on the back-azimuth of the earthquake-station pair, we use the grey wedge to show the confidence interval of the fast direction. This is represented by (mean-stdev, mean+stdev), with mean and stdev representing the mean and standard deviation of the fast directions calculated by assuming the back-azimuth ranges from 0° to 360° with an increment of 2°, for each station. White boxes show the two zoomed regions in Fig. 4.9, with the numbers below indicating the mean angular misfits for the two regions. We refer to Miller and Becker (2012) for the format of this figure and Figure 4.9.

Interestingly, we find the effect of Amazonian Craton is minor in the formation of the observed east-west SWS pattern in the region, which contradicts to earlier studies (Assumpção et al., 2011; Miller and Becker, 2012). This is revealed by the comparison of the best-fit model with another model that only includes a 100 km-thick uniform continent without any cratonic roots (Fig. 4.8). We find the two models produce equally good SWS predictions (Fig. 4.8) in the plate margin. We notice that the velocity fields at the asthenospheric depths in this region are very similar with

or without the cratons, suggesting the large-scale asthenosphere flow is mainly diverted by the secondary slab at the Antilles trench rather than the thick cratonic root in the south.

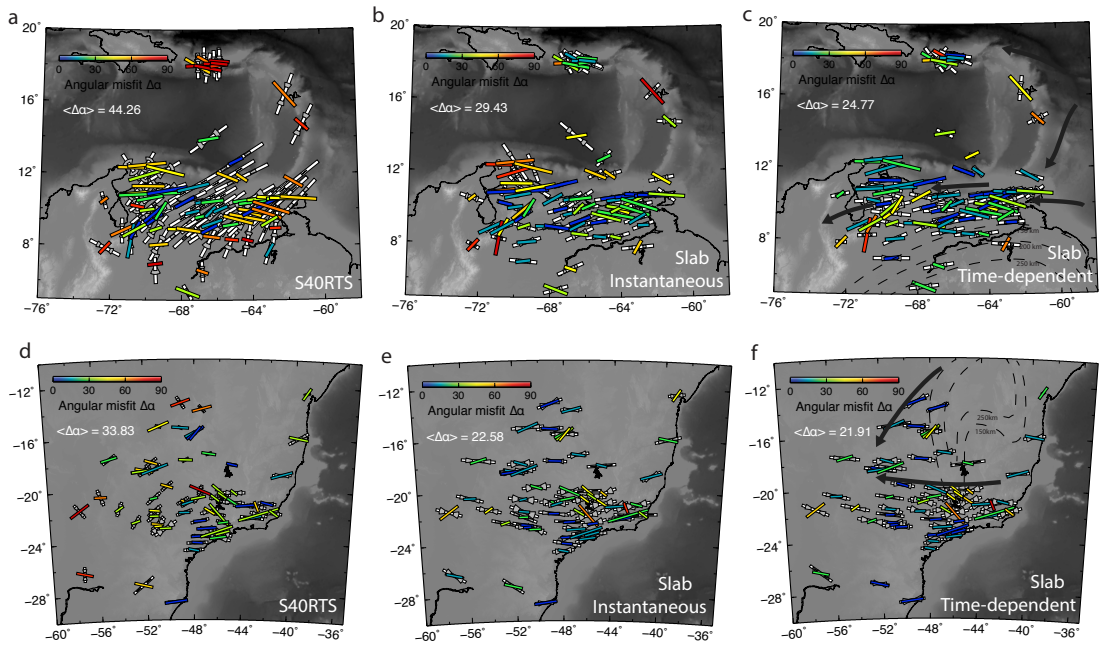

Figure 4.9. SWS fitting for three different geodynamic models at the Caribbean-South American plate margin. (**a**) Instantaneous tomography (S40RTS) -based model, (**b**) instantaneous slab model, (**c**) time-dependent slab model. All the models use the plate reconstruction of Müller et al. (2016). In each subplot, the observed station-averaged splitting is colored by angular misfit. The predicted splitting is shown with white sticks with the grey wedges representing the confidence interval of the fast direction. The black lines in (**c**) delineate the proposed flow direction. (d-f) Same as a-c, but for southeast Brazil.

4.4.3.2 SWS in southeast Brazil

The tectonic setting of southeast Brazil is relatively simple due to its location at a passive margin. However, the relative contributions on SWS from cratonic root modulation (Figs. 4.1 and 4.8) and that from deeper mantle convection remain debated (Conrad, 2007; Assumpcao et al., 2011). Another potential uncertainty is the contribution of fossil anisotropy from within the continental lithosphere (James and Assumpcao , 1996; Marone and Romanowicz, 2007; Yuan and Beghein, 2013).

The SWS measurements in southeast Brazil demonstrate a clear local convergence from east to west (Figs. 4.1, 4.8 and 4.9). This observation is well reproduced in both slab models (Fig. 4.9e,f) with a regional average angular misfit of ~22°, indicating the dominance of mantle flow over fossil lithospheric anisotropy in defining SWS, although the fossil anisotropy may explain local

variations of SWS at a wavelength < 100 km. We also notice that the SWS measurements are best reproduced with a thin SFC lithosphere (Fig. 4.8b). The geometry and thickness of this small craton slightly affect the flow pattern (Fig. B.6g-i) and SWS prediction (Fig. 4.8b vs. Fig. 4.8c), with the thin-craton model producing a regionally averaged misfit at ~19° (Fig. 4.8b), while that with a thick craton producing a larger misfit at ~22° (Fig. 4.8c). This suggests that the un-modulated asthenosphere flow can well explain the SWS, while a thick SFC lithosphere degrades the fit. We suggest that the craton root of SFC is either absent or remobilized due to Cenozoic deformation.

More insights arise from comparing different models (Fig. 4.9d-f). The fact that both the time-dependent slab model and the instantaneous slab model well predict the regional SWS pattern (Fig. 4.9e and Fig. 4.9f) implies that anisotropy in simple tectonic settings can be well approximated by the present mantle flow, as suggested by Conrad et al. (2007). In contrast, the tomography-based model produces a notably poorer prediction with an average misfit of ~34° (Fig. 4.9d), which is likely due to the assumed negative buoyancy of the fast anomalies underneath and thus local convection patterns, as discussed earlier. This is further confirmed in the calculation using SMEAN, which is smoother than S40RTS (Fig. 4.3a vs. Fig. 4.3b), resulting in improved orientations of predicted SWS (Fig. B.7a vs. Fig. B.7b). We emphasize that this does not support SMEAN as a better tomography image, since its apparent smoothness is due to lack of resolving power. Instead, this reinforces our earlier conclusion on the existence of compositional anomalies below the southern Atlantic margin. While further tuning the viscosity and density in such tomography-based calculations may improve the fit as earlier studies implied (e.g., Becker et al., 2014), changes in these model parameters, especially viscosity, are unlikely to satisfy the time-dependent subduction history from this study. Therefore, we suggest that estimation of mantle flow using tomography images is not a straightforward exercise.

4.5 Discussion and conclusion

In this study, we investigate the origin of seismic anisotropy in South America using data-oriented geodynamic models (Fig. 4.2). These models reveal the dominant role of subduction-induced mantle flow in generating the observed azimuthal anisotropy (Yuan and Beghein, 2013) (Fig. 4.5) and shear wave splitting (Becker et al., 2012) (Figs. 4.8 and 4.9). Comparatively, other tectonic factors, including absolute plate motion, fossil lithospheric anisotropy, and cratonic root diverting flow, play small to negligible roles in causing the observed anisotropy in South America.

We also find that mantle flow estimated by converting tomography images to buoyancy as traditionally done cannot accurately reproduce the pattern of seismic anisotropy, due to both its poor representation of slab geometry and the uncertain nature of non-slab seismic anomalies.

Furthermore, our results reveal two different flow regimes for the development of mantle mineral fabrics: seismic anisotropy below an active subducting plate usually follows the Couette flow drive by absolute plate motion, while that below an overriding plate is more subject to the slab-induced Poiseuille flow. This finding naturally explains the observation that seismic anisotropy aligns with absolute plate motions in the Australian Plate (Debayle et al., 2005) and plates within the Pacific Ocean (Smith et al., 2004; Becker et al., 2014), since all these plates represent subducting plates during the Cenozoic (Müller et al., 2016).

In comparison, mantle deformation beneath an overriding plate, such as South America, strongly relies on the past evolution and resulting geometry of the subducting slab. In South America, the upper mantle flow converges toward the concaved Nazca slab to the west (Figs. 4.5, B.4). Consequently, the pattern of seismic anisotropy may deviate significantly from the recent plate motion. Another example is North America, where the observed anisotropy is sub-parallel to the absolute plate motion (Vinnik et al., 1992; Fouch et al. 2000; Marone and Romanowicz, 2007). Although North America has been an overriding plate since the Mesozoic, subduction along its west coast is close to an end, and the young subducting slab beneath the Pacific Northwest is highly segmented (Liu and Stegman, 2011; Burdick et al., 2008; Sigloch, 2011; Schmandt and Lin, 2014). Relative to the massive and continuous Nazca slab (Fig. 4.2), the slab below North America probably no long forms a large-scale Poiseuille flow in the asthenosphere. Consequently, mantle deformation due to the plate motion plays an important role in generating the largely east-west oriented seismic anisotropy below central and eastern North America (Vinnik et al., 1992; Fouch et al. 2000; Marone and Romanowicz, 2007).

The large-scale Poiseuille flow beneath an overriding continent also sheds light on the mechanism of plate motion. In South America, the fast motion of the large-scale asthenosphere flow exerts an overall westward drag on the above lithosphere, which should contribute to the westward drift of the South American Plate (Fig. 4.6). This scenario implies that the lithosphere and asthenopshere are likely coupled, consistent with the “basal drag” hypothesis (Gurnis and Torsvik, 1994; Alvarez, 2010; Becker and Faccenna, 2011; Dal Zilio et al., 2017). However, we

emphasize that the asthenosphere flow may deviate from the absolute plate motion locally, as the latter is the manifestation of the net "basal drag" from the asthenosphere beneath the entire plate (Fig. 4.6).

Our models further demonstrate that cratons have small effects in SWS formation: in Southeast Brazil, models with a thin Sao Franciscan Craton better fit observation, and the fit at the Caribbean-South America margin does not require a thick Amazonian Craton (Fig. 4.8), which contradicts the earlier conclusions, made by Assumpção et al. (2006; 2011) and Miller and Becker (2012), respectively. We emphasize that the cratons do change mantle flow and the individual SWS prediction at some sites, such as those within and at the southeastern edge of the Amazonian Craton (Fig. 4.8). However, the regional behavior of SWS does not change much. This suggests that craton modulation of mantle flow plays a minor role for SWS formation.

By simultaneously predicting the regional-scale azimuthal anisotropy and shear wave splitting in South America, these data-oriented models also promise a better understanding of finer-scale anisotropy such as that along subduction zones. Future modeling effects may focus on further addressing the sub-slab anisotropy (e.g. Lynner and Long, 2014), anisotropy in the mantle wedge (e.g. Nakajima and Hasegawa, 2004) and that within the slab (e.g. Eakin et al., 2016). It may also be necessary to further assimilate slow seismic anomalies in the current slab models, especially for regions near hot spots (Ito et al., 2014) and mid-ocean ridges (Li and Detrick, 2003; French et al., 2013).

4.6 References

Alvarez, W. (2010). Protracted continental collisions argue for continental plates driven by basal traction. Earth and Planetary Science Letters, 296(3), 434-442.

Assumpção, M., Heintz, M., Vauchez, A., & Silva, M. E. (2006). Upper mantle anisotropy in SE and Central Brazil from SKS splitting: evidence of asthenospheric flow around a cratonic keel. Earth and Planetary Science Letters, 250(1), 224-240.

Assumpção, M., Guarido, M., van der Lee, S., & Dourado, J. C. (2011). Upper-mantle seismic anisotropy from SKS splitting in the South American stable platform: A test of asthenospheric flow models beneath the lithosphere. Lithosphere, 3(2), 173-180.

Becker, T. W., & Boschi, L. (2002). A comparison of tomographic and geodynamic mantle models. Geochemistry, Geophysics, Geosystems, 3(1).

Becker, T. W., Kellogg, J. B., Ekström, G., & O'Connell, R. J. (2003). Comparison of azimuthal seismic anisotropy from surface waves and finite strain from global mantle-circulation models. Geophysical Journal International, 155(2), 696-714.

Becker, T. W., Chevrot, S., Schulte-Pelkum, V., & Blackman, D. K. (2006a). Statistical properties of seismic anisotropy predicted by upper mantle geodynamic models. Journal of Geophysical Research: Solid Earth, 111(B8).

Becker, T. W., Schulte-Pelkum, V., Blackman, D. K., Kellogg, J. B., & O'Connell, R. J. (2006b). Mantle flow under the western United States from shear wave splitting. Earth and Planetary Science Letters, 247(3), 235-251.

Becker, T. W., & Faccenna, C. (2011). Mantle conveyor beneath the Tethyan collisional belt. Earth and Planetary Science Letters, 310(3), 453-461.

Becker, T. W., Lebedev, S., & Long, M. D. (2012). On the relationship between azimuthal anisotropy from shear wave splitting and surface wave tomography. Journal of Geophysical Research: Solid Earth, 117(B1).

Becker, T. W., Conrad, C. P., Schaeffer, A. J., & Lebedev, S. (2014). Origin of azimuthal seismic anisotropy in oceanic plates and mantle. Earth and Planetary Science Letters, 401, 236-250.

Beghein, C., Yuan, K., Schmerr, N., & Xing, Z. (2014). Changes in seismic anisotropy shed light on the nature of the Gutenberg discontinuity. Science, 343(6176), 1237-1240.

Benthem, S., Govers, R., Spakman, W., & Wortel, R. (2013). Tectonic evolution and mantle structure of the Caribbean. Journal of Geophysical Research: Solid Earth, 118(6), 3019-3036.

Browaeys, J. T., & Chevrot, S. (2004). Decomposition of the elastic tensor and geophysical applications. Geophysical Journal International, 159(2), 667-678.

Burdick, S., Li, C., Martynov, V., Cox, T., Eakins, J., Mulder, T., ... & van der Hilst, R. D. (2008). Upper mantle heterogeneity beneath North America from travel time tomography with global and USArray transportable array data. Seismological Research Letters, 79(3), 384-392.

Capitanio, F. A., & Faccenda, M. (2012). Complex mantle flow around heterogeneous subducting oceanic plates. Earth and Planetary Science Letters, 353, 29-37.

Chevrot, S. (2000). Multichannel analysis of shear wave splitting. Journal of Geophysical Research: Solid Earth, 105(B9), 21579-21590.

Conrad, C. P., Behn, M. D., & Silver, P. G. (2007). Global mantle flow and the development of seismic anisotropy: differences between the oceanic and continental upper mantle. Journal of Geophysical Research: Solid Earth, 112(B7).

Conrad, C. P., & Behn, M. D. (2010). Constraints on lithosphere net rotation and asthenospheric viscosity from global mantle flow models and seismic anisotropy. Geochemistry, Geophysics, Geosystems, 11(5).

Dal Zilio, L., Faccenda, M., & Capitanio, F. A. (2017). The role of deep subduction in supercontinent breakup. Tectonophysics, in press

Debayle, E., Kennett, B., & Priestley, K. (2005). Global azimuthal seismic anisotropy and the unique plate-motion deformation of Australia. Nature, 433(7025), 509-512.

Debayle, E., & Ricard, Y. (2013). Seismic observations of large-scale deformation at the bottom of fast-moving plates. Earth and Planetary Science Letters, 376, 165-177.

Eken, T., Plomerová, J., Roberts, R., Vecsey, L., Babuška, V., Shomali, H., & Bodvarsson, R. (2010). Seismic anisotropy of the mantle lithosphere beneath the Swedish National Seismological Network (SNSN). Tectonophysics, 480(1), 241-258.

Eakin, C. M., Long, M. D., Scire, A., Beck, S. L., Wagner, L. S., Zandt, G., & Tavera, H. (2016). Internal deformation of the subducted Nazca slab inferred from seismic anisotropy. Nature Geoscience, 9(1), 56-59.

Favier, N., & Chevrot, S. (2003). Sensitivity kernels for shear wave splitting in transverse isotropic media. Geophysical Journal International, 153(1), 213-228.

Faccenda, M., Burlini, L., Gerya, T. V., & Mainprice, D. (2008). Fault-induced seismic anisotropy by hydration in subducting oceanic plates. Nature, 455(7216), 1097-1100.

Faccenda, M., & Capitanio, F. A. (2012). Development of seismic anisotropy during subduction-induced 3-D mantle flow. Geophysical Research Letters, 39, doi:10.1029/2012GL051988.

Faccenda, M., & Capitanio, F. A. (2013). Seismic anisotropy around subduction zones: Insights from three-dimensional modeling of upper mantle deformation and SKS splitting calculations. Geochemistry, Geophysics, Geosystems, 14(1), 243-262.

French, S., V. Lekic, & B. Romanowicz, Waveform tomography reveals channeled flow at the base of the oceanic asthenosphere, *Science*, 342(6155), 227-230 (2013).

Foster, K., Dueker, K., Schmandt, B., & Yuan, H. (2014). A sharp cratonic lithosphere–asthenosphere boundary beneath the American Midwest and its relation to mantle flow. Earth and Planetary Science Letters, 402, 82-89.

Fouch, M. J., Fischer, K. M., Parmentier, E. M., Wysession, M. E., & Clarke, T. J. (2000). Shear wave splitting, continental keels, and patterns of mantle flow. Journal of Geophysical Research: Solid Earth, 105(B3), 6255-6275.

Gung, Y., Panning, M., & Romanowicz, B. (2003). Global anisotropy and the thickness of continents. Nature, 422(6933), 707-711.

Gurnis, M., & Torsvik, T. H. (1994). Rapid drift of large continents during the late Precambrian and Paleozoic: Paleomagnetic constraints and dynamic models. Geology, 22(11), 1023-1026.

Hasterok, D. (2013), A heat flow based cooling model for tectonic plates, Earth Planet. Sci. Lett., 361, 34-43.

Hayes, G. P., Wald, D. J., & Johnson, R. L. (2012). Slab1. 0: A three-dimensional model of global subduction zone geometries. Journal of Geophysical Research: Solid Earth, 117(B1).

Hess, H. H. (1964). Seismic anisotropy of the uppermost mantle under oceans, Nature, 203(4945), 629–631

Höink, T., Lenardic, A., & Richards, M. (2012). Depth-dependent viscosity and mantle stress amplification: implications for the role of the asthenosphere in maintaining plate tectonics. Geophysical Journal International, 191(1), 30-41.

Hu, J., Liu, L., Hermosillo, A., & Zhou, Q. (2016). Simulation of late Cenozoic South American flat-slab subduction using geodynamic models with data assimilation. Earth and Planetary Science Letters, 438, 1-13.

Hu, J., & Liu, L. (2016). Abnormal seismological and magmatic processes controlled by the tearing South American flat slabs. Earth and Planetary Science Letters, 450, 40-51.

Ismaıl, W. B., & Mainprice, D. (1998). An olivine fabric database: an overview of upper mantle fabrics and seismic anisotropy. Tectonophysics, 296(1), 145-157.

Ito, G., Dunn, R., Li, A., Wolfe, C. J., Gallego, A., & Fu, Y. (2014). Seismic anisotropy and shear wave splitting associated with mantle plume-plate interaction. Journal of Geophysical Research: Solid Earth, 119(6), 4923-4937.

James, D. E., & Assumpção, M. (1996). Tectonic implications of S-wave anisotropy beneath SE Brazil. Geophysical Journal International, 126(1), 1-10.

Jung, H., & Karato, S. I. (2001). Water-induced fabric transitions in olivine. Science, 293(5534), 1460-1463.

Kaminski, E., & Ribe, N. M. (2001). A kinematic model for recrystallization and texture development in olivine polycrystals. Earth and Planetary Science Letters, 189(3), 253-267.

Kaminski, E., & Ribe, N. M. (2002). Timescales for the evolution of seismic anisotropy in mantle flow. Geochemistry, Geophysics, Geosystems, 3(8), 1-17.

Kaminski, E., Ribe, N. M., & Browaeys, J. T. (2004). D-Rex, a program for calculation of seismic anisotropy due to crystal lattice preferred orientation in the convective upper mantle. Geophysical Journal International, 158(2), 744-752.

Karato, S. I., Jung, H., Katayama, I., & Skemer, P. (2008). Geodynamic significance of seismic anisotropy of the upper mantle: new insights from laboratory studies. Annu. Rev. Earth Planet. Sci., 36, 59-95.

Kendall, J. M., & Silver, P. G. (1996). Constraints from seismic anisotropy on the nature of the lowermost mantle. Nature, 381(6581), 409-412.

King, S. D., & Ritsema, J. (2000). African hot spot volcanism: small-scale convection in the upper mantle beneath cratons. Science, 290(5494), 1137-1140.

Li, A., & Detrick, R. S. (2003). Azimuthal anisotropy and phase velocity beneath Iceland: implication for plume–ridge interaction. Earth and Planetary Science Letters, 214(1), 153-165.

Lin, P. Y. P., Gaherty, J. B., Jin, G., Collins, J. A., Lizarralde, D., Evans, R. L., & Hirth, G. (2016). High-resolution seismic constraints on flow dynamics in the oceanic asthenosphere. Nature, 535(7613), 538-541.

Liu, L., & Stegman, D. R. (2011). Segmentation of the Farallon slab. Earth and Planetary Science Letters, 311(1), 1-10.

Loewy, S. L., Connelly, J. N., & Dalziel, I. W. (2004). An orphaned basement block: The Arequipa-Antofalla Basement of the central Andean margin of South America. Geological Society of America Bulletin, 116(1-2), 171-187.

Long, M. D., & van der Hilst, R. D. (2005). Estimating shear-wave splitting parameters from broadband recordings in Japan: a comparison of three methods. Bulletin of the Seismological Society of America, 95(4), 1346-1358.

Long, M. D., & Silver, P. G. (2008). The subduction zone flow field from seismic anisotropy: A global view. science, 319(5861), 315-318.

Long, M. D., & Silver, P. G. (2009). Shear wave splitting and mantle anisotropy: measurements, interpretations, and new directions. Surveys in Geophysics, 30(4-5), 407-461.

Long, M. D., & Becker, T. W. (2010). Mantle dynamics and seismic anisotropy. Earth and Planetary Science Letters, 297(3), 341-354.

Lynner, C., & Long, M. D. (2014). Sub-slab anisotropy beneath the Sumatra and circum-Pacific subduction zones from source-side shear wave splitting observations. Geochemistry, Geophysics, Geosystems, 15(6), 2262-2281.

Mainprice, D., & Nicolas, A. (1989). Development of shape and lattice preferred orientations: application to the seismic anisotropy of the lower crust. Journal of Structural Geology, 11(1-2), 175-189.

Marone, F., & Romanowicz, B. (2007). The depth distribution of azimuthal anisotropy in the continental upper mantle. Nature, 447(7141), 198-201.

Marquardt, H., & Miyagi, L. (2015). Slab stagnation in the shallow lower mantle linked to an increase in mantle viscosity. Nature Geoscience, 8(4), 311-314.

Menke, W., & Levin, V. (2003). The cross-convolution method for interpreting SKS splitting observations, with application to one and two-layer anisotropic earth models. Geophysical Journal International, 154(2), 379-392.

Miller, M. S., & Becker, T. W. (2012). Mantle flow deflected by interactions between subducted slabs and cratonic keels. Nature Geoscience, 5(10), 726-730.

Müller, R. D., Sdrolias, M., Gaina, C., & Roest, W. R. (2008). Age, spreading rates, and spreading asymmetry of the world's ocean crust. Geochemistry, Geophysics, Geosystems, 9(4).

Müller, R. D., Seton, M., Zahirovic, S., Williams, S. E., Matthews, K. J., Wright, N. M., ... & Bower, D. J. (2016). Ocean basin evolution and global-scale plate reorganization events since Pangea breakup. Annual Review of Earth and Planetary Sciences, 44(1), 107-138.

Nakajima, J., & Hasegawa, A. (2004). Shear-wave polarization anisotropy and subduction-induced flow in the mantle wedge of northeastern Japan. Earth and Planetary Science Letters, 225(3), 365-377.

Nicolas, A., & Christensen, N. I. (1987). Formation of Anisotropy in Upper Mantle Peridotites-A Review. Composition, structure and dynamics of the lithosphere-asthenosphere system, 111-123.

Pérez, O. J., Bilham, R., Bendick, R., Velandia, J. R., Hernández, N., Moncayo, C., ... & Kozuch, M. (2001). Velocity field across the southern Caribbean plate boundary and estimates of Caribbean/South-American plate motion using GPS geodesy 1994–2000. Geophysical Research Letters, 28(15), 2987-2990.

Ribe, N. M. (1992). On the relation between seismic anisotropy and finite strain. Journal of Geophysical Research: Solid Earth, 97(B6), 8737-8747.

Ritsema, J., Deuss, A., Van Heijst, H. J., & Woodhouse, J. H. (2011). S40RTS: a degree-40 shear-velocity model for the mantle from new Rayleigh wave dispersion, teleseismic traveltime and

normal-mode splitting function measurements. Geophysical Journal International, 184(3), 1223-1236.

Rudolph, M. L., Lekić, V., & Lithgow-Bertelloni, C. (2015). Viscosity jump in Earth's mid-mantle. Science, 350(6266), 1349-1352.

Schaeffer, A. J., Lebedev, S., & Becker, T. W. (2016). Azimuthal seismic anisotropy in the Earth's upper mantle and the thickness of tectonic plates. Geophysical Journal International, 207(2), 901-933.

Schmandt, B., & Lin, F. C. (2014). P and S wave tomography of the mantle beneath the United States. Geophysical Research Letters, 41(18), 6342-6349.

Sigloch, K. (2011). Mantle provinces under North America from multifrequency P wave tomography. Geochemistry, Geophysics, Geosystems, 12(2).

Silver P G, Chan W W. Shear wave splitting and subcontinental mantle deformation[J]. Journal of Geophysical Research: Solid Earth, 1991, 96(B10): 16429-16454.

Silver, P. G. (1996). Seismic anisotropy beneath the continents: Probing the depths of geology. Annual review of earth and planetary sciences, 24, 385-432.

Smith, D. B., Ritzwoller, M. H., & Shapiro, N. M. (2004). Stratification of anisotropy in the Pacific upper mantle. Journal of Geophysical Research: Solid Earth, 109(B11).

Sun, D., Miller, M. S., Agostinetti, N. P., Asimow, P. D., & Li, D. (2014). High frequency seismic waves and slab structures beneath Italy. Earth and Planetary Science Letters, 391, 212-223.

Tan, E., Choi, E., Thoutireddy, P., Gurnis, M., & Aivazis, M. (2006). GeoFramework: Coupling multiple models of mantle convection within a computational framework. Geochemistry, Geophysics, Geosystems, 7(6).

Vecsey, L., Plomerová, J., Kozlovskaya, E., & Babuška, V. (2007). Shear wave splitting as a diagnostic of variable anisotropic structure of the upper mantle beneath central Fennoscandia. Tectonophysics, 438(1), 57-77.

Vecsey, L., Plomerová, J., & Babuška, V. (2008). Shear-wave splitting measurements—Problems and solutions. Tectonophysics, 462(1), 178-196.

Vinnik, L. P., Makeyeva, L. I., Milev, A., & Usenko, A. Y. (1992). Global patterns of azimuthal anisotropy and deformations in the continental mantle. Geophysical Journal International, 111(3), 433-447.

Wang, X., Ni, J. F., Aster, R., Sandvol, E., Wilson, D., Sine, C., ... & Baldridge, W. S. (2008). Shear-wave splitting and mantle flow beneath the Colorado Plateau and its boundary with the Great Basin. Bulletin of the Seismological Society of America, 98(5), 2526-2532.

Yuan, K., & Beghein, C. (2013). Seismic anisotropy changes across upper mantle phase transitions. Earth and Planetary Science Letters, 374, 132-144.

Zandt, G., & Humphreys, E. (2008). Toroidal mantle flow through the western US slab window. Geology, 36(4), 295-298.

Zhang, S., & Karato, S. I. (1995). Lattice preferred orientation of olivine aggregates deformed in simple shear. Nature, 375(6534), 774-777.

Zhong, S., McNamara, A., Tan, E., Moresi, L., & Gurnis, M. (2008). A benchmark study on mantle convection in a 3-D spherical shell using CitcomS. Geochemistry, Geophysics, Geosystems, 9(10).

Chapter 5

Modification of the Western Gondwana Craton by Plume-lithosphere Interaction

5.1 Abstract[4]

The longevity of cratons is generally attributed to persistence of neutrally-to-positively buoyant and mechanically strong lithosphere that shields the cratonic crust from underlying mantle dynamics. Here we show that large portions of the cratonic lithosphere in South America and Africa, however, experienced significant modification during and since the Mesozoic, as demonstrated by widespread Cretaceous uplift and volcanism, present-day high topography, thin crust, and the presence of seismically fast but neutrally buoyant upper-mantle anomalies. We suggest that these observations reflect a permanent increase in lithospheric buoyancy due to plume-triggered delamination of deep lithospheric roots during the Late Cretaceous and early Tertiary. Lithosphere in these regions has been thermally reestablished since then, as confirmed by its present-day low heat flow, high seismic velocities and realigned seismic anisotropy. We conclude that the original lowermost cratonic lithosphere is compositionally denser than the asthenospheric mantle and can be removed when perturbed by underlying mantle upwelling. Therefore, it is the buoyancy of the upper mantle lithosphere that perpetuates stabilization of cratons.

[4]This chapter has been published as: Hu, J., Liu, L., Faccenda, M., Zhou, Q., Fischer, K. M., Marshak, S., & Lundstrom, C. (2018). *Modification of the Western Gondwana craton by plume–lithosphere interaction.* Nature Geoscience, 11(3), 203.

5.2 Introduction

The stability and persistence of cratons (the long-lived, relatively stable portions of continents) has been a focus of sustained research for the past four decades. According to the traditional isopycnicity hypothesis, cratonic mantle lithospheres are highly depleted due to extensive melt extraction (Jordan, 1978; Durrheim and Mooney, 1994; Carlson et al., 2005; Lee et al., 2011), which results in a highly viscous and neutrally to positively buoyant thermal boundary layer that persists for billions of years. This model, although elegant, does not readily explain apparent temporal variations in cratons, including significant elevation changes over time and episodic destruction of the deep lithosphere (Carlson et al., 2005; Lee et al., 2011). Recent measurements of seismic anisotropy suggest that the upper portion (<100-150 km depth) of the cratonic lithosphere has a seismic fabric that differs from the lithosphere below (Yuan and Romanowicz, 2010; Yuan and Beghein, 2013; Debayle and Kennett, 2000). This new lithospheric structure is consistent with models that assume a compositionally stratified thermal boundary layer whose shallower depths are more depleted (King, 2005; Eaton and Perry, 2013). Such models spark questions about the buoyancy and stability of the cratonic lithosphere (Durrheim and Mooney, 1994; Carlson et al., 2005; Lee et al., 2011), especially as regards the relative contribution to density from composition and temperature at different depths (King, 2005; Eaton and Perry, 2013; Kaban et al., 2015). Consequently, questions concerning how cratons can remain "stable" over billions of years and how they respond to dynamic processes in the underlying asthenosphere, still await an answer.

Here we investigate the density structure and temporal evolution of the cratonic lithosphere using diverse observational constraints including topographic evolution, gravity anomalies, seismic tomography and anisotropy, tectonic reconstructions, and mantle flow. To avoid potential effects of Mesozoic-Cenozoic subduction on craton evolution (Durrheim and Mooney, 1994; Griffin et al., 1998; Levander et al., 2011), we focus on cratons bordering the South Atlantic passive margins (Fig. 5.1). This study area includes Precambrian regions of South America and Africa hosting cratons and Neoproterozoic orogens (Alkmim et al., 2006), regions that were once part of western Gondwana. A prominent feature of these continents is the widespread high (1 km or more) surface topography inside or on the edges of the São Francisco (SF), Congo (CG), and Kalahari (KH) cratons (Fig. 5.1**a**). Elevation of these regions is in sharp contrast to that of other

cratons like West Africa (WA), Amazonian (AZ), and North American (NA) that mostly display low topography (Kaban et al., 2003; Mooney and Kaban, 2010).

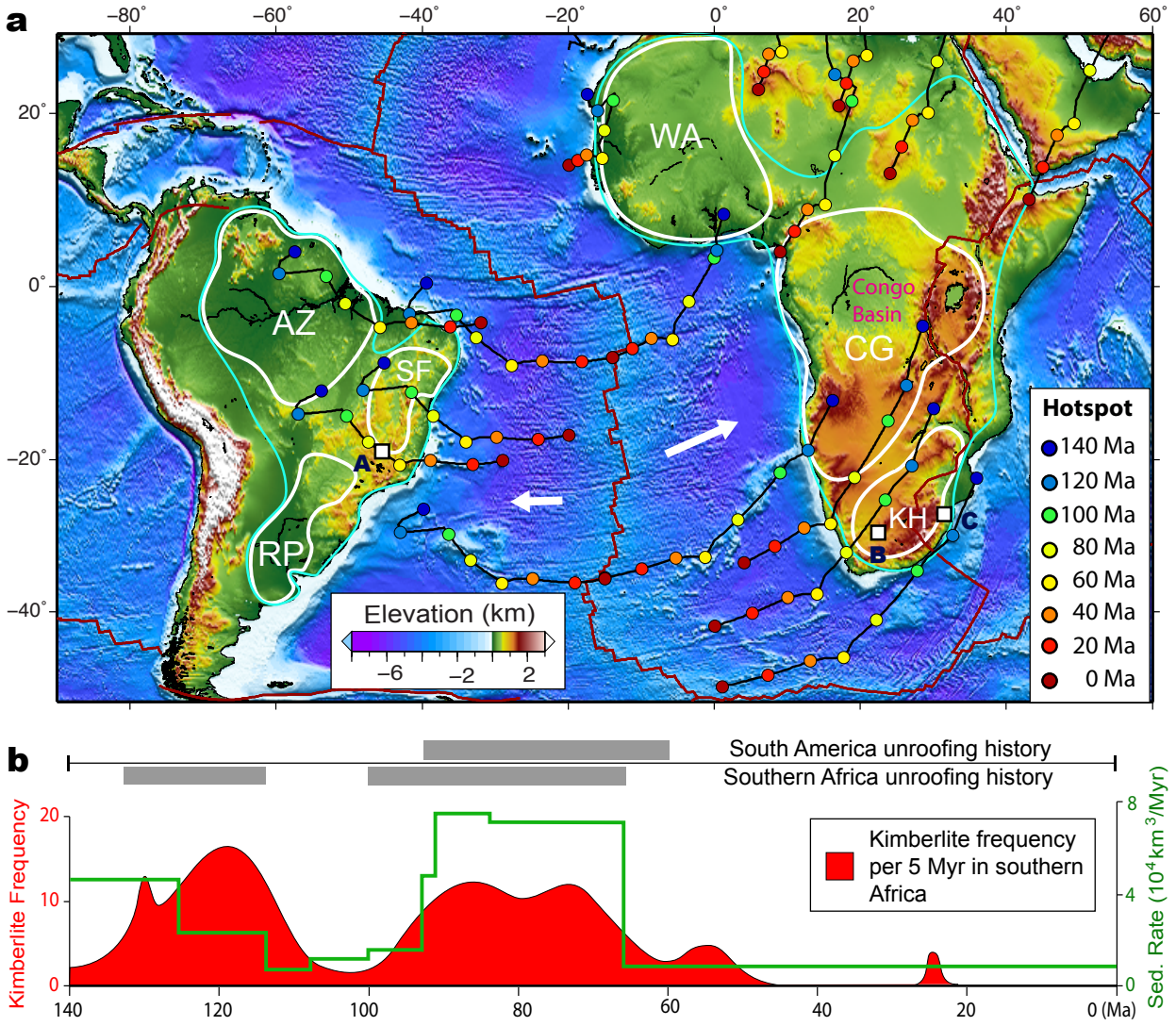

Figure 5.1. Topography and tectonic history of the South Atlantic margins. **a**) Anomalously high elevations in the Kalahari (KH), Congo (CG) and Sao Francisco (SF) cratons. In contrast, Amazonia (AZ), Rio de la Plata (RP) and Western Africa (WA) cratons display low topography. White and cyan contours outline major cratons and Precambrian shields (Alkmim et al., 2006). Colored dots and black lines are reconstructed hotspot tracks. Thick white arrows indicate average Cenozoic plate motion directions. White squares are several Cretaceous volcanic eruptions (Hanson et al., 2009; Read et al., 2004). **b**) Kimberlite (red region) ages in southern Africa (Jelsma et al., 2009), accumulative sedimentation rate (green line) along southern African coast (modified from Guillocheau et al., 2012), and unroofing history (thick gray bars) of the high-topography cratons (CG, KH & SF) (Cogné et al., 2011; Read et al., 2004; Stanley et al., 2013).

Subsequently, we will address several key aspects related to the topographic evolution of the study area. First, most high topography in the region is isostatically supported by sub-crustal lithospheric mantle (Fig. 5.2). Second, this high topography developed during and since the late Mesozoic (Fig. 5.1**b**), as indicated by the presence of earlier marine-lacustrine depositional environments (Arai and Chapadas, 2000; Catuneanu et al., 2005) and of widespread Cretaceous volcanic eruptions (Harman et al., 1998; Hanson et al., 2009) and associated surface uplift (Cogné et al., 2011; Read et al., 2004; Stanley et al., 2013) in these regions. Third, the upper mantle beneath the study area contains anomalous zones that have high seismic velocity but are close to being neutrally buoyant (Fig. 5.3), a feature characteristic of delaminated lithospheric mantle of cratons. Fourth, seismic anisotropy of lower cratonic lithosphere below these regions shows realignment to directions of the Cenozoic mantle flow (Fig. 5.4). Taken together, our analyses indicate that the western Gondwana cratonic lithosphere was modified through delamination beginning in the late Mesozoic, due to its interaction with mantle plumes.

5.3 Origin of high cratonic topography

Recent seismic studies (Laske et al., 2012; Reid et al., 2012; Assumpção et al., 2012; Liu et al., 2016; Globig et al., 2016) suggest that crustal thickness below significant portions of the high-topography regions (the SF and KH cratons and the periphery of the CG craton) is notably thinner than the surrounding continental regions (Fig. D.1**a** in APPENDIX D), probably in response to extensive Mesozoic surface erosion (Harman et al., 1998; Hanson et al., 2009; Cogné et al., 2011; Read et al., 2004; Stanley et al., 2013). This relatively thin crust cannot compensate high topography and thus must reflect positive buoyancy from the underlying mantle. Since high topography occurs within only part of the CG craton (Fig. 5.1**a**), density differences between cratonic and non-cratonic crust also cannot explain the observed topographic variation.

To gain further insight into the cause of topographic variation, we estimated the lithospheric residual topography by removing contributions of the crust (Fig. D.2**a**) and the sub-lithospheric mantle (Fig. D.3**a**), neither of which can explain the high surface topography (see Supplementary Materials). In addition to the lack of correlation of crustal thickness with topography discussed above, recent geodynamic studies reveal neutral-to-negative dynamic topography in our study region (Shephard et al., 2010; Flament et al., 2012; Moucha and Forte, 2011), a result confirmed by our calculations using recent tomography images (French et al., 2012;

Ritsema et al., 2011) (Fig. D.4). Consequently, the resulting lithospheric residual topography displays a peak-to-trough variation of up to 2 km (Fig. 5.2**a**), with positive areas correlating with the prominent high land-surface topography (Fig. 5.1). Most high residual topography occurs inside the cratons, with only a minor portion over the Neoproterozoic (Brasiliano or Pan African) orogens (Fig. 5.2**a**). This result suggests that high cratonic topography, in regions of thin crust, reflects lithospheric buoyancy heterogeneities. A similar analysis of the gravity field further supports this conclusion, with negative lithospheric gravity anomalies in high-topography regions (Fig. 5.2**b**).

To evaluate whether inferred lithospheric buoyancy heterogeneity is thermal or compositional in origin, we examine seismic, heat-flow, and xenolith data. The presence of high shear velocities (French et al., 2012; Ritsema et al., 2011; Pasyanos et al., 2014; Priestley and McKenzie, 2013; Adams and Nyblade, 2011; Feng et al., 2007) (Figs. 5.3, D.5, D.6), low attenuation (Dalton et al., 2017) and cold geotherms inferred from heat flow (Artemieva, 2006) beneath both high-topography regions of KH, CG and SF and the two low-topography cratons of WA and AZ (Figs. 5.3, D.5, D.6) indicates that cold lithosphere extends down to depths of >200 km (Priestley and McKenzie, 2013; Dalton et al., 2017). Lithosphere thermal thicknesses inferred from shear velocities (Priestley and McKenzie, 2013) vary by <25 km among the KH, CG, SF, WA, and AZ cratons. Also, residual topography (Fig. 5.2**a**) does not correlate consistently with regional variations in thermal buoyancy of the mantle inferred from attenuation (Dalton et al., 2017), either within or between cratons. Lithosphere thermal thickness inferred from heat flow (Artemieva, 2006) varies by <100 km, with high-topography cratons being slightly thinner (Fig. D.7). Lithospheric temperature estimates from mantle xenoliths also reveal similar to slightly higher (by <150 K) temperature beneath the KH craton compared to intact cratons like the Slave (Lee et al., 2011). Taking an upper limit (150 K) of these inferred temperature variations within the lower 100 km of the lithosphere, the associated thermal buoyancy could account for <500 meters of topography, in sharp contrast to the much larger variation (up to 2 km) of lithospheric residual topography (Fig. 5.2). Thus, we conclude that a significant fraction of the apparent lithospheric buoyancy reflects composition.

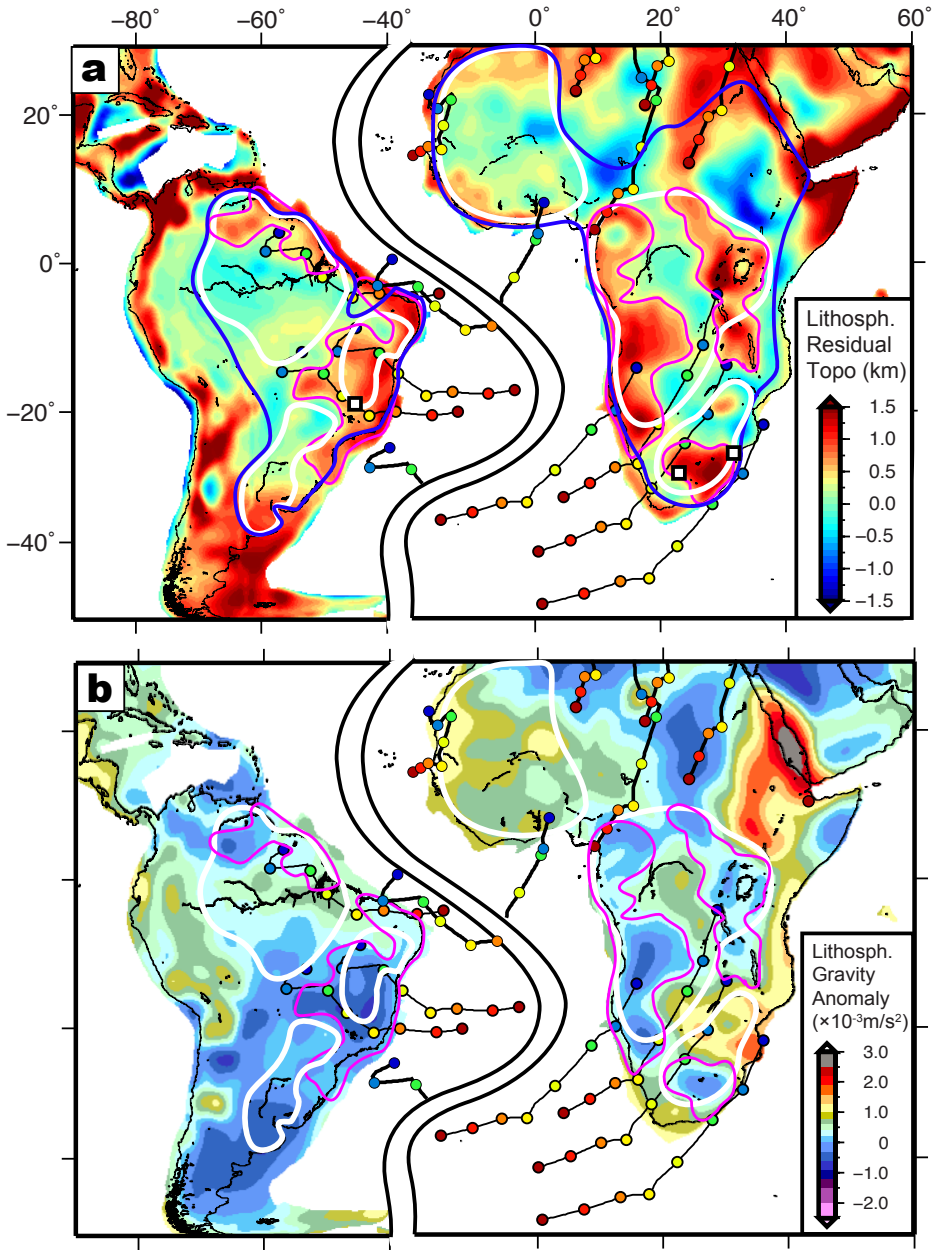

Figure 5.2. Lithospheric residual topography and gravity. **a**) Residual topography corrected for both Airy compensation of crustal effect and sub-lithospheric dynamic topography (Fig. D.3**a**). Magenta contours outline the regions with positive residual topography, implying the spatial extent of delamination. Note the association of positive residual topography with cratons. **b**) Residual gravity anomaly obtained by removing crustal, topographic, and sub-lithospheric contributions (Fig. D.3**b**) from free-air gravity (refer to Method in APPENDIX C for details). Other notations are the same as those in Figure 5.1.

5.4 Cretaceous uplift due to lithospheric delamination

To better understand the origin of high-topography cratons, we also evaluated their temporal evolution. The SF craton has gained >1 km of surface elevation since the Cretaceous, relative to the adjacent AZ craton (Arai and Chapadas, 2000). As a result, Late Jurassic-Early Cretaceous shallow-marine to lacustrine sedimentary strata in eastern Brazil now lie well above sea level (Arai and Chapadas, 2000). Most of the uplift likely occurred during the Late Cretaceous in association with >3 km of denudation in eastern Brazil (Fig. 5.1**b**); the greatest denudation occurred along the northeastern edge of AZ (Arai and Chapadas, 2000) and over the entire SF (Cogné et al., 2011; Read et al., 2004), regions that presently have positive residual topography (Fig. 5.2**a**). Similarly, southern Africa — a region that had undergone subsidence during the Jurassic as indicated by occurrence of sedimentary deposits of this age (Catuneanu et al., 2005) — experienced rapid uplift and denudation during the Cretaceous (Fig. 5.1**b**), as revealed by analysis of kimberlite diatremes (Hanson et al., 2009), by thermochronology studies of the KH (Stanley et al., 2013), and by evaluation of sedimentation history along the southern African coast (Guillocheau et al., 2012).

Dynamic topography due to sub-lithospheric convection is unlikely to have caused the Cretaceous uplift and present high residual topography (Fig. 5.2**a**), for two reasons. First, recent estimates on changes in dynamic topography due to mantle convection since 100 Ma reveal subsidence, not uplift, in eastern South America (Shephard et al., 2010; Flament et al., 2012). Similarly, little Cenozoic dynamic uplift took place in southern Africa (Flament et al., 2012; Moucha and Forte, 2011). Second, observed residual topography in our study area has a wavelength of <500 km (Fig. 5.2), while dynamic topography usually occurs over a wavelength of >1000 km (Figs. D.4).

Since dynamic topography cannot explain observed uplift, we also examined the role that lithosphere delamination may have served in increasing cratonic lithospheric buoyancy, for delamination can cause isostatic uplift. A rapid increase of heat flow during the Late Cretaceous in both South America and southern Africa (Hanson et al., 2009; Read et al., 2004) and the contemporaneous disappearance of high-pressure garnet-facies in South America (Read et al., 2004), provides independent evidence that the lowermost (likely >200 km depth) lithosphere was removed. In addition, the temporal correlation (Fig. 5.1**b**) among the two-pulse history of

kimberlite eruption with more fertile composition from the second phase (Griffin et al., 2003), the circum-Africa sedimentation rate (Guillocheau et al., 2012), and the unroofing history for the KH, further supports regional modification of the southern African lithosphere (Griffin et al., 2003).

In regions far from subduction zones, mantle upwelling in plumes represents the most likely candidate for triggering lithosphere delamination. By reconstructing the trajectory of southern Atlantic hotspots (Courtillot et al., 2003) back to the Early Cretaceous using a recent plate reconstruction (Müller et al., 2016) (Fig. 5.1), we find that Cretaceous-aged hotspot tracks coincide with regions of high topography in both South America and southern Africa (Figs. 5.1, 5.2). An independent validation of this reconstruction comes from the match of hotspots with dated Late Cretaceous volcanism (white squares in Fig. 5.1) in both Brazil and South Africa. This correlation implies a potential causal relationship among these phenomena. The most intense Late Cretaceous kimberlitic volcanism in the SF and KH cratons occurred primarily along their edges (Fig. 5.1), possibly implying the location of initial lithosphere delamination. Thermochronology studies in southern Africa reveal a migration of exhumation from the edge to the interior of KH during 90-60 Ma (Stanley et al., 2013), consistent with a progressive pealing off of cratonic lithosphere toward the center.

Both warming of the lithosphere and delamination of high-density materials can result in local buoyancy increase and surface uplift. The coherently fast seismic velocities of the thick lithospheres (French et al., 2012; Ritsema et al., 2011; Pasyanos et al., 2014; Priestley and McKenzie, 2013; Adams and Nyblade, 2011; Feng et al., 2007) and low present-day surface heat flow (Artemieva, 2006) suggest that the thermal perturbation caused by the Cretaceous plume-lithosphere interaction has now largely disappeared (Figs. 5.3, D.5). This disappearance is consistent with the time required for a new thermal boundary layer to replace the delaminated lower lithosphere (Fig. D.8). Therefore, the present-day high topography must reflect a permanent loss of a compositionally dense layer of material from the original lithosphere.

Can the proposed delaminated lithosphere be detected within the present-day mantle? A 3-D representation of mantle seismic structure (Fig. 5.3) reveals multiple voluminous high velocity anomalies within the sub-lithosphere mantle below the south Atlantic margins. These mantle structures seem to be well resolved, as they are similar among different tomography models (Figs. D.5, D.6). Since these regions have not experienced subduction since the early Mesozoic (Müller

et al., 2016), these anomalies cannot represent subducted slabs. Previously, they were interpreted as zones of cold downwelling along lithospheric margins, due to edge-driven convection (King and Ritsema, 2000). We suggest instead that they represent the foundered segments of lithospheric mantle.

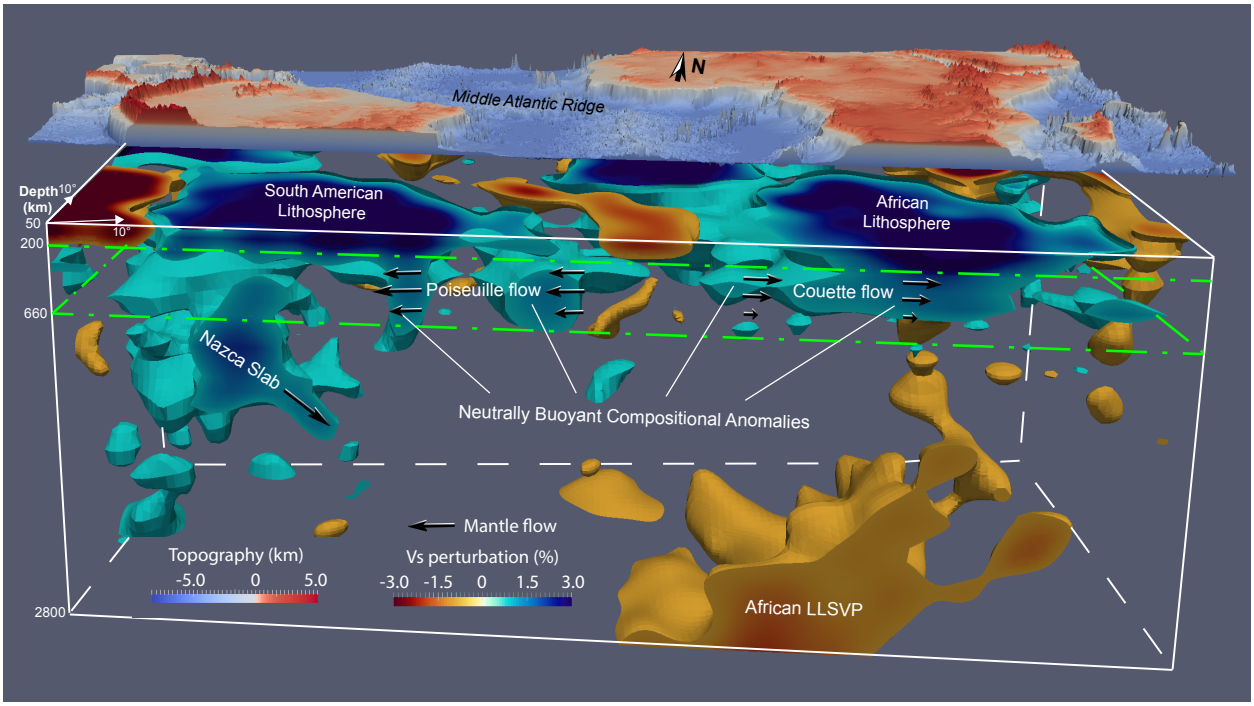

Figure 5.3. Seismic structure of the lithosphere and underlying mantle in the study region. The 3D visualization is based on the S40RTS tomography model (Ritsema et al., 2011), with the volume of fast structure showing anomalies at >0.8%, and that for slow structure at <-1.0%. Color on top highlights the topography contrasts. Black arrows indicate Cenozoic mantle flow, and interpretations of various high velocity mantle structures are inferred from our geodynamic modeling of seismic anisotropy (Hu et al., 2017). Note the overall westward drift of the upper mantle beneath the South American plate driven by Nazca subduction. LLSVP – large low shear wave velocity province.

This concept is supported by a separate study in which we quantitatively evaluated the mantle flow associated with the subduction of the Nazca Plate relative to the other high velocity anomalies in Figure 5.3 by simultaneously matching mantle flow predictions to observations of surface-wave anisotropy and shear-wave splitting (Hu et al., 2017) (Figs. D.10, D.11). Fits to both regional and local anisotropy measurements require that the Nazca slab be the dominant cause of downwelling and that other high-velocity anomalies are mostly passively drifting and generating

negligible vertical mantle flow (Fig. 5.3). This result requires the south Atlantic upper-mantle anomalies to be close to neutrally buoyant.

According to our previous subduction model (Hu et al., 2017), the mantle beneath an overriding plate, such as South America, undergoes pressure-gradient driven Poiseuille flow. In contrast, beneath plates not near a subduction zone, mantle undergoes plate-motion driven Couette flow (Fig. 5.3). Consequently, present-day mantle structure further supports the lithosphere delamination hypothesis in that the geometry and location of these high velocity anomalies (Fig. 5.3) are best explained as foundered lithosphere fragments left behind as South America and Africa moved apart since the Cretaceous (Figs. 5.3, D.5, D.6). The tendency for the delaminated materials to remain on the South American side of the Atlantic may reflect the stronger westward upper-mantle Poiseuille flow drawn by the down-going Nazca slab (Hu et al., 2017) (Fig. 5.3).

5.5 Cenozoic realignment of lithospheric seismic anisotropy

Lithospheric mantle that has undergone shear during the Cenozoic should display seismic anisotropy similar to that of recent asthenosphere flow. Comparison of azimuthal anisotropy[6] with that predicted by Cenozoic mantle flow, as a function of depth, (see supplementary materials), therefore, can provide another important test of our model (Hu et al., 2017). Robust anisotropy predictions within the asthenosphere below continental South America and surrounding oceans (Figs. D.10, D.11) allow us to apply the modeling results to the interior of the cratonic lithosphere.

Lack of correlation between the observed anisotropy in the uppermost mantle (<100 km) with that of the asthenosphere below suggest that fabrics at this depth are mostly "fossil" signals (Fig. 5.4**a**, 5.4**e**), meaning relicts of pre-Cenozoic shear. At depths of ≥100 km, the correlation clearly improves in most non-cratonic regions (Fig. 5.4), consistent with their thin lithospheres (Fig. 5.3) and increasing influence of Cenozoic shear. The East African Rift region does not display anisotropy compatible with Cenozoic shear at >150 km depth (Fig. 5.4**g**, 5.4**h**), probably because of perturbations by upper-mantle upwelling (Figs. 5.3, D.2). In contrast, correlation of anisotropy is poor below the low-topography cratons, which are inferred to have intact mantle lithospheres (AZ and WA). This lack of correlation emphasizes that mantle deformation did not take place within the intact cratonic lithosphere during the Cenozoic (Yuan and Romanowicz, 2010; Yuan and Beghein, 2013).

However, in most high-topography cratonic regions, observed anisotropy aligns with predicted mantle shear at depths as shallow as 100 km, such as in SF (Fig. 5.4). A similar correlation of observed and predicted anisotropy results when a different anisotropy model (Schaeffer and Lebedev, 2016) is employed (Fig. D.12**a**, D.12**c**). This obvious regional realignment of lower lithosphere anisotropy with Cenozoic mantle flow in regions of Mesozoic modification suggests that the lithospheric fabrics of these cratons were reset. Another recent anisotropy model (Debayle et al., 2016) confirms this conclusion for depths of <150 km, but displays significant discrepancy at greater depths (Fig. D.12**b**, 5.12**d**). Since this model fails to match our well-predicted asthenospheric deformation and likely the shear-wave splitting observations over South America[44] as well (Fig. D.12), we suggest that the other two anisotropy models (Yuan and Beghein, 2013; Schaeffer and Lebedev, 2016) better represent lowermost lithosphere fabric in our study region.

Mechanically, fabric resetting could be due to either local deformation of the original lithosphere (Griffin et al., 1998) or growth of a new thermal boundary layer after delamination (Fig. 5.5). We suggest a combination of both mechanisms. On the one hand, the isostatic uplift of topography requires removal of dense lithospheric materials. On the other hand, the observed high-velocity (>2%) lithosphere at 200 km and below (Figs. 5.3, D.5) requires compositional (e.g. garnet or MORB, Fig. D.9) in addition to thermal effects (Fig. D.8). Therefore, we propose that delamination happened mostly within the lowermost cratonic lithosphere where high-density materials exist, and that lithosphere below ~100 km was not necessarily removed entirely but instead underwent shear sufficient to realign its crystallographic anisotropy with that of the ambient mantle. This concept can be further verified by examining the spatial extent of anisotropy realignment, where the realigned area in Africa is much larger than the zones of high residual topography (Fig. 5.2), with the former also closely correlating with the province of Cretaceous kimberlites (Yaxley et al., 2013) (Fig. D.13).

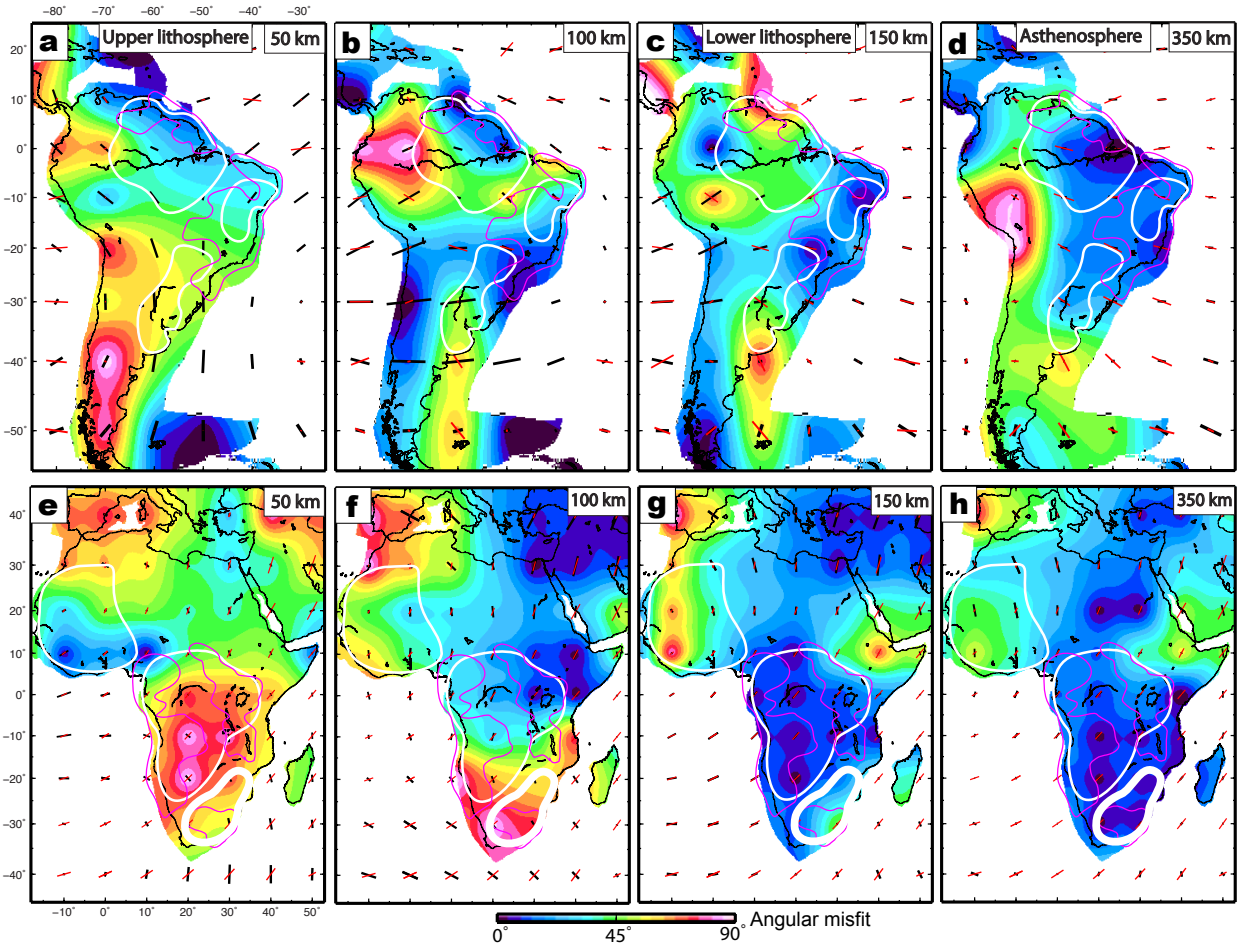

Figure 5.4. Comparison of observed and mantle-flow induced seismic anisotropy. **a-d**) Azimuthal anisotropy at different depths beneath South America. Black bars are observations from YB12sv (Yuan and Beghein, 2013), and red bars are predictions (Hu et al., 2017). The background color represents the angular misfit between the two. The 350 km depth represents the asthenosphere. Note the increasing fit of anisotropy with depth in regions where deep lithosphere delamination (magenta contours) is inferred, implying Cenozoic shearing of these parts of the craton lithosphere. **e-h**) Same as **a-d**, but for Africa, where the comparison of observed and predicted anisotropy yields a similar conclusion. The poor fit in northern Eastern Africa Rift at depths >100 km is likely due to active mantle upwelling that is not modeled in our anisotropy calculation.

5.6 Implications for density and evolution of cratonic lithosphere

In order for the lowermost cratonic lithosphere to delaminate, its density must be greater than that of the surrounding asthenosphere (Fig. 5.5**a**). Also, since present-day craton topography in our study area rises significantly higher than the pre-delamination topography reflected in Cretaceous uplift and present positive residual topography, the delaminated lithosphere must also have been denser than the subsequently formed thermal boundary layer. This proposal also

explains why “intact cratons” (e.g., WA and AZ) have lower topography than those that of "delaminated cratons" (e.g., SF, CG, and KH). More reasoning along this line is in the Method section. Our proposal contrasts with the traditional view that cratonic roots have approximately neutral buoyancy at all depths (Jordan, 1978; Carlson et al., 2005; Lee et al., 2011). We propose instead that the upper lithospheric mantle of cratons is highly depleted and chemically buoyant, perhaps even more so than has been yet inferred from mantle xenoliths (Lee et al., 2011; Griffin et al., 2003). In intact cratons, the lower lithospheric mantle is more fertile, grades downward into a purely thermal boundary layer, which contains zones or layers (>200 km in depth) enriched in high-density minerals (Fig. 5.5**a**).

Our model is consistent with the occurrence of garnet-peridotite in lower portions of intact cratons, such as Slave and pre-Cenozoic KH cratons (Carlson et al., 2005; Lee et al., 2011; Read et al., 2004; Griffin et al., 2003), and with high seismic velocities in the average lowermost (150-250 km) cratonic lithosphere (Adams and Nyblade, 2011). Assuming a 50-km thickness of this high-density layer, the residual topography and gravity (Fig. 5.2) require 20% excess garnet-peridotite relative to a neutrally buoyant lowermost lithosphere, if the density of garnet-peridotite is ~10% higher than that of peridotite (Lee et al., 2011). We propose that this high-density layer may have been emplaced during craton formation (Walter, 1998) and/or represents secular accumulation of basaltic melts from the deep mantle (Rader et al., 2015).

Our lithosphere-density model also explains several enigmatic properties of the prominent upper-mantle high velocity seismic anomalies below the south Atlantic (Figs. 5.3, D.5). These include the presence of such anomalies in regions far away from subduction zones. Notably, delaminated lithosphere consisting of both dense garnet-peridotite and buoyant harzburgite (Fig. 5.5**b**) should have small initial negative buoyancy whose magnitude would also decrease with depth as temperature increases. A delayed post-garnet transformation within the warming delaminated root at 660-km depth (Stixrude and Lithgow-Bertelloni, 2011) would generate additional positive buoyancy and further prohibit penetration into the lower mantle. This concept explains, first, the stagnation of the delaminated materials at the base of the upper mantle (Figs. 5.3, 5.5**c**), and, second, their minimal net buoyancy, thus avoiding generation of local convection as required by seismic anisotropy (Figs. D.10, D.11). Finally, the high seismic velocities of these

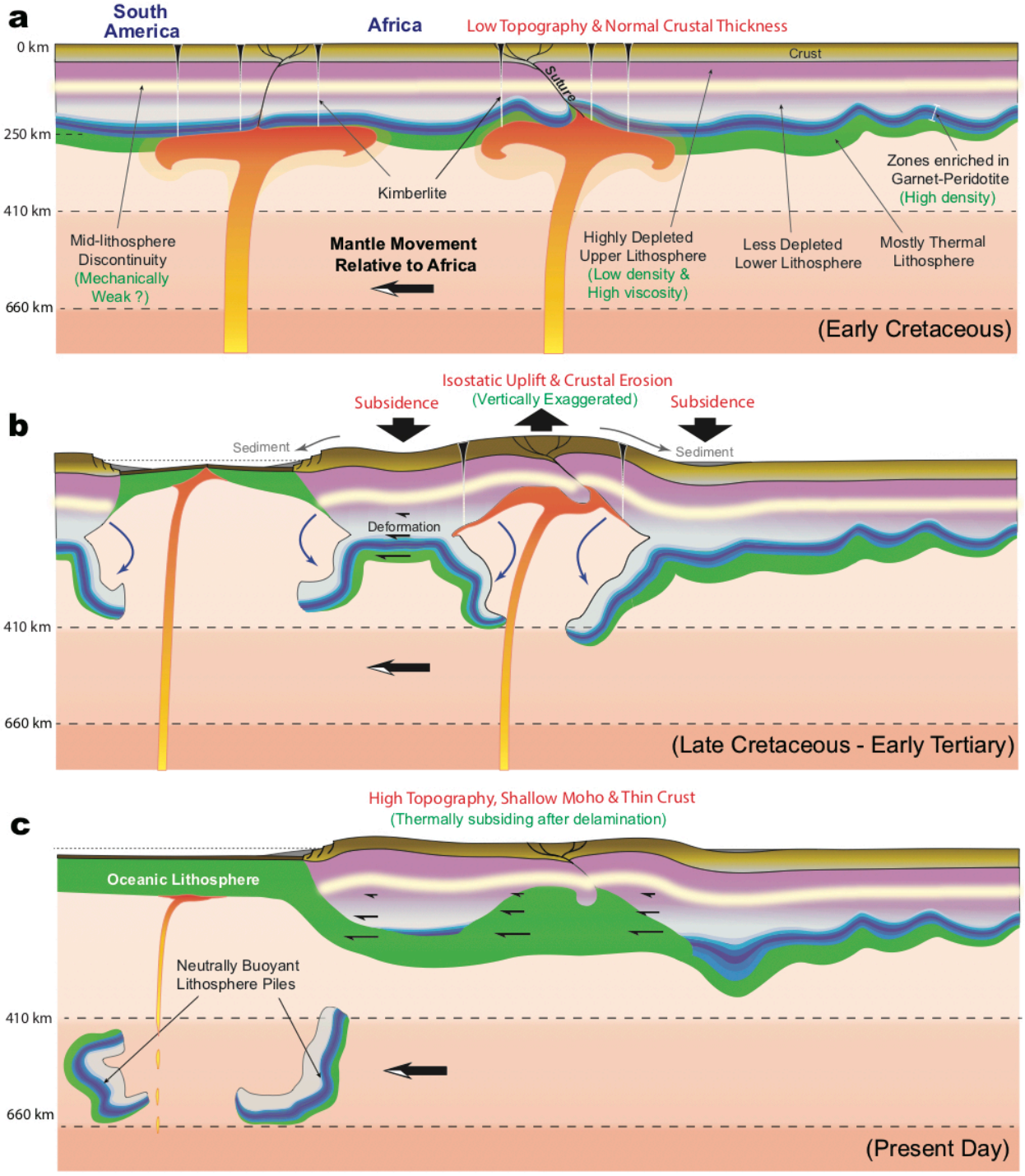

Figure 5.5. Schematic illustration of proposed cratonic lithosphere evolution since the Cretaceous. **a**) Sustained plume activity weakens the intact cratonic lithosphere by warming and metasomatism, forming kimberlites. **b**) Removal of deep mantle lithosphere including the garnet-peridotite layer and some harzburgite lithosphere. Both the surface and the Moho uplift isostatically, with erosion causing crustal thinning. **c**) Both internal shear of the lithosphere below the mid-lithosphere discontinuity and growth of a new thermal boundary in regions of delamination record recent mantle

Figure 5.5. (cont.)

deformation with seismic anisotropy. The foundered lithosphere segments stagnate above the lower mantle due to their overall neutral buoyancy. Both high topography and shallow Moho reflect the lower density of the new thermal lithosphere compared to the intact lithosphere.

anomalies (Figs. 5.3, D.5) are consistent with the enrichment of harzburgite and garnet at relatively low temperatures (Fig. D.9). We note that the minimum depth (~100 km) of anisotropy realignment broadly correlates with the mid-lithospheric discontinuities (MLDs) commonly found beneath continents (Liu et al., 2016; Wittlinger and Farra, 2007; Sodoudi et al., 2013; Selway et al., 2015; Fischer et al., 2010). This correlation implies that the MLD may represent a mechanically weak layer inside the lithosphere, below which shear deformation (>100 km) and ultimately delamination (>150-200 km) could occur more easily than in the lithosphere layer above. This conclusion is consistent with recent suggestions that the MLD represents the top of a weak layer of solidified volatile-rich melt accumulation (Rader et al., 2015; Chen et al., 2014). Such a weak layer could serve as a decoupling surface between the upper and lower lithospheres during extension (Liao et al., 2013), and thereby could facilitate mobilization and delamination of dense deep lithosphere (Fig. 5.5).

Taken together, results presented in this paper indicate that lowermost cratonic mantle lithosphere may be episodically removed when sufficiently perturbed by mantle processes (Fig. 5.5**b**), while the depleted buoyant lithosphere tends to remain stable so that its crust maintains cratonic characteristics through geological time (Fig. 5.5**c**). Figure 5.5 emphasizes the key features of cratonic lithosphere destabilization, during which deformation and removal of the dense root facilitates kimberlite volcanism (Harman et al., 1998; Hanson et al., 2009; Cogné et al., 2011; Read et al., 2004; Stanley et al., 2013), isostatic surface uplift (Figs. 5.1, 5.2**a**), and shallow Moho and thin crust (Fig. D.1**a**). We further propose that zones where lower lithosphere was removed take tens of millions of years to recover thermally, but the density of the new thermal root would remain less than that of the intact root. Indeed, cratons lacking Phanerozoic hotspot activity and nearby subduction, such as those in the northern hemisphere, have not undergone delamination since the Mesozoic and therefore display negative residual topography (Fig. D.14**a**) and positive mantle gravity anomalies (Fig. D.14**b**) in contrast to cratons affected by subduction, such as those in East Asia (Griffin et al., 1998) and western North America (Levander et al., 2011), and cratons affected by mantle plumes, such as those in the southern hemisphere (Fig. D.13).

5.7 References

Adams, A., and A. Nyblade, Shear wave velocity structure of the southern African upper mantle with implications for the uplift of southern Africa. Geophys. J. Int., 186(2), 808-824 (2011).

Alkmim, F.F., S. Marshak, A.C. Pedrosa-Soares, G.G. Peres, S.C.P. Cruz, A. Whittington, Kinematic evolution of the Araçuaí-West Congo orogen in Brazil and Africa: Nutcracker tectonics during the Neoproterozoic assembly of Gondwana, Precam. Res., 149, 43-64 (2006).

Arai, M., Chapadas: relict of mid-Cretaceous interior seas in Brazil, in Revista Brasileira de Geociencias 30, 436-438 (2000).

Artemieva, I., Global 1 degrees x 1 degrees thermal model TC1 for the continental lithosphere: Implications for lithosphere secular evolution, Tectonophys., 416, 245-277 (2006).

Assumpção, M., M. Feng, A. Tassara, J. Julià, Models of crustal thickness for South America from seismic refraction, receiver functions and surface wave tomography, Tectonophy., 609, 82-96 (2013).

Bonvalot, S., Balmino, G., Briais, A., M. Kuhn, Peyrefitte, A., Vales, Biancale, R., Gabalda, G., Moreaux, G., Reinquin, F. Sarrailh, M. World Gravity Map, 1:50000000 map, Eds. : BGI-CGMW-CNES-IRD, Paris (2012).

Carlson, R. W., Pearson, D. G. & James, D. E. Physical, chemical, and chronological characteristics of continental mantle. Rev. Geophys. 43, doi: 10.1029/ 2004rg000156 (2005).

Catuneanu, O., H. Wopfner, P.G. Eriksson, B. Cairncross, B.S. Rubidge, R.M.H. Smith, P.J. Hancox, The Karoo basins of south-central Africa, J. African Earth Sci., 3, 211-253 (2005).

Chen, L., M. Jiang, J. Yang, Z. Wei, C. Liu, and Y. Ling, Presence of an intralithospheric discontinuity in the central and western North China Craton: Implications for destruction of the craton, Geology, 42, 223-226 (2014).

Cogné, N., K. Gallagher, and P.R. Cobbold, Post-rift reactivation of the onshore margin of southeast Brazil: Evidence from apatite (U-Th)/He and fission-track data, Earth Planet. Sci. Lett., 309, 118-130 (2011).

Conrad, C.P., and Husson, L., Influence of dynamic topography on sea level and its rate of change, Lithosphere, 1, 110-120 (2009).

Courtillot, V., A. Davaille, J. Besse, J. Stock, Three distinct types of hotspots in the Earth's mantle, Earth Planet. Sci. Lett., 205, 295-308 (2003).

Dalton, C.A., X. Bao, & Z. Ma, The thermal structure of cratonic lithosphere from global Rayleigh wave attenuation, Earth Planet. Sci. Lett., 457, 250-262 (2017).

Debayle E, Kennett B L N. The Australian continental upper mantle: structure and deformation inferred from surface waves [J]. Journal of Geophysical Research: Solid Earth, 2000, 105(B11): 25423-25450.

Debayle, E., F. Dubuffet, and S. Durand, An automatically updated S-wave model of the upper mantle and the depth extent of azimuthal anisotropy, Geophys. Res. Lett., 43, doi:10.1002/2015GL067329 (2016).

Durrheim, R. J., & W. D. Mooney, Evolution of the Precambrian Lithosphere: Seismological and geochemical constraints, J. Geophys. Res., 99, 15359-15374 (1994).

Eaton, D.W. and H.K.C. Perry, Ephemeral isopycnicity of cratonic mantle keels, Nature Geosci., 6, 967-970 (2013).

Feng, M., Assumpção, M., and Van der Lee, S., Group velocity tomography and lithospheric S-velocity structure of the South American continent, Phys. Earth Planet. Inter., 147, 315-331 (2007).

Fischer, Karen M., Ford, Heather A., Abt, David L., Rychert, Catherine A. The Lithosphere-Asthenosphere Boundary Annual Review of Earth and Planetary Sciences. 2010; 38 (1) : 551-575.

Flament, N., M. Gurnis, and R. D. Müller, A review of observations and models of dynamic topography, Lithosphere, 5, 189-210 (2012).

French, S., V. Lekic, & B. Romanowicz, Waveform tomography reveals channeled flow at the base of the oceanic asthenosphere, Science, 342(6155), 227-230 (2013).

Globig, J., M. Fernàndez, M. Torne, J. Vergés, A. Robert, and C. Faccenna, New insights into the crust and lithospheric mantle structure of Africa from elevation, geoid, and thermal analysis, J. Geophys. Res. Solid Earth, 121, 5389-5424, doi:10.1002/2016JB012972 (2016).

Griffin W. L., S. Y. O'Reilly, N. Abe, S. Aulbach, R. M. Davies, et al. The origin and evolution of Archean lithospheric mantle, Precambrian Res., 127, 19-41 (2003).

Griffin, W. L., and S. Y. O'Reilly, Chapter 8.2 The Earliest Subcontinental Lithospheric Mantle, in Developments in Precambrian Geology, edited by R. H. S. Martin J. van Kranendonk and C. B. Vickie, 1013-1035, Elsevier, doi:http://dx.doi.org/10.1016/S0166-2635(07)15082-9 (2007).

Griffin,W. L., Andi, Z., O'Reilly, S. Y. & Ryan, C. G. Phanerozoic evolution of the lithosphere beneath the Sino-Korean Craton. Mantle Dyn. Plate Interact. East Asia, 27, 107-126 (1998).

Guillocheau, F., D. Rouby, C. Robin, C. Helm, N. Rolland, L. Carlier, C. de Veslud, and J. Braun, Quantification and causes of the terrigeneous sediment budget at the scale of a continental margin: A new method applied to the Namibia-South Africa margin, Basin Res., 24, 3-30 (2012).

Hanson, E.K., Moore, J.M., Bordy, E.M., Marsh, J.S., Howarth, G., and Robey, J.V.A., Cretaceous erosion in central South Africa: Evidence from upper-crustal xenoliths in kimberlite diatremes, South African J. Geol., 112, 125-140 (2009).

Harman, R., K. Gallagher, R. Brown, A. Raza, and L. Bizzi, Accelerated denudation and tectonic/geomorphic reactivation of the cratons of northeastern Brazil during the Late Cretaceous, J. Geophys. Res., 103, 27091-27105 (1998).

Hu, J., M. Faccenda and L. Liu, Subduction-controlled mantle flow and seismic anisotropy in South America, Earth Planet. Sci. Lett., 470, 13-24 (2017).

Jordan, T. H., Composition and development of the continental tectosphere, Nature, 274, 544-548 (1978).

Kaban, M. K., W. D. Mooney and A. G. Petrunin, Cratonic root beneath North America shifted by basal drag from the convecting mantle, Nature Geosci., 8, 797-800 (2015).

Kaban, M.K., P. Schwintzer, I. M. Artemieva, W.D. Mooney, Density of the continental roots: compositional and thermal contributions, Earth Planet. Sci. Lett., 209, 53-69 (2003).

King, S. & J. Ritsema, African Hot Spot Volcanism: Small-Scale Convection in the Upper Mantle Beneath Cratons, Science, 290, 1137-1140 (2000).

King, S. D. Archean cratons and mantle dynamics. Earth Planet. Sci. Lett. 234, 1-14 (2005).

Kopylova, M. G., and G. Caro, Mantle Xenoliths from the Southeastern Slave Craton: Evidence for Chemical Zonation in a Thick, Cold Lithosphere, J. Petrology, 45(5), 1045-1067 (2004).

Laske, G., G. Masters, Z. Ma, and M. Pasyanos, Update on CRUST1.0 - A 1-degree Global Model of Earth's Crust, Geophys. Res. Abstracts, 15, Abstract EGU2013-2658 (2013).

Lee, C.-T. A., Luffi, P. & Chin, E. J. Building and destroying continental mantle, Annu. Rev. Earth Planet. Sci. 39, 59-90 (2011).

Levander, A., B. Schmandt, M. S. Miller, K. Liu, K. E. Karlstrom, R. S. Crow, C. T. Lee, and E. D. Humphreys, Continuing Colorado plateau uplift by delamination-style convective lithospheric downwelling, Nature, 472, 461-465 (2011).

Liao, J., Gerya, T., Wang, Q., Layered structure of the lithospheric mantle changes dynamics of craton extension, Geophys. Res. Lett., 40, 5861- 5866 (2013).

Liu, L., K. Liu and S. Gao, Lithospheric layering beneath southern Africa constrained by S-to-P receiver functions, AGU abstract DI51A-2660 (2016).

Masters, G., G. Laske, H. Bolton, A. Dziewonski, The Relative Behavior of Shear Velocity, Bulk Sound Speed, and Compressional Velocity in the Mantle: Implications for Chemical and Thermal Structure, AGU Monograph 117 (2000).

McNamara, A. and S. Zhong, Thermochemical structures beneath Africa and the Pacific Ocean, Nature, 437, 1136-1139 (2005).

Mooney, W.D. and M.K. Kaban, The North American upper mantle: Density, composition, and evolution, J. Geophys. Res., 115, B12424 (2010).

Moucha, R. & A.M. Forte, Changes in African topography driven by mantle convection, Nature Geosci., 4, 707-712 (2011).

Müller, R.D., M. Seton, S. Zahirovic, S.E. Williams, K.J. Matthews, N.M. Wright, G.E. Shephard, K.T. Maloney, N. Barnett-Moore, M. Hosseinpour, D.J. Bower, J. Cannon, Ocean basin evolution and global-scale plate reorganization events since Pangaea breakup, Annu. Rev. Earth Planet. Sci., 44, 107-138 (2016).

Ni, S., E. Tan, M. Gurnis, D. Helmberger, Sharp sides to the African superplume, Science, 296, 1850-1852 (2002).

Pasyanos, M. E., T. G. Masters, G. Laske, and Z. Ma, LITHO1.0: An updated crust and lithospheric model of the Earth, J. Geophys. Res., 119, 2153-2173, doi:10.1002/2013JB010626 (2014).

Priestley, K., and D. McKenzie, The relationship between shear wave velocity, temperature, attenuation and viscosity in the shallow part of the mantle. Earth and Planet. Sci. Lett., 381, 78-91 (2013).

Rader, E., E. Emry, N. Schmerr, D. Frost, C. Cheng, J. Menard, C. Yu, and D. Geist, Characterization and Petrological Constraints of the Midlithospheric Discontinuity, Geochem. Geophys. Geosys., 16, 3484-3504 (2015).

Read, G., H. Grutter, S. Winter, N. Luckmand, F. Gaunt, F. Thomsen, Stratigraphic relations, kimberlite emplacement and lithospheric thermal evolution, Quiricó Basin, Minas Gerais State, Brazil, Lithos, 77, 803-818 (2004).

Reid, A.B., J. Ebbing and S.J. Webb, Comment on 'A crustal thickness map of Africa derived from a global gravity field model using Euler deconvolution' by Getachew E. Tedla, M. van der Meijde, A. A. Nyblade and F. D. van der Meer, Geophys. J. Int., 189, 1217-1222 (2012).

Ritsema, J., A. Deuss, H.J. van Heijst, & J.H. Woodhouse, S40RTS: a degree-40 shear-velocity model for the mantle from new Rayleigh wave dispersion, teleseismic traveltime and normal-mode splitting function measurements. Geophys. J. Int., 184(3), 1223-1236 (2011).

Schaeffer, A.J., S. Lebedev, T.W. Becker; Azimuthal seismic anisotropy in the Earth's upper mantle and the thickness of tectonic plates, Geophys. J. Int., 207, 901-933 (2016).

Selway, K., H. Ford, and P. Kelemen, The seismic mid-lithosphere discontinuity. Earth Planet. Sci. Lett., 414, 45-57 (2015).

Shephard, G.E., R.D. Müller, L. Liu, M. Gurnis, Miocene drainage reversal of the Amazon River driven by plate-mantle interaction, Nature Geosci., 3, 870-875 (2010).

Simmons, N. A., A. M. Forte, and S. P. Grand, Joint seismic, geodynamic and mineral physical constraints on three-dimensional mantle heterogeneity: Implications for the relative importance of thermal versus compositional heterogeneity, Geophys. J. Int., 177, 1284-1304 (2009).

Sodoudi, F., X. Yuan, R. Kind, S. Lebedev, J. M. C. Adam, E. Kästle, E., and F. Tilmann, Seismic evidence for stratification in composition and anisotropic fabric within the thick lithosphere of Kalahari Craton. Geochem. Geophys. Geosys., 14(12), 5393-5412 (2013).

Stanley, J.R., R.M. Flowers, and D.R. Bell, Kimberlite (U-Th)/He dating links surface erosion with lithospheric heating, thinning, and metasomatism in the southern African Plateau, Geology, 41, 1243-1246 (2013).

Steinberger, B., Effects of latent heat release at phase boundaries on fl ow in the Earth's mantle, phase boundary topography and dynamic topography at the Earth's surface, Physics of the Earth and Planetary Interiors, 164, 2-20 (2007).

Stixrude, L., Lithgow-Bertelloni, C., Thermodynamics of mantle minerals -II. Phase equilibria. Geophys. J. Int. 184, 1180-1213 (2011).

Walter, M.J., Melting of Garnet Peridotite and the Origin of Komatiite and Depleted Lithosphere, J. Petrol., 39, 29-60 (1998).

Wang, H., J. van Hunen & D.G. Pearson. The thinning of subcontinental lithosphere: the roles of plume impact and metasomatic weakening. Geochem. Geophys. Geosys., DOI: 10.1002/2015GC005784 (2015).

Wittlinger, G., and V. Farra, Converted waves reveal a thick and layered tectosphere beneath the Kalahari super-craton. Earth and Planet. Sci. Lett., 254(3), 404-415 (2007).

Yaxley, G.M., V.S. Kamenetsky, G.T. Nichols, R. Maas, E. Belousova, A. Rosenthal & M. Norman, The discovery of kimberlites in Antarctica extends the vast Gondwanan Cretaceous province, Nature Comm., 4, 2921, DOI: 10.1038/ncomms3921 (2013).

Yuan, H., & Romanowicz, B., Lithospheric layering in the North American craton, Nature, 466(7310),1063-1069 (2010).

Yuan, K. and C. Beghein, Seismic anisotropy changes across upper mantle phase transitions, Earth. Planet. Sci. Lett., 374, 132-144 (2013).

Chapter 6

Broader Implications and Discussions

6.1 The Central Andean orogenic system

The Cenozoic Andean orogenic system is characterized by rapid shortening, stage-wise surface uplift, high magmatic flux and episodes of flat slabs (Oncken et al., 2006; Decelles et al., 2009) (Fig. 6.1). Several models have been proposed to construct the deformation history of central Andes (e.g. Arriagada et al., 2008; Eichelberger et al., 2013). According to these models, the shortening in central Andes started in early Eocene, with the shortening front shifted from East Cordillera at about 20 Ma to subandean Ranges at about 10 Ma. The shortening rate was relative small before 30 Ma. It increased significantly at 30 Ma and has remained large since then (Fig. 6.1b, Oncken et al., 2006). The amount of shortening tapers off towards both ends of the trench.

The temporal-spatial variations of magmatic activity for the past 60 Myr are well constrained (Thrumbull et al., 2006). Before ~25 Ma, there was no magmatic activity at 14-20°S, which might correspond to the Altiplano flat slab, while south of 20°S, the volcanism formed a narrow, regular magmatic arc. Since ~25 Ma, abrupt landward broadening of volcanic activities took place along the entire central Andes, accompanied by extensive and massive ignimbrite flare-ups. Different explanations have been proposed for this episode of high volcanic flux, including removal of flat slabs (e.g. Humphreys, 2009), subduction erosion (e.g. Kukowski and Oncken, 2006) and lithosphere delamination (e.g. DeCelles et al., 2009). These magmatic activities provide many implications on the underlying geodynamic processes.

The topographic evolution of the orogenic system, compared to its shortening and volcanism, is less well constrained. In central Andes, different portions of the Altiplano-Puna plateau may have gained their elevation at different times (Fig. 6.1c, Eichelberger et al., 2015). However, the first-order observations such as the average height and the width of the plateau is of interest for geodynamic models (Capitanio et al., 2011; Chen et al., 2017). In addition, other processes such as the drying up of the inland Pebas system, the drainage reversal of the Amazon river, the uplift of the Sierras Pampeanas and the uplift of Patagonia have all been related to mantle

dynamics (Flament et al., 2015). These processes can be used as powerful constraints for geodynamic models.

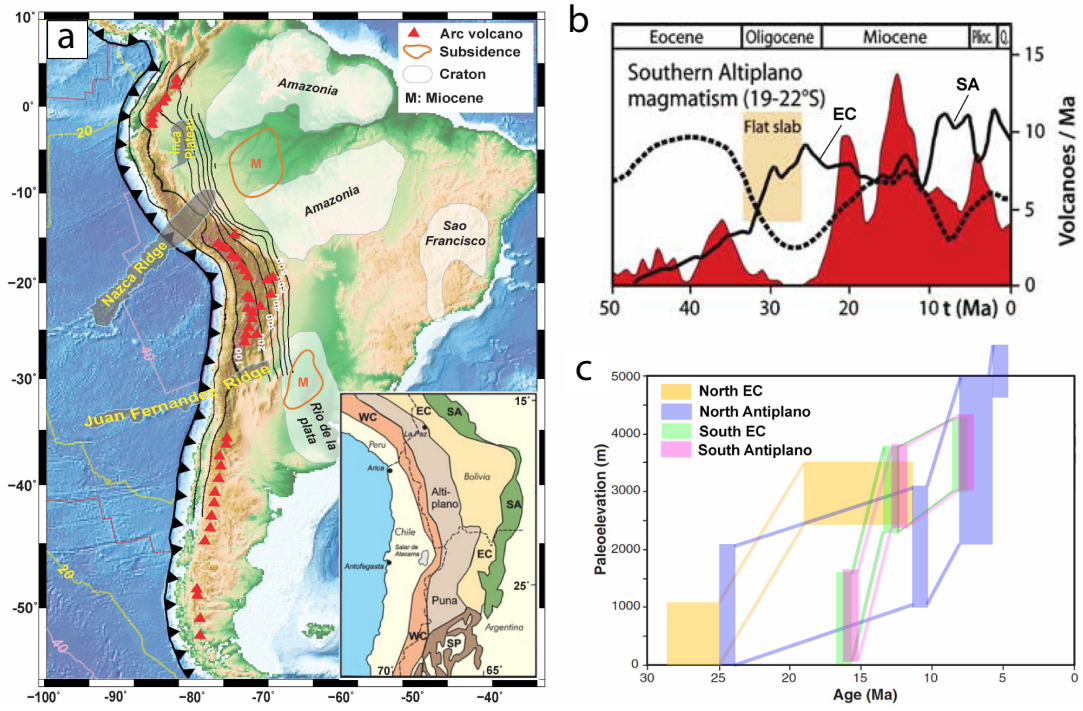

Figure 6.1. a) Tectonic settings of South America. Background color shows the topography of South America, with cratons outlined by semi-transparent white regions and Miocene basins delineated by red lines. The slab geometry is presented by Benioff zone with depth contours (black lines). b) The variation of magmatic production (red region), shortening rates (solid line) and slab dip angle (dashed line) with time over the past 50 Myr (from Oncken et al., 2006). c) Uplift histropy of Andean plateau constrained by oxygen isotopes and Δ_{47} paleothermometry (from Eichelberger et al., 2015).

Despite the intensive study on Andean-style orogeny, a lot of fundamental questions remain unsolved. Among them, the most significant ones include what have caused the central Andean shortening starting at ~50 Ma and whether and how it is related to the subsequent events such as the development of the high plateau, the intensive magmatism, the evolution of multiple sedimentary basins and the occurrence of flat slabs.

Various geodynamic models have been proposed to explain the central Andean shortening and the concave margin of South America. Schellart et al. (2007) has shown that for a wide slab, trench retreat rate increases from the center toward the edges of the slab, resulting in a concave trench. However, Capitanio et al. (2011) argued that when the age of the subducting plate is not uniform and gets older from the edges towards the center, the trench would develop a convex geometry, opposite to that observed in South America. To reconcile this discrepancy, a thick overriding plate is required (Capitanio et al., 2011). On the contrary, Faccenna et al. (2017)

proposed that the shortening in the Andes is caused by the slab anchoring inside the lower mantle, instead of slab age or continental thickness. There are many more models related to other aspects of the Andean orogeny, such as the formation of flat slabs (O'Driscroll et al., 2009; Manea et al., 2012; Hu et al., 2016), flat slab-South American plate interaction (Dávila et al., 2010; O'Driscroll et al., 2012) and lithospheric delamination processes (Beck et al., 2014; Currie et al., 2015; DeCelles et al., 2014).

Most of the earlier studies are either conceptual or idealized models that cannot be directly compared with the specific geological records, which makes it hard to verify their correctness. On the contrary, a geodynamic model with data assimilation could potentially reconcile these controversies. With constraints from central Andean shortening, magmatic activities and plateau uplift, a data-oriented geodynamic model could most likely explain the processes that have occurred in the orogenic system.

For example, based on the previous models, we formulate a geodynamic model with hybrid velocity boundary condition. Fig. 6.2 shows the topographic evolution of the preliminary results. The model predicts the onset of Andean shortening at ~50 Ma, consistent with observation. This is the time when the slab enters the lower mantle, which supports the proposition by Faccenna et al. (2017) to the first-order. However, the shortening mostly occurs in the northern half of the trench, rather than in central Andes, and the amount of shortening is also over-predicted. This suggest other processes that are not considered in this model have played a role in the shortening history. More models are needed to better explain the exact shortening history.

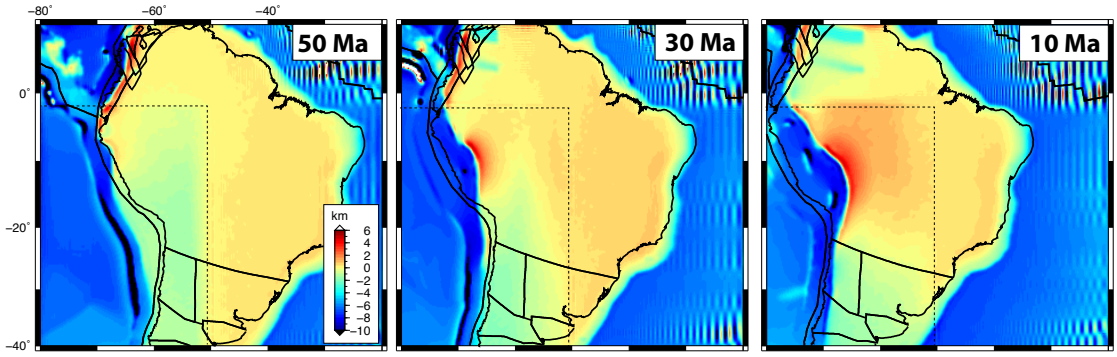

Figure 6.2. Topographic evolution of the preliminary results. Background color represents topography. The strong oscillation outside the dashed box are numerical artifacts associated with the imposed velocity boundary condition. Readers should focus on the region within the box whose solution is more robust due to a free-slip boundary condition applied here.

6.2 Wrapping everything up: A global convection model[5]

6.2.1 Introduction

While our regional models can explain many tectonic features in South America, it is important to extend the technique to a global model where some subduction systems are much more complex than that in South America. In addition, global models have obvious advantages in resolving large-scale, whole-mantle dynamics over regional models. For example, global models do not have artificial vertical walls as those in regional ones, thus are more reliable if the far-field influences are significant.

However, the computational power has been a rate-limiting factor. By now, published global time-dependent models (McNarama and Zhong, 2005; Foley and Becker, 2009; Crameri et al., 2012; Coltice et al., 2012; Bello et al., 2015; Bower et al., 2015) largely fall into two categories. The first category adopts a free-slip upper surface with self-merging plate motion (e.g. Crameri et al., 2012; Coltice et al., 2012). These models are often used to investigate the physical properties that control the plate behavior (Mallard et al., 2016; Coltice et al., 2012). Another category of models assimilates plate motion on the surface that guide subduction over time (e.g. McNarama and Zhong, 2005; Bello et al., 2015; Bower et al., 2015). These models, although not fully dynamic, are geographically oriented and better for studying real Earth processes, such as the evolution of LLSVPs (McNarama and Zhong, 2005), the motion of hotspots (Hassan et al., 2016) and the topographic evolution (Flament et al., 2014). However, most of these models could not simultaneously generate all realistic subduction characteristics, including single-sided subduction, temporally varying slab dip angle, complex slab deformation and tearing, realistic mantle flow, and the present-day mantle structures.

---

[5]This section is based on: Hu, J., Liu, L., & Zhou, Q. (2018). *Reproducing Past Subduction and Mantle Flow Using High-Resolution Global Convection Models*. Earth and Planetary Physics, 2(3), 189-207.

In this section, we upgrade the techniques used in previous regional models and present a high-resolution global mantle convection model since the mid-Mesozoic using an adaptive approach of sequential data assimilation. In this model, we incorporate a relatively realistic rheology, including temperature- and depth-dependent viscosity, composition-based weak oceanic crust and arc-like plate boundary features, all ensuring the generation of realistic subduction. Relative to published works of its kind, our model could better represent the evolution and morphology of slabs, especially at upper mantle depths. Consequently, this will allow us to better investigate the local-scale subduction dynamics, the temporal evolution of mantle deformation, and the origin and implication of mantle seismic structures, for the global Earth.

6.2.2 Method

We simulate global subduction since 150 Ma using the sequential data-assimilation technique (Liu and Stegman, 2011; Hu et al., 2016). Compared to our previous work, this new model is more advanced in that it now assimilates thermal-chemical lithosphere and allows more realistic trench configuration and subduction dynamics including formation of new subduction zones and reversal of subduction polarity. The simulation was carried out using the 3D spherical finite element code CitcomS (Tan et al., 2006; Zhong et al., 2008). We assume that the mantle is incompressible and satisfies the Boussinesq approximation. The model covers the whole mantle domain, which is discretized into 12 caps, and each cap has 257×257×97 nodes. The model has a uniform lateral resolution, which is ~23 km. The vertical resolution varies with depth, and is finer as it approaches the surface (~12 km) and the core-mantle boundary (~20 km). The average resolution of this model is much higher than that in earlier similar studies. For example, the total number of grids is about 6 times higher than two recent global models (Bower et al., 2015; Bello et al., 2015). The model properly resolves the thermal-mechanical structure of the lithosphere, such as the weak oceanic crust, which is critical in generating single-sided subduction (Crameri et al., 2012).

6.2.2.1 Assimilating plate motion and thermal lithosphere

The model takes the plate motion from recent plate reconstruction of Müller et al. (2016) as the surface boundary condition (Fig. 6.3a). These data are processed using the open source paleo-geographic software GPlates (www.gplates.org/; Gurnis et al., 2012), and output at every Myr. At each model time step that is much smaller than 1 Myr, the surface velocity condition is

interpolated between two adjacent input conditions. The assimilation of plate motion ensures the slab subducts at the proper geographic location, which is important for matching the observed present-day slab geometry (Liu and Stegman, 2011) and the associated mantle flow (Hu et al., 2017).

We also assimilate and update the thermal structure of the lithosphere at each time step according to the reconstructed seafloor ages (Fig. 6.4a). In an oceanic lithosphere, we use a modified half-space cooling model to define its thermal structure:

$$T_l(z,t) = T_m \mathrm{erf}\left(\frac{z}{2A\sqrt{t/\kappa}}\right) \quad (1)$$

where T_l is lithosphere temperature, T_m mantle temperature, z depth, t seafloor age, κ thermal diffusivity and A modification factor as a function of t. As in most global models, the limited numerical resolution restricts its capability of reproducing real Earth convection vigor while maintaining a thin thermal boundary layer and subducting slabs (e.g., Davies et al., 2007). Therefore, we use a Rayleigh number of 2.6×10^8 (with the length scale being Earth's radius) and a non-dimensional mantle temperature of 0.7 that corresponds to 700 °C, about half of that of the real Earth. In order to maintain the buoyancy flux of the subducting oceanic plate and thus the correct convection vigor, we introduce an age-dependent modification factor A, which decreases the temperature gradient of the lithosphere, so that the depth integral of lithospheric thermal buoyancy equals that of the exact half-space cooling profile with a mantle temperature of 1300°. This way, we make sure the buoyancy of the subducting plates remains similar to that in real Earth, which is important for the study of mantle flow and associated surface expressions. Within the continental lithosphere, we assume an initial conductive thermal profile whose temperature increases from 0 on the surface to 0.5 at a depth of ~160 km (Fig. 6.4a). This way, interiors of the continental lithosphere eventually grows thicker than most oceanic plates, maintaining a quasi-steady state thermal structure (e.g., Fig. 6.6), similar to the real Earth (McKenzie et al., 2005).

To guarantee a smooth thermal profile extends from within the surface plates into the down-going slab, and to make sure other plate boundary properties like composition and viscosity could evolve self-consistently, we avoid updating the temperature of the subducting and overriding plates within 600 km horizontal distance from the trench. As discussed later, we also avoid updating the corresponding composition in the vicinity of the trench, such that tracer-carried

properties (density and viscosity) will behavior naturally over time. We name this an *adaptive data assimilation* approach.

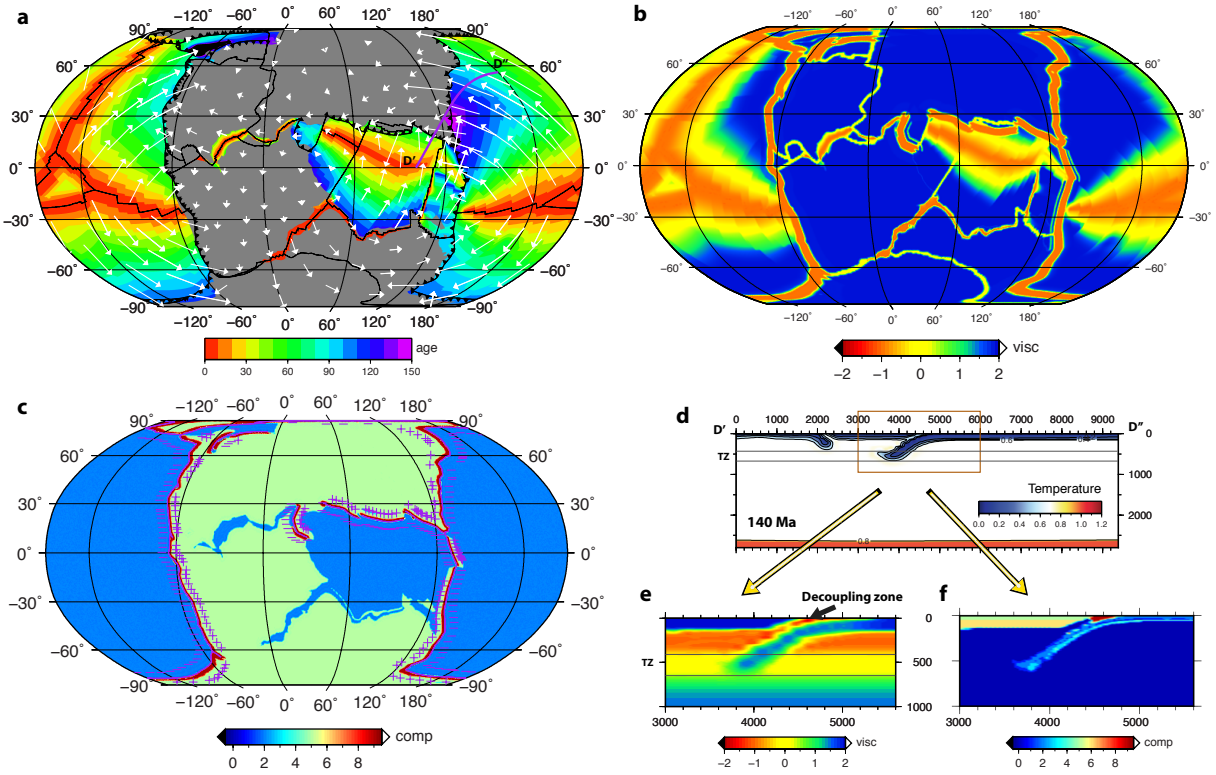

Figure 6.3. Model setup. (a) Imposed plate motion and seafloor age at 150 Ma from a recent plate reconstruction (Müller et al., 2016). The background color represents the seafloor age. Continents are shown in gray. White arrows indicate plate motion. The thick purple line marks the location of the cross section in (d), (e) and (f). (b) Viscosity field at 100 km depth at 150 Ma. (c) Composition field on the surface at 150 Ma. (d) A cross section that shows the temperature field at 140 Ma. Background color represents the non-dimensional temperature, on top of which the black lines are the temperature contours. The orange box outlines the region shown in e) and (f). (e) Viscosity structure at the subduction zone in (d) at 140 Ma. (f) Same as (e), but for the composition field.

6.2.2.2 Assimilating chemical composition

The lithosphere is assumed to be chemically stratified both in the oceanic and continental lithosphere. The buoyancy and viscosity associated with different compositions significantly affect the dynamics of the system (e.g. Crameri et al., 2012). In our model, the compositional density anomaly is defined using the ratio method:

$$B = \Delta\rho_{ch}/(\rho_0\alpha_0\Delta T) \quad (2)$$

where B is the buoyancy ratio (Table 6.1), an input parameter that varies with different compositions, $\Delta\rho_{ch}$ the compositional density anomaly, ρ_0 the reference density, α_0 the reference thermal expansivity and ΔT the maximum temperature contrast across the mantle. For the viscosity field, its effect due to composition is achieved through a multiplication factor that is a geometric mean for all the compositions within the element:

$$\mathrm{C} = \prod_i C_i^{r_i} \quad (3)$$

where C is a prefactor, C_i is the viscosity multiplier for composition i (Table 6.1), r_i is the fraction of composition i over the total elemental composition.

Table 6.1. Basic model parameters

Parameter	Symbol	Nondimensional value	Dimensional value	Units
Earth radius	R_0	1	6371e+3	m
reference density	ρ_0	-	3340.0	kg m^{-3}
thermal diffusivity	κ	-	1.0e-6	m^2 s^{-1}
gravitational acceleration	g	-	9.81	m s^{-1}
thermal expansivity	α_0	-	3.0e-5	K^{-1}
reference viscosity	η_0	1	1.0e+21	Pa s
Rayleigh number Ra	Ra	-	2.6e+08	-
Mantle temperature	T_m	0.7	700	K
Buoyancy ratios for compositions*	$B_1, B_2, B_3, B_4, B_5, B_6$	-	*-5.3, -0.5, -5.3, -1.0, 0.8*	-
Viscosity multipliers for compositions*	$C_1, C_2, C_3, C_4, C_5, C_6$	-	*0.0001, 1, 1, 0.0001, 1, 0.1*	-
Maximum viscosity cutoff	η_{max}	100	1.0e+23	Pa s
Minimum viscosity cutoff	η_{min}	0.01	1.0e+19	Pa s

* Composition 1 to 6 are weak oceanic crust, continental crust, continental lithosphere, arc-like structure, buoyant layer within the oceanic plates and thermal-chemical layer above CMB, respectively. Refer to Fig. 3 for composition 1 to 5.

Within the oceanic plates, we define two chemical layers distinct from the ambient mantle: a weak crustal layer and a buoyant layer (Fig. 6.3c, f). The former represents the uppermost portion of the oceanic plate and has a thickness of ~25 km. This layer is neutrally buoyant but has a low viscosity at 10^{19} Pa · s, which acts as a lubricating layer to decouple the subducting plate from the overriding plate (Fig. 6.3e; Crameri et al., 2012). However, since we impose the surface velocities, we turn off this viscosity effect beyond 200 km away from the subduction zone on the side of the subducting plate. We also assimilate a buoyant layer within the oceanic plates at a depth of 40-60 km. This layer has a buoyancy ratio of -1.0. The total buoyancy of this layer is similar to that of an oceanic crustal layer with a thickness of 7 km and a density of 3.0 g/cm^3. Effectively, this layer carries the buoyancy of the oceanic crust, but avoids getting accreted to the upper plate during subduction since it is within the relatively strong slab. We also assimilate the thickened crust of some aseismic ridges and oceanic plateaus, such as those on the Nazca plate (Hu et al., 2016).

We approximate the continental plate as two compositional layers, the crust and the mantle lithosphere (Fig. 6.3f). The crust extends from 0 to 38 km depth and has a buoyancy ratio of -5.3, while the mantle lithosphere extends from 38 km to 160 km depth and has a buoyancy ratio of -0.5. The buoyancy ratio of the crust is consistent with a mean density of 2.8 g/cm^3, while that of the mantle lithosphere largely cancels out that of the thermal effect, resulting in a neutrally buoyant lithosphere. For simplicity, we neglect the possible viscosity and density layering of the cratonic lithosphere. When a new subduction zone forms, an arc-like weak zone on the overriding side will be created, in order to facilitate the formation of the new trench (Fig. 6.3c, f). This tracer-defined arc has a buoyancy ratio of -5.3 and a viscosity of 10^{19} Pa · s, mimicking those of the arcs in real Earth. It helps to decouple the two plates on both sides of the subduction zone during subduction. In addition, to allow the composition of the mantle wedge to evolve self-consistently, we do not assimilate the composition of the overriding plate > 600 km away from the trench.

At the initial time step, we also define a uniform thermal-chemical layer above the core-mantle boundary (CMB), which represents the source of the LLSVPs beneath Africa and Pacific. This layer initially has a thickness of 250 km, a buoyancy ratio of 0.8 and a viscosity multiplier of 0.1, and the temperature is 500 °C higher than the ambient mantle. It eventually evolves into two thermal-chemical piles after 150 Myr, similar to findings in previous studies (e.g. McNamara and Zhong, 2005).

6.2.2.3 Viscosity structure

The viscosity of this model is depth-, temperature- and composition-dependent (Fig. 6.3b, e). The radial variation of viscosity for the initial condition is shown beneath both continental and oceanic plates (Fig. 6.4b). In these viscosity profiles, we use a strong lithosphere whose viscosity reaches 10^{23} Pa · s, and a relatively weak asthenosphere whose viscosity is 10^{20} Pa · s. The viscosity increases from the asthenosphere to the transition zone, and then to the middle lower mantle with a maximum of 10^{23} Pa · s. Then it decreases to 2×10^{20} Pa · s as it approaches the CMB. This radial viscosity profile is similar to those constrained by geophysical inversions (e.g. Steinberger and Calderwood, 2006) and by reproducing present slab geometry (e.g. Hu et al., 2016). The existence of slabs, weak crustal layer, arc-like weak zones, thermal-chemical piles and the variation of lithosphere thickness introduces significant lateral viscosity variations (Fig. 6.3b, e), which reach 4 orders of magnitude, ranging from 10^{19} to 10^{23} Pa · s. This lateral viscosity variation

is critical in generating Earth-like plate subduction. In addition, we reduce the viscosity of the slab hinge by imposing a maximum viscosity cut-off at $2.5 \times 10^{22} \mathrm{Pa} \cdot \mathrm{s}$, to mimic the effect of plastic yielding (Billen and Hirth, 2007).

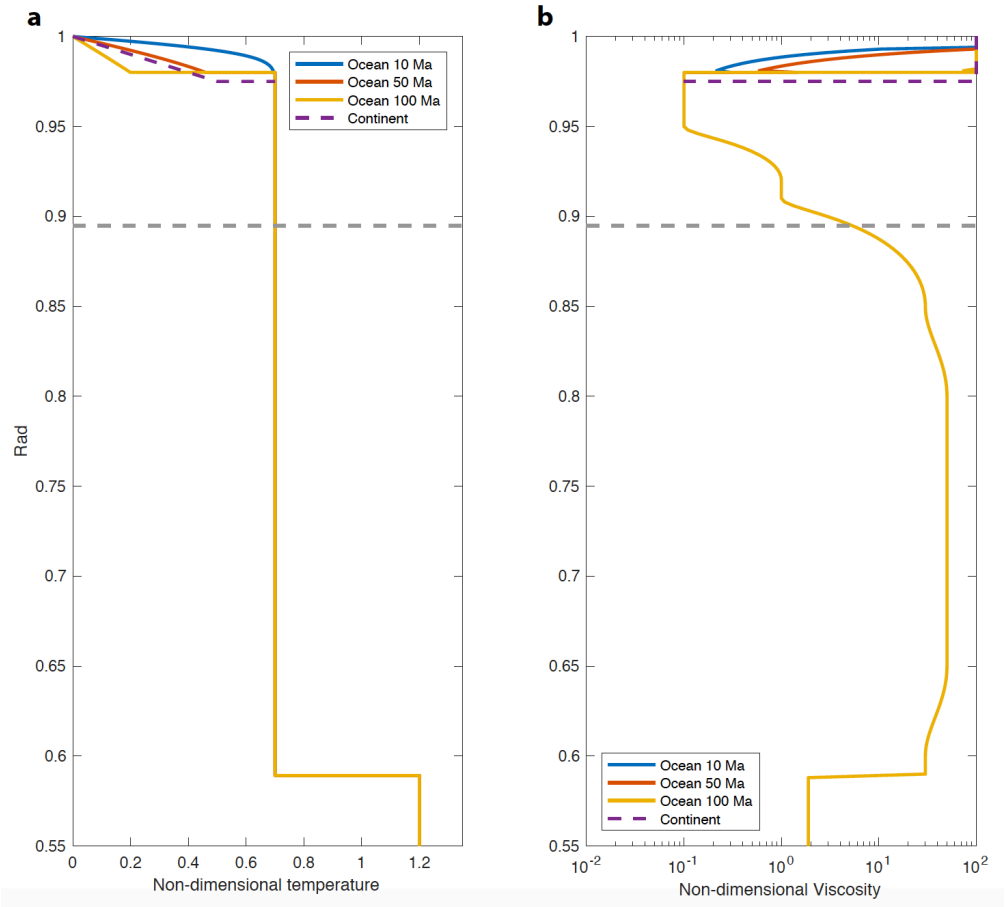

Figure 6.4. (a) Initial radial temperature profiles for different regions. Blue, red and orange lines represent the non-dimensional temperature profiles beneath the ocean with an age of 10, 50 and 100 Ma, respectively. The dashed line represents that of the continents. (b) Same as (a), but for initial radial viscosity profiles.

6.2.3 Results

As stated earlier, published global models using data assimilation do not always produce realistic upper mantle processes. In this section, we present several examples on how the complex subduction dynamics is realized in our model, including formation of a new subduction system and subduction polarity reversal. Then, we will show the predicted present-day slab structure and further compare with seismic observations. Importantly, our model reproduces the past evolution

of subduction and mantle flow, which are useful for better connecting tectonic/geologic phenomena with relevant deep mantle processes. Examples include the formation of abnormal subduction like the Farallon flat slab and the evolving 3D mantle flow.

6.2.3.1 Simulating complex subduction dynamics

The Earth's subduction history is very complex. For example, a number of trenches have formed during the past 150 Myr, along with several events of subduction polarity reversal (Müller et al., 2016). In addition, some trenches migrate very fast, such as the South Sandwich Trench in the east of Scotia Sea (Barker, 2001). Sometimes trenches interact with each other, resulting in a complex situation such as those surrounding the Philippine Sea Plate (Wu et al., 2016). Modeling the appearance, disappearance and changing morphology of trenches have been challenging for geodynamic models, even if with imposed surface kinematics such as done in regional models (Liu and Stegman, 2011; Hu et al., 2016). This is because modeling Earth-like subduction with complex trench kinematics requires both high numerical resolution and sophisticated rheology, neither of which is practical in global simulations. To overcome such difficulties, some earlier models adopted a "slab assimilation" approach where the morphology, thermal structure and sinking velocity of slabs are imposed down to upper mantle depths (Bower et al., 2015). Obviously, these kinematic prescriptions limit the models' capability to capture the dynamics associated with slab evolution.

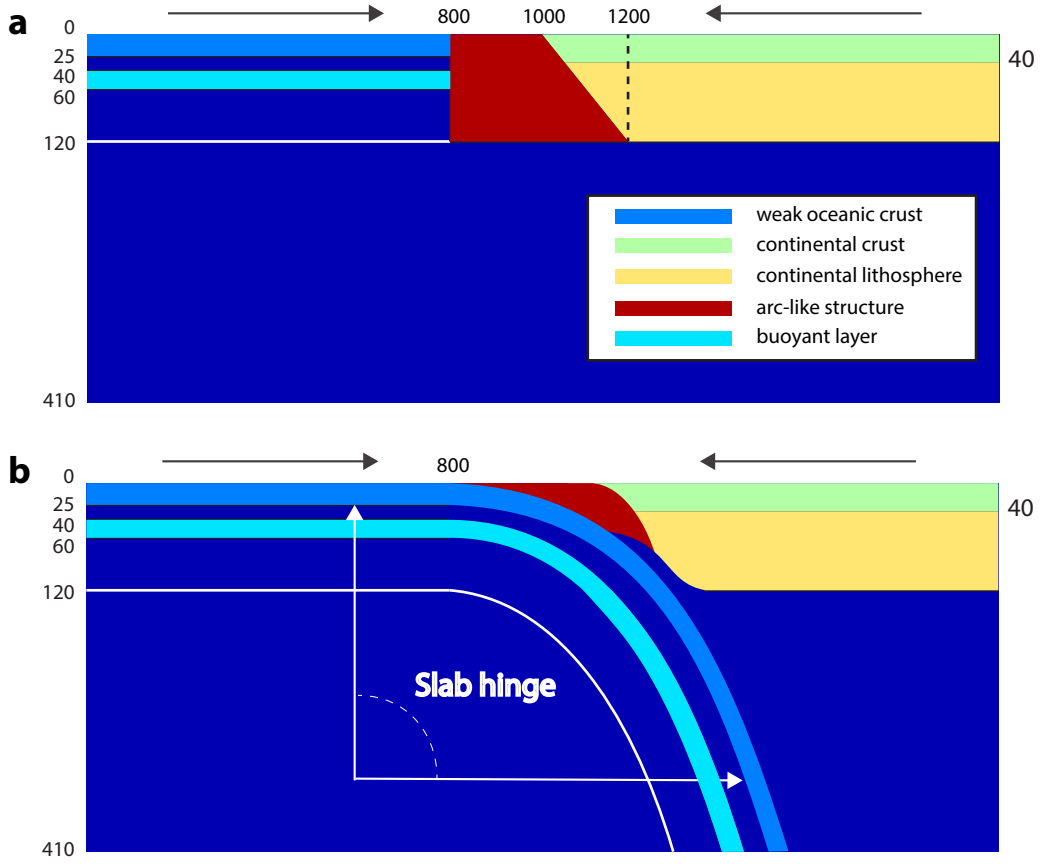

Figure 6.5. Schematic of the chemical composition at a subduction zone for (a) when a new trench appears and (b) after a new slab forms. Different colors represent different chemical compositions. The arc-like structure, the weak oceanic crust and weakening of the slab hinge are critical for the temporal evolution from stage (a) to stage (b).

Here, we simulate subduction in a more dynamic fashion, where we use a weak oceanic crust, a weak slab hinge and self-evolving plate boundary properties to reproduce Earth-like asymmetric subduction under complex trench kinematics (Fig. 6.5). Take the formation of a new subducting slab as an example: when a new trench appears, the composition of the emerging mantle wedge changes to be buoyant and low viscosity, mimicking the property of a volcanic arc as mentioned in Method (Fig. 6.5a). This arc-like structure increases lateral density variation within the subduction zone, which helps to initiate slab subduction. In addition, the low viscosity of this structure facilitates convection and return flow inside the mantle wedge. Meanwhile, the weak oceanic crust effectively decouples the slab from the overriding plate, and the weakened slab hinge further facilitates slab bending (Fig. 6.6b). Consequently, the new slab responds naturally to the convergent surface boundary condition, without the formation of congested slab at shallow

depth (Bello et al., 2015). As subduction proceeds, the weak mantle wedge initially accommodate convergence through internal deformation (Fig. 6.6b, d), followed by the establishment of a well-behaving slab lubricated by the weak oceanic crust from the overriding plate (Fig. 6.6f, h). The asymmetric subduction will continue as long as the two plates keep converging. It is also important to realize that, during this simulation, the adaptive data assimilation scheme avoids overwriting properties near the convergent boundaries, and thus allows the key subduction features to evolve self-consistently over time.

Figure 6.6 illustrates how this process works during the formation of an intra-oceanic subduction zone, where the Farallon plate subducted beneath the proto-Caribbean plate (Müller et al., 2016). At 85 Ma, the subduction just started (Fig. 6.6a), so there was no subducting slab yet (Fig. 6.6b). Initially, the mantle wedge was weakened due to the emerging arc-like structure and there was a weak spot on the surface of the plate right on the trench representing the weak oceanic crust (Fig. 6.6b). 5 Myr later, a clear asymmetric thermal structure beneath the trench developed, as resulted from the upwelling within the mantle wedge and downwelling of the slab along the trench (Fig. 6.6d). At 70 Ma, a subducting slab developed and had reached ~350 km depth (Fig. 6.6f). However, the slab was slightly thicker than a normal subducting lithosphere, likely due to the downward entrainment of the arc-like structure above the slab. Between 73 Ma and 61 Ma, the convergence between the two plates increased (Fig. 6.6a, c, e; Müller et al., 2016). As a result, the slab had reached the lower mantle by 60 Ma and its thickness inside the upper mantle became normal. By then, the asymmetric subduction was fully developed (Fig. 6.6h).

In this model, we could reproduce mantle dynamics associated not only with subduction initiation but also with trench polarity reversal. For example, part of the southwestern Pacific trench shifted its polarity at 85 Ma (Fig. 6.7 Müller et al., 2016). Before 85 Ma, the Pacific plate subducted obliquely beneath the Australian Plate, resulting in a segmented westward-dipping slab (Fig. 6.7a, b). After the polarity reversal occurred, the slab started to subduct eastward (Fig. 6.7c, d). At 70 Ma, an eastward-dipping slab was formed (Fig. 6.7e, f). Significantly, because we allow the temperature and composition of the overriding plate near the trench to deform dynamically, the resulting evolution of these features in the mantle wedge look very natural (Figs. 6.6h, 6.7f).

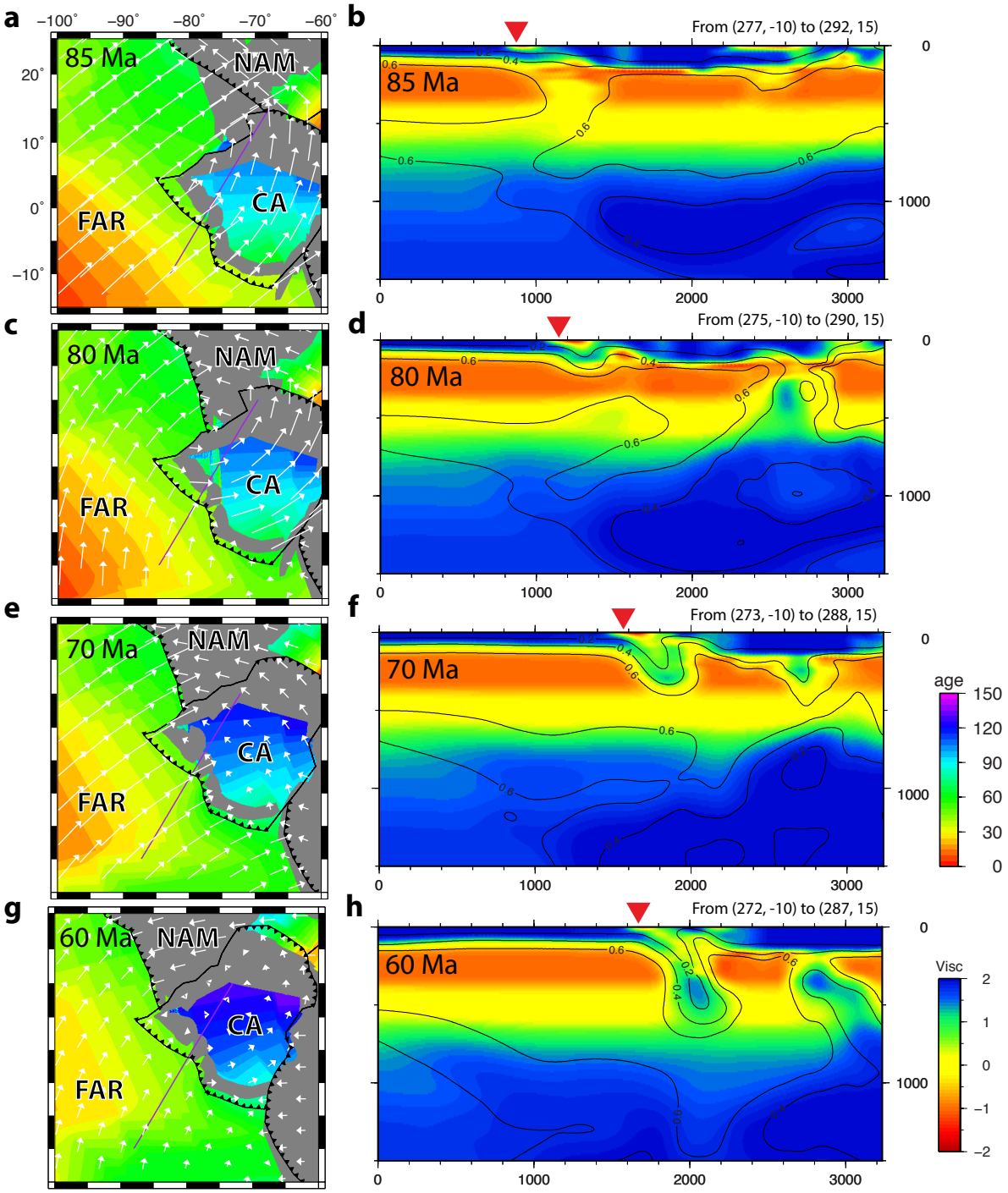

Figure 6.6. Subduction initiation in west Caribbean between 85 Ma and 60 Ma. (a), (c), (e) and (g) present the plate motion shown as white arrows and seafloor age with background color from a recent plate reconstruction (Müller et al., 2016) at 85, 80, 70 and 60 Ma, respectively. (b), (d), (f) and (h) show the evolution of temperature and viscosity along the purple-colored cross section in (a), (c), (e) and (g), respectively. The background color represents viscosity, while back lines indicate the non-dimensional temperature contours. The formation of the new slab takes more than

Figure 6.6. (cont.)

10 Myr, as is due to the slow convergence rate. Abbreviations: CA, Caribbean Plate; FAR, Farallon Plate; NAM, North American Plate.

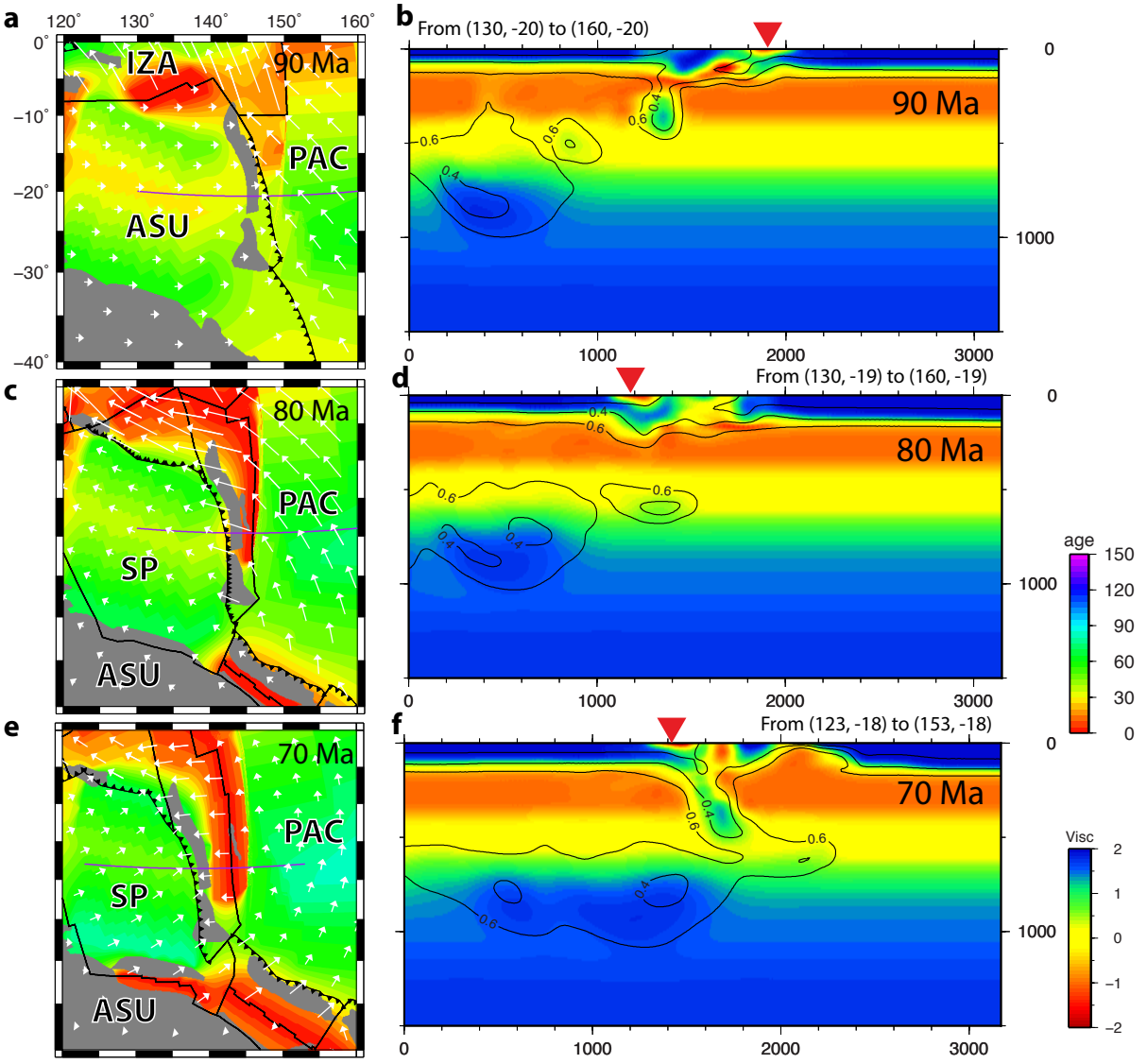

Figure 6.7. A scenario of trench polarity reversal in western Pacific from 80 Ma to 60 Ma. (a), (c) and (e) present the plate motion shown as white arrows and seafloor age shown with background color from the plate reconstruction (Müller et al., 2016) at 90, 80 and 70 Ma, respectively. (b), (d) and (f) show the evolution along cross sections in (a), (c) and (e), respectively. The background color represents viscosity, while the back lines indicate the non-dimensional temperature contours. Abbreviations: ASU, Australian Plate; IZA, Izanagi Plate; PAC, Pacific Plate; SP, Sepik Plate.

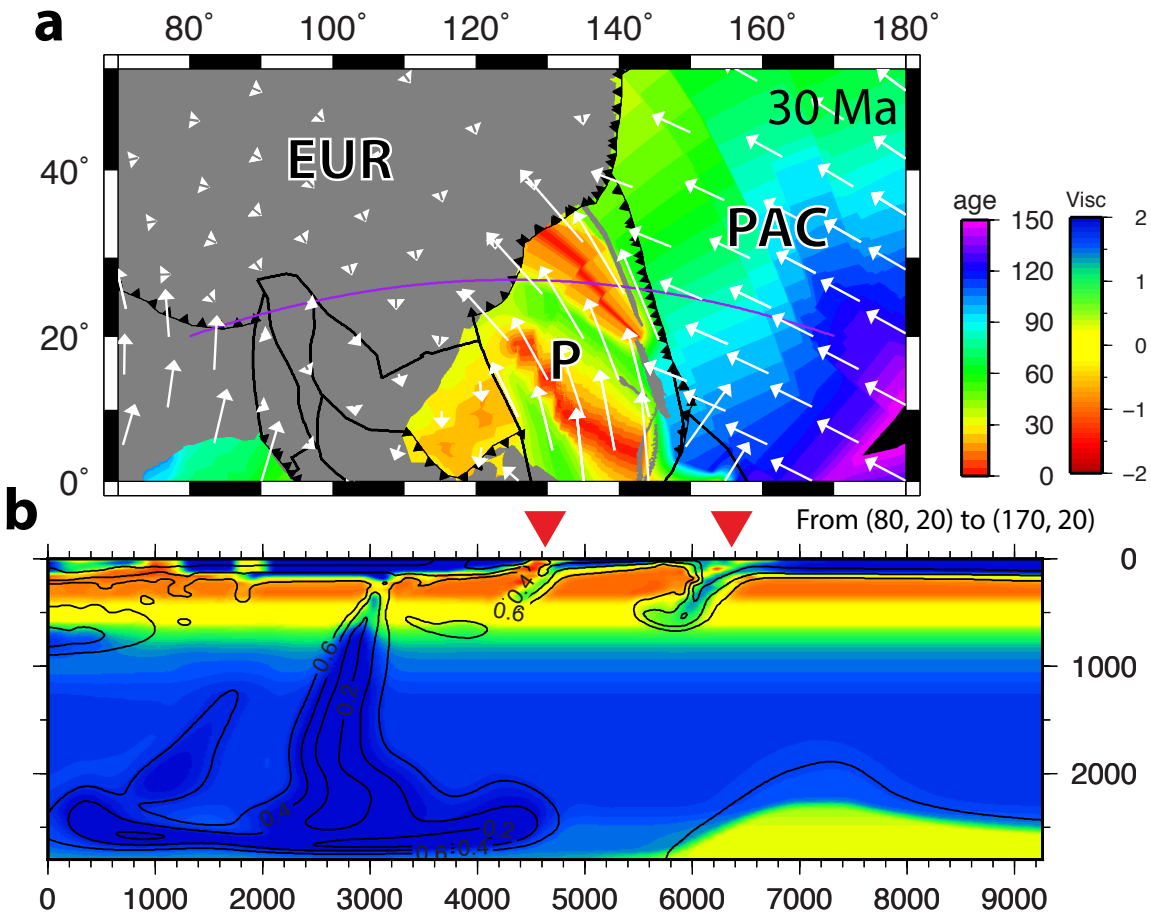

Figure 6.8. A cross section that intersects eastern Asia and Philippine Sea at 30 Ma. (a) The plate motion is shown as white arrows and seafloor age is shown with background color, both for 30 Ma. (b) Mantle structure along the cross section outlined in (a). The background color represents viscosity and the black contours indicate the non-dimensional temperature. The complex slab system is well resolved in this model. Abbreviations: EUR, Eurasian Plate; PAC, Pacific Plate; P, Philippine Sea Plate.

Our adaptive data assimilation scheme could also reproduce complex subduction systems where multiple trench segments intersect with each other or where fast trench migration occurs. One such example is the double subduction system surrounding the Philippine Sea Plate (Fig. 6.8). The Izu-Bonin-Mariana trench intersected with the Ryuku-Nankai trench and migrated northeastward rapidly between ~50 Ma and ~30 Ma (Müller et al., 2016). In a cross section that transects the Philippine Sea and South China, we found that the double slab system beneath the two trenches were well resolved (Fig. 6.8b). Even the prominent slab beneath China resulted from the subduction of former Izanagi Plate was also reproduced. Therefore, we demonstrate that with

the fine model resolution and sophisticated compositional functions, our adaptive data assimilation approach, likely for the first time, is able to simulate complex subduction dynamics occurring on Earth.

6.2.3.2 Reproducing the present-day mantle structure

The present-day mantle seismic structure is one of the most important constraints on the validity of all realistic subduction models. At regional to local scales, the predicted slab structures are evaluated against observations that include Benioff zones (Hayes et al., 2012) and seismic tomography (e.g. Ritsema et al., 2011; Obayashi et al., 2013). We first consider a recent P-wave model GAP_P4 (Fig. 6.9; Obayashi et al., 2013) and a S-wave model S40RTS (Fig. 6.10; Ritsema et al., 2011) in map view from 250 to 1500 km depth. In the upper mantle (above 660 km), the predicted slabs almost always coincide with seismically fast regions (Fig. 6.9a, b, c; Fig. 6.10a, b, c). In the lower mantle, the predicted slabs are also generally consistent with fast anomalies in these tomography models (Fig. 6.9d, e, f; Fig. 6.10d, e, f). For example, the predicted Nazca slab fits the tomography down to 1000 km beneath South America for both the P-wave and S-wave models. The Sumatra slab fits the tomography down to 1000 km as well and its disappearance at 1500 km depth is also consistent with tomography models.

To better examine the fit between the predicted and observed slab structure, we further plot several cross sections along different locations (Fig. 6.11). The first is an east-west cross section through the North American plate under which the ancient Farallon slab subducts (Fig. 6.11a). The predicted present Farallon slab is located under the eastern part of North America with an east-dipping orientation. This slab is now disconnected from the trench, due to the subduction of the Pacific-Farallon mid-ocean ridge since ~30 Ma and the cessation of convergence afterwards (Müller et al., 2016). Both the location and geometry of the Farallon slab are consistent with those outlined by tomography including GAP_P4 (Obayashi et al., 2013), S40RTS (Ritsema et al., 2011) and LLNL_G3Dv3 (Simmons et al., 2012).

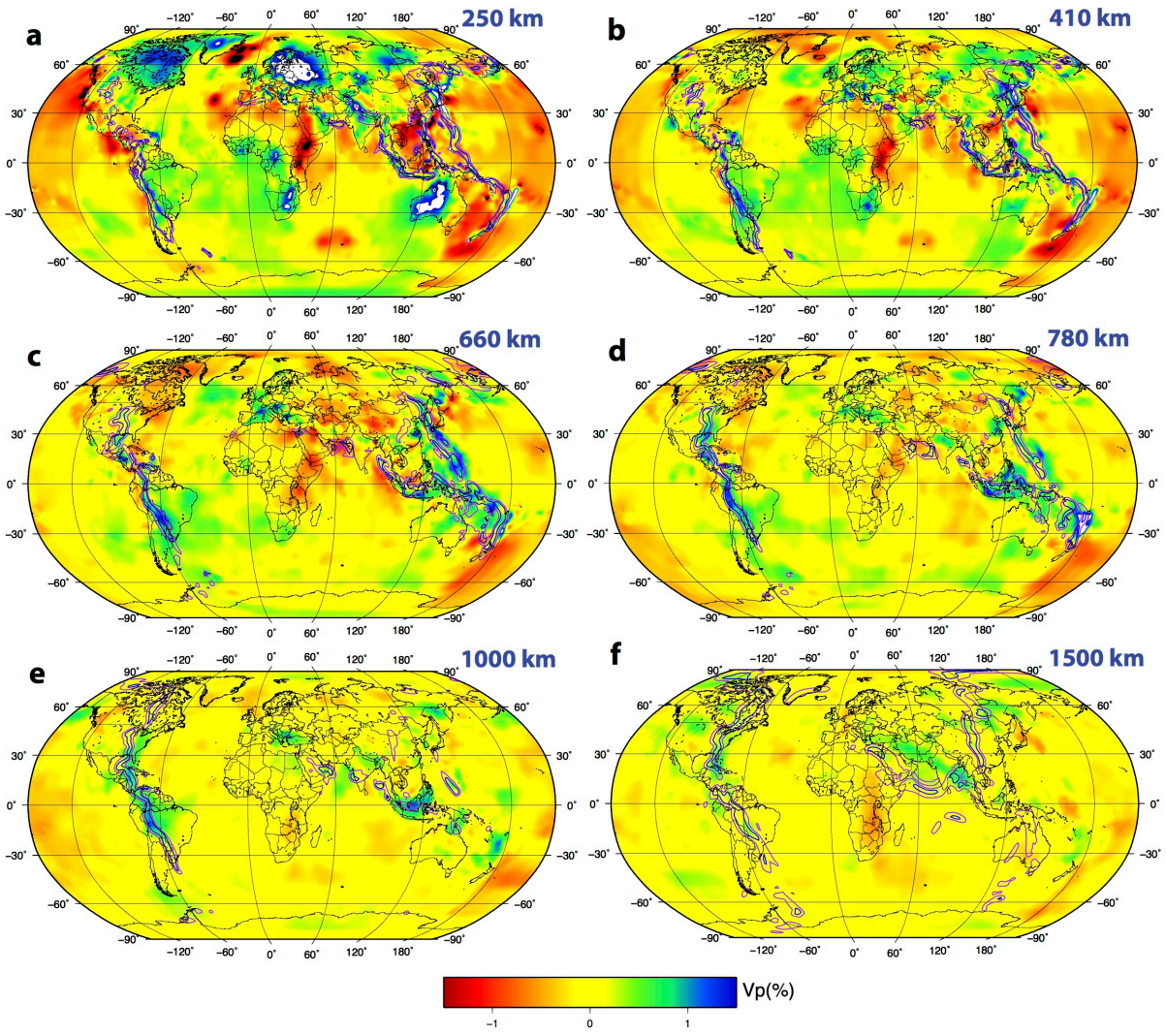

Figure 6.9. Map-view comparison between the predicted slab and P-wave tomography GAP_P4 (Obayashi et al., 2013) at depth (a) 250 km, (b) 410 km, (c) 660 km, (d) 780 km, (e) 1000 km and (f) 1500 km. The background color represents the velocity anomaly. The purple and blue lines represent slab temperature profile at non-dimensional values of 0.3 and 0.5, respectively.

In another cross section that runs across eastern Asia (Fig. 6.11b), the predicted slabs are also largely consistent with fast anomalies in tomography. For example, the subducted Izanagi slab piles up above the CMB, resembling the fast anomalies in the lower mantle, especially for the P-wave tomography GAP_P4 and IINL_G3Dv3 (Fig. 6.11b). In the transition zone, however, our model does not predict the large amount of flat-lying fast anomaly as shown in tomography models (Fig. 6.11b), traditionally interpreted as a stagnant Pacific slab (Huang and Zhao, 2006). In the upper mantle, the dip angle of the Pacific slab at the Izu trench is slightly shallower than the

interpolated Benioff zone (Hayes et al., 2012). This is mainly because the slab is too close to the trench-trench-trench triple junction on the north, which is dynamically challenging to reproduce.

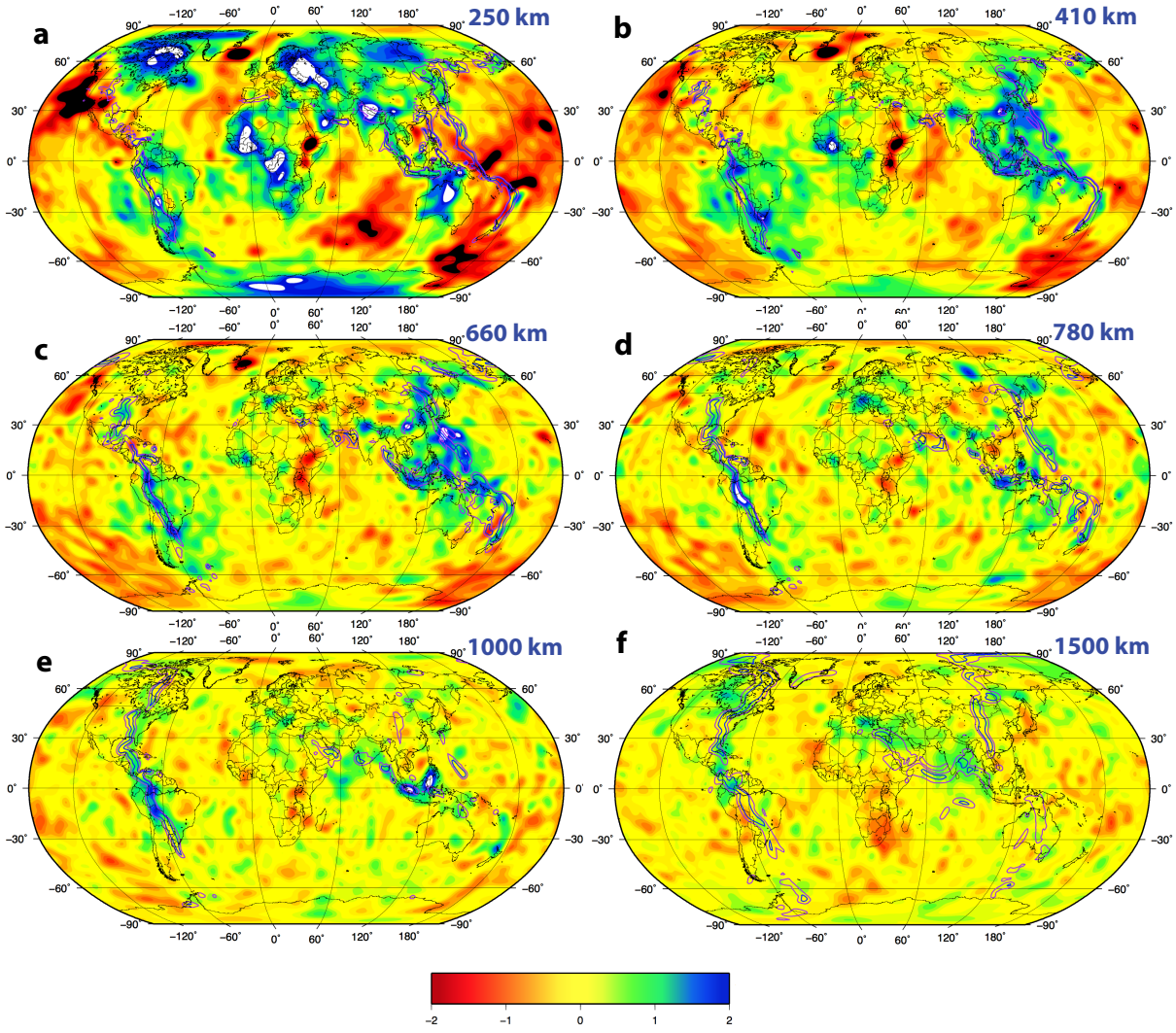

Figure 6.10. Maps showing comparison between the predicted slab and S-wave tomography S40RTS (Ritsema et al., 2011) at depth (a) 250 km, (b) 410 km, (c) 660 km, (d) 780 km, (e) 1000 km and (f) 1500 km. The background color represents velocity anomalies. The purple and blue lines represent the slab temperature contour at a non-dimensional value of 0.3 and 0.5, respectively.

The last cross section shows the slab structure across the Sumatra-Java trench (Fig. 6.11c). The predicted slab extends to ~1000 km depth, which is consistent with tomography models. The interpolated Benioff zone (Hayes et al., 2012) reveals a normally dipping slab that also fits our prediction quite well. Some mismatches occur above the CMB and in the transition zone.

Compared with tomography, the predicted slab on the CMB has a larger volume, while that in transition zone is less voluminous.

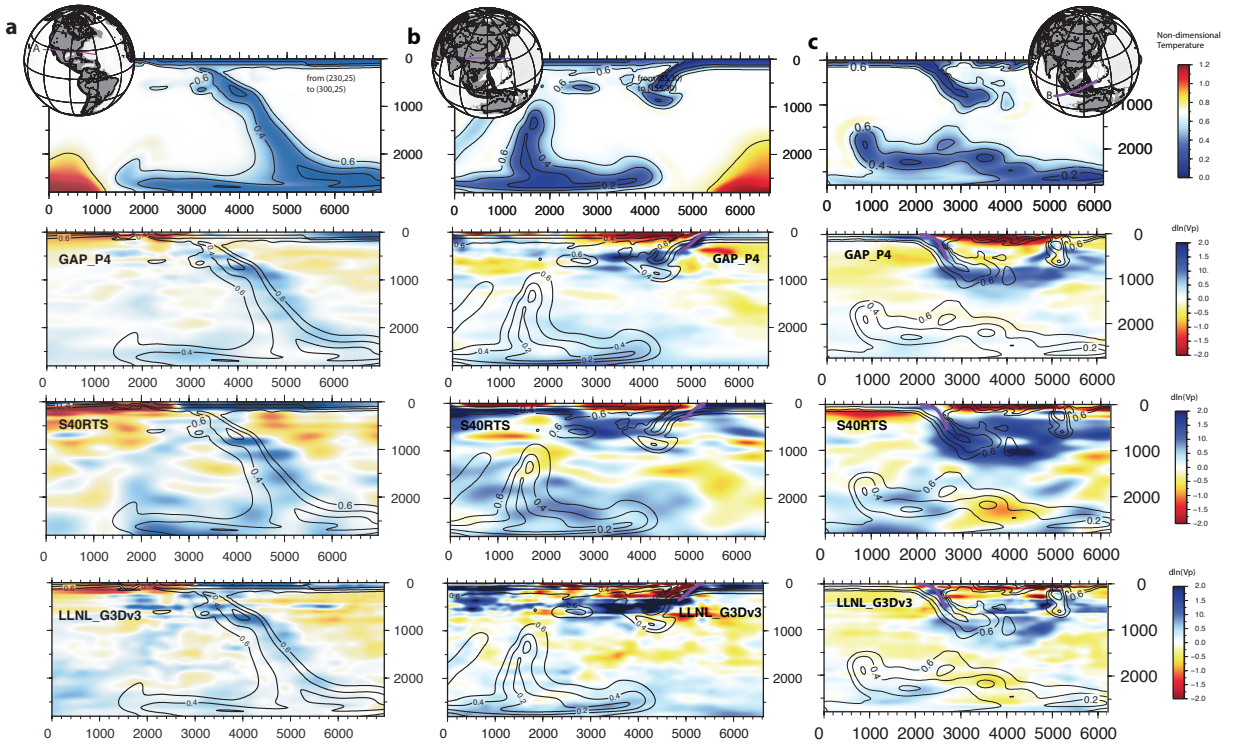

Figure 6.11. Cross sections showing the comparison between the predicted slab and three different tomography models, including GAP_P4 (Obayashi et al., 2013), S40RTS (Ritsema et al., 2011) and LLNL_G3Dv3 (Simmons et al., 2012). (a) A cross section that goes through the U.S. (b) a cross section through East Asia and (c) one across the Sumatra-Java trench. The upper panels show the temperature field from our model, while those lower panels show the velocity anomaly from the tomography models. All panels are overlain with black lines that represent the non-dimensional temperature contours. The thick purple lines are the interpolated Benioff zones (Hayes et al., 2012). Note that there are no Benioff zones beneath the eastern U.S.

Overall, an obvious mismatch between the predicted and observed mantle structure is the widespread transition zone fast anomalies below East and Southeast Asia, most of which are not reproduced by the known subduction history of the region. Observationally, these structures are prominent and have long been interpreted as stagnant Pacific slabs (Fukao et al., 1992; 2009; Huang and Zhao, 2006; Wu et al., 2016). Although a stronger mechanical barrier at the 660-km depth might result in more slabs accumulating inside the transition zone, this does not seem to be the case because slabs at other parts of the world in the current model match observations quite well. Alternatively, these transition zone fast

anomalies may represent structures not associated with oceanic slabs, and one such example is delaminated lithospheric roots as suggested below the southern Atlantic (Hu et al., 2018). However, future work is required to better understand these features.

6.2.3.3 Temporal evolution of subduction and mantle flow

Relative to earlier global studies, our model has the advantage of better reproducing upper-mantle subduction and mantle flow, both of which are crucial for understanding the Earth's tectonic evolution. Here we use the formation of the Farallon flat-slab and the history of mantle flow as examples.

The particular tectonic history of the western United States, including the Laramide orogeny (e.g. Saleeby, 2003; DeCelles, 2004), inboard migration of crustal deformation and arc magmatism (e.g. Snyder et al., 1976; Coney and Reynolds, 1977) and the formation of Western Interior Seaway (e.g. Cross and Pilger, 1978; DeCelles, 2004), suggests that the Farallon slab was flatly subducting during the Late Cretaceous to early Cenozoic (Bird, 1988; Liu et al., 2008). Reproducing this flat slab has remained a challenge in geodynamics. Earlier studies have either focused on modeling flat slab in idealized 2D or 3D settings (O'Driscoll et al., 2009; Liu and Currie, 2016) or assumed a known geometry of flat slab (Bird, 1988; English et al., 2003). The recent global models with data assimilation have not properly reproduced the evolution of this subduction process either (Bower et al., 2015; Bello et al., 2015).

Here we show that a Farallon flat slab can be naturally reproduced (Fig. 6.12). At ~80 Ma, the Farallon slab developed a shallower-than-normal dip angle (Fig. 6.12a). Since then, the slab dip angle progressively decreased and reached a maximum flatness at ~50 Ma (Fig. 6.12b), when the flat slab extended more than 1000 km inland from the trench. Subsequently, the flat slab began to detach from the upper plate. At the present day, this slab is located mostly beneath the eastern US (Fig. 6.12c), with the predicted configuration matching tomography quite well (Fig. 6.9, 6.10, 6.11a). According to our analysis, the slab anchoring in the lower mantle, the fast west-ward motion of the overriding plate, and the progressive younging of the Farallon plate since the Cretaceous all contribute to the flattening of the slab. However, the predicted slab in the mid-lower mantle is slightly too steep compared with tomography, which seems to suggest other mechanisms may have also played a role, such as hydrodynamic suction of the thick Colorado Plateau

(O'Driscoll et al., 2009; Liu and Currie, 2016) or the subduction of Shatsky and Hess conjugates (Liu et al., 2010).

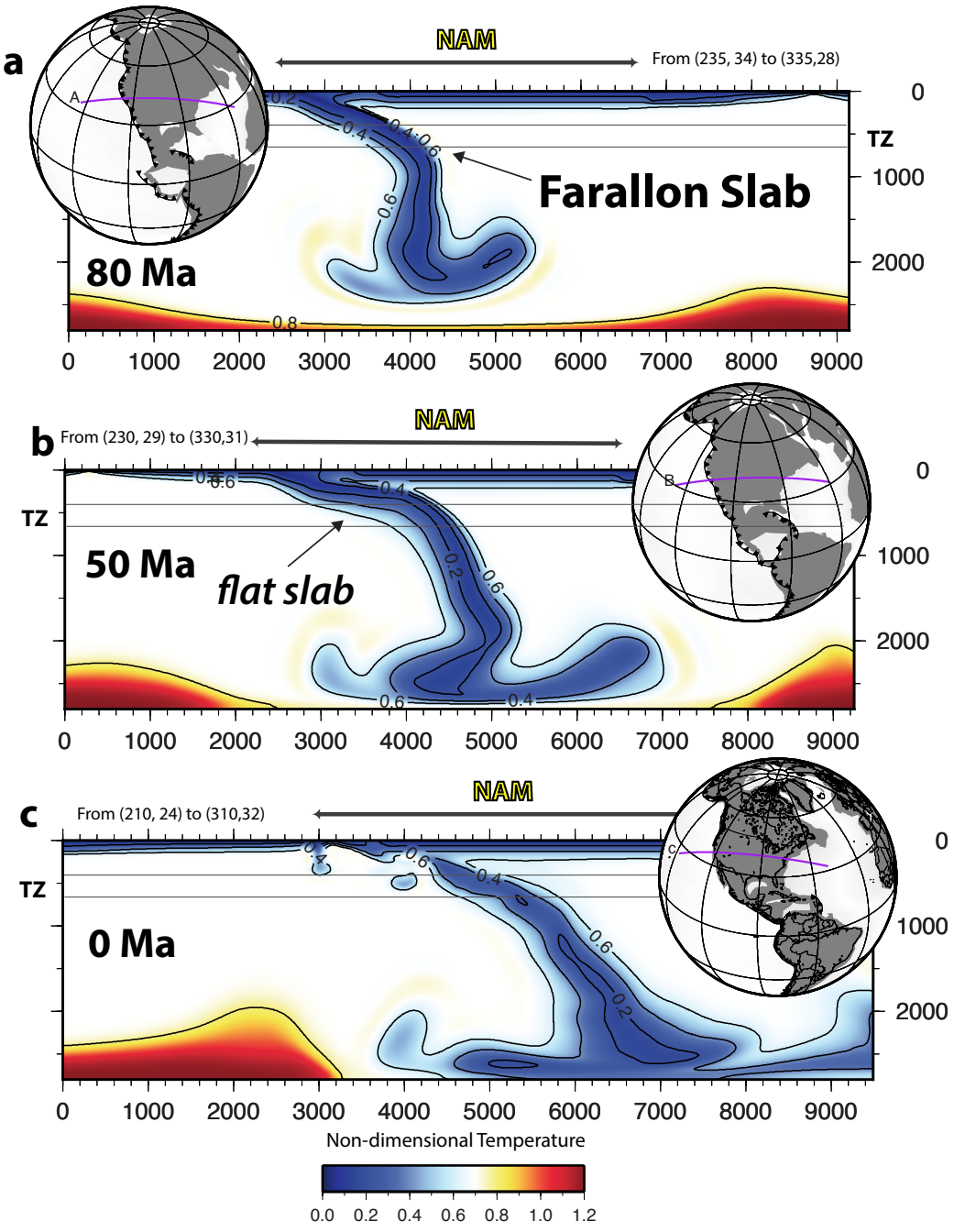

Figure 6.12. Temporal evolution of the Farallon slab at (a) 80 Ma, (b) 50 Ma and (c) present day. The background color represents non-dimensional temperature. The black lines are temperature contours. The slab at 50 Ma is lying flatly beneath the U.S. and extends more than 1000 km inland.

Mantle flow represents another key aspect of Earth evolution, since it could drive plate motion (e.g. Becker and Faccenna, 2011), transport chemical compositions (e.g. Hassan et al., 2016) and produce seismic anisotropy (e.g. Hu et al., 2017). Our high-resolution global subduction model has produced a complex, evolving mantle flow field that may have many important implications. At the plate scale, the upper-mantle flow pattern changes both with space and with time (Fig. 6.13). Spatially, the flow beneath a subducting plate is mostly influenced by the surface plate motion through Couette flow, such as that below Pacific, Australia, India, and Africa. In contrast, mantle flow below an overriding plate sees a stronger influence from the nearby sinking slab that forms the Poiseuille flow above, as is seen in the Americas and Eurasia. This finding is consistent with our recent conclusion based on a regional subduction model (Hu et al., 2017). Similarly, the temporal variation of upper-mantle flow is also affected by both changes in surface motion and the evolution of slabs. For example, the flow history beneath Pacific mostly follows the plate reorganization at the surface, while that below Nazca and South America is more subject to the geometry of the slab. It is also clear that thus predicted mantle flow history should have important implications on the resulting mantle and lithosphere deformation and the interpretation of seismic anisotropy.

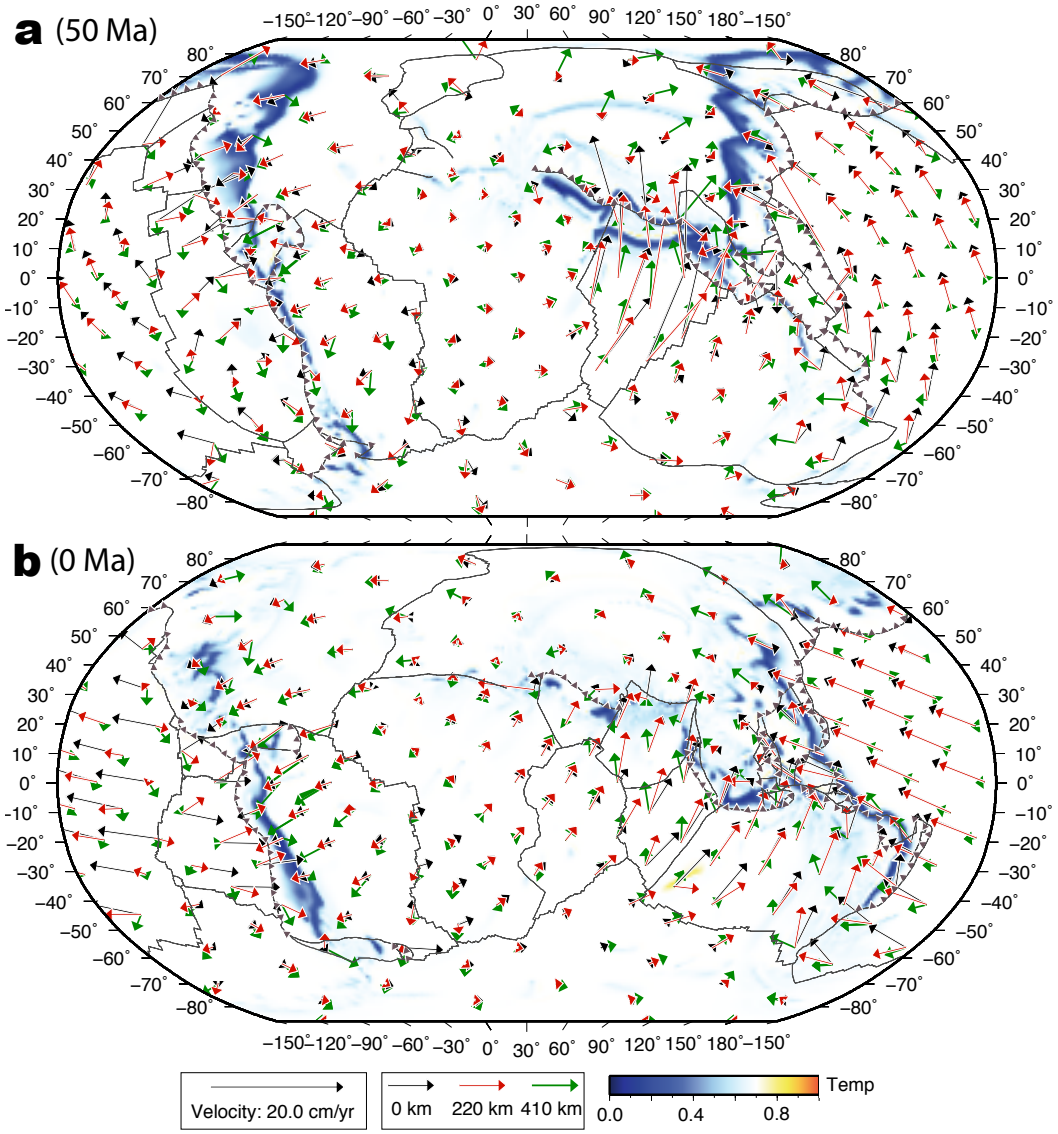

Figure 6.13. Predicted mantle flow at (a) 50 Ma and (b) 0 Ma. Three depths are shown: surface (black arrows), 220 km (red) and 410 km (green). The background color shows normalized mantle temperature, with blue indicating slabs.

6.2.4 Conclusion

We develop a high-resolution geodynamic model that simulates global subduction since 150 Ma using adaptive data assimilation. Figure 6.14 summarizes the predicted present-day mantle structure and flow. With the assimilated surface kinematics and lithosphere thermal profile, composition-dependent rheological features, such as the weak oceanic crust, arc-like weak zones and weak slab hinges, facilitate the realization of asymmetric subduction and dynamically evolving down-going slabs. This improved model capability can better deal with many other natural complexities, such as the initiation of subduction zones, subduction polarity reversal, and detailed

plate-boundary dynamics. More importantly, the model produces a global mantle slab structure that well fits the Benioff zones and seismic tomography (especially above 1500 km depth). Consequently, the model captures the temporal and spatial variation of slab dip angle, such as that associated with the formation and cessation of the Farallon flat slab. It also predicts the temporally and spatially varying mantle flow associated with evolving slab geometry and buoyancy flux. Due to the nature of data assimilation, i.e. geographically oriented, this model can be used to further study many geological events related to subduction processes.

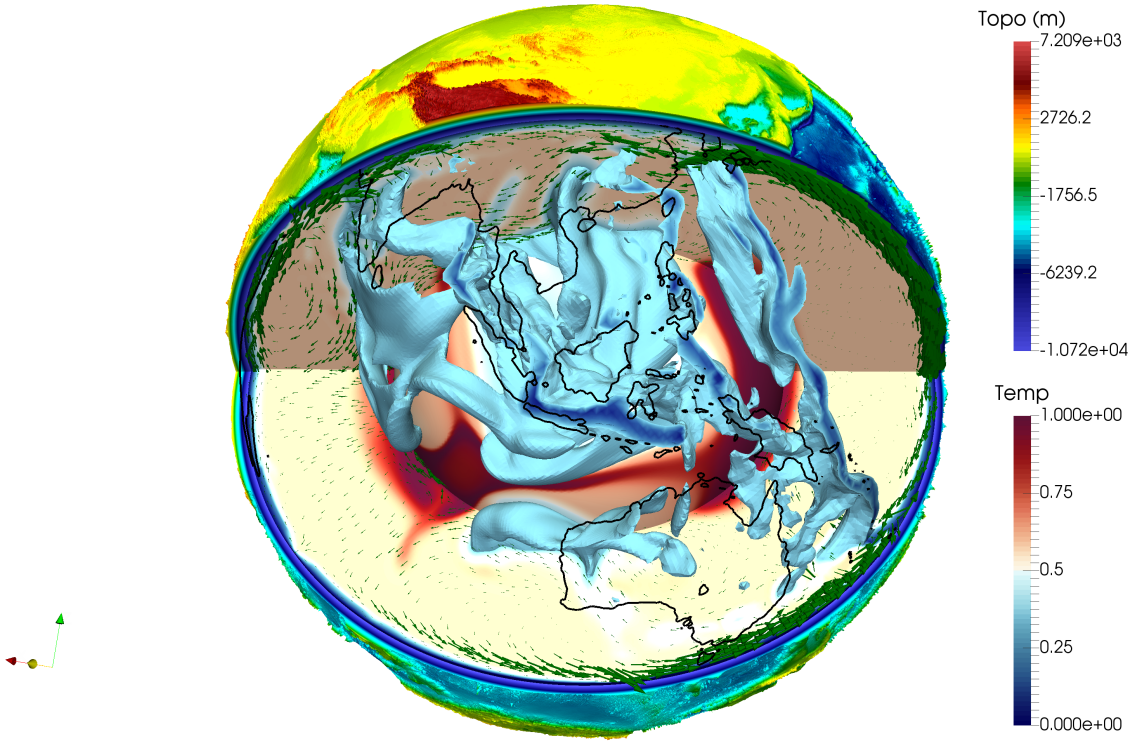

Figure 6.14. Present-day mantle structure and flow centered on eastern hemisphere. The isovolume represents the predicted slab with a non-dimensional temperature less than 0.4. Colors on the surface represent topography, while those for sub-surface structures represent the non-dimensional temperature. The white lines on the surface are the coastlines. Green arrows indicate the mantle flow within the cross sections.

6.3 References

Arriagada, César, et al. "Paleogene building of the Bolivian Orocline: Tectonic restoration of the central Andes in 2-D map view." Tectonics 27.6 (2008).

Barker, P.F. Scotia Sea regional tectonic evolution: implications for mantle flow and palaeocirculation, Earth Sci. Rev., 55, 1-39 (2001).

Beck, Susan L., et al. "Multiple styles and scales of lithospheric foundering beneath the Puna Plateau, central Andes." Geological Society of America Memoirs 212 (2014): MWR212-03.

Becker, T.W., and C. Faccenna. Mantle conveyor beneath the Tethyan collisional belt, Earth Planet. Sci. Lett. 310, 453-461 (2011).

Bello, L., N. Coltice, P.J. Tackley, et al. Assessing the role of slab rheology in coupled plate-mantle convection models, Earth Planet. Sci. Lett., 430, 191-201 (2015).

Billen, M.I., G. Hirth, Rheologic controls on slab dynamics, Geochem.Geophys. Geosyst., 8(8) (2007).

Bird, P., Formation of the Rocky Mountains, western United States- A continuum computer model, Science, 239.4847, 1501-1507 (1988).

Bower, D.J., M. Gurnis, N. Flament, Assimilating lithosphere and slab history in 4-D Earth models, Phys. Earth Planet. Inter., 238, 8-22 (2015).

Capitanio, F. A., Faccenna, C., Zlotnik, S., & Stegman, D. R. (2011). Subduction dynamics and the origin of Andean orogeny and the Bolivian orocline. Nature, 480(7375), 83-86.

Chen, Lin, et al. "Crustal rheology controls on the Tibetan plateau formation during India-Asia convergence." Nature Communications 8 (2017): ncomms15992.

Coltice, N., T. Rolf, P.J. Tackley, et al. Dynamic causes of the relation between area and age of the ocean floor, Science, 336(6079), 335-338 (2012).

Coney, P.J. and S.J. Reynolds, Cordilleran benioff zones, Nature, 270(5636), 403-406 (1977).

Crameri, F, P.J. Tackley, I. Meilick, et al, A free plate surface and weak oceanic crust produce single‐sided subduction on Earth, Geophys. Res. Lett., 39(3) (2012).

Cross, T.A., and R.H. Pilger, Tectonic controls of Late Cretaceous sedimentation, western interior, USA, Nature, 274.5672, 653-657 (1978).

Currie, Claire A., et al. "Geodynamic models of Cordilleran orogens: Gravitational instability of magmatic arc roots." Geological Society of America Memoirs 212 (2015): 1-22.

DeCelles, P.G., Late Jurassic to Eocene evolution of the Cordilleran thrust belt and foreland basin system, western USA, Am. J. Sci., 304.2, 105-168 (2004).

DeCelles, P. G., Ducea, M. N., Kapp, P., & Zandt, G. (2009). Cyclicity in Cordilleran orogenic systems. Nature Geoscience, 2(4), 251-257.

Dávila, F. M., Lithgow-Bertelloni, C., & Giménez, M. (2010). Tectonic and dynamic controls on the topography and subsidence of the Argentine Pampas: The role of the flat slab. Earth and Planetary Science Letters, 295(1), 187-194.

Eichelberger, N., McQuarrie, N., Ehlers, T. A., Enkelmann, E., Barnes, J. B., & Lease, R. O. (2013). New constraints on the chronology, magnitude, and distribution of deformation within the central Andean orocline. Tectonics, 32(5), 1432-1453.

Eichelberger, N., McQuarrie, N., Ryan, J., Karimi, B., Beck, S., & Zandt, G. (2015). Evolution of crustal thickening in the central Andes, Bolivia. Earth and Planetary Science Letters, 426, 191-203.

English, J.M., S.T. Johnston, and K.L. Wang, Thermal modelling of the Laramide orogeny: testing the flat-slab subduction hypothesis, Earth Planet. Sci. Lett., 214.3, 619-632 (2003).

Faccenna, Claudio, et al. "Initiation of the Andean orogeny by lower mantle subduction." Earth and Planetary Science Letters 463 (2017): 189-201.

Flament, N., M. Gurnis, S. Williams, et al, Topographic asymmetry of the South Atlantic from global models of mantle flow and lithospheric stretching, Earth Planet. Sci. Lett., 387, 107-119 (2014).

Flament, N., Gurnis, M., Müller, R. D., Bower, D. J., & Husson, L. (2015). Influence of subduction history on South American topography. Earth and Planetary Science Letters, 430, 9-18.

Foley, B.J. and T.W. Becker, Generation of plate-like behavior and mantle heterogeneity from a spherical, viscoplastic convection model, Geochem.Geophys. Geosyst., 10(8) (2009).

Fukao, Y., Obayashi, M., Inoue, H. & Nenbai, M., Subducting slabs stagnant in the mantle transition zone, J. Geophys. Res., 97, 4809-22 (1992).

Fukao, Y., M. Obayashi, T. Nakakuki, et al., Stagnant slab: a review, Annu. Rev. Earth. Planet. Sci., 37, 19-46 (2009).

Gurnis, M., M. Turner, S. Zahirovic, et al., Plate tectonic reconstructions with continuously closing plates, Computers & Geosciences, 38(1), 35-42 (2012).

Hassan, R., R.D. Müller, M. Gurnis, et al., A rapid burst in hotspot motion through the interaction of tectonics and deep mantle flow, Nature, 533(7602), 239-242 (2016).

Hayes, G.P., D.J. Wald, R.L. Johnson, Slab1. 0: A three-dimensional model of global subduction zone geometries, J. Geophys. Res., 117(B1) (2012).

Hu, J.S., L.J. Liu, A. Hermosillo & Q. Zhou, Simulation of late Cenozoic South American flat-slab subduction using geodynamic models with data assimilation, Earth Planet. Sci. Lett., 438, 1-13 (2016).

Hu, J.S., M. Faccenda, and L.J. Liu, Subduction-controlled mantle flow and seismic anisotropy in South America, Earth Planet. Sci. Lett., 470, 13-24 (2017).

Hu, J.S., L.J. Liu, M. Faccenda, Q. Zhou, K. Fischer, S. Marshak, C. Lundstrom, Modification of the Western Gondwana craton by plume-lithosphere interaction, Nature Geosci., doi:10.1038/s41561-018-0064-1 (2018).

Huang, J.L. and D.P. Zhao, High-resolution mantle tomography of China and surrounding regions, J. Geophys. Res., 111(B9) (2006).

Humphreys, Eugene. "Relation of flat subduction to magmatism and deformation in the western United States." Geological Society of America Memoirs 204 (2009): 85-98.

Kukowski, Nina, and Onno Oncken. "Subduction Erosion-the "Normal" Mode of Fore-Arc Material Transfer along the Chilean Margin?." The Andes. Springer Berlin Heidelberg, 2006. 217-236.

Liu, L.J., S. Spasojević, and .l Gurnis, Reconstructing Farallon plate subduction beneath North America back to the Late Cretaceous, Science, 322.5903, 934-938 (2008).

Liu L.J., M. Gurnis, M. Seton, J. Saleeby, R.D. Müller, J.M. Jackson, The role of oceanic plateau subduction in the Laramide orogeny, Nature Geosci., 3(5), 353-7 (2010).

Liu, L.J., and D.R. Stegman, Segmentation of the Farallon slab, Earth Planet. Sci. Lett., 311.1 1-10 (2011).

Liu, S.B., and C.A. Currie, Farallon plate dynamics prior to the Laramide orogeny: Numerical models of flat subduction, Tectonophysics, 666, 33-47 (2016).

Mallard, C., N. Coltice, M. Seton, et al., Subduction controls the distribution and fragmentation of Earth's tectonic plates, Nature, 535(7610), 140-143 (2016).

Manea, Vlad C., Marta Pérez-Gussinyé, and Marina Manea. "Chilean flat slab subduction controlled by overriding plate thickness and trench rollback." Geology 40.1 (2012): 35-38.

McKenzie, D., J. Jackson, K. Priestley, Thermal structure of oceanic and continental lithosphere, Earth Planet. Sci. Lett., 233, 337-349 (2005).

McNamara, A.K and S.J. Zhong, Thermochemical structures beneath Africa and the Pacific Ocean, Nature, 437(7062), 1136-1139 (2005).

Müller, R.D., M. Seton, S. Zahirovic, et al., Ocean basin evolution and global-scale plate reorganization events since Pangea breakup, Ann. Rev. Earth Planet. Sci., 44, 107-138 (2016).

O'Driscoll, L.J., E.D. Humphreys, and F. Saucier, Subduction adjacent to deep continental roots: Enhanced negative pressure in the mantle wedge, mountain building and continental motion, Earth Planet. Sci. Lett., 280.1, 61-70 (2009).

O'Driscoll, Leland J., Mark A. Richards, and Eugene D. Humphreys. Nazca-South America interactions and the late Eocene-late Oligocene flat-slab episode in the central Andes, Tectonics 31.2 (2012).

Obayashi, M., J. Yoshimitsu, G. Nolet, et al., Finite frequency whole mantle P wave tomography: Improvement of subducted slab images, Geophys. Res. Lett., 40(21), 5652-5657 (2014).

Oncken, O., Chong, G., Franz, G., Giese, P., Götze, H. J., Ramos, V. A., ... & Wigger, P. (Eds.). (2006). The Andes: active subduction orogeny. Springer Science & Business Media.

Ritsema, J., H.J. van Heijst, and J.H. Woodhouse, Complex shear wave velocity structure imaged beneath Africa and Iceland, Science, 286.5446, 1925-1928 (1999).

Saleeby, J., Segmentation of the Laramide slab-Evidence from the southern Sierra Nevada region, GSA Bull., 115.6, 655-668 (2003).

Schellart, W. P., Freeman, J., Stegman, D. R., Moresi, L., & May, D. (2007). Evolution and diversity of subduction zones controlled by slab width. Nature, 446(7133), 308-311.

Simmons, N.A., S. C. Myers, G. Johannesson, and E. Matzel, LLNL-G3Dv3: Global P wave tomography model for improved regional and teleseismic travel time prediction, J. Geophys. Res., 117, B10 (2012).

Snyder, W.S., W.R. Dickinson, and M.L. Silberman, Tectonic implications of space-time patterns of Cenozoic magmatism in the western United States, Earth Planet. Sci. Lett., 32.1, 91-106 (1976).

Steinberger, B., A.R. Calderwood, Models of large-scale viscous flow in the Earth's mantle with constraints from mineral physics and surface observations, Geophys. J. Int., 167(3), 1461-81 (2006).

Tan, E., E. Choi, P. Thoutireddy, et al., GeoFramework: Coupling multiple models of mantle convection within a computational framework, Geochem. Geophys. Geosyst., 7(6) (2006).

Trumbull, Robert B., et al. "The time-space distribution of Cenozoic volcanism in the South-Central Andes: a new data compilation and some tectonic implications." The Andes. Springer Berlin Heidelberg, 2006. 29-43.

Wu, J., J. Suppe, R.Q. Lu, and R. Kanda, Philippine Sea and East Asian plate tectonics since 52 Ma constrained by new subducted slab reconstruction methods. J. Geophys. Res., 121, 4670-4741 (2016).

Zhong, S.J., A. McNamara, E. Tan, et al., A benchmark study on mantle convection in a 3-D spherical shell using CitcomS, Geochem. Geophys. Geosyst., 9(10) (2008).

APPENDIX A: SUPPLEMENTARY TO CHAPTER 3

Supplementary Materials:

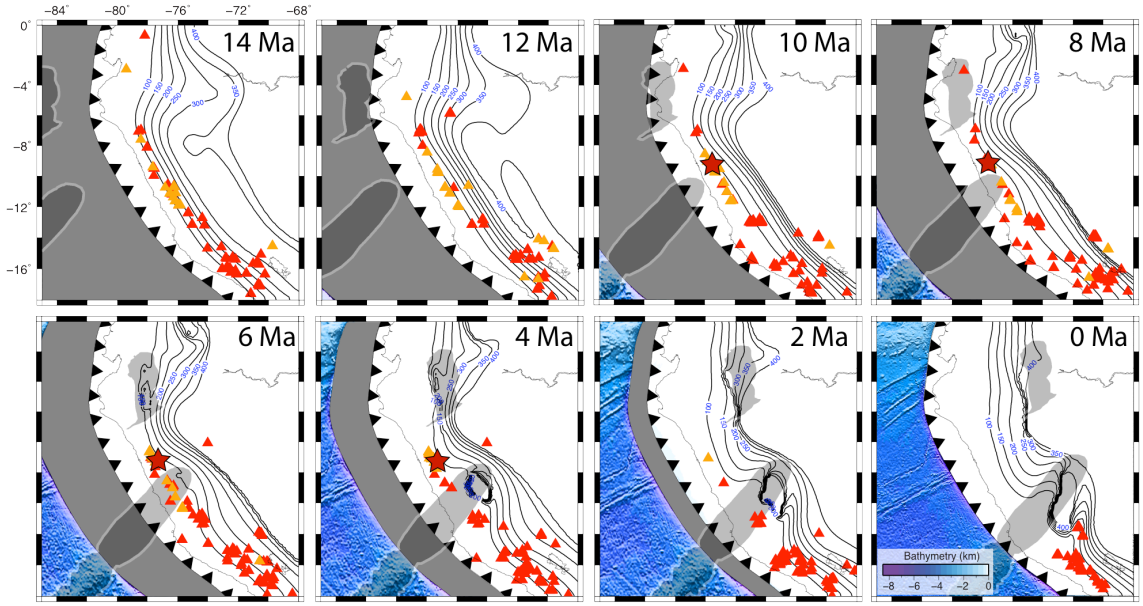

Figure A.1. The evolution of volcanic distribution in Peru from 14 Ma to the present day. Black lines represent the slab upper surface (300 °C cooler than the ambient mantle) at different depths. Dark gray patterns show the reconstructed locations of the Inca Plateau and the Nazca Ridge. Light gray area represents subducted seafloors at the present. Red triangles indicate the location of extrusive volcanism, while orange triangles represent that of intrusive volcanism (online catalog of Peruvian Mining and Metallurgical Geological Institute – INGEMMET, http://www.ingemmet.gob.pe). Red stars represent the adakitic eruption.

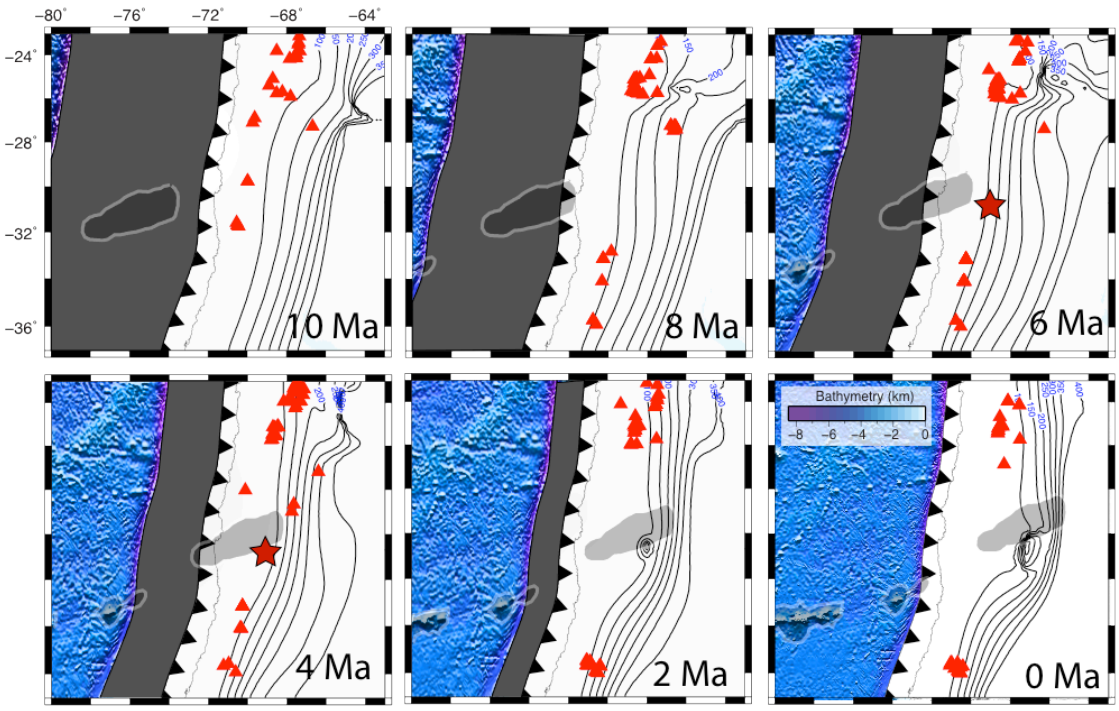

Figure A.2. Same as Figure A.1, except that the volcanic data is from Isotopic Dates: Andean Igneous Rocks LE 150 Ma (http://bbs.keyhole.com/ubb/showflat.php/Cat/0/Number/994404/an/0/page/0# 994404)

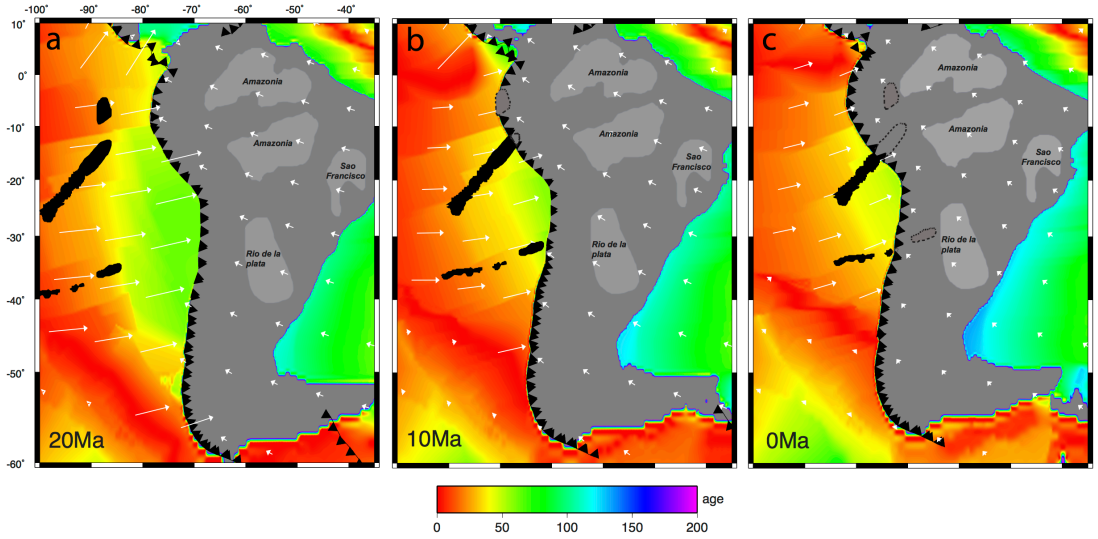

Figure A.3. Plate velocity and seafloor age at (a) 20 Ma, (b) 10 Ma and (c) the present day. White arrows show the plate velocity. Background color represents the seafloor age. Black regions represent the reconstructed position of oceanic plateau and aseismic ridges with dashed contours delineating the already subducted part. Dark gray region shows the South American continent and light gray regions show the cratons in South America.

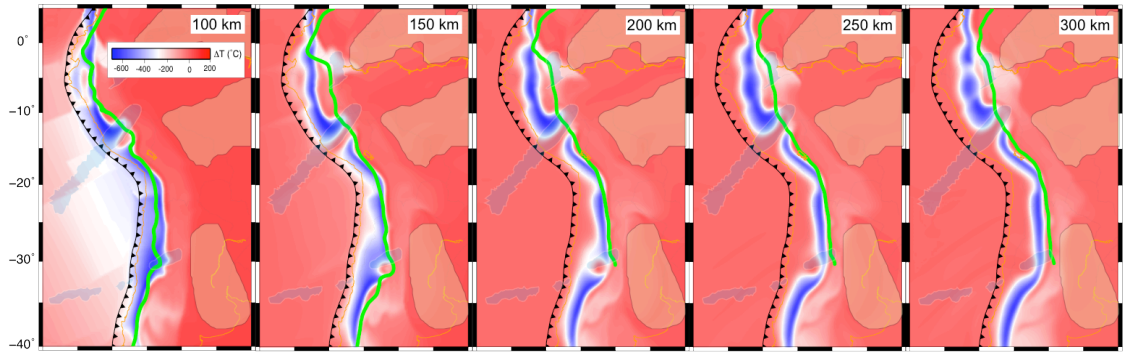

Figure A.4. Comparison of predicted slab geometry (background color representing temperature) with Slab1.0 (Hayes et al., 2012) depth contour (thick green lines) at five different depths. Brown and transparent blue outline the reconstructed geometry of continental cratons and oceanic plateaus (including aseismic ridges). Notice the overall fit of our model with slab 1.0.

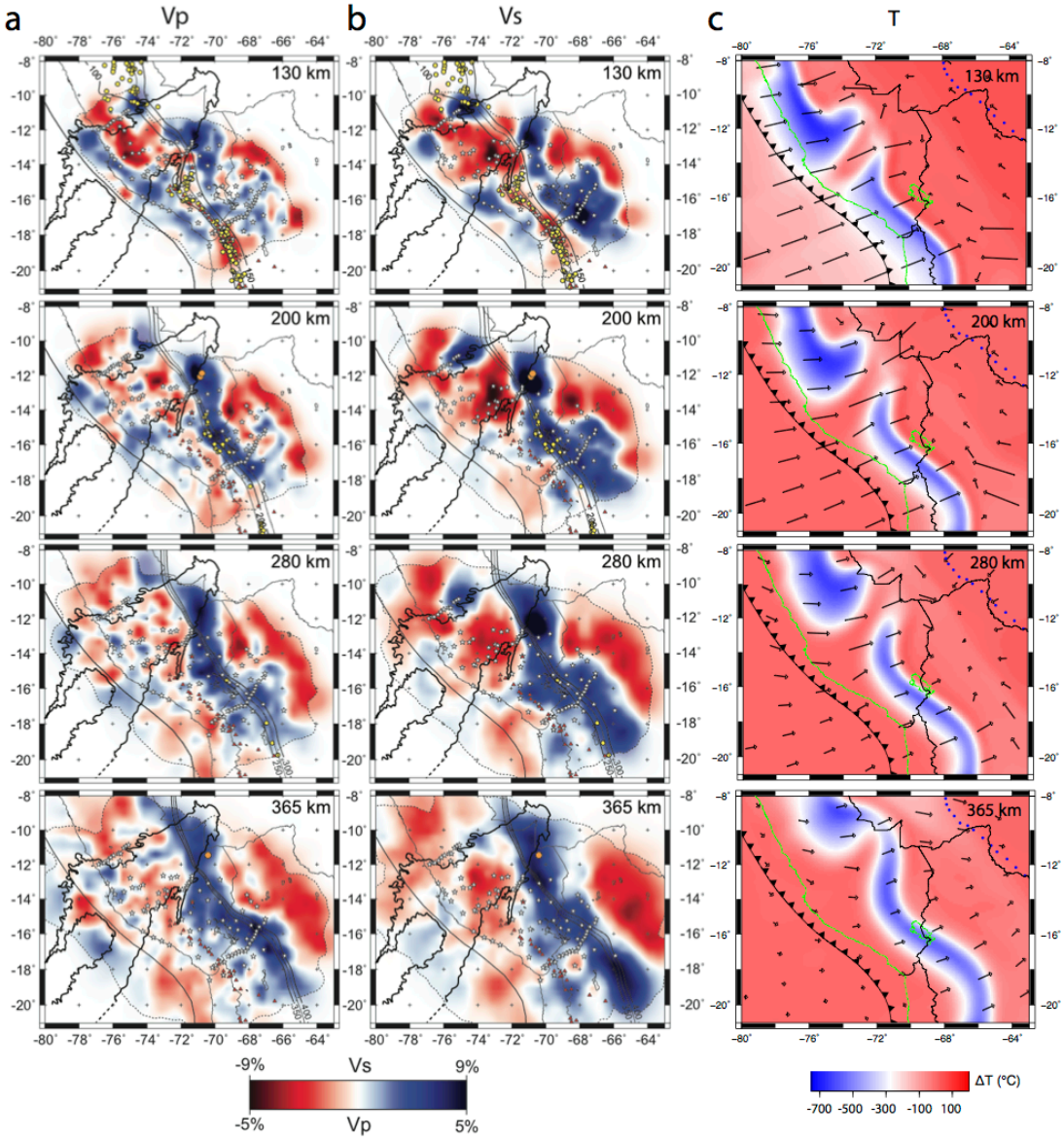

Figure A.5. Further comparison of predicted slab geometry (c) where background color represents temperature variation with a recent tomography model where both P-wave velocity (a) and S-wave velocity (b) are shown (sub-figures a and b are from Scire et al., 2016).

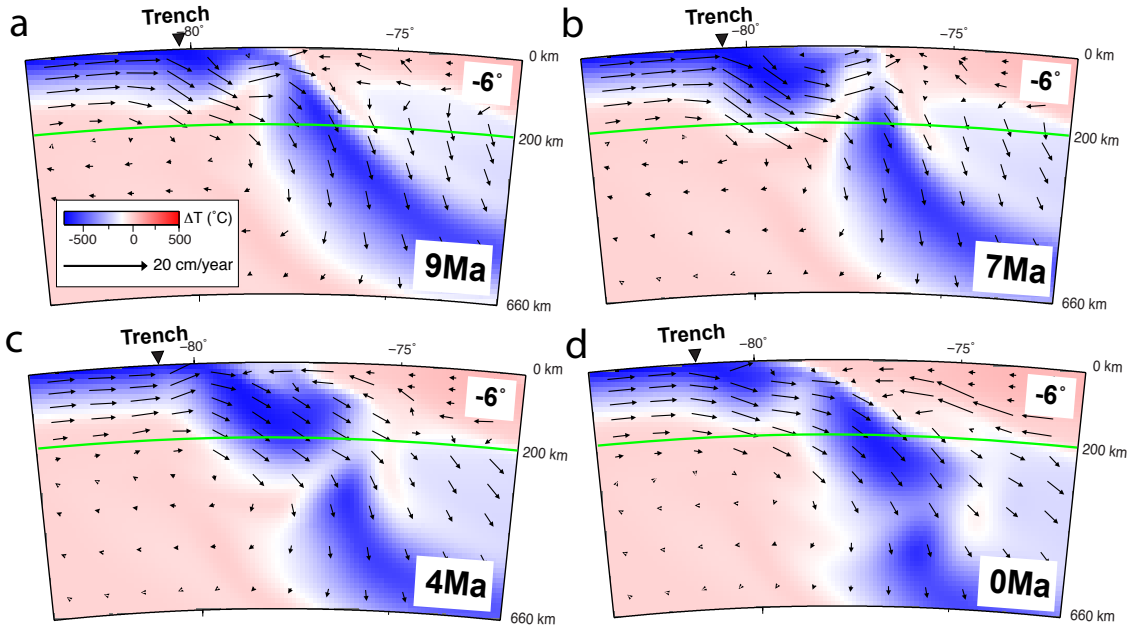

Figure A.6. Cross sections showing the subduction of Inca Plateau at (a) 9 Ma, (b) 7 Ma, (c) 4 Ma and (d) present day. All the cross sections are E-W along 6°S latitude. We see strong upwellings at 9 Ma and 7 Ma when the Inca Plateau began to subduct.

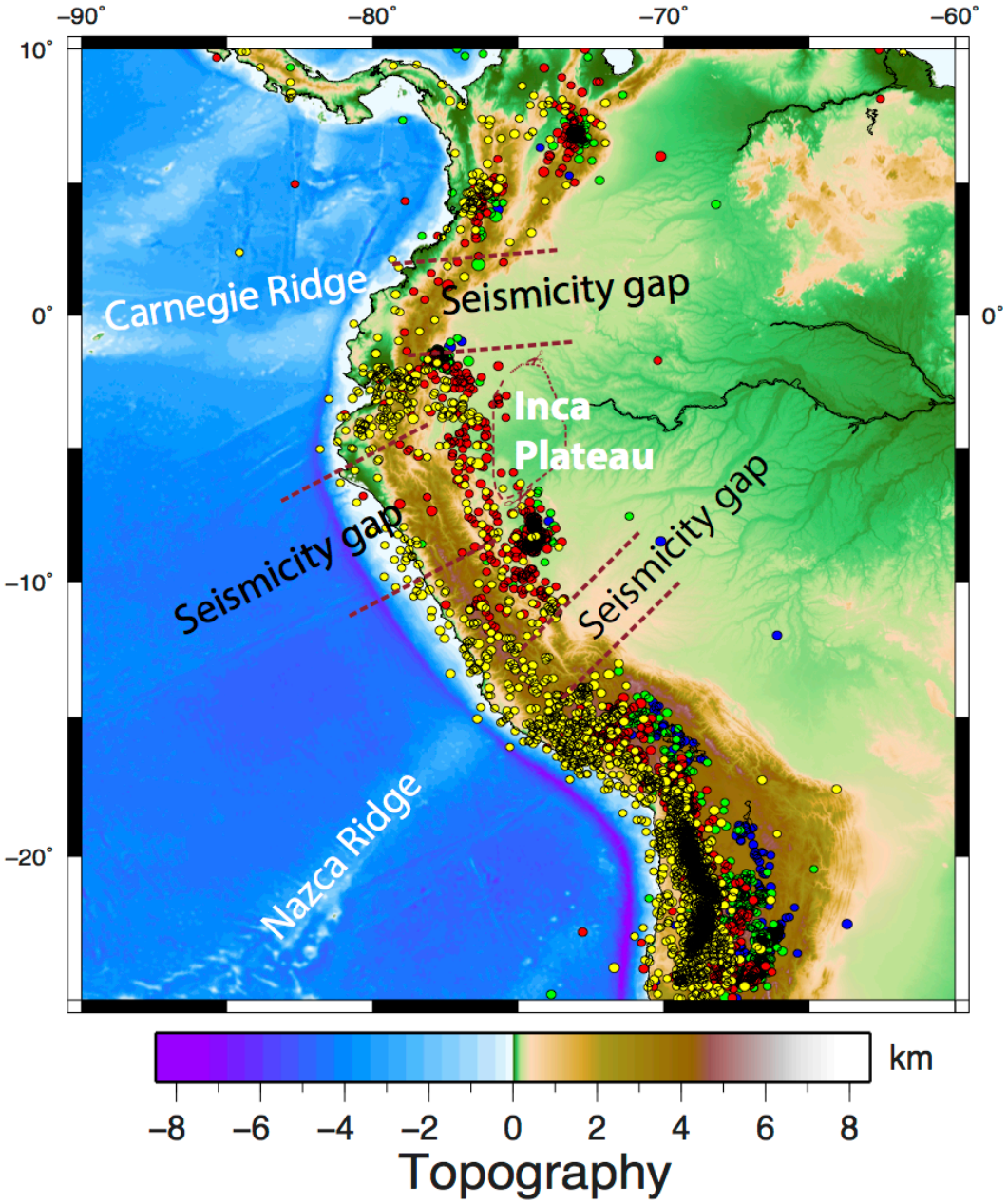

Figure A.7. Intermediate-depth seismicity distribution (Mb > 4, from ISC seismic catalog) at the trench where Carnegie Ridge subducts. Yellow dots represent earthquakes at depth between 70 km and 115 km; red dots at depth between 115 km and 160 km; green dots at depth between 160 km and 205 km; blue dots at depth between 205 km and 250 km.

References

Hayes, G.P., D.J. Wald & R.L. Johnson, Slab1.0: A three-dimensional model of global subduction zone geometries, J. Geophys. Res., 117, B01302 (2012).

Scire, Alissa, George Zandt, Susan Beck, Maureen Long, Lara Wagner, Estela Minaya, Hernando Tavera, Imaging the transition from flat to normal subduction: variations in the structure of the Nazca slab and upper mantle under southern Peru and northwestern Bolivia. Geophysical Journal International, 204(1), 457-479 (2016).

APPENDIX B: SUPPLEMENTARY TO CHAPTER 4

Supplementary Material:

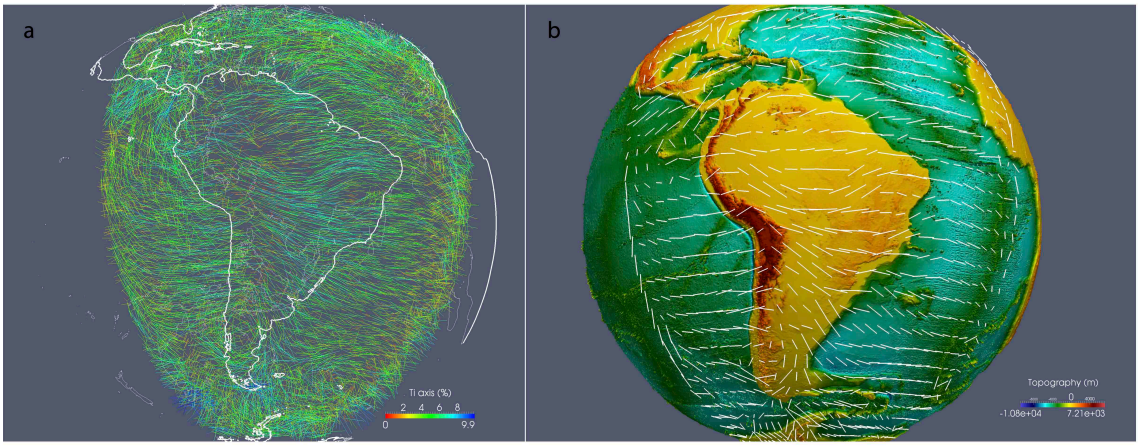

Figure B.1. Anisotropy fabrics (**a**) and shear wave splitting (**b**) computed with DRexS and FSTRACK, respectively, for one of our best-fit slab models that uses the plate reconstruction of Müller et al. (2016). In (**a**), the colored lines are the TI axes of hexagonal anisotropy with the color representing the percentage of the hexagonal component of the full elastic tensor. In (**b**), the white bars indicate the synthetic shear wave splitting at 30 km × 30 km regularly placed seismic stations.

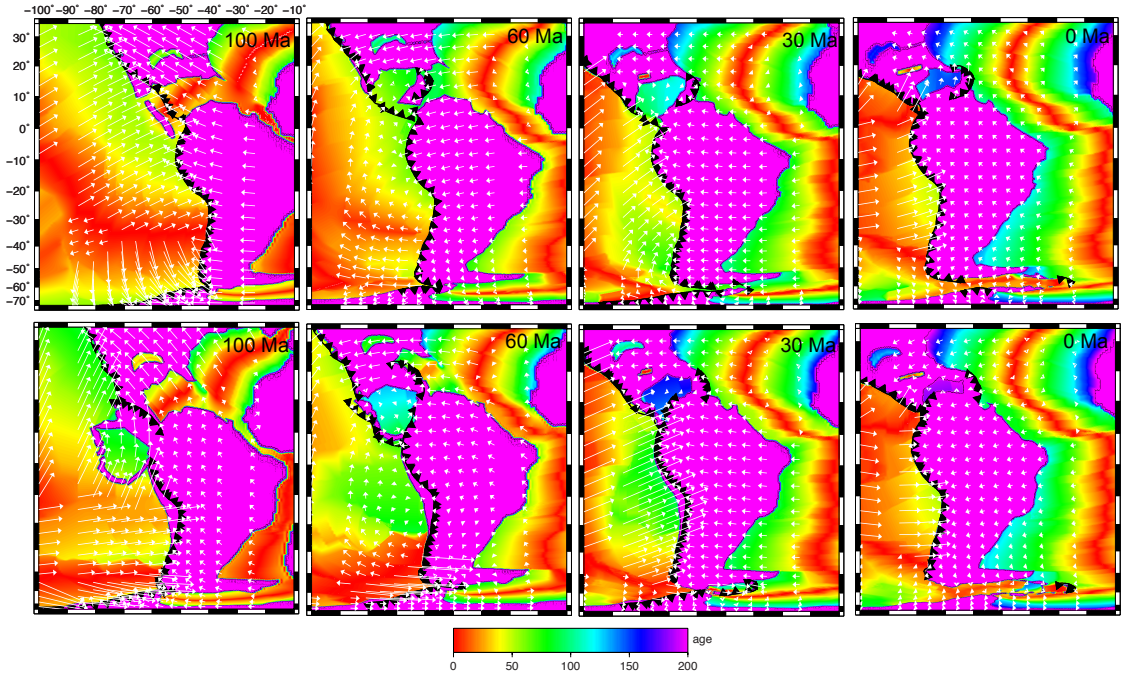

Figure B.2. Comparison of the two plate reconstruction models: (top row) Müller et al. (2008) and (bottom row) Müller et al. (2016) at 100 Ma, 60 Ma, 30 Ma and 0 Ma. The motion of South American Plate and Nazca Plate has remained similar for the last 20 Myr for both models.

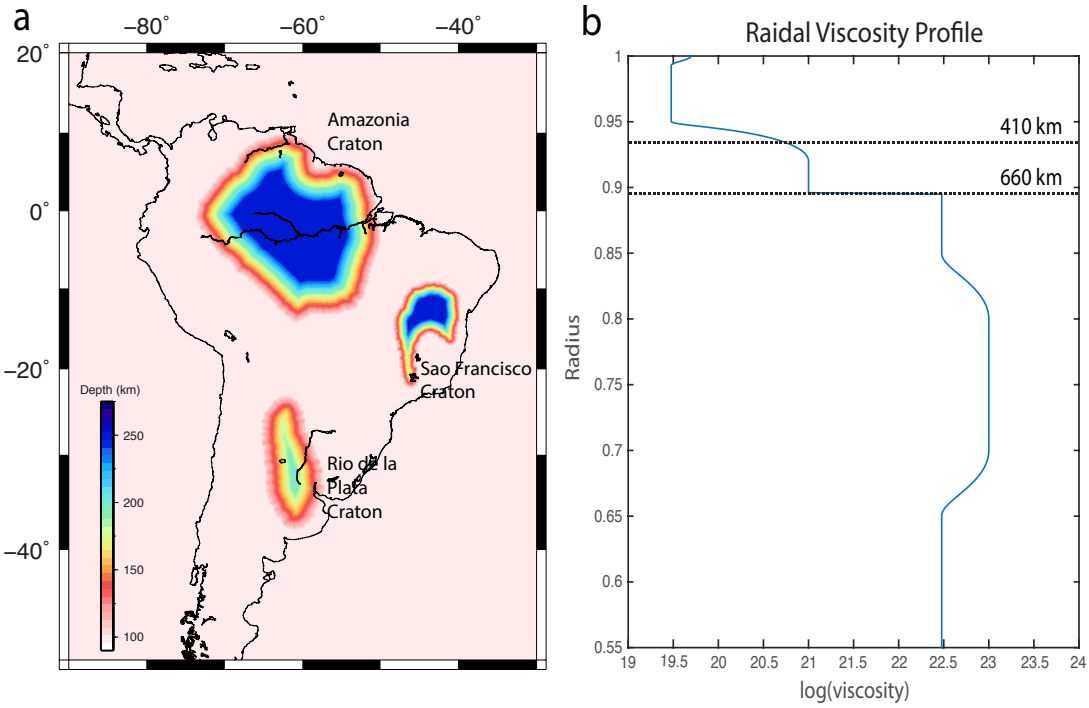

Figure B.3. The shape of the cratons (**a**) and the radial viscosity profile (**b**) used in the models. (**a**) The background color represents the maximum depth of the cratons. The ambient continent is about 100 km thick, while the maximum depth of craton is 250 km. The transition from ambient continent to craton is smoothed. (**b**) shows the change of background viscosity with depth. The models have included a low-viscosity asthenosphere and a high-viscosity mid-lower mantle.

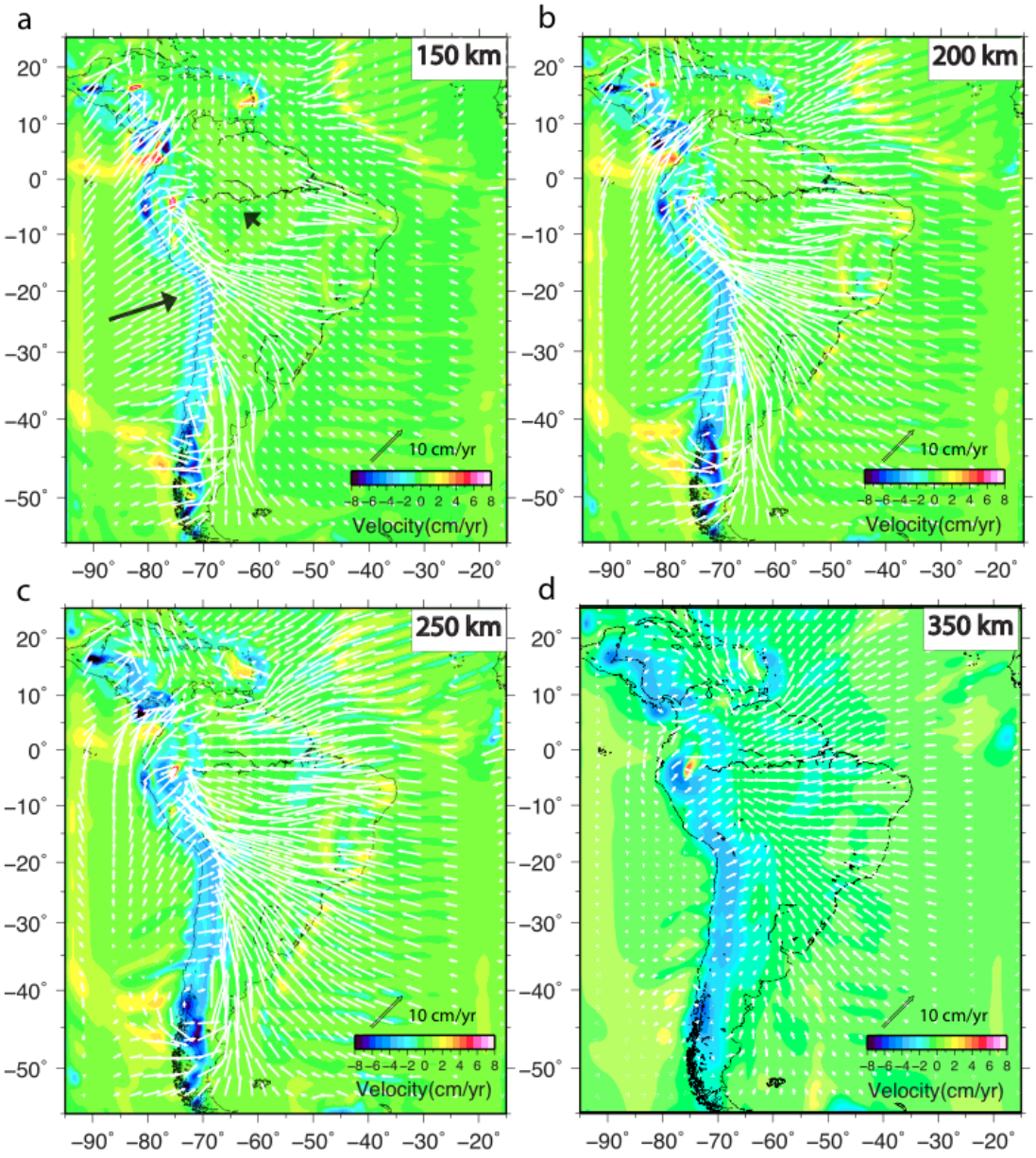

Figure B.4. Present mantle flow fields at depths of (**a**) 150 km, (**b**) 200 km, (**c**) 250 km and (**d**) 350 km from the slab model with the plate reconstruction of Müller at al. (2008). White arrows are the horizontal components of the velocity vectors, while background colors represent the vertical components of the velocity vectors. Black arrows in (**a**) indicate the present absolute plate motion.

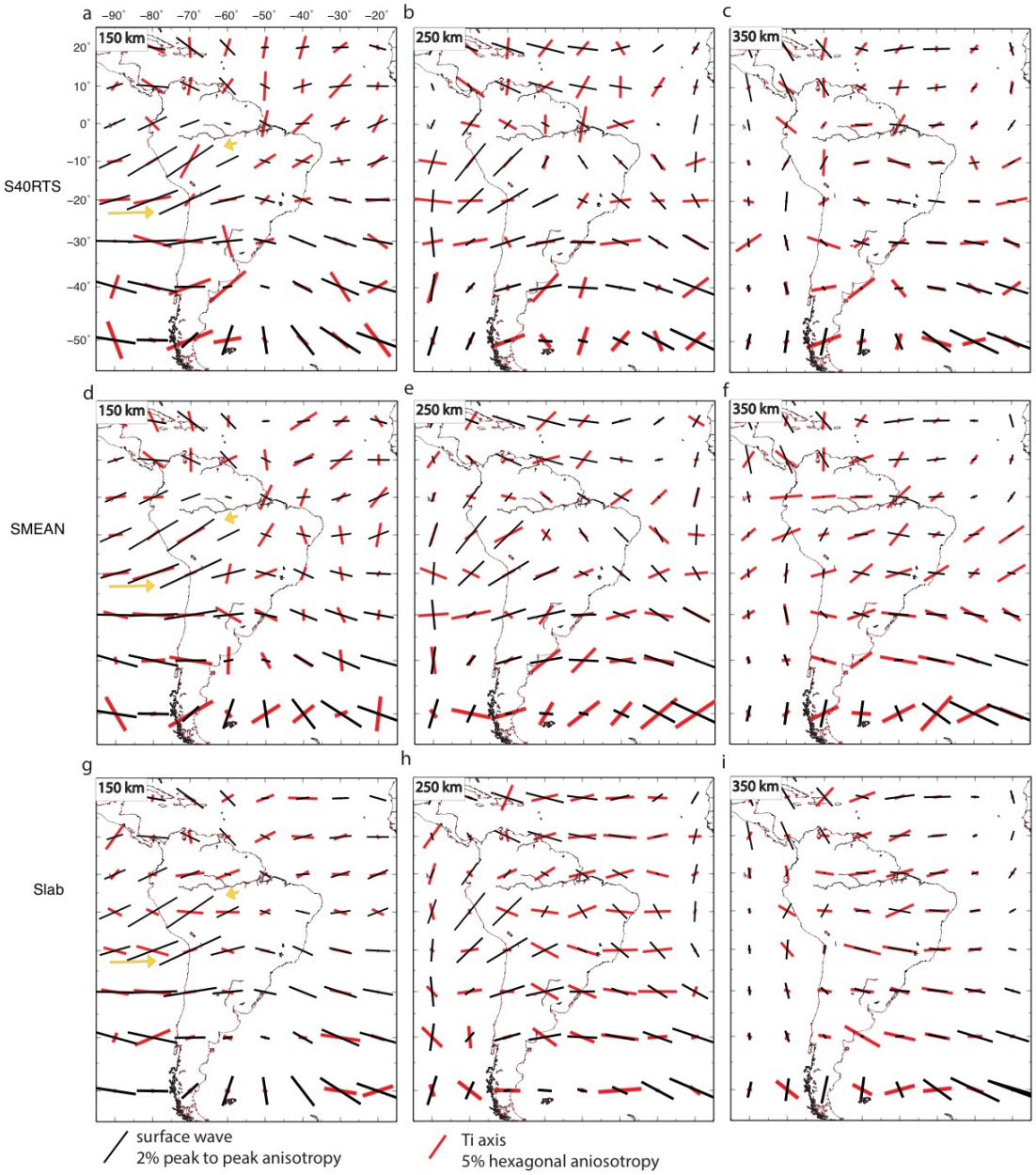

Figure B.5. Comparison of the observed and predicted azimuthal anisotropy for the instantaneous model based on S40RTS (**a**, **b**, **c**), the instantaneous model based on SMEAN (**d**, **e**, **f**) and the time-dependent slab model (**g**, **h**, **i**). All the three models are run with the plate reconstruction of Müller et al. (2016). Observed azimuthal anisotropy (Yuan and Beghein, 2013) are shown with thin black bars, and the TI axes of predicted LPO are represented as thick red bars. Yellow arrows in (**a, d, g**) indicate the present absolute plate motion.

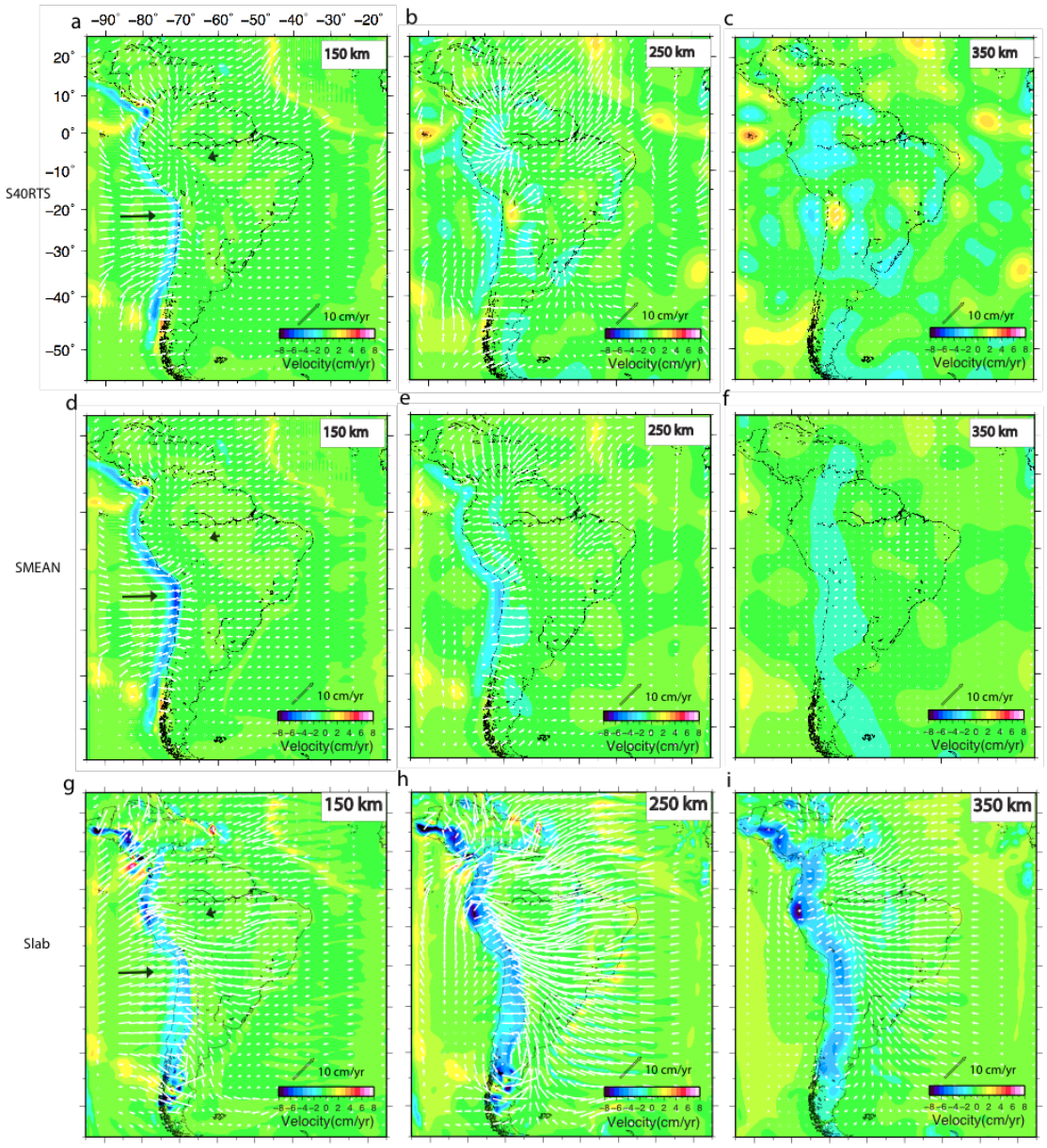

Figure B.6. Velocity fields of the instantaneous model based on S40RTS (**a**, **b**, **c**), the instantaneous model based on SMEAN (**d**, **e**, **f**) and the time-dependent slab model (**g**, **h**, **i**). The three models are the same as those in Fig. B.5. White arrows are the horizontal components of the velocity vectors, while background colors represent the vertical components of the velocity vectors. Black arrows in (**a, d, g**) indicate the present absolute plate motion.

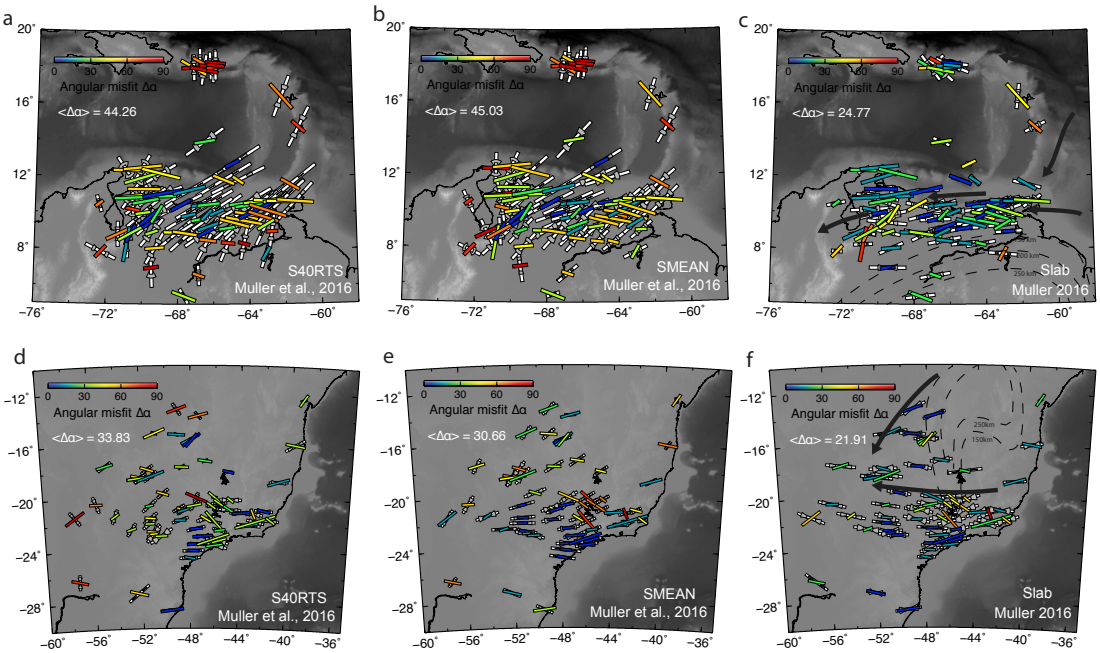

Figure B.7. The observed (Becker et al., 2012) and predicted shear wave splitting for the instantaneous model based on S40RTS (**a**, **d**), the instantaneous model based on SMEAN (**b**, **e**) and the time-dependent slab model (**c**, **f**). The three models are the same as those in Fig. B.5 and B.6. All the models have included the cratons, with the plate reconstruction of Müller et al. (2016). In each subplot, the observed station-averaged splitting is colored by angular misfit. The predicted splitting is shown with white sticks with the grey wedges representing the confidence interval of the fast direction. The black lines in (d) delineate the proposed flow direction. The average angular misfit is computed for each subplot.

APPENDIX C: METHODS OF CHAPTER 5

C.1 Calculating mantle and lithosphere residual topographies

We first calculate the mantle residual topography by removing the Airy isostatic topography from the observed topography assuming an average crustal density of 2.8×10^3 kg/m^{-3}. Since Crust1.0 model (Laske et al., 2013) (Fig. D.1**a**) and other seismic studies (Reid et al., 2012; Assumpção et al., 2013; Liu et al., 2016; Globig et al., 2016) demonstrate similar regional-scale crust thickness variations, we use the former to estimate mantle residual topography. We also find that using the spatially varying crustal density from Crust1.0 does not change the pattern of residual topography. Geographically, the resulting positive mantle residual topography of up to 1.5 km (Fig. D.2**a**) correlates closely with the prominent high surface topography (Fig. 5.1**a**), confirming its mantle origin. However, these residual topography signals have a wavelength of 200-500 km, precluding a lower mantle origin that suggest a wavelength of >1000 km. This observation is further consistent with recent understanding that the prominent Large Low Shear Wave Velocity Provinces (LLSVP) in the lowermost mantle are compositionally distinct from the ambient mantle (Masters et al., 2000; Ni et al., 2002; McNamara and Zhong, 2005) and likely posses a neutral net buoyancy, leading to little dynamic uplift at the surface (Guillocheau et al., 2012; Griffin et al., 2003; Steinberger, 2007; Conrad and Husson, 2009).

To isolate the topographic contributions from the lithosphere and sub-lithosphere mantle, we further estimate the convection-induced mantle dynamic topography with a global instantaneous model that has a lateral resolution of ~25 km and a variable vertical resolution that reaches a maximum of 5.5 km on the top. Here we define dynamic topography as due to sub-lithospheric (>300 km depth) mantle convection. We first converted seismic velocity perturbations to effective density anomalies using an empirical scaling (Moucha and Forte, 2011; Simmons et al., 2009), and adopted a radial mantle viscosity profile consistent with our forward subduction modeling[44]. Estimated dynamic topographies using tomography model SEMum2 (French et al., 2013) and S40RTS (Ritsema et al., 2011) are similar over South America and Africa, and we use the former in the final calculation since it is a more recent tomography model. The resulting dynamic topography (Fig. D.3**a**) is very similar to published models (Flament et al., 2012; Moucha and Forte, 2011; Steinberger, 2007; Conrad and Husson, 2009). Our calculations suggest small-

amplitude (<250 meters), long-wavelength (>2000 km) dynamic topography in most of the positive-residual-topography regions, implying little contribution. One exception is the Eastern African Rift (EAR), where prominent dynamic uplift is due to localized sub-lithospheric hot upwelling below the region (Moucha and Forte, 2011).

We then estimated the residual topography associated with lithosphere buoyancy (Fig. 5.2**a**) by removing the topographic effect due to sub-lithospheric convection (Fig. D.3**a**) from the net mantle residual topography (Fig. D.2**a**). Thus estimated lithospheric residual topography within the craton regions (Fig. 5.2**a**) remains nearly identical to the net mantle residual tomography (Fig. D.2**a**). This is due to the lack of upper-mantle positive buoyancy, especially that associated with slow seismic anomalies, below these regions (Figs. 5.3, D.5). In this case, the lower-mantle large low shear wave velocity province (LLSVP; Fig. 5.3) does not affect the prominent but localized positive residual topography whose wavelength is <500 km (Fig. 5.2**a**), because the LLSVP mostly affects the topography at a much larger wavelength (>1000 km) and with a smaller amplitude (<300 meter) (Fig. D.3**a**). Therefore, the high cratonic topography with elevated Moho should reflect mostly lithospheric buoyancy heterogeneities.

C.2 Mantle and lithospheric gravity anomalies

Gravity anomalies (Bonvalot et al., 2012) provide another important constraint on lithosphere density structure. We first derived the mantle gravity anomaly (Fig. D.2**b**) by removing both the topographic and crustal effects from the free-air gravity anomaly (Fig. D.1**b**). We adopt the same approach as in earlier studies (Kaban et al., 2003; Mooney and Kaban, 2010) using the Crust1.0 model (Laske et al., 2013) to calculate the gravity of the crust. Using a constant crustal density or the density structure provided in Crust1.0 leads to similar results. For the map shown in Fig. 5.2, we corrected the crustal effect with Bouguer slab formula for different layers, while the density and the thickness of the layers are taken from Crust1.0. We find that the locations of the prominent negative (as low as -2×10^{-3} m/s^2) mantle gravity anomalies (Fig. D.2**b**) match almost exactly with those of mantle residual topography (Fig. D.2**b**). Since all topographic effects are removed from the mantle gravity calculation, its correlation with residual topography strongly supports the existence of low-density mantle underneath these regions, especially at lithospheric depths (Mooney and Kaban, 2010).

To quantify the lithospheric contribution to the gravity anomaly, we further removed the effects associated with the sub-lithospheric mantle density structure and that due to the dynamic topography of the core-mantle boundary (CMB). When calculating the sub-lithospheric mantle gravity, we assume a spherical Earth that is discretized by 16.8 million tesseroids with a size of 1° × 1° × 10 km. The same mantle density and viscosity profile are used as that employed in estimating mantle dynamic topography. We found that the gravity effect of CMB topography cancels much of the LLSVP density effect, and that the resulting sub-lithospheric gravity anomaly (Fig. D.3**b**) is mostly affected by upper mantle buoyancy, especially the localized sub-lithospheric hot mantle beneath northeast Africa (Figs. 5.3**a**, D.5). Encouragingly, the inferred lithospheric gravity anomaly map (Fig. 5.2**b**) highlights the prominent negative gravity features associated with the high residual topography (Fig. 5.2**a**), almost all of which fall in cratonic regions. Consequently, these results reinforce the existence of local buoyancy heterogeneities within the cratonic lithosphere.

C.3 Modeling mantle flow and seismic anisotropy in South America and Africa

The plate velocities of South America and Africa have remained largely unchanged since 60 Ma (Fig. 5.1), implying a relatively stable mantle shear direction. Therefore, we approximate mantle-flow-induced anisotropy beneath Africa using the relative motion between the lithosphere and the deep mantle. However, mantle flow below South America has also been influenced by Cenozoic subduction of the Nazca plate, causing a deviation of flow from the absolute plate motion of South America (Hu et al., 2017). Therefore, we designed a geodynamic model that reproduces the Nazca subduction history since 100 Ma and used the resulting mantle flow history to compute anisotropy below South America (Hu et al., 2017).

To quantitatively estimate the Cenozoic mantle flow and the resulting lattice preferred orientation of mantle minerals, we simulate the subduction history surrounding the South American continent since 100 Ma. The numerical model is centered on South American continent and covers a 100° × 100° × 2900 km physical domain in the EW × NS × vertical directions, respectively, to best represent the mantle dynamics. We adopt a forward model using a sequential data assimilation technique, such that the past subduction history is consistent with the reconstructed plate motions and seafloor age from Müller et al. (2016), and that resulting present-day slab structure satisfies that inferred seismically (Benioff zones in the upper mantle and seismic

tomography in the lower mantle). A simultaneous match of all these observational data results in a tightly constrained history of mantle flow, as well as thermal and viscosity profiles of the geodynamic model. More details of the model set up and mantle flow analysis can be found in Hu et al. (2017). Thus predicted mantle flow beneath South America differs significantly from the direction of its absolute plate motion, indicating the dominant role of the subduction Nazca slab along the west coast and the secondary effects from slabs in the north (Hu et al., 2017).

Subsequently, we utilized the resulting Cenozoic mantle flow to calculate the present-day seismic anisotropy below South America. We assumed an initial mantle condition with randomly oriented olivine crystals, and then advected these crystals through the mantle flow to the present. The resulting anisotropy is mostly sensitive to the flow during the past 60 million years (Hu et al., 2017). In order to evaluate the relationship between the observed surface wave anisotropy at lithosphere depths with that predicted from the mantle flow, we systematically vary the geometry and thickness of the South American cratons. We found that the best-fit model requires thick (>200 km) AZ and RP cratons to match the observed anisotropy that is both low-amplitude and mis-aligned with the mantle flow. However, in order to predict the large-amplitude and flow-parallel anisotropy beneath southeast Brazil, the model requires a thin (<100 km) SF craton and its surrounding continent. Although we didn't model the thermal growth of the SF craton during the Cenozoic due to the limited numerical resolution of the large-scale model, the implication from the temporal development of seismic anisotropy suggests that the cratonic root must be largely absent during early Cenozoic and that subsequent growth of the root should have had the same anisotropy signature as presented in Figure 5.4.

The above approach of approximating seismic anisotropy is further confirmed by the data assimilation model: beneath an overriding plate like South America, mantle flow is controlled more by the slab-induced Poiseuille flow, and that beneath a non-overriding plate is dominated by plate-motion-controlled Couette flow (Fig. 5.3). This means we can estimate the overall anisotropy pattern using the surface plate motion in regions far away from subduction zones, such as Africa.

C.4 Discussion about lithosphere density and delamination

Here we provide more discussions about the logic of lithosphere structure and evolution.

First, the compositionally denser lowermost lithospheric layer is inferred by comparing Cretaceous uplift (several kms) and present high topography of the delaminated craton (without

the original dense layer) to that of intact cratons (with the original dense layer). This observation suggests that the buoyancy of the cratonic lithosphere after delamination increases relative to pre-delamination, even after the full thermal recovery, as it has now. This increase cannot be due to upper lithosphere modification, since most changes in the depleted lithosphere should decrease, instead of increase, its buoyancy. Therefore, the best candidate for the buoyancy change is through the loss of original high-density material that most likely resides at the bottom of the lithosphere. In fact, the great depth of this layer (>200 km, see Fig. 5.5), together with its tendency to sink instead of rise, may have been inadequately sampled by xenoliths, which usually come from a depth range of <200 km. Seismological images clearly show that most cratonic lithosphere extends to below 200 km, providing room for this layer to exist. In cratons that have experienced shearing or delamination in the lower lithosphere, the re-stabilized or regrown thermal boundary would be cooler than but not necessarily chemically distinct from the asthenosphere. However, the negative thermal buoyancy of this lowermost lithosphere would be partially offset by the compositional buoyancy of the shallower cratonic mantle, enabling the persistence of the observed high residual topography (Figs. 5.2a, 5.5c). This new model implies a greater density stratification than that already inferred from mantle xenoliths that sample the lithosphere down to ~200 km depth (Lee et al., 2011; Guillocheau et al., 2012).

Second, we suggest that xenolith data actually support our inferred lithosphere structure. As many earlier studies show, the extent of lithosphere depletion (through measuring Mg #) decreases with depth. Meanwhile, more high-density minerals, such as garnet, occur in the lower portion of the cratonic lithosphere, so the lowermost cratonic lithosphere could be compositionally denser than the ambient mantle, if enough garnet is present. In fact, some earlier studies already imply a similar lithosphere structure as we present in this study. For example, Table 1 in Kopylova and Caro (2004) showed the mineral abundances of peridotites from the southeast Slave Craton. The percentage of garnet in coarse garnet peridotite and deformed garnet peridotite can reach up to 10%, while that of garnet-rich wehrlites can reach ~20%, which could significantly increase the density. From equilibrium pressure and temperature estimates, these mantle xenoliths represent a depth range of ~160-250 km in the Slave Craton (Fig. 5.8 in Kopylova and Caro, 2004). Similarly, Griffin and O'Reilly (2007) inferred an eclogite-enriched layer at the base of the depleted subcontinental lithospheric mantle from xenoliths and proposed that eclogites may make up at least 30% of the mantle in this layer. These are potentially consistent with our model, in which a

garnet-enriched zone represents our inferred dense basal layer (Fig. 5.5). We realize, however, that a systematic study of the depth-distribution of iron depletion and garnet-enrichment from xenoliths is necessary in future research.

Finally, we suggest that several tectonic drivers should exist for delamination to take place. These include 1) long-lived mantle plumes like those occurred since the Jurassic (Yaxley et al., 2013) must develop, in order to efficiently weaken the lower lithosphere by thermal softening and metasomatism (Wang et al., 2015); 2) Additional density increase during metasomatism and plume impingement would enhance lower lithosphere instability; 3) Both the Precambrian Pan-African orogeny (Alkmim et al., 2006) and the Mesozoic opening of the Atlantic margins created internal weakness and lateral thickness variations in the lithosphere, favoring edge-driven convection (King and Ritsema, 2000) and delamination (Fig. 5.5). The coexistence of these preconditions could explain localized lithosphere removal and resulting high residual topography along the south Atlantic margins (Fig. 5.2a), as well as the more widespread realignment of lithospheric fabric (Fig. 5.4).

C.5 Code availability

The original version of the CitcomS code used to simulate mantle convection can be accessed at www.geodynamics.org/cig/software/citcoms/. The code used to generate plate-motion data can be accessed at www.gplates.org. The code used to make the figures can be accessed at www.soest.hawaii.edu/gmt/ and www.paraview.org/.

C.6 Data availability

The tomography model SEMum2, the crustal model CRUST1.0 and the surface wave anisotropy model of Debayle et al. (2016) can be accessed at www.ds.iris.edu/ds/products/emc/. The tomography model S40RTS can be downloaded at http://jritsema.earth.lsa.umich.edu//Research.html. The surface wave anisotropy model of Yuan and Beghein (2013) and (Schaeffer and Lebedev, 2016) are available through the links http://faculty.epss.ucla.edu/~cbeghein/research/models-download/ and https://andrewjschaeffer.wordpress.com/tomography/sl2016sva/#ModelDownloads, respectively.

APPENDIX D: SUPPLEMENTARY TO CHAPTER 5

Supplementary Materials:

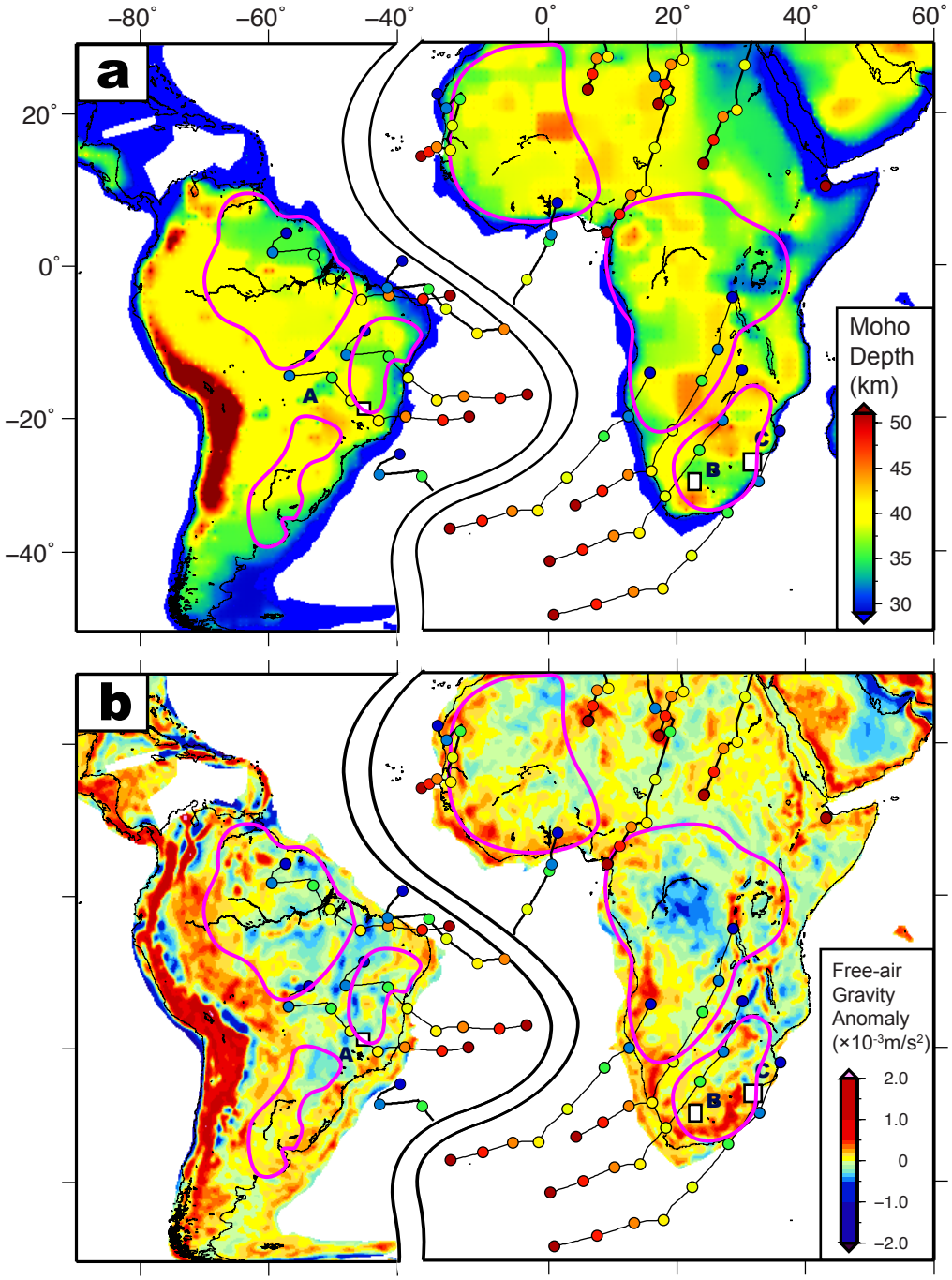

Figure D.1. Moho depth and Free-air gravity anomaly. **a**) Moho depth from Crust1.0 (Laske et al., 2013). Note the overall shallower Moho at regions with high surface topography (Fig. 5.1). This correlation remains robust from multiple regional seismic studies (Reid et al., 2012; Assumpção et al., 2013; Liu et al., 2016; Globig et al., 2016). **b**) Free-air gravity anomaly from the World Gravity Map database (Bonvalot et al., 2012).

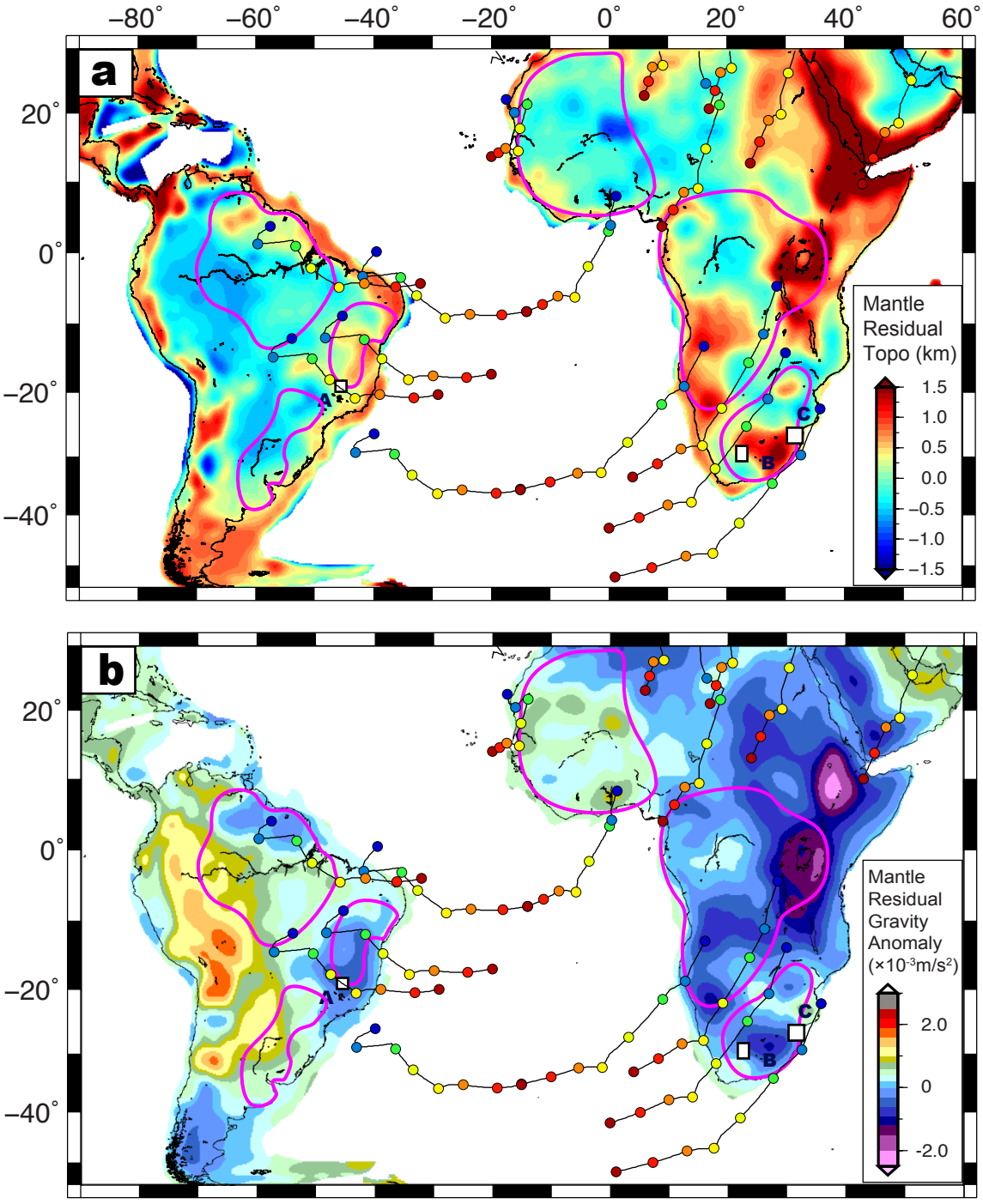

Figure D.2. Mantle residual topography and mantle residual gravity anomaly. **a**) Airy corrected isostatic residual topography, using the Crust1.0 model (Laske et al., 2013). This is effectively the mantle residual topography that includes both lithosphere and sub-lithospheric mantle contributions. **b**) Same as **a**)**,** but for gravity. Here effects from both surface topography and crustal mass anomalies from Crust1.0 are removed from the free-air gravity anomaly map. Note the strong correlation between two maps, indicating the control from the mantle.

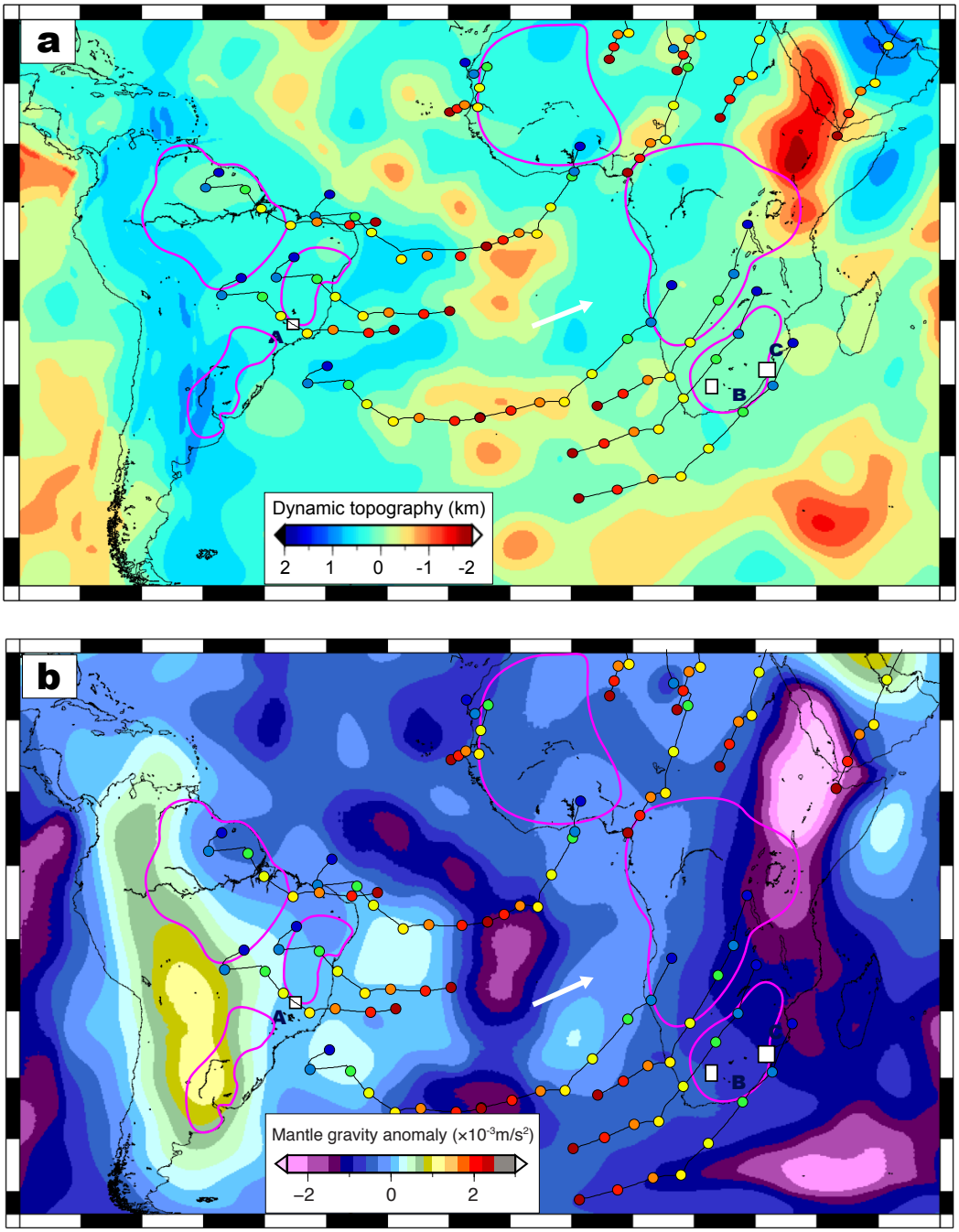

Figure D.3. Present-day dynamic topography and sub-lithospheric gravity contribution in South America and Africa. **a**) Calculation dynamic topography due to sub-lithospheric convection based on tomography SEMum2 (French et al., 2013), using the empirical seismic velocity to density conversion from Simmons et al. (2009) and by assuming an overall neutrally buoyant continental lithosphere above 300 km. The apparent discontinuity in topography along the South American trench is due to the assume lithosphere thickness variation at this location. **b**) Calculated sub-lithospheric gravity anomaly due to the same density structure as in **a**) and the core-mantle boundary topographic effect. Note the uplift pattern in EAR and neutral-to-negative topography over other regions of the continents.

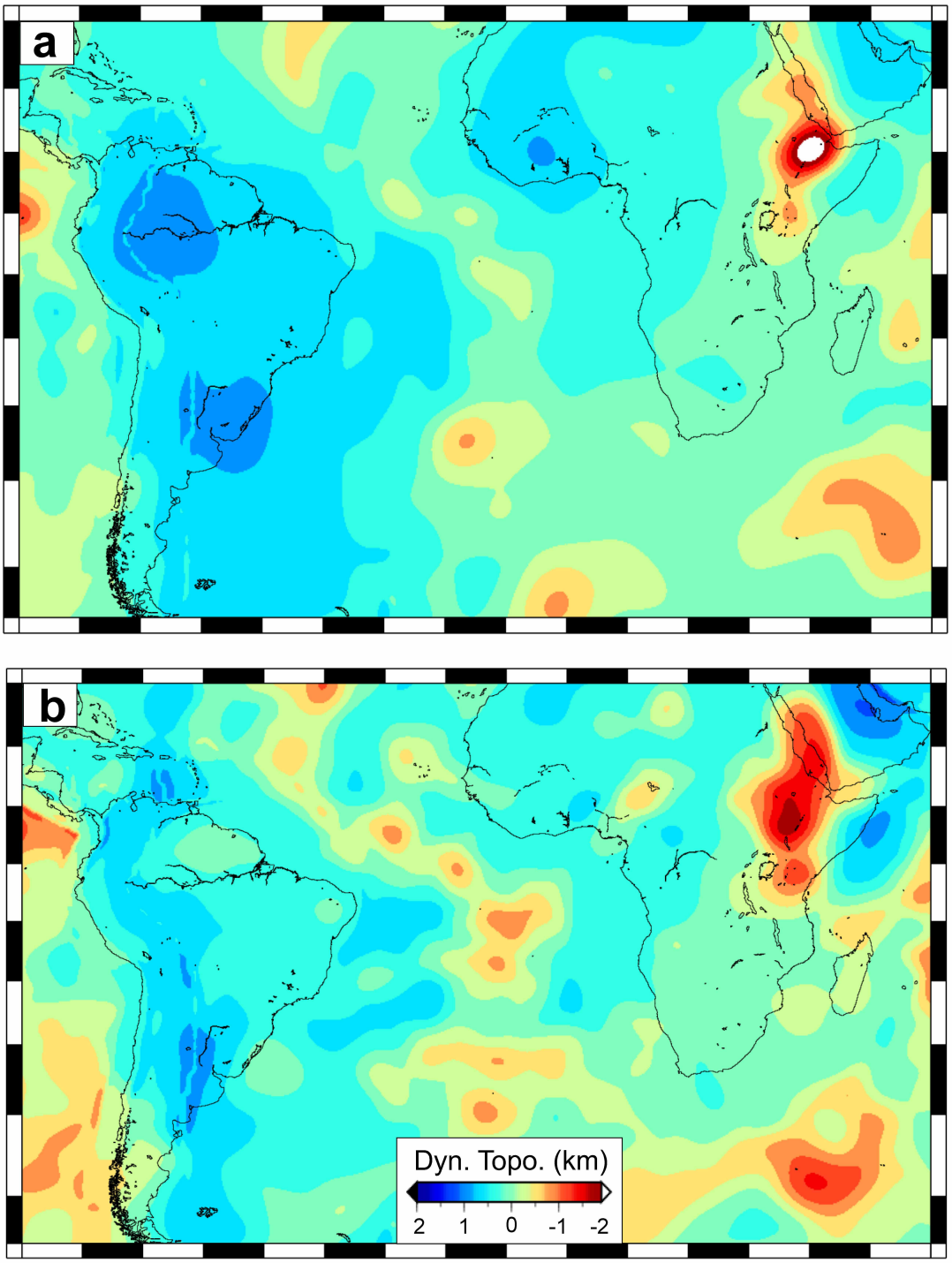

Figure D.4. Dynamic topography calculated based on S40RTS (a) and SEMum2 (b). The two models generate similar topography patterns, including both long- and short-wavelengths.

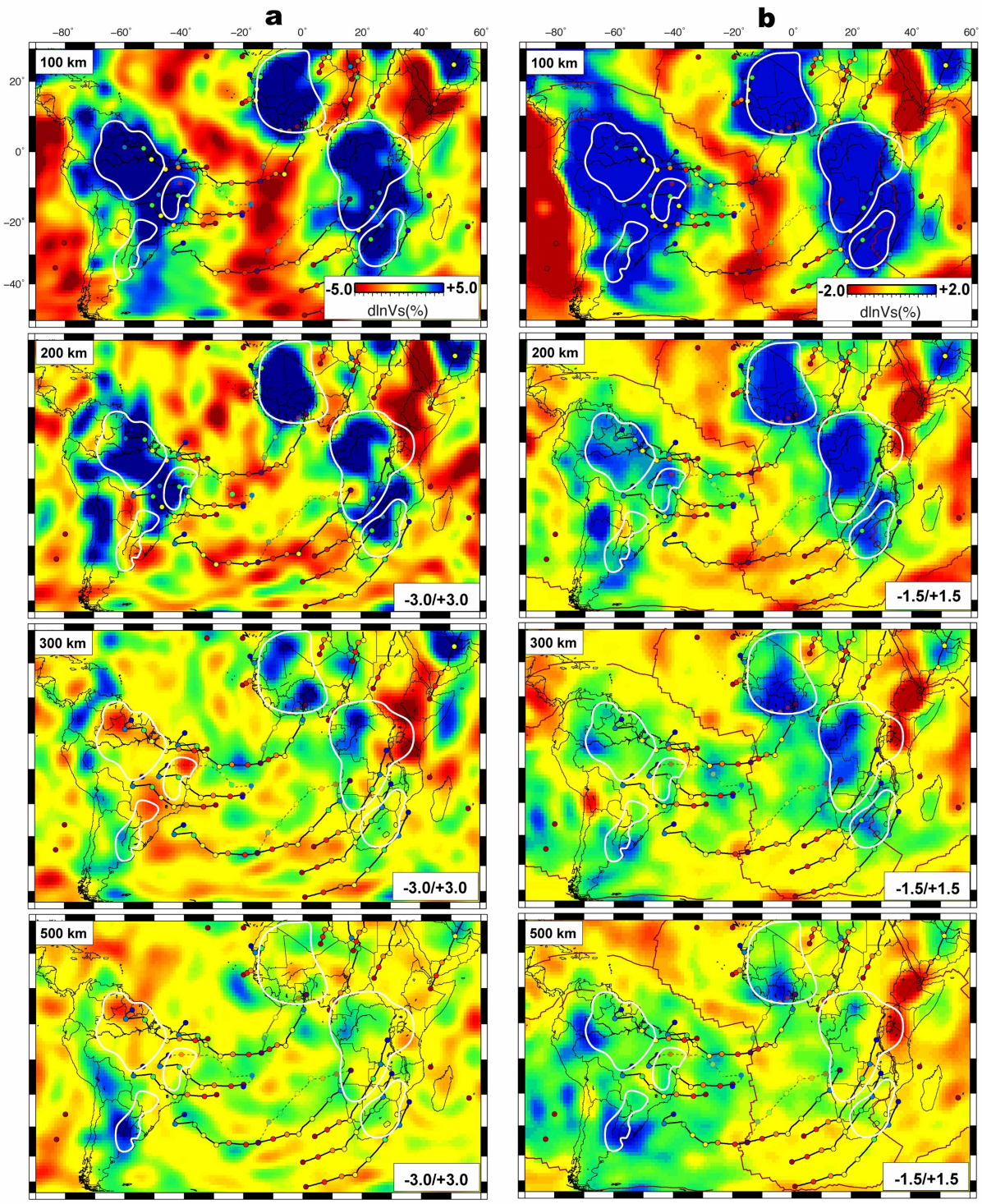

Figure D.5. Upper mantle seismic structures from **a**) SEMum2 and **b**) S40RTS. White dashed contours outline major cratons. Note the presence and similar distributions of fast seismic velocity features between South American and African continents in both tomography models. These fast anomalies also generally align with the hotspot tracks.

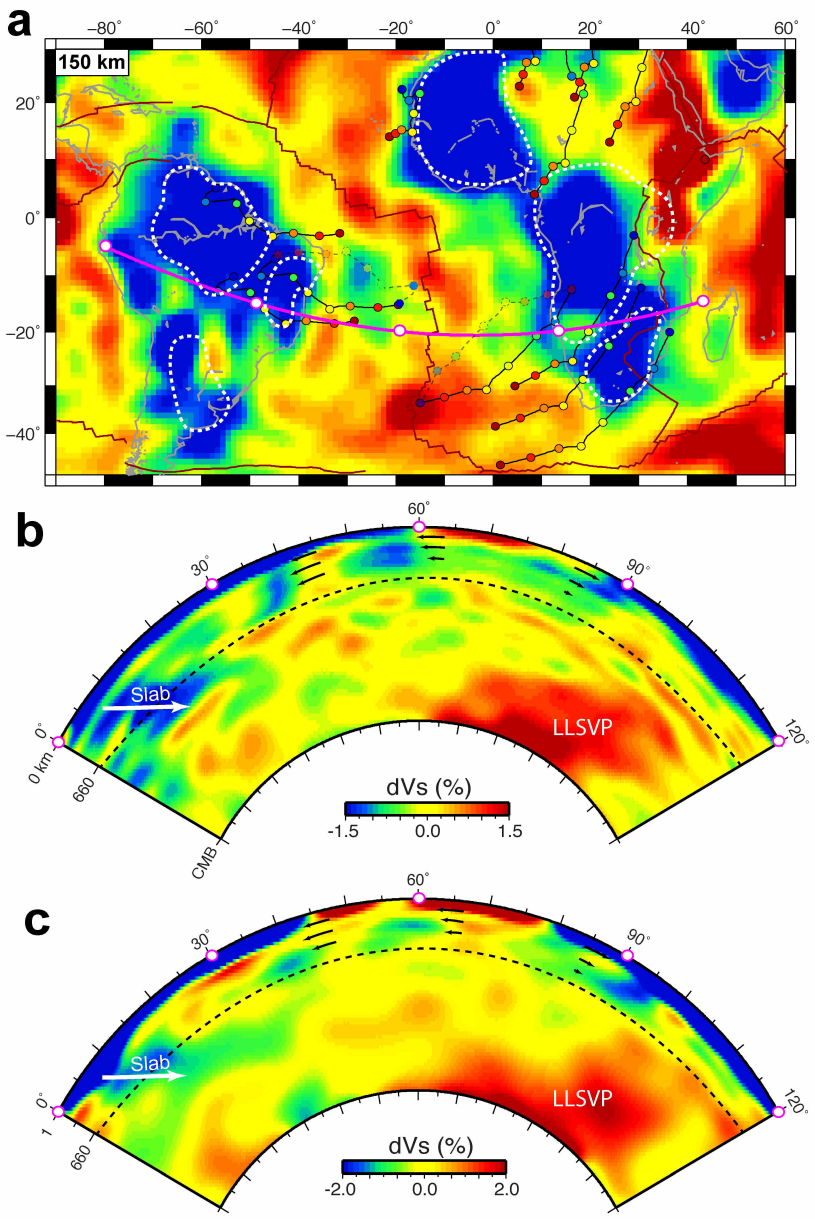

Figure D.6. Mantle seismic structure below the study region. a) Map view at 150 km from S40RTS. b) Cross section view from S40RTS along the profile shown in a. c) Same as b, but for SEMum2. Notice the similar distribution of fast upper mantle anomalies beneath the Atlantic.

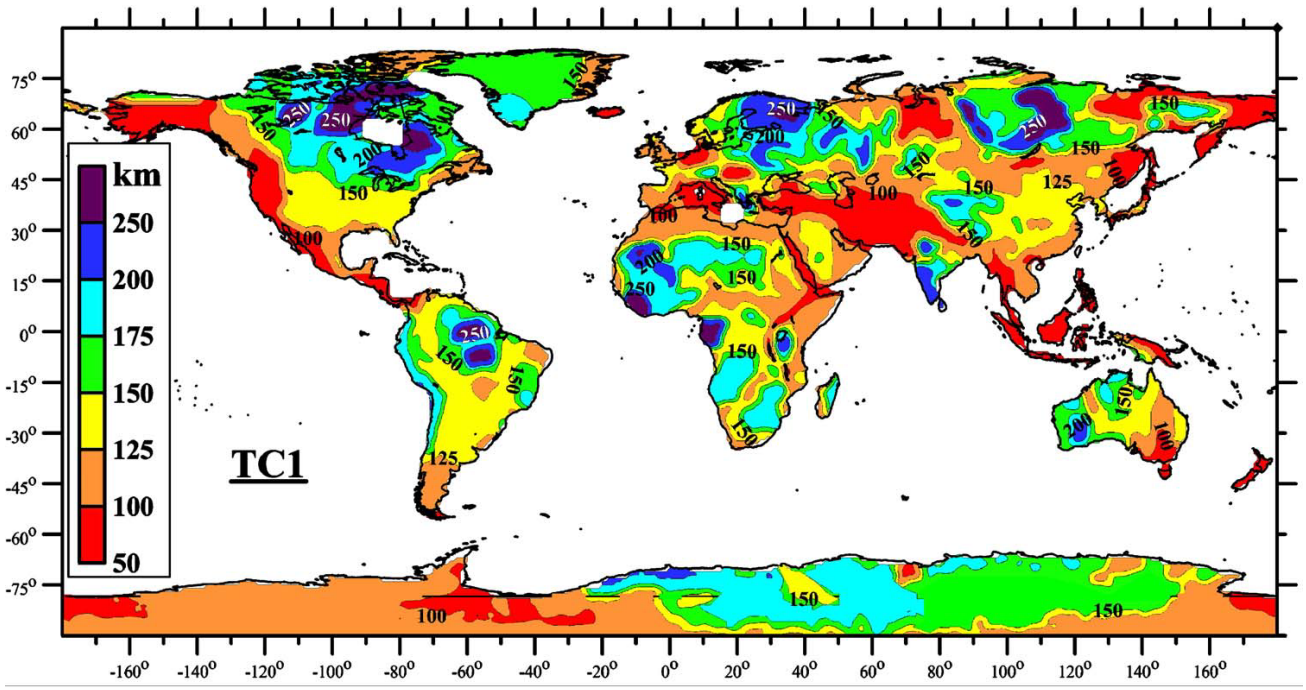

Figure D.7. Global thermal thickness of continental lithospheres on a 1° × 1° grid. The values are based on typical continental geotherms and tectonic age of the basement (From Artemieva, 2006). Note the similar thermal thickness (~200 km) of major South American and African cratons and their similarity to other cratons on Earth. Also note the lack of correlation between the lithosphere thickness and the pattern of positive residual topography and mantle gravity anomaly shown in Fig. 5.2.

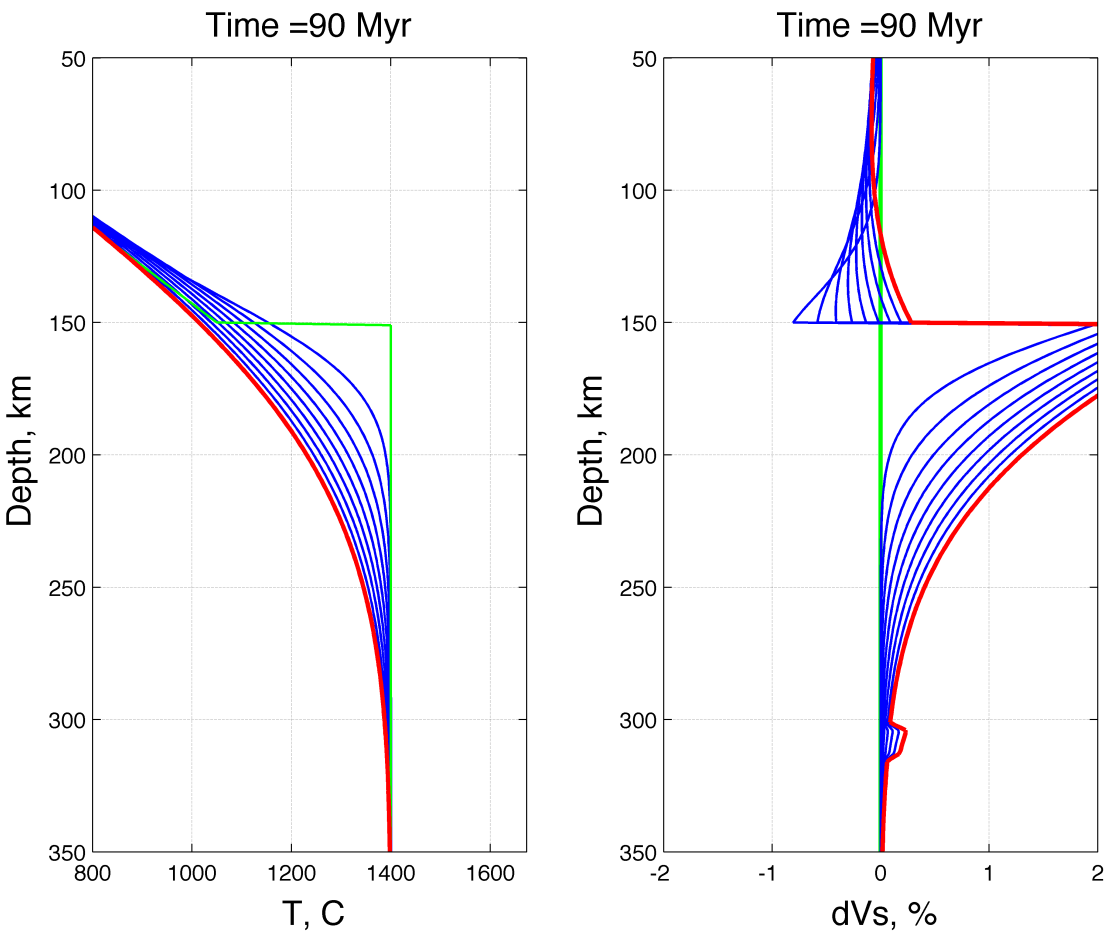

Figure D.8. Thermal restoration of an initially lost cratonic root. (Left) Temporal growth of a new thermal root over a period of 90 Myr. (Right) Corresponding Vs profile relative to the initial condition. The green and red curves represent the initial (90 Ma) and final (0 Ma) profiles, assuming an initial root loss below 150 km. Blue curves outline thermal growth with a 10-Myr increment. Note that Vs anomaly at 200-300 km depths is <2 % after a 90-Myr growth, smaller than that observed in tomography (Fig. D.5, D.6). This suggests that part of the lowermost cratonic roots survived delamination.

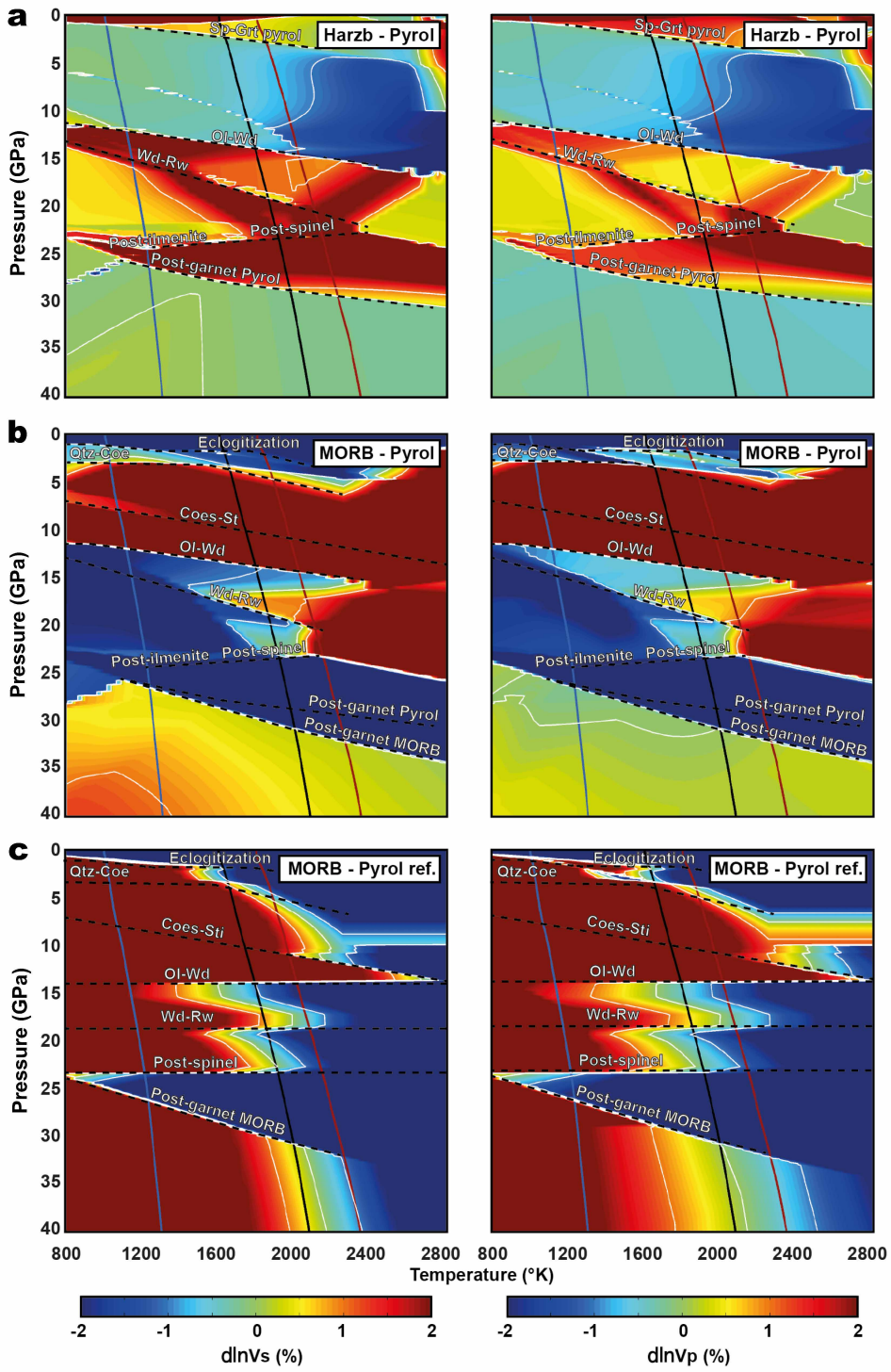

Figure D.9. Depth-dependent shear (left) and compressional (right) wave velocity anomalies of different mantle temperatures and compositions, relative to a pyrolitic mantle (computed with HeFESTo, Wittlinger and Farra, 2007). **a**) Thermal effects on velocities for a pyrolitic mantle. **b**) Combined effects of composition and temperature for harzburgite (depleted cratonic lithosphere) relative to a pyrolitic mantle at ambient conditions (black curve). **c**) Same as b but for MORB (garnetitic assemblages). The blue, black and magenta lines are the 1000, 1600 and 1800 K

Figure D.9. (cont.)
adiabats, corresponding to approximately the slab interior, ambient mantle and hot plume. Thin white lines indicate -1, 0 and +1 % velocity anomaly isocontours. Dashed black lines indicate major phase transitions. Abbreviations: Sp = Spinel; Grt = Garnet; Qtz = Quartz; Coe = Coesite; Sti= Stishovite; Ol = Olivine; Wd = Wadsleyite; Rw= Ringwoodite.

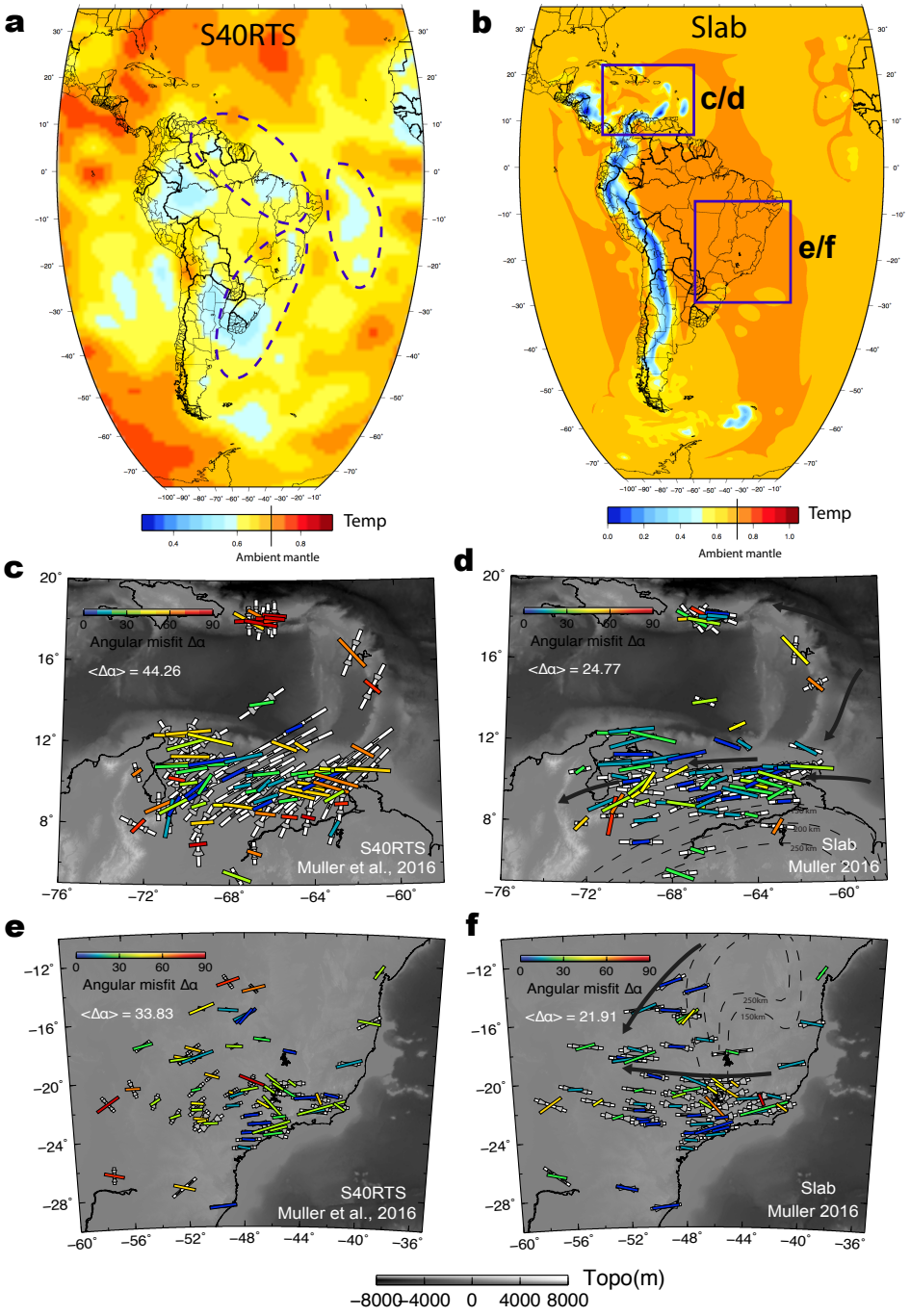

Figure D.10. The non-dimensional temperature fields at 450 km depth of instantaneous flow models based on S40RTS (**a**) and that of the time-dependent slab model (**b**). Shear wave splitting

Figure D.10. (cont.)

(SWS) fit (from Hu et al., 2017) for the two flow models at (**c**, **d**) and the Caribbean Plate region and (**e**, **f**) eastern South America, where SWS data are available. Background color represents the topography. Note the significantly improved fits in the slab model compared to the tomography-based model for both regions. This can be seen from both the spatial distribution (color shows angular misfit at each station) and regional average misfit (numbers) of the seismic anisotropy. The reason the tomography-based model fits the data much worse is because of the local convection from the fast anomalies (outlined in **a**) below the Atlantic margin. This suggests that these anomalies should be neutrally buoyant.

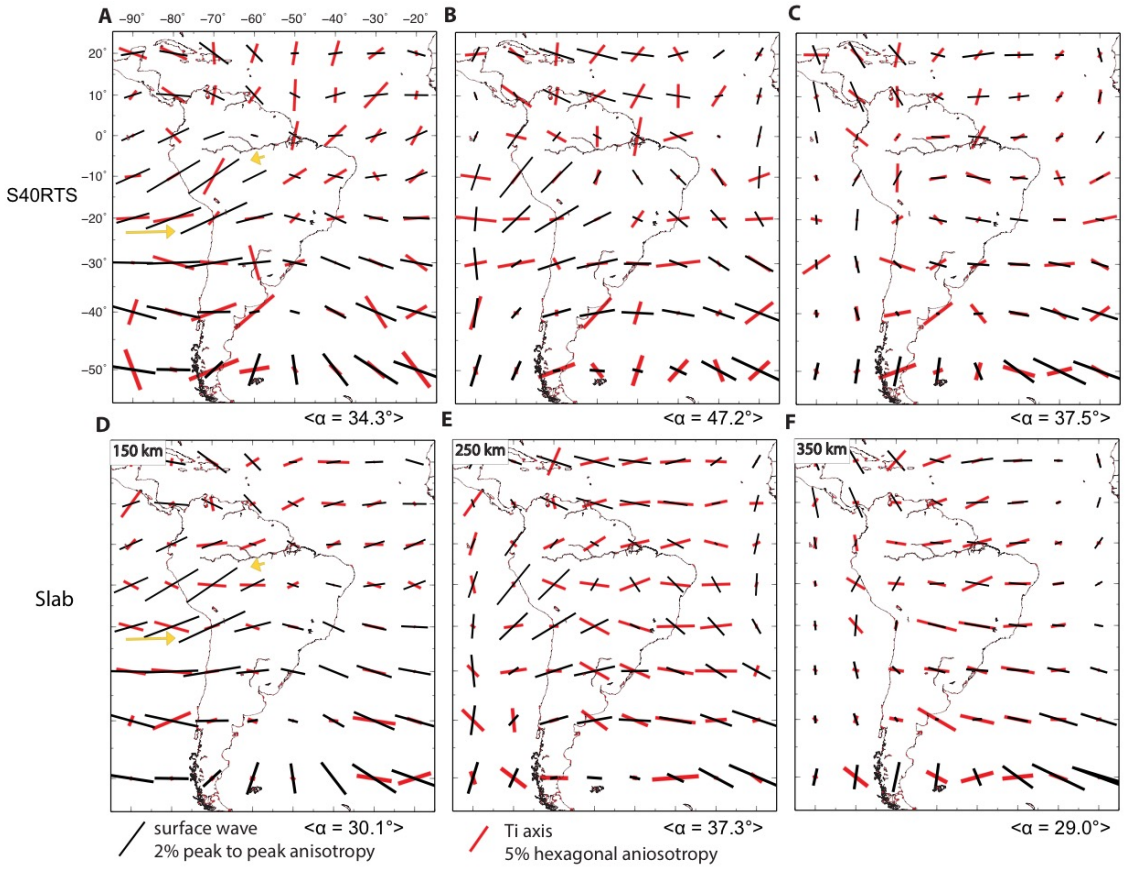

Figure D.11. Comparison of the observed and predicted azimuthal anisotropy (from ref. 45) for the instantaneous model based on S40RTS (**a-c**), and the time-dependent slab model (**d-f**). Observed azimuthal anisotropy from Yuan and Beghein (2013) is shown with thin black bars, and the TI axes of predicted LPO (Hu et al., 2017) are represented as thick red bars. Yellow arrows in **a** and **d** indicate the present absolute plate motion. The average misfit is shown below each figure. Note that the time-dependent slab model better matches the depth-dependent anisotropy than the tomography-based model.

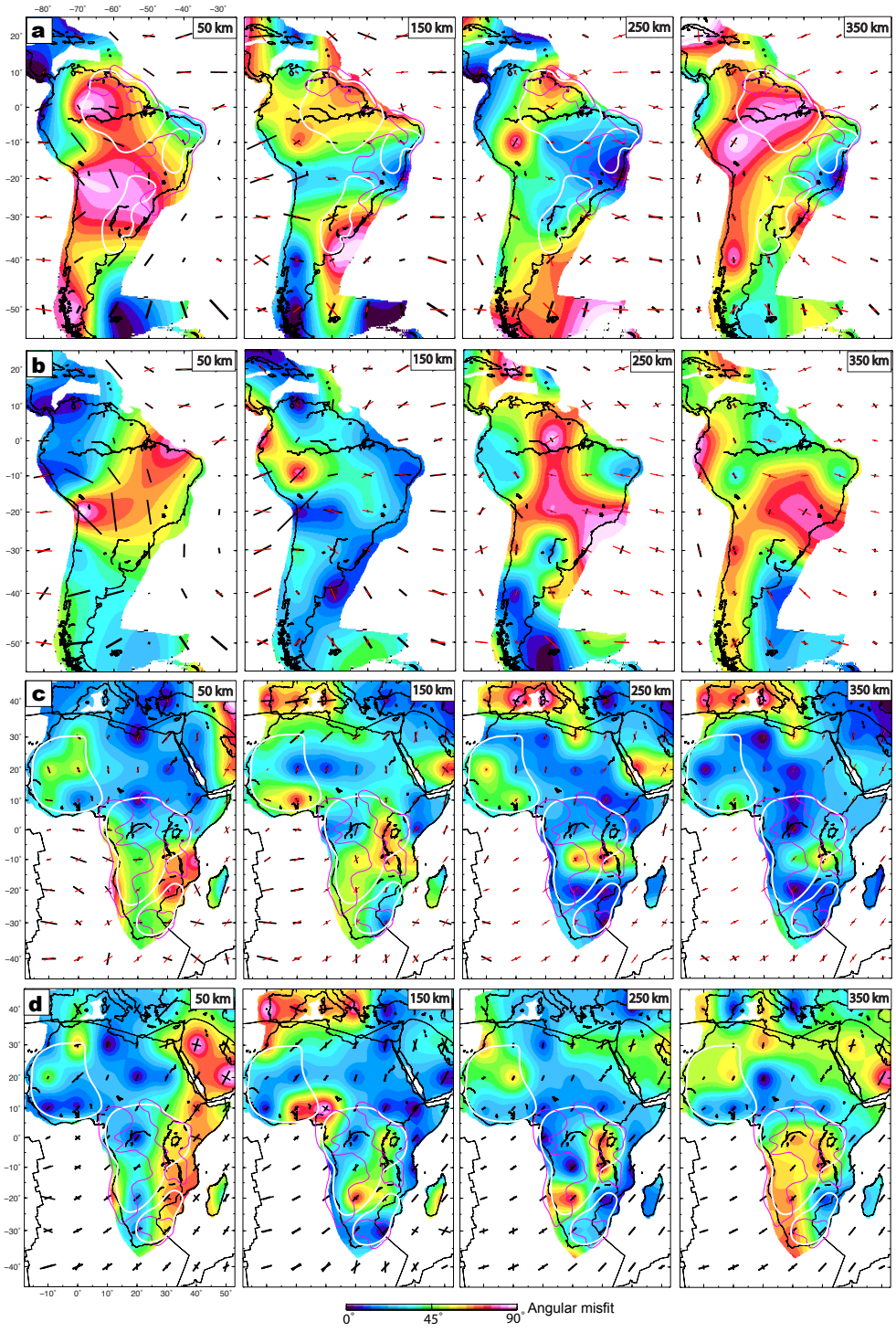

Figure D.12. Comparison of observed and mantle-flow induced seismic anisotropy. Similar to Figure 5.4, but with observed anisotropy from Schaeffer and Lebedev (2016) (**a, c**) and that from Debayle et al. (2016) (**b, d**). In a & c, the realignment of lithospheric seismic anisotropy in the thermally reestablished lithosphere (including SF, western CG and KH) below 100-150 km remains similar to that observed in Figure 5.4, confirming the main conclusion of lower lithosphere deformation in this study. The relatively large misfit at asthenosphere depth (350 km) below South

Figure D.12. (cont.)
America seems to suggest that the model of Schaeffer and Lebedev (2016) has an inadequate resolution at this depth, because our recent systematic study of upper mantle flow (Hu et al., 2017) supports mantle-flow-driven deformation in this region. The model from Debayle et al. (2016) (**b, d**) is similar to the Schaeffer & Lebedev model at depth above 150 km, but shows dramatically different anisotropy pattern at great depths. Since this model fails to match our well-predicted asthenospheric deformation and likely the shear-wave splitting observations over South America[44] (Fig. D.12), we suggest that the other two anisotropy models (Yuan and Beghein, 2013; Scheaffer and Lebedev, 2016) better represent lower-lithosphere fabric in our study region.

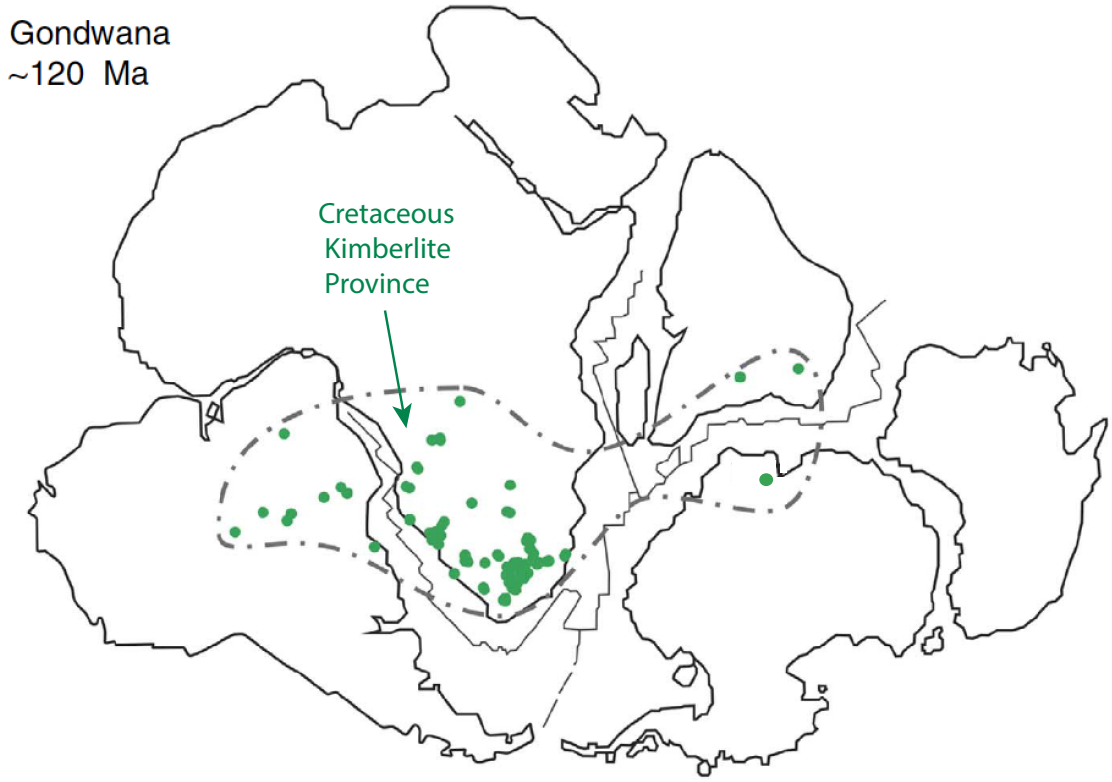

Figure D.13. Localities of Cretaceous-aged kimberlites across the Gondwana Lands (modified from Yaxley et al., 2013). Reconstruction of Gondwana is at ~120 Ma, and Cretaceous kimberlites are shown as smaller green dots surrounded by a dashed line. Note the close similarity of the kimberlites province with the regions where present-day lower lithosphere seismic anisotropy is realigned by the Cenozoic mantle flow (Fig. 5.4).

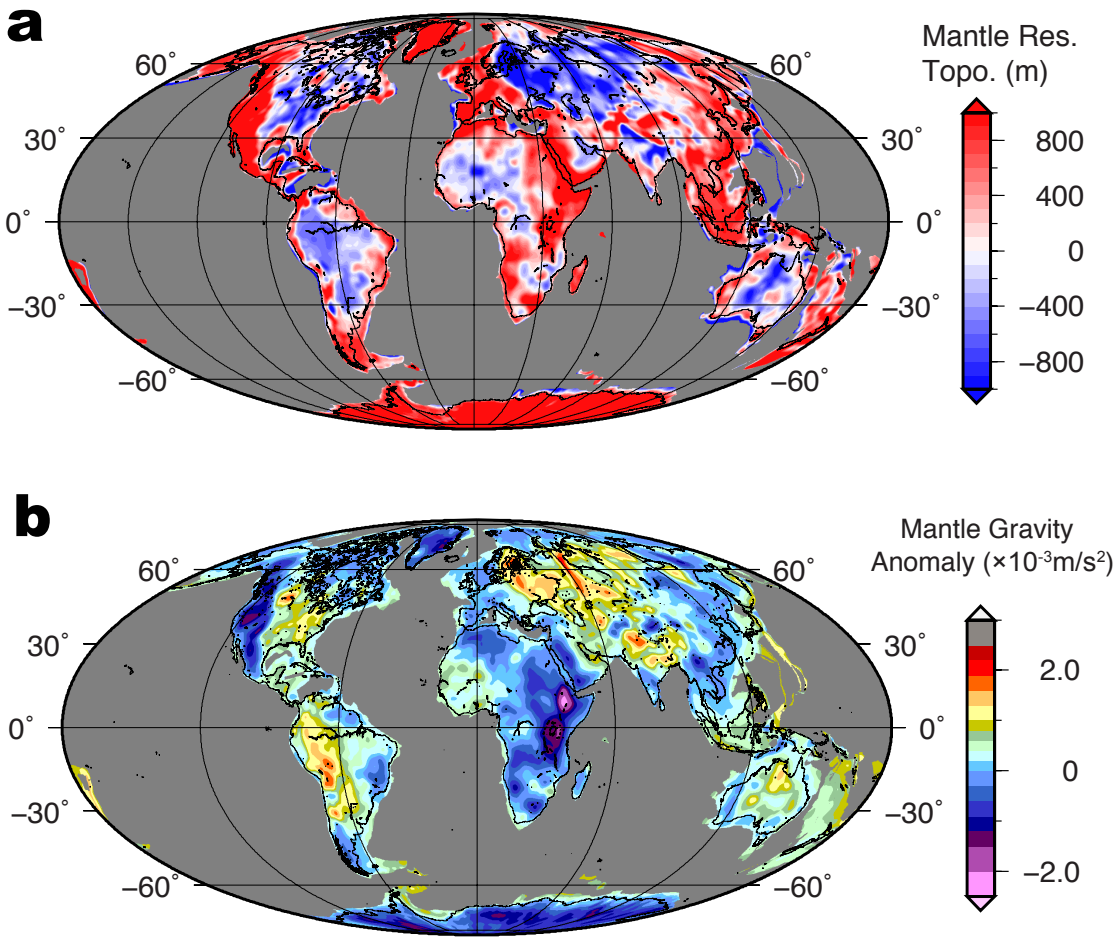

Figure D.14. Mantle residual topography (**a**) and mantle gravity anomaly (**b**) at the global scale. These are with identical calculations to those in Figure D.2. Note the similar positive residual topography and negative mantle gravity in other destructed craton regions including East Asia and western North America.